Uniwersytet Wrocławski
Wydział Fizyki i Astronomii

mgr Michał Naskręt

Energy dependence of negatively charged pion production in nucleus-nucleus collisions

Zależność energetyczna produkcji ujemnie naładowanych mezonów pi w zderzeniach jądro-jądro

Praca doktorska wykonana pod kierunkiem
prof. dr. hab. Ludwika Turko
w Instytucie Fizyki Teoretycznej UWr

Wrocław 2021

UNIVERSITY OF WROCLAW

Abstract

Institute of Theoretical Physics
Department of Physics and Astronomy

Doctor of Physics

Energy dependence of negatively charged pion production in nucleus-nucleus collisions

by mgr Michał Naskręt

The thesis is focused on yields and spectra of primary negatively charged pions produced in strong and electromagnetic processes in inelastic ^{40}Ar+^{45}Sc collisions at six beam momenta: 13*A*, 19*A*, 30*A*, 40*A*, 75*A* and 150*A* GeV/*c*. The data was taken by the NA61/SHINE experiment at the CERN Super Proton Synchrotron (SPS) in year 2015.

The data was analyzed utilizing the so-called h^- method. The method is based on the fact that the vast majority of hadrons produced in a heavy ion collision are pions. Using this fact we can apply a correction based on Monte-Carlo generated pion spectra. The correction will be mostly geometric, but excludes also weak decays, secondary interactions and contamination of particles other than pions.

The corrected spectra undergo an extrapolation procedure in order to obtain full solid angle 4π spectra. This consists of an extrapolation using exponential formula in transverse momentum and a sum of two Gaussian functions in rapidity.

In order to compare obtained results with other measurements, a calculation of the number of wounded nucleons is necessary. This can't be done experimentally and the number is obtained using different Monte-Carlo generators. This allows us to normalize the pion production to collision system size.

Final experimental results consist of two-dimensional transverse momentum versus rapidity and transverse mass versus rapidity spectra, one-dimensional transverse momentum, transverse mass and rapidity distributions, and finally per event negatively charged pions multiplicities. These are discussed in view of predictions for the Quark-Gluon Plasma and compared to string-hadronic models which do not have the Quark-Gluon Plasma.

UNIWERSYTET WROCŁAWSKI

Streszczenie

Instytut Fizyki Teoretycznej
Wydział Fizyki i Astronomii

Doktor Fizyki

Zależność energetyczna produkcji ujemnie naładowanych mezonów pi w zderzeniach jądro-jądro

mgr Michał Naskręt

Głównym tematem pracy są krotności i widma ujemnie naładowanych mezonów pi, które powstały w oddziaływaniach silnych i elektromagnetycznych w nieelastycznych zderzeniach ^{40}Ar+^{45}Sc dla sześciu pędów wiązki: 13A, 19A, 30A, 40A, 75A i 150A GeV/c. Dane zostały zebrane przez eksperyment NA61/SHINE w ośrodku badawczym CERN na synchrotronie SPS (Super Proton Synchrotron) w 2015 roku.

Do analizy danych została wykorzystana tak zwana metoda h^-, która wykorzystuje fakt, że większość hadronów wyprodukowanych w zderzeniach ciężkich jonów to mezony pi. Metoda ta pozwala na poprawienie danych doświadczalnych za pomocą widm ujemnie naładowanych mezonów pi wygenerowanych z symulacji Monte-Carlo. Głównym elementem poprawki jest zwiększenie akceptancji geometrycznej. Poprawka eliminuje również produkty rozpadów słabych i oddziaływań wtórnych oraz cząstki inne niż mezony pi.

Poprawione widma są ekstrapolowane w celu uzyskania akceptancji w pełnym kącie bryłowym 4π. Procedura ta składa się z ekstrapolacji w pędzie poprzecznym z wykorzystaniem funkcji wykładniczej oraz ekstrapolacji sumy dwóch funkcji gaussowskich w pośpieszności.

Do obliczenia liczby zranionych nukleonów wykorzystuje się generatory Monte-Carlo. Pozwala to na znormalizowanie danych o produkcji mezonów pi względem początkowego rozmiaru systemu.

Na ostateczne wyniki doświadczalne składają się: dwuwymiarowe rozkłady pędu poprzecznego względem pośpieszności oraz masy poprzecznej względem pośpieszności, jednowymiarowe widma pędu poprzecznego, masy poprzecznej i pośpieszności, oraz średnie krotności ujemnie naładowanych mezonów pi na przypadek. Wielkości te są omawiane w kontekście przewidywań dotyczących plazmy kwarkowo-gluonowej oraz modeli, które nie uwzględniają istnienia plazmy kwarkowo-gluonowej.

Acknowledgements

I would like to pay my great respects to my beloved wife Karolina for dealing with me in the difficult time being PhD student. She gave me a great deal of much needed support and love.

Many thanks need to be addressed to the NA61/SHINE collaboration members for scientific support, advise and hard work needed to accomplish this thesis. In particular, Peter Seyboth and Marek Gaździcki deserve my deepest appreciation for great experience and knowledge they shared with me and for patiently dealing with my numerous flaws.

In the end, I would like to thank my supervisor – Ludwik Turko for teaching me a long lesson of being scientifically independent.

Contents

List of Figures

List of Tables

List of Abbreviations

SPS	**S**uper **P**roton **S**ynchrotron
NA61/SHINE	**North A**rea experiment number **61/S**PS **H**eavy **I**on and **N**eutrino **E**xperiment
QGP	**Q**uark-**G**luon **P**lasma
SM	**S**tandard **M**odel
QCD	**Q**uantum **C**hromo**d**ynamics
TPC	**T**ime **P**rojection **C**hamber
ToF	**T**ime **of F**light
PSD	**P**rojectile **S**pectator **D**etector
CP	**C**ritical **P**oint
SMES	**S**tatistical **M**odel of the **E**arly **S**tage
MWPC	**M**ulti**W**ire **P**roportional **C**hamber
ECR	**E**lectron **C**yclotron **R**esonance
LEIR	**L**ow **E**nergy **I**on **R**ing
BPD	**B**eam Position Detector
GEANT	**GE**eometry **AN**d **T**racking
MC	**M**onte-**C**arlo
PID	**P**article **ID**entification

Dedicated to my newborn child – Helena.

Chapter 1

Introduction

1.1 The Quark-Gluon Plasma

Due to the intriguing features of Quantum Chromodynamics (QCD), quarks and gluons under normal conditions are confined within hadrons and never detected free. However, hadrons in a system where pressure or temperature is high enough overlap. Deconfinement then occurs and a new enigmatic state of matter called the Quark-Gluon Plasma (QGP) is formed.

The QGP is believed to have existed in the Universe shortly after the Big Bang. This state of matter quickly cooled down as the Universe expanded and the quarks and gluons coalesced to form hadrons, in particular protons and neutrons. They, in turn, formed nuclei. The QGP is anticipated to exist in the cores of heavy neutron stars, where pressure is high enough to form this state. The only way to obtain the QGP for experimental observation is to accelerate nuclei to velocities close to the speed of light and collide them. Then, the energy density created in a collision might be enough to ”melt” the structure of hadrons and form a dense medium consisting of quarks and gluons. Signatures of existence of the new state of matter in heavy ion collisions were first observed in the measurements of the CERN SPS (Super Proton Synchrotron) heavy-ion experiments [1]. This was followed by first description of the properties of the QGP by experiments working on Relativistic Heavy Ion Collider (RHIC) at BNL, namely that the QGP can develop collective flow according to laws of hydrodynamics [2]. Presently, CERN experiments at LHC are focused on exploring the properties of the QGP in low baryon number density limit, which allows for comparisons with lattice QCD calculations [3], whereas NA61/SHINE at SPS (described in this thesis) and RHIC with its Beam Energy Scan (BES) program [4] are focused on investigating the phase diagram of strongly interacting matter. The latter activity will be also pursued by new experiments below the SPS energy range – NICA [5] and SIS-100 [6].

1.1.1 QGP production in high-energy collisions

High-energy experiments are performed using particle accelerators, which can accelerate protons and nuclei to velocities close to the speed of light. A bunch of particles traveling through an accelerator is directed into either a fixed target built from a single chemical element or beams traveling in opposite direction are made to collide. In such reactions, part of the collision energy is transferred into the production of new particles. An overview of a collision in a fixed target experiment is presented in Fig. 1.1. This state does not last long, as it quickly expands and cools down. At low enough energy density quarks and gluons of the QGP recombine into hadrons. Hadrons continue interacting. First, their yields and then their momenta stop to change. These moments are called chemical and kinetic freeze-outs, respectively. After kinetic freeze-out the particles fly without further interactions to the detector system in which their properties are measured.

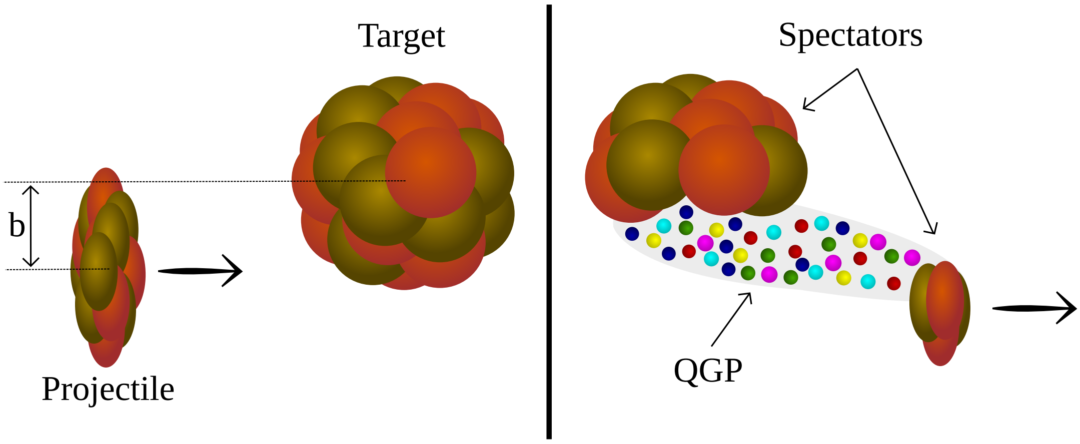

FIGURE 1.1: An overview of a heavy-ion high-energy collision in a fixed target experiment. Left-hand side presents the situation before and right-hand side after a collision.

1.2 Phase transition from hadronic matter to Quark-Gluon Plasma

Quarks and gluons at sufficiently high density are no longer confined inside the hadrons and become free. The process is known as the deconfinement. On the other hand, in a very hot and dense medium, the phase transition – chiral symmetry restoration – is expected to occur. These transitions – deconfinement and chiral symmetry restoration – are happening at essentially the same conditions [7].

The dependence of the phase of matter on the conditions of the system is usually shown on the "T-μ_B" plane, the phase diagram of strongly interacting matter. The plot in Fig. 1.2 shows the dependence of the phase in which the system exists on two variables – temperature T and baryo-chemical potential μ_B. In experimental high-energy collisions, by increasing the collision energy the temperature at the chemical freeze-out increases and the chemical potential decreases whereas by increasing the system size the temperature lowers and the chemical potential is approximately constant [8] (see Fig. 1.3).

Most of our theoretical knowledge of the phase diagram is restricted to the vicinity of $\mu_B = 0$, where lattice QCD methods can be employed. For this limit, lattice calculations have shown [11] that the change from the low temperature phase, where the degrees of freedom are hadrons, to the high temperature phase described by quarks and gluons is an analytic crossover. Present empirical estimates of the (pseudo) critical temperature give $T_C = 156.5 \pm 1.5$ MeV [12] and 164 ± 5 MeV [13], while lattice QCD calculation is 154 ± 9 MeV [14].

The nuclear matter in nuclei has low temperature $T \approx 0$ and baryon chemical potential of $\mu_B \approx 939$ MeV, which corresponds to the proton and neutron mass. A number of different model approaches indicate that the transition at large μ_B and small T is strongly first order [15, 16]. Since the first order phase transition cannot end at the starting point of the cross-over line, a critical point (CP) is expected somewhere in the middle of the diagram. The existence of the CP has not yet been proven experimentally. The points on the plot in Fig. 1.2 show approximate positions of experimentally established chemical freeze-out parameters of different collision energy.

1.3 Statistical Model of the Early Stage

The Statistical Model of the Early Stage (SMES) was developed in the late 90's based on the first measurements of central Pb+Pb collisions at CERN SPS energies (see Ref. [17]). The

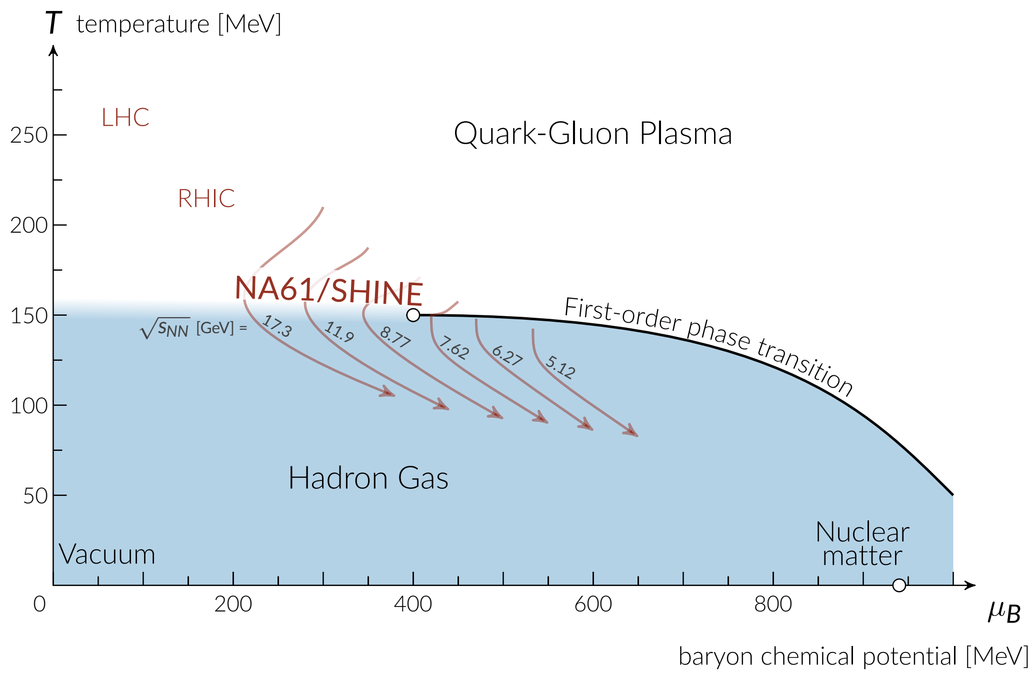

FIGURE 1.2: The phase diagram of strongly interacting matter. For low μ_B and temperatures $T \approx 155$ MeV a crossover between hadron gas and QGP occurs. For higher values of μ_B a first order phase transition is expected. Areas that are available to different experiments are marked with red text, whereas the red curves show a schematic visualization of the evolution of the produced matter for all the beam momenta used in ^{40}Ar+^{45}Sc collisions. The figure is taken from [9].

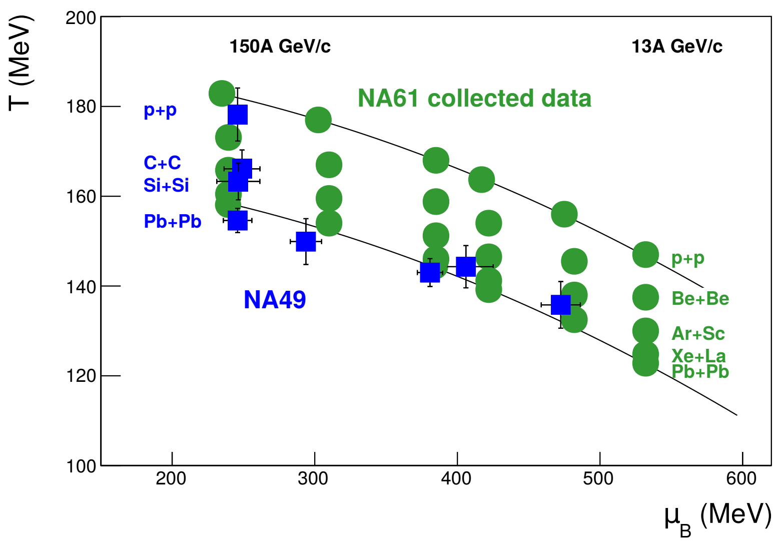

FIGURE 1.3: Region of the T-μ_B phase diagram explored by NA61/SHINE and NA49 experiments. Estimated chemical freeze-out points in NA49 (blue squares) and those expected in NA61/SHINE (circles) according to the different versions of thermal hadron gas model [8], including its questionable p+p application. This is an updated version of figure taken from Ref. [10].

model describes the transition between hadronic matter and the QGP and proposes a number of signals of the onset of deconfinement that can be tested experimentally. In the SMES, only systems produced with all conserved charges equal to zero are considered. Therefore, the properties are fully defined by the available energy and the volume in which production takes place. Only a fraction of the total collision energy is transformed into new degrees of freedom production (new particles), the rest escapes the fireball in forward and backward directions. The most important postulate of the SMES is that at the early stage of a heavy-ion collision, a maximum entropy equilibrium state is always created. The probability of a macroscopic state is proportional to the number of its microscopic realizations and formation of all microscopic states is equally probable.

The SMES predicts that at high collision energies the pure QGP state exists, whereas at low energies only hadronic gas is present. For intermediate SPS energies, existence of a mixed phase is postulated. The change from one state to the other should be reflected by a rapid change in the energy dependence of some properties of the produced particles.

The Landau model [18] describes the system's expansion process by hydrodynamical equations of the perfect fluid incorporating the conservation laws. In the model, the entropy and initial temperature of matter are proportional to the $F\left(\sqrt{\mathrm{GeV}}\right)$, the Fermi-Landau variable:

$$F = \left[\frac{\left(\sqrt{s_{NN}} - 2m_N\right)^3}{s_{NN}} \right]^{1/4},$$

where s_{NN} is the total center-of-mass energy and m_N is the nucleon mass. The use of the Fermi-Landau energy variable is convenient for future considerations since the mean multiplicity of pions in nucleon-nucleon[1] collisions is approximately proportional to F.

1.3.1 Signals of the onset of deconfinement from the SMES

Since the lightest and the most abundant particle produced in a heavy-ion collision is the pion, it will carry the majority of the entropy produced in a collision. The model predicts that the entropy will rise with the collision energy, but for the QGP phase the entropy increase will be faster than in the confined phase. The experimental probe of the model prediction is the average number of π mesons produced per collision ($\langle\pi\rangle$– the mean pion multiplicity). Since the collision system size will vary with the mass number of collided ions, one has to normalize $\langle\pi\rangle$ to the mean number of wounded nucleons $\langle W\rangle$ (the number of nucleons which interacted inelastically in the heavy ion collision). According to the SMES the ratio of the two $\langle\pi\rangle/\langle W\rangle$ can tell us which phase of strongly interacting matter a given collision system exists in. The change in the slope of the $\langle\pi\rangle/\langle W\rangle$ ratio will indicate the onset of deconfinement. The number of wounded nucleons is not measured experimentally and can only be calculated from models.

This signal of the onset of deconfinement is often called the "kink" and presented as a dependence of the $\langle\pi\rangle/\langle W\rangle$ ratio on the Fermi-Landau energy measure. Figure 1.4 shows an example of such a plot.

Another possible signal is called the "horn". In the deconfined phase the mass of the strange quark ($m_s \approx 100$ MeV) is lower than the temperature of the system ($T > 150$ MeV). Therefore, the strangeness to entropy ratio does not change significantly with the collision energy in this region. For the hadron gas state, the same ratio increases with F because the mass of the strangeness carriers ($m_K \approx 500$ MeV) is bigger then the system temperature

[1] For p+p interactions the values are isospin symmetrized and denoted as N+N [19]

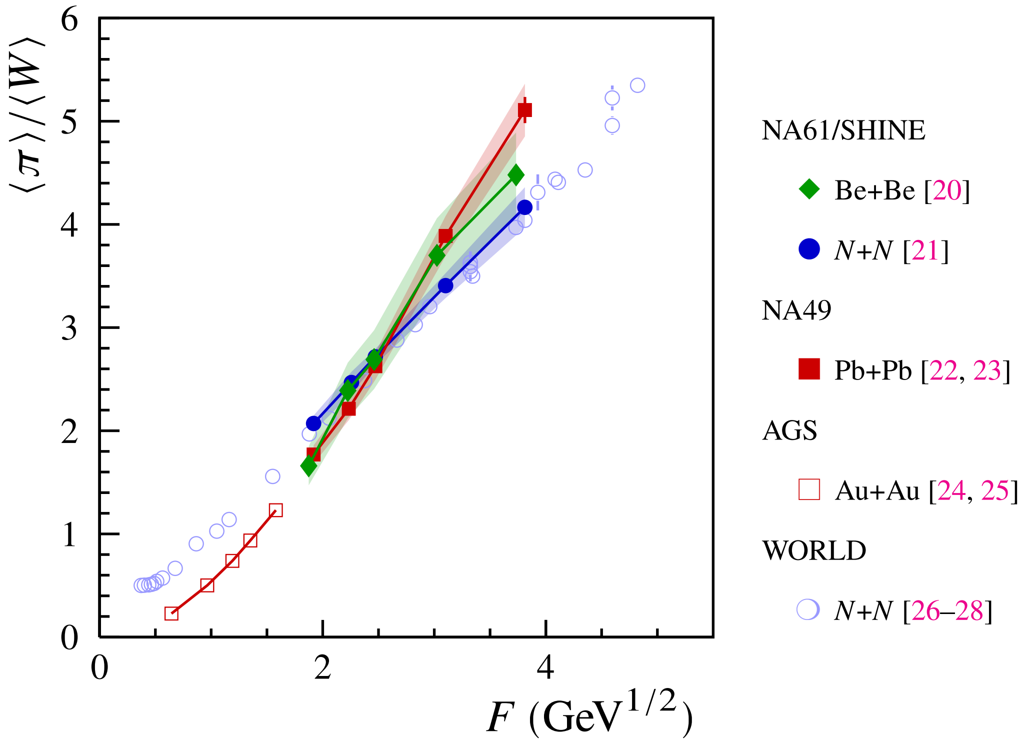

FIGURE 1.4: The "kink" plot showing the ratio of mean pion multiplicity $\langle\pi\rangle$ to the number of wounded nucleons $\langle W\rangle$ versus the Fermi energy variable $F \approx \sqrt[4]{s_{NN}}\left(\sqrt{\text{GeV}}\right)$. Results for inelastic nucleon-nucleon reactions and central nucleus-nucleus collisions are compared.

($T < 150$ MeV). In addition, at $T \approx T_c$ the ratio is higher than in the QGP phase. An experimental observable proposed to verify this observation was the ratio between the mean number of produced positively charged kaons to the mean number of positively charged pions $\langle K^+\rangle/\langle\pi^+\rangle$. SMES predicts the maximum of the ratio $\langle K^+\rangle/\langle\pi^+\rangle$ at mid-rapidity at the onset of deconfinement. The experimental data on the $\langle K^+\rangle/\langle\pi^+\rangle$ ratio reported in Ref. [29] is presented in Fig. 1.5.

1.4 NA61/SHINE and the search for the onset of deconfinement

NA61/SHINE (**N**orth **A**rea experiment number **61 / S**PS **H**eavy **I**on and **N**eutrino **E**xperiment) at the CERN SPS is a fixed target experiment which studies final hadronic states produced in interactions between various particles at different collision energies. The study of the onset of deconfinement of strongly interacting matter is the main part of the experiment's physics program. NA61/SHINE provides also reference measurements for neutrino and cosmic-ray physics.

NA61/SHINE's strong interactions program is focused on a two-dimensional scan varying the size and energy of the collision system. The scan in the collision energy axis is performed in vicinity of the onset of deconfinement in the beam momentum range of 13*A*-150*A* GeV/*c*. In the system size axis, the experiment varies between smallest collision system of *p*+*p* and heaviest Pb+Pb using elements which are stable and user-friendly. NA61/SHINE measured *p*+*p*, *p*+^{208}Pb, ^{7}Be+^{9}Be, ^{40}Ar+^{45}Sc, ^{131}Xe+^{139}La and ^{208}Pb+^{208}Pb.

An overview of the two-dimensional scan performed by the NA61/SHINE collaboration is presented in Fig. 1.6. The area of the scan can be roughly translated to the T-μ_B plane using the hadron gas model [8], which is presented in Fig. 1.3. The systematic scan done by NA61/SHINE shows that ^{40}Ar+^{45}Sc may be the smallest system to experience the phase transition between hadronic matter and the QGP in the CERN SPS energy range.

An advantage of using a fixed target in heavy ion collisions is that it allows to cover low transverse momentum region of the phase space and to select events based on the energy of spectators from the beam nucleus independently from measurements of produced particles.

1.5 Novelty and author's contribution

The work presented here will focus on the analysis of experimental data from ^{40}Ar+^{45}Sc collisions. The data was taken by the NA61/SHINE collaboration in year 2015 at six beam momenta 13*A*, 19*A*, 30*A*, 40*A*, 75*A* and 150*A* GeV/*c*. Utilizing the so-called h^- method (described in detail in Section 5.2) the spectra and mean multiplicities of negatively charged pions are obtained. The method is based on the fact that $\approx 90\%$ of particles produced in a heavy-ion collision are pions. Results refer to negatively charged pions produced in strong and electromagnetic interactions.

The analysis of ^{40}Ar+^{45}Sc is a novel and interesting research topic. It allows to add earlier unmeasured ^{40}Ar+^{45}Sc data points to the "kink" plot in Section 7.4. This is indicative as a possible signal of the onset of deconfinement in the respective T-μ_B conditions and gives an insight into properties of the strongly interacting matter. Results obtained in this work will be helpful to improving theoretical models.

The data is one of the first, unique NA61/SHINE results on intermediate size systems with number of baryons between p+p and Pb+Pb collision systems. One of the novelties in the analysis is the use of the PSD (Projectile Spectator Detector) detector, that allows for precise measurement of the event forward energy. This, in turn, is a proxy for the event centrality. The ^{40}Ar+^{45}Sc data-taking was one of the first uses of this detector in NA61/SHINE.

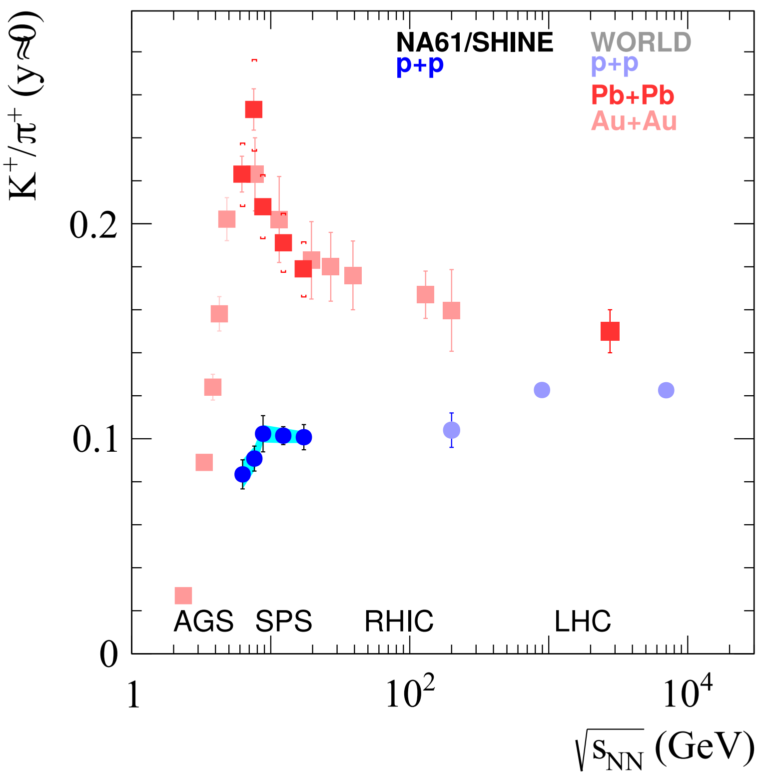

FIGURE 1.5: Energy dependence of the $\langle K^+\rangle/\langle\pi^+\rangle$ ratio at the mid-rapidity presented in Ref. [29]. The NA61/SHINE results for inelastic *p*+*p* interactions are shown together with the world data on *p*+*p* interactions as well as central Pb+Pb and Au+Au collisions [30–45]. Shaded bands show the systematic uncertainty.

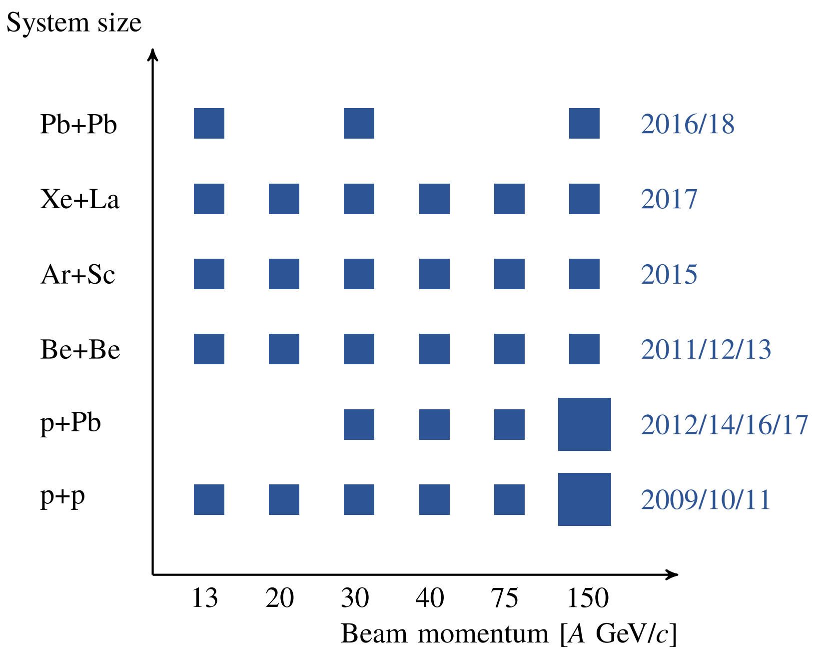

FIGURE 1.6: An overview of the NA61/SHINE's system size and collision energy scan. The boxes show the data that has already been taken and the large boxes mark systems for which large statistics were obtained.

The data on hadron production at the top SPS [46] energies indicated that the ratio of yields of pions and strange hadrons is approximately independent of the size of the colliding nuclei for central collisions of nuclei with mass number $A \geq 30$-40. Furthermore, results obtained within statistical models [8, 47] show that for these collisions calculations using an infinite volume approximation are valid. For average quantities this means that simple thermodynamical models can be used already for central Ar+Sc collisions in the whole SPS energy domain.

On the other hand, the duration of the expansion stage with purely hadronic degrees of freedom increases with increasing mass of the colliding nuclei. Consequently, the matter freezes out further away from the transition line. In order to minimize the role of hadronic re-scattering, collisions of medium nuclei are preferred. Collisions of nuclei of about the size of argon or xenon seem to be optimal for the study of the properties of the transition between the Quark-Gluon Plasma and hadron gas.

The analysis procedure started with creating and applying quality cuts on events and tracks in experimental data as well as in the Monte-Carlo (MC) simulation. Following this, centrality selection was performed utilizing information from the PSD detector. These two steps are described in Chapter 4. Next, the MC-generated correction factor was applied to experimental data to obtain the corrected spectra. In order to present results in full 4π phase space, the spectra had to be extrapolated. The two latter steps were accomplished according to prescription given in Section 5.2. A detailed analysis of statistical and systematic uncertainties is described in Section 5.3. The main result of the aforementioned steps are p_T, y spectra and the mean multiplicity of negatively charged pions produced in strong and electromagnetic interactions in 4π for the 5% most *central* events. The results are presented in Chapter 7.

Additionally, a detailed analysis of the mean number of wounded nucleons was performed in order to compare the results to other measurements and model calculations. The newly developed procedure for the analysis uses the Wounded Nucleon Model [48] calculation supported by the estimation of event forward energy to select the 5% most central events. This is described in Chapter 6 and a similar prescription will be used for other analyses by the NA61/SHINE collaboration.

In order to perform the analysis, a heavy involvement in the development and validation of the new NA61/SHINE Monte-Carlo software Luminance, as well as mass production of MC-generated events was necessary. The simulation was primarily used to correct the experimental data for 13*A* GeV/*c* beam momentum. This was necessary since an incorrect magnetic field configuration was used for producing the old *Legacy* MC-generated events for 13*A* GeV/*c* beam momentum. Other beam momenta were not affected by the configuration mismatch and *Legacy* MC-generated events were used.

The results presented in this thesis are also a subject of the NA61/SHINE collaboration publication [49]. At the moment of finishing this thesis the publication was reviewed by the collaboration, passed a CERN review process and was submitted to European Physical Journal C.

Chapter 2

NA61/SHINE experimental setup

2.1 NA61/SHINE detector overview

The NA61/SHINE detector is a large acceptance spectrometer located on the H2 beamline of the CERN SPS accelerator. The main part of the setup was inherited from the NA49 collaboration – four Time Projection Chambers (TPCs), two Time of Flight (ToF) walls and superconducting magnets. The novelty in NA61/SHINE is a high precision calorimeter, the Projectile Spectator Detector (PSD), and a new data acquisition system which allowed to increase data rate by a factor of 10, to 100 Hz.

NA61/SHINE plans on continuing the physics program at CERN after the Long Shutdown 2. The proposed measurements will focus on the direct charm hadron production in Pb+Pb collisions, nuclear fragmentation cross sections for cosmic ray physics, and hadron production in hadron-induced reactions for neutrino physics. The new measurements require upgrades of the NA61/SHINE detector: construction of the Vertex Detector and a further tenfold increase in the data taking rate– to about 1 kHz. The details of the proposed upgrade are described in Ref. [50].

2.2 Beam, target and triggering system

NA61/SHINE uses beams consisting of variety of different ions – starting from hadrons and ending with lead nuclei. The beam comes with different momentum supplied by the SPS. NA61/SHINE mostly uses six beam momenta: 13*A*, 19*A*, 30*A*, 40*A*, 75*A* and 150*A* GeV/*c* or similar. The beam can be of primary origin (e.g. Ar, Xe, Pb and primary protons) or secondary – produced via primary beam interactions.

Ionized ^{40}Ar beam was produced in Electron Cyclotron Resonance (ECR) source, where repetitive microwave pulses accelerate free electrons which collide with gas atoms and ionize them. The acceleration of beam starts with a linear accelerator LINAC3, which can give ions momentum of 4.2*A* MeV/*c*. Next, ions are injected into Low Energy Ion Ring (LEIR), where they can reach 72*A* MeV/*c*. Then, ions are accelerated to 25*A* GeV/*c* in Proton Synchrotron (PS). Finally, the target momentum is reached in the SPS. An overview of the acceleration chain is presented in Fig. 2.1.

After the final acceleration in the SPS, beam is transported through the H2 beamline to the CERN North Area where the NA61/SHINE detectors are located. The H2 beamline is able to select a beam type based on its rigidity using a set of two large spectrometers. This allows for secondary beam production. The beam intensity is reduced by a set of collimators placed downstream of the spectrometers to a rate of a few 10^5 ions per single spill lasting few seconds. The beamline can also provide important beam characteristics thanks to an array of detectors. The detectors can inform about precise beam position, its profile and intensity.

Schematic overview of the beam detectors used with ^{40}Ar beam is presented in the bottom of Fig. 2.2. Two scintillator counters S1 and S2 detect beam particles and are located on the

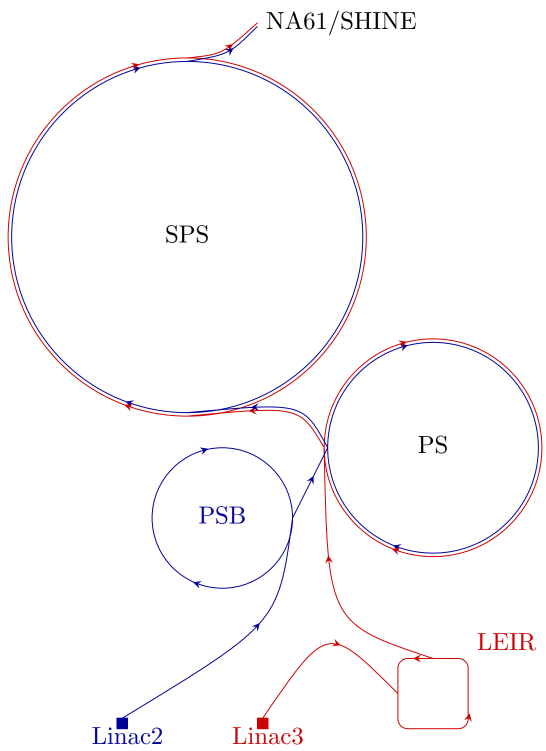

FIGURE 2.1: A schematic overview of the CERN accelerator chain relevant to NA61/SHINE operation. The red path is the acceleration chain of ions, whereas the blue path is for protons.

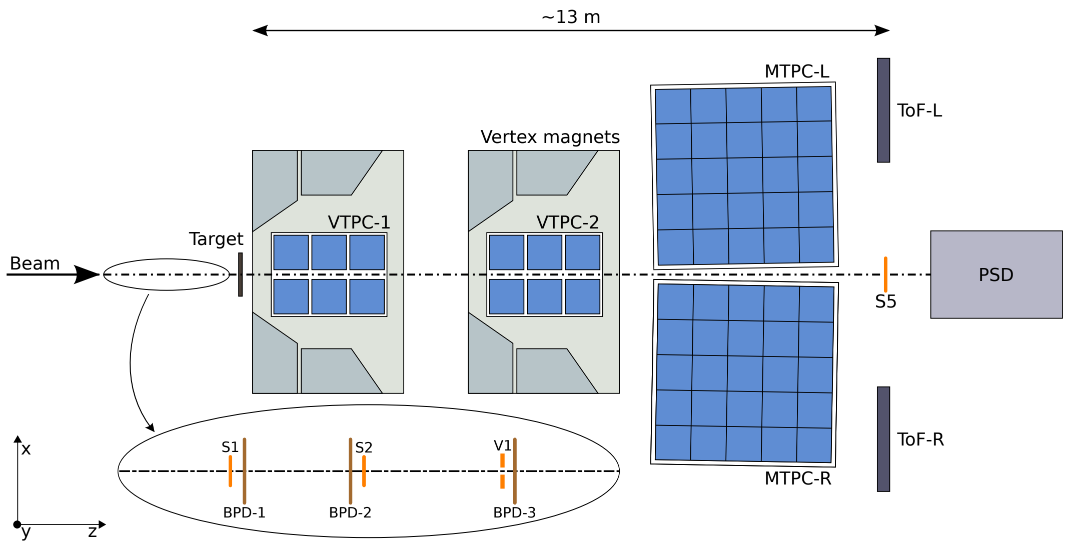

FIGURE 2.2: A schematic overview of the NA61/SHINE detector setup. The most important are four Time Projection Chambers (TPCs). VTPCs are located inside superconducting magnets. Downstream of the MTPCs, there are two Time of Flight (ToF) walls. The right-most detector is the Projectile Spectator Detector (PSD). The figure was prepared on my request by Antoni Aduszkiewicz.

beam axis. They provide precise timing reference for the NA61/SHINE triggering system. The veto scintillator counter with a 1 cm diameter hole (V1) selects particles traveling close to the beam axis and rejects the beam halo. Three Beam Position Detectors (BPDs) measure the trajectory of beam particles in the x-y plane. The S5 detector is an interaction counter and tags interactions of the beam particles. The S5 is located behind the MTPCs.

The target was a stack of 2 x 2 cm^2 wide ^{45}Sc plates placed ≈ 80 cm upstream of the VTPC-1. The target was fixed at $z \approx -580$ cm in the experiment's coordinate system. For a part of 150A GeV/c run the target was 4 mm thick and for other runs additional 2 mm plate was added, which totaled in 6 mm target thickness. The purity of the ^{45}Sc plates was 99.95%.

The triggering system is used in order to reduce amount of stored data (when for example an interaction with target did not occur) or to tag different types of events. Beam particles are selected by the trigger system requiring the coincidence $T1 = S1 \wedge S2 \wedge \overline{V1}$. The minimum bias trigger is based on the breakup of the beam ion due to interactions in and downstream of the target $T4 = S1 \wedge S2 \wedge \overline{V1} \wedge \overline{S5}$. In addition, central collisions were selected by requiring an energy signal below a set threshold from the 16 central modules of the PSD which measure mainly the energy of projectile spectators. The cut was set to retain only approximately 30% of interactions with the smallest energy of projectile spectators. Exact percentage for each beam momentum is presented in Table 2.1. The event trigger condition thus was $T2 = T1 \wedge \overline{S5} \wedge \overline{PSD}$. The summary of all triggers used in the ^{40}Ar+^{45}Sc data sets is presented in Table 2.2.

2.3 Time Projection Chambers

TPCs are detectors which allow for measurement of 3-dimensional trajectories and energy deposited by traversing particles inside the active TPC volume. The first TPC was built for PEP-4 collider experiment at SLAC in 1981. Since then, the technology is widely used by many modern experiments as ALICE, STAR or NA61/SHINE.

A TPC is a box filled with a working medium which could be gas or liquid. The active volume is enclosed within a field cage, generating an uniform electric field. A charged particle traversing through the volume of a TPC ionizes the gas inside the volume. In the process, electrons are freed and drift towards the readout plane because of the electric field. Charge amplification grids are located near the readout plane in order to strengthen the signal. Small and flat readout pads on the readout plane are responsible for registering drifting electrons. Charge location on the readout plane is a projection of two coordinates (x and z) of the track. Knowing the drift velocity v_D and the drift time t of the primary ionization charge, we are able to calculate the third coordinate y:

$$y = y_0 - v_D t, \tag{2.1}$$

TABLE 2.1: Percentage of the most central events chosen by the T2 trigger with 16 PSD modules together with the value of PSD voltage threshold.

$p_{beam}A$ (GeV/c)	PSD threshold (mV)	percentage (%)
13	75	30
19	135	35
30	230	30
40	350	35
75	325	20
150	230	23

TABLE 2.2: Definition of triggers used in the ^{40}Ar+^{45}Sc data sets.

Name	Definition	Description
T1	$S1 \wedge S2 \wedge \overline{V1}$	beam particles
T2	$S1 \wedge S2 \wedge \overline{V1} \wedge \overline{S5} \wedge \overline{PSD}$	central collision
T3	$S1 \wedge S2$	beam halo
T4	$S1 \wedge S2 \wedge \overline{V1} \wedge \overline{S5}$	minimum bias

where y_0 is the position of the readout plane. A TPC is also able to calculate the energy loss of a particle in the active volume (often referred to as dE/dx – energy loss per unit length). When combined with momentum measurement, it allows to identify particle type. When placed in a magnetic field, a TPC is able to determine the sign of the electric charge q of the particle, and the track rigidity R:

$$R = p/q, \tag{2.2}$$

where p is the particle momentum. A schematic overview of a TPC is presented in Fig. 2.3

A charged particle passing through a TPC ionizes gas and therefore looses energy. The number of electrons in the primary ionization clusters depends on the gas properties and on the energy lost by the particle. The mean energy loss per unit length, $-\langle dE/dx \rangle$, of a moderately relativistic particle ($0.5 < \beta\gamma < 500$) is described by the Bethe formula [51]:

$$\left\langle \frac{dE}{dx} \right\rangle = Kz^2 \frac{Z}{A} \frac{1}{\beta^2} \left[\frac{1}{2} ln \frac{2m_e c^2 \beta^2 \gamma^2 T_{max}}{I^2} - \beta^2 - \frac{\sigma(\beta\delta)}{2} \right], \tag{2.3}$$

where $\gamma = (1 - \beta^2)^{-1/2}$, $\beta = v/c$, v – velocity of a particle, c -speed of light, z – particle charge in electron units, Z – atomic number of absorber, A – atomic mass of absorber, m_e – mass of an electron, T_{max} – maximum kinetic energy that can be imparted to a free electron in a single collision, I – mean excitation energy of absorber, $K = 0.307075$ MeV g$^-$1 cm^2 (constant), $\delta(\beta\gamma)$ – density effect correction to ionization energy loss.

2.3.1 Time Projection Chambers in NA61/SHINE

There are four large volume TPCs used in the NA61/SHINE experiment. Two of them are located in a region where magnetic field is applied, these are called vertex TPCs: VTPC-1 and VTPC-2. Two remaining are called main TPCs: MTPC-L and MTPC-R. The latter are located downstream of the superconducting magnets, symmetrically to the beam.

The drift volume of each TPC is covered on sides with electrodes forming the electric field inside. They are made of aluminized Mylar strips of 25 μm thickness and 0.5 inch width. They are close to the chamber walls and arranged perpendicular to the drift direction. The voltage applied to the strips is gradually decreased with the distance from the readout plane to about -19 kV in MTPCs and -13 kV in VTPCs by a resistor voltage divider chain.

In the upper part of the TPCs, near the readout pads, there is a MWPC (MultiWire Proportional Chamber). It consist of a plane of very thin – 20 μm wires in close proximity, which makes a density of electric field very high close to them. Electrons, while approaching the wires gain energy which allows them to further ionize gas. The process called gas amplification creates an avalanche of 10^3-10^6 electrons for each electron from primary ionization. This results in clusters covering 3-4 pads on the readout plane.

The gating grid is used to select appropriate events. The gate is open only during charge collection from the drift volume. In order to prevent unwanted events or debris from the drift volume from entering the readout region, the wires are polarized with alternating positive and

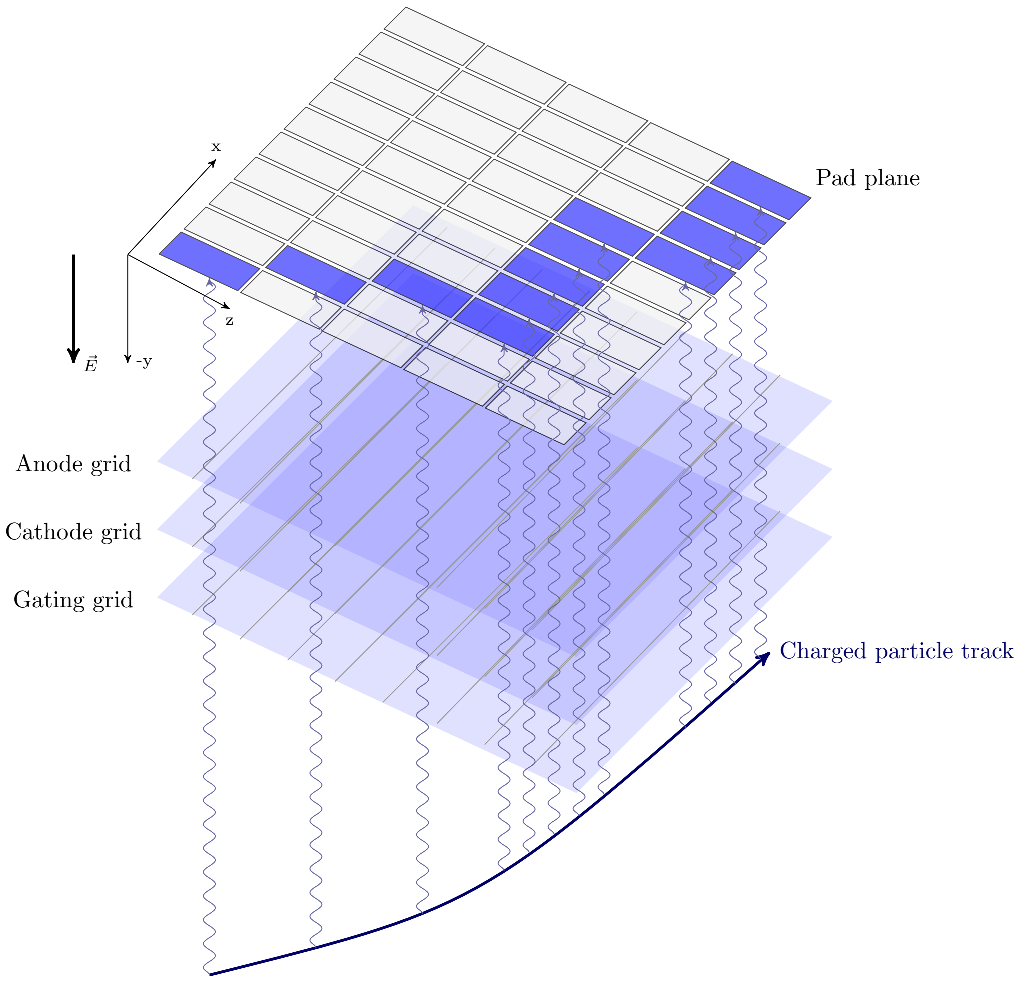

FIGURE 2.3: A schematic overview of a TPC and its operation. A charged particle enters the active volume and traverses ionizing the gas on the way. Electrons knocked out of gas molecules in the ionization process drift towards the readout plane. The readout pads emit a signal when hit by a charged particle.

negative voltage of $\pm$50 V. To open the gate one has to apply the same voltage to all the wires. The gating grid opens only for 50 μs in each event.

Each detector is divided into sectors and each sector has its own multiwire chamber. Sectors are subdivided into padrows and padrows in turn consist of pads. The shape of a pad is rectangular or trapezoidal and is optimized to minimize the angle between the track trajectory and the pad which is important for determining the cluster position. The characteristic of the pads in each TPC differ:

- **VTPC-1** All pads are 3.5 mm wide in the direction perpendicular to the beam. Pads in the sectors closest to the target (1 and 4) are 16 mm long and pads in other sectors are 28 mm long. The tilt angle is adjusted individually for each pad depending on its position from the beam and target,
- **VTPC-2** All pads are 3.5 mm wide and 28 mm long. The tilt angle is increasing linearly with the distance from the beamline,
- **MTPC-L/R** All pads are 40 mm long. The five sectors closest to the beamline (21-25 in MTPC-L and 1-5 in MTPC-R) are called high resolution sectors. The pads are 3.6 mm wide and are not tilted. The next five sectors (16-20 in MTPC-L and 6-10 in MTPC-R) are called standard resolution sectors. They are 5.5 mm wide and are not tilted. The remaining sectors (1-15 in MTPC-L and 11-25 in MTPC-R) are called standard resolution prime. They are 5.5 mm wide and are tilted by an angle of 15 °.

Two vertex TPCs are located inside the superconducting magnets. The magnets are oriented vertically to bend charged particles' trajectories in x-z plane. Positively charged particles' trajectories are bent towards left-hand side (relative to beamline), whereas negatively charged particles in the opposite direction. The maximum magnetic field generated by the VERTEX-1 magnet is 1.5 T, and 1.1 T for VERTEX-2 magnet. The magnetic field is uniform in the majority of the VTPC-1 and VTPC-2 volume, but any inhomogeneities are taken care of by magnetic field maps implemented in software reconstructing particle tracks.

The details of the NA61/SHINE TPCs parameters are resented in Table 2.3.

2.4 Projectile Spectator Detector

The Projectile Spectator Detector (PSD) is a calorimeter, which measures the energy E_{PSD} emitted in the forward region and in case of nucleus-nucleus collisions dominated by the projectile spectators. The PSD measurements are used to determine centrality classes of recorded

TABLE 2.3: Parameters of the TPCs in NA61/SHINE.

Chamber	VTPC-1	VTPC-2	MTPC-L/R
Size (cm)	$250 \times 200 \times 98$	$250 \times 200 \times 98$	$390 \times 390 \times 180$
No. of pads/ TPC	26886	27648	63360
Pad size (mm)	$3.5 \times 28(16)$	3.5×28	$3.6 \times 40, 5.5 \times 40$
Drift length (cm)	66.60	66.60	111.74
Drift velocity (cm/μs)	1.4	1.4	2.3
Drift field (V/cm)	195	195	170
Drift voltage (kV)	13	13	19
Gas mixture	Ar/CO_2(90/10)	Ar/CO_2(90/10)	Ar/CO_2(95/5)
# of sectors	2×3	2×3	5×5
# of padrows	72	72	90
# of pads/padrow	192	192	192,128

events. It is also used in the trigger logic to preliminarily select a percentage of central events. The information on events extracted from the PSD helps eliminate effects connected with event-to-event variation of the number of wounded nucleons, W. In a simple approach, the higher the E_{PSD}, the less nucleons interacted in the collision.

The Ar+Sc collisions are selected by requiring a low value of the PSD energy – the energy emitted into the region mostly populated by projectile spectators. These collisions are referred to as *central* collisions and a selection of collisions based on the forward energy is called a centrality selection. Although for Ar+Sc collisions the forward energy is not tightly correlated with geometric parameters of the interaction such as the impact parameter of the collision, the terms central and centrality are adopted following the convention widely used in heavy-ion physics. For details see Sec. 4.1.

The PSD is located most downstream of the target and consists of an array of 44 modules covering a transverse area of 120×120 cm^2 in total. A schematic front view of the PSD is presented in Fig 2.4. In the center of the PSD there are 16 small modules with a transverse area of 10×10 cm^2 each, whereas peripheral part consists of 28 modules of 20×20 cm^2 each. Every module, longitudinally consists of 60 pairs of alternating lead and scintillator plates. The longitudinal length of each module is 120 cm and corresponds to 5.7 nuclear interaction lengths.

An incident collision remnant on contact with the lead absorber generates a particle cascade consisting of hadrons, heavy fragments, and electro-magnetic components as well. The cascade is formed due to various processes, i.e. inelastic interactions, ionization, and excitation. The energy deposited inside the calorimeter is probed by the PSD active material – scintillators. As the beam is directed into the center of the PSD, the modules are affected by the cascade depending on its starting point in the PSD volume. If the cascade starts near the front of the calorimeter, it will have a chance to deposit energy in all modules. Approximately 10% of the particle's energy is lost due to the backside leakage of the PSD (limited length of the PSD) and another ≈ 10% is lost because of the side leakage. The effects are largely removed thanks to the modular structure of the PSD and the fact that the cascade leakage from one module is detected by neighboring modules.

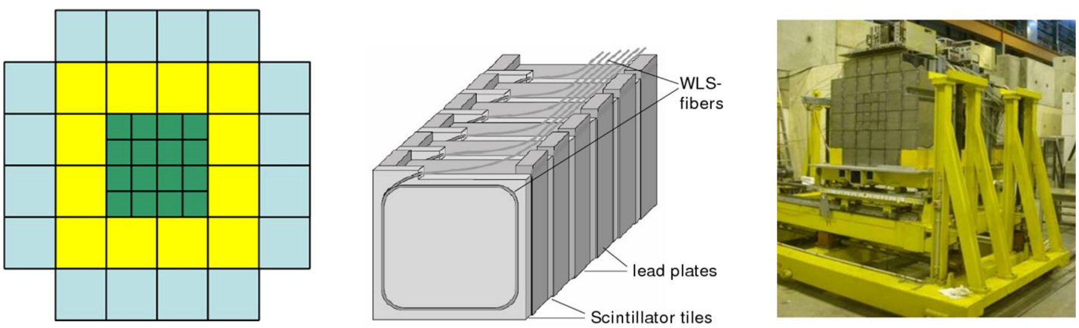

FIGURE 2.4: A schematic view of PSD's front (*left*), single module (*middle*) and the fully assembled detector (*right*). The figure is taken from Ref. [52].

Chapter 3

Data processing and Monte-Carlo simulations

Charge measurements in TPC pads are not enough to perform an analysis of the produced hadrons. There are a number of effects that have to be included in order to improve the quality of the data. In order to optimize, time-dependent corrections (e.g. electron drift velocity or specific energy loss per unit length), require a calibration procedure. Afterwards, the clusters are used to reconstruct tracks, a process which matches clusters into a single track and fits its momentum. In the final step, a Monte-Carlo simulation of all important processes on the path of a particle has to be performed in order to derive the geometrical acceptance of the detector, the contribution of weak decays and the interactions of primary particles with the detector.

3.1 Data processing

In high multiplicity events (e.g. ^{208}Pb+^{208}Pb or ^{40}Ar+^{45}Sc) the number of clusters is extremely high and the distances between them very low. Thus, it may not be possible to identify all the clusters belonging to the same particle's track. Therefore, the reconstruction algorithm was optimized in order to pick up clusters coming from the same particle's track and at the same time to minimize the inclusion of clusters from neighboring tracks. The track reconstruction is performed in the following steps:

1. Finding points – looking at a two-dimensional map of clusters in a single row of pads (x coordinate) and all 256 time bins (y coordinate) we define points as signals from at least two adjacent cells of the array in both directions. Typically, a point will consist of 3-5 adjacent pads and 2-4 time slices. The position of a point is calculated with the center of gravity method.

2. Local tracking in each TPC – adjacent points are merged into segments of tracks in each TPC separately. In MTPCs points on a straight line are connected into track pieces, whereas points on curved tracks are searched for in VTPCs. The track piece momentum is fitted based on its curvature and distribution of magnetic field in the detectors.

3. Global tracking – matched track pieces from different TPCs are connected into a single track. Momenta of the connected tracks are fitted once again, including the distribution of the magnetic field inside TPCs and between them.

4. Finding interaction vertex – the merged tracks are extrapolated upstream in order to find a single common vertex. Its z position is fitted based on all tracks found in TPCs in a given event. The x and y coordinates of the vertex are calculated by extrapolating the beam track measured by the BPDs to the vertex z coordinate. Momenta of tracks are fitted again using the interaction vertex as an additional constraint. The distances in x-y

plane between the vertex position measured by the BPDs and the extrapolated track is called the impact point and it is a measure used to reject non-vertex tracks.

5. Finding secondary vertices – for each pair of tracks, the algorithm checks if they may originate from a decay by trying to fit a common secondary vertex.

After the reconstruction process, the data consists of tracks with the following set of properties:

1. electric charge sign,
2. momentum vector at the interaction vertex.
3. average charge loss dE/dx,
4. number of measured and potential points in each TPC,
5. coordinates of the impact point b_x, b_y.

The calibration procedure optimizes detector parameters utilizing their time dependence. One of the most important parameters is the electrons' drift velocity v_D, which in a given drift volume filled with a given gas mixture depends on a number of variables – electric field E, pressure P, and temperature T. These parameters are constantly monitored during data taking periods. After data taking the drift velocity v_D is calibrated by the reconstruction software in the global tracking procedure. If the v_D value deviates from the real value, there is a vertical offset between local tracks selected for the global track construction.

An overview of a reconstructed ^{40}Ar+^{45}Sc event for beam momentum $p_{beam} = 150A$ GeV/c is presented in Fig. 3.1.

3.2 Monte-Carlo simulations

Corrections for the following biases were evaluated using Monte-Carlo simulations:

1. procedure of selecting *central* collisions,
2. geometrical acceptance,
3. contribution of particles other than primary (see below) negatively charged pions produced in Ar+Sc interactions,
4. losses of produced negatively charged pions due to their decays and secondary interactions.

The final results refer to π^- produced in *central* Ar+Sc interactions by strong interaction processes and in electromagnetic decays of produced hadrons. Such hadrons are referred to as primary hadrons. The definition of *central* collisions is given in Sec. 4.1.

Due to reasonably good agreement with previous NA61/SHINE measurements and constant developers' support, EPOS1.99 [53] was used as the event generator. EPOS is a multiple scattering approach based on partons and Pomerons (parton ladders). EPOS-produced particles are injected into the detector simulation with the GEeometry ANd Tracking (GEANT) 4 software [54]. This allows for simulation of relevant physical processes as particle decays or secondary interactions. The GEANT output passes through the Detector Response Simulator to produce TPC clusters with a given position and charge. Next, the produced MC events are processed through the reconstruction procedure in exactly the same way as the real data.

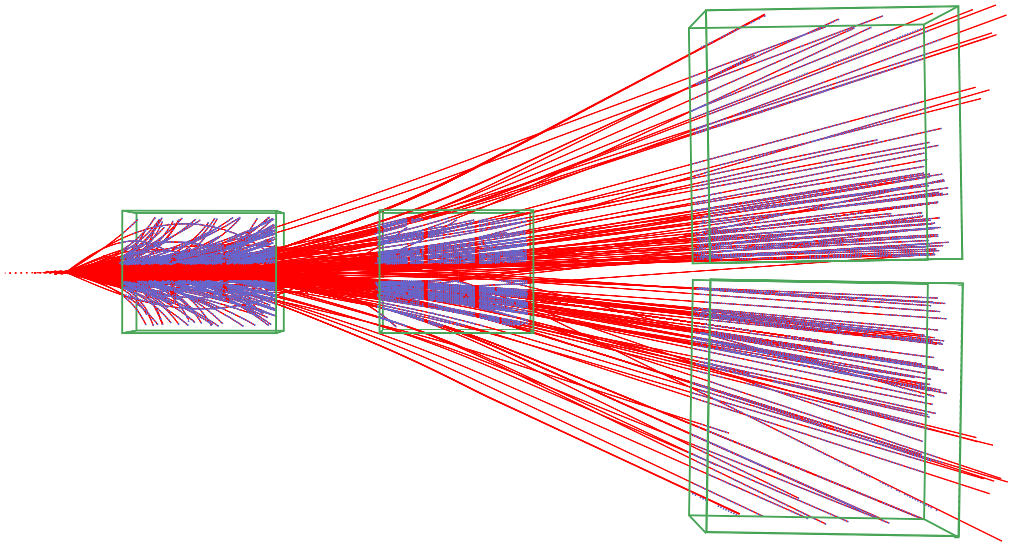

FIGURE 3.1: An example of an ^{40}Ar+^{45}Sc event for beam momentum p_{beam} = 150*A* GeV/*c*. The green lines outline the NA61/SHINE TPCs, blue points represent data points recovered from pad clusters and the red curves are reconstructed particle tracks. The interaction vertex is on the left-hand side, where all the tracks originate.

Finally, a matching procedure is performed in order to find for each reconstructed track a corresponding simulated track. This is done choosing for each reconstructed track the simulated track with the highest number of generated MC points in common with reconstructed MC clusters. Thanks to matching, we can determine the particle type and its origin. Finally, reconstructed MC events go through the PSD detector simulation to calculate deposited energy.

Chapter 4

Data selection

This sections starts with a definition of *central* events which will be used throughout the thesis and applied to data selection.

In order to perform a precise analysis of the data, only events and tracks with the best quality will be chosen. Additionally, as the event geometry changes significantly depending on the impact parameter, events will also be selected by centrality classes. There are two types of event cuts, namely non-biasing and biasing. The former is mostly related to beam properties, whereas the latter concerns detector performance, off-target interactions and uncertainties in the reconstruction software.

As a prerequisite for the analysis, a number of pre-selection cuts was applied to the data in order to reject periods of malfunctioning detectors or unstable detector operation. The cuts removed affected run periods, no matter the quality of data taken.

4.1 *Central* collisions

Final results presented in this thesis refer to the 5% of Ar+Sc collisions with the lowest value of the forward energy E_F (*central* collisions). The quantity E_F is defined as the total energy in the laboratory system of all particles produced in Ar+Sc collisions via strong and electromagnetic processes in the forward momentum region defined by the acceptance map in Ref. [55]. Final results on *central* collisions, derived using this procedure, allow a precise comparison with predictions of models without any additional information about the NA61/SHINE setup and used magnetic field.

For analysis of the data the event selection was based on the $\approx$ 5% of collisions with the lowest value of the energy E_{PSD} measured by a subset of PSD modules (see Fig. 4.1) in order to optimize the sensitivity to projectile spectators. The acceptance resulting from the definition of the forward energy E_F corresponds closely to the acceptance of this subset of PSD modules.

Online event selection by the hardware trigger (T2) used a threshold on the sum of electronic signals from the 16 central modules of the PSD set to accept $\approx$ 30% (for exact values see Tab. 4.1) of the inelastic interactions. Measured distributions of E_{PSD} for minimum-bias and T2 trigger selected events, calculated in the offline analysis, are shown in Fig. 4.2 at beam momenta of 19*A* GeV/*c* and 150*A* GeV/*c*, respectively. The accepted region corresponding to the 5% most *central* collisions is indicated by shading. The minimum-bias distribution was obtained using the data from the beam trigger T1 with offline selection of events by requiring an event vertex in the target region. A properly normalized spectrum for target removed events was subtracted.

The forward energy E_F cannot be measured directly. However, both E_F and E_{PSD} can be obtained from simulations using the Epos1.99 model. A global factor c_{cent} (listed in Table 4.2) was then calculated as the ratio of mean negatively charged pion multiplicities obtained with the two selection procedures in the 5% most *central* events. The resulting factors c_{cent} range

TABLE 4.1: Basic beam properties and number of events recorded and used in the analysis for ^{40}Ar+^{45}Sc interactions at incident momenta of 13*A*, 19*A*, 30*A*, 40*A*, 75*A* and 150*A* GeV/*c*.

p_{beam} (GeV/c)	$\sqrt{s}$ (GeV)	Percentage of events recorded with T2 trigger	Recorded event triggers	Number of events after quality cuts and centrality selection
13	5.1	30	$3.0 \cdot 10^6$	251356
19	6.1	35	$3.7 \cdot 10^6$	262551
30	7.6	30	$4.8 \cdot 10^6$	456312
40	8.8	35	$8.9 \cdot 10^6$	644098
75	11.9	20	$4.4 \cdot 10^6$	579540
150	16.8	23	$0.99 \cdot 10^6$	133953

from 1.002 to 1.005 and correspond to only a small correction compared to the systematic uncertainties of the measured particle multiplicities. A possible dependence of the scaling factor on rapidity and transverse momentum was neglected. The corrections (c_{cent}) are negligibly small compared to the systematic uncertainties of the measured particle multiplicities and are therefore not applied in the calculation of π^- yields and neglected in the quoted systematic uncertainties.

TABLE 4.2: The numerical values of the c_{cent} factor.

p_{beam} (A GeV/c)	13	19	30	40	75	150
c_{cent}	1.005	1.005	1.002	1.003	1.005	1.002

4.2 Event cuts in data

The non-biasing event cuts performed in this analysis are the following:

I) beam properties: all accepted events had to have a well defined beam trajectory measured by the BPD detectors. This means that for two BPDs: BPD1 and BPD2 a correct signal from at least three planes out of four was present and a correct signal from both planes in BPD3 was detected.

II) beam off-time: this cut ensures that only one beam particle was present within one registered event. No off-time beam particle can be detected within $\pm$ 4 μs window with respect to trigger particle S1 signal. Additionally, no off-time particle can be detected within $\pm$ 25 μs window with respect to T4 trigger.

The biasing cuts performed in this analysis are the following:

III) interaction vertex fit quality: this ensures that during the reconstruction process, the interaction vertex was fitted and that the fit quality is good enough.

IV) interaction vertex z position: the cut chooses only events for which reconstructed interaction vertex is within $\pm$ 10 cm around the position of the center of the target. An overview of the fitted z vertex position for target inserted and target removed in a broad range together with explanation of the origin of different peaks is presented in Fig. 4.3. A closeup of the cut region is presented in the Fig. 4.4. In both cases, the distribution for the data recorded with the ^{45}Sc target removed was multiplied by a factor of $\epsilon = N_{\mathrm{I}}[z > -500\ \mathrm{cm}]/N_{\mathrm{R}}[z > -500\ \mathrm{cm}]$, where $N_{\mathrm{I}}[z > -500\ \mathrm{cm}]$ and $N_{\mathrm{R}}[z > -500\ \mathrm{cm}]$ are the numbers of events with T2 trigger for the two data sets – with ^{45}Sc target inserted and removed, respectively, in the normalization region $z > -500$ cm. Resulting factors are $\epsilon_{19} = 4.34$ and $\epsilon_{150} = 1.08$ for 19A (*left*) and 150A GeV/c, respectively.

V) centrality selection: the cut is important to ensure that the analysis is performed on the same class of collision geometry events. This is enforced choosing only events with a specific energy measurement by the PSD calorimeter. The energy deposited in the PSD is proportional to the number of projectile spectators and therefore can be a measure of event centrality. In the first step, for all beam momenta separately, a set of modules which showed an anticorrelation between the energy observed in the module and the charged particle track multiplicity reconstructed in TPCs is established. The modules selection for different beam momenta is presented in Fig. 4.1. For these modules selections, a histogram of the PSD energy was created (see Fig. 4.2). Choosing events with the energy lower than certain threshold, we are selecting events in the same centrality class. This analysis will only be performed for 0 – 5% centrality class. For details on the definition of *central* events see Sec. 4.1.

The summary of the number of events after each cut is presented in Table 4.3. The basic properties of data-sets before and after event cuts are presented in the Table 4.1.

TABLE 4.3: Number of events after selection criteria listed in Section 4.2 applied. The numbers are given in thousands (k= 10^3), round brackets present the percentage of the initial number of events and square brackets express the percentage with respect to the previous cut.

Cut	Data			EPOS MC		
p_{beam} = 150*A* GeV/*c*						
-	781.9 k	(100.0)	-	19,682.2 k	(100.0)	-
I)	769.0 k	(98.4)	[98.4]	-	-	-
II)	637.3 k	(81.5)	[82.9]	-	-	-
III)	631.6 k	(80.8)	[99.1]	19,510.4	(99.1)	[99.1]
IV)	622.7 k	(79.6)	[98.6]	19,306.5	(98.1)	[99.0]
V)	134.0 k	(17.1)	[21.5]	982.9	(5.0)	[5.1]
p_{beam} = 75*A* GeV/*c*						
-	3,138.5 k	(100.0)	-	19,305.0 k	(100.0)	-
I)	3,023.4 k	(96.3)	[96.3]	-	-	-
II)	2,551.5 k	(81.3)	[84.4]	-	-	-
III)	2,426.9 k	(77.3)	[95.1]	19,065.9	(98.8)	[98.8]
IV)	2,368.2 k	(75.5)	[97.6]	18,850.6	(97.6)	[98.9]
V)	579.5 k	(18.5)	[24.5]	965.3	(5.0)	[5.1]
p_{beam} = 40*A* GeV/*c*						
-	6,381.0 k	(100.0)	-	4,616.4 k	(100.0)	-
I)	6,168.1 k	(96.7)	[96.7]	-	-	-
II)	5,235.9 k	(82.1)	[84.9]	-	-	-
III)	4,916.9 k	(77.1)	[93.9]	4,531.9	(98.2)	[98.2]
IV)	4,638.9 k	(72.7)	[94.3]	4,491.8	(97.3)	[99.1]
V)	644.1 k	(10.1)	[13.9]	230.9	(5.0)	[5.1]
p_{beam} = 30*A* GeV/*c*						
-	4,086.1 k	(100.0)	-	9,004.3 k	(100.0)	-
I)	3,944.2 k	(96.5)	[96.5]	-	-	-
II)	3,094.1 k	(75.7)	[78.4]	-	-	-
III)	2,938.6 k	(71.9)	[95.0]	8,816.5	(97.9)	[97.9]
IV)	2,780.0 k	(68.0)	[94.6]	8,746.0	(97.1)	[99.2]
V)	456.3 k	(11.2)	[16.4]	451.1	(5.0)	[5.2]
p_{beam} = 19*A* GeV/*c*						
-	2,924.5 k	(100.0)	-	4,951.4 k	(100.0)	-
I)	2,775.5 k	(95.0)	[95.0]	-	-	-
II)	2,205.4 k	(75.4)	[79.5]	-	-	-
III)	2,021.3 k	(69.1)	[91.7]	4,820.2	(97.4)	[97.4]
IV)	1,872.6 k	(64.0)	[92.6]	4,785.1	(96.6)	[99.3]
V)	262.6 k	(9.0)	[14.0]	247.7	(5.0)	[5.2]
p_{beam} = 13*A* GeV/*c*						
-	2,530.7 k	(100.0)	-	4,829.9 k	(100.0)	-
I)	2,415.0 k	(95.4)	[95.4]	-	-	-
II)	1,792.7 k	(70.8)	[74.2]	-	-	-
III)	1,630.5 k	(64.4)	[91.0]	4,665.2	(96.6)	[96.6]
IV)	1,510.1 k	(59.7)	[92.6]	4,630.5	(95.9)	[99.3]
V)	251.4 k	(9.9)	[16.6]	241.4	(5.0)	[5.2]

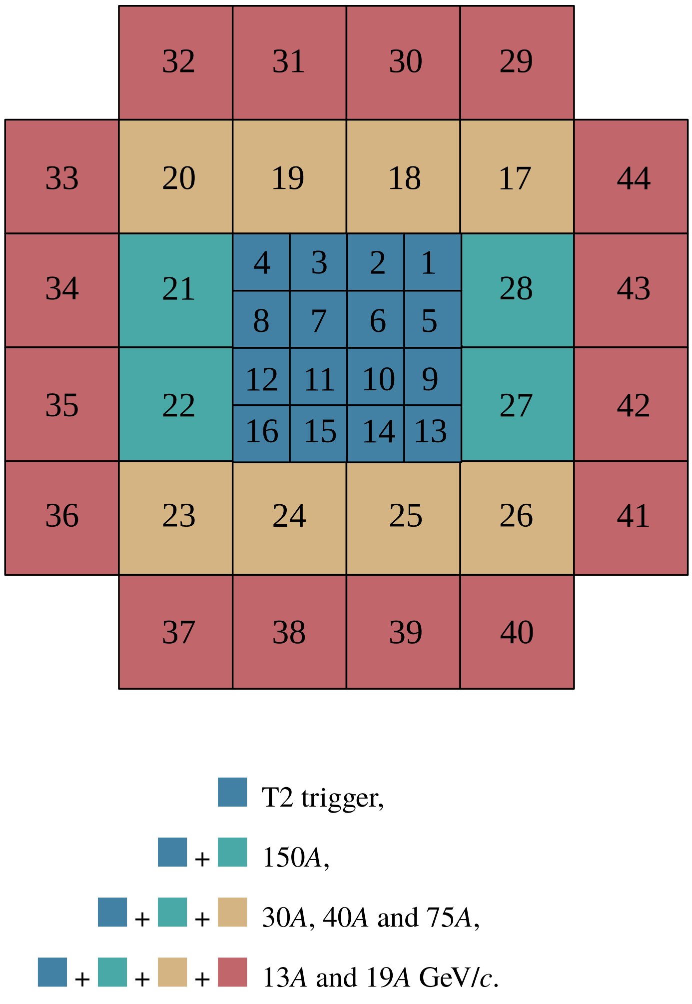

FIGURE 4.1: Event centrality selection using the PSD energy. Modules used in the centrality class determination were chosen based on anti-correlation between the measured energy and the track multiplicity in a given event. All modules were used for 13*A* and 19*A* GeV/*c*. For 30*A*, 40*A* and 75*A* GeV/*c* 28 central modules were chosen. For 150*A* GeV/*c* 16 central modules were selected together with modules 21, 22, 27 and 28. For the T2 trigger, 16 central modules were used.

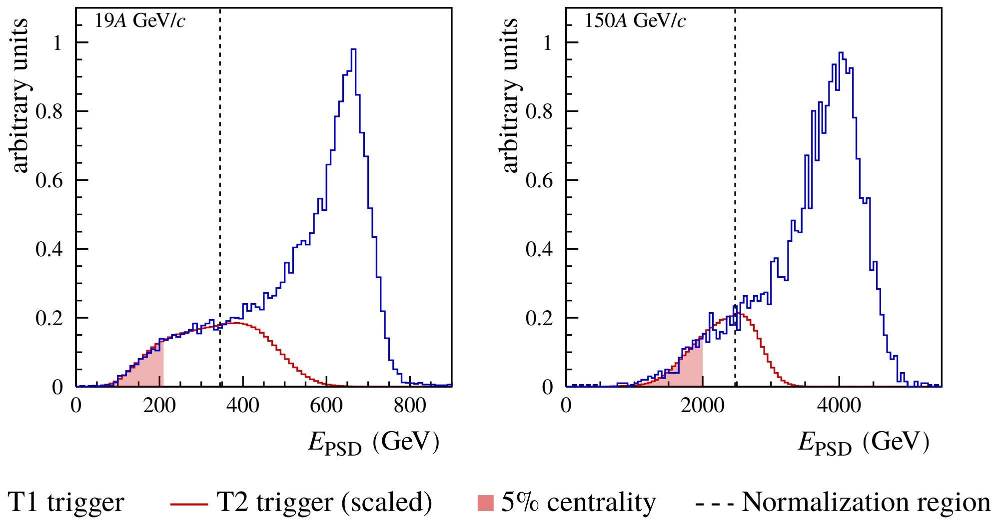

FIGURE 4.2: Event centrality selection using the energy measured by the PSD calorimeter E_{PSD}. Distributions of measured forward energy are shown for 19*A* (*left*) and 150*A* GeV/*c* (*right*) beam momenta. Events selected with the T1 beam trigger are marked with blue line and with red line for events selected by the central interaction trigger T2 set to accept ≈ 30% of the inelastic cross section. Histograms are normalized to agree in the overlap region (from the beginning of the distribution to the black dashed line). The detailed information about T2 trigger settings are presented in Table 4.1. Accepted regions for 5% centrality are indicated by red shading. Choice of modules included for the centrality determination is based on correlation studies between forward energy and track multiplicity and presented in Fig. 4.1.

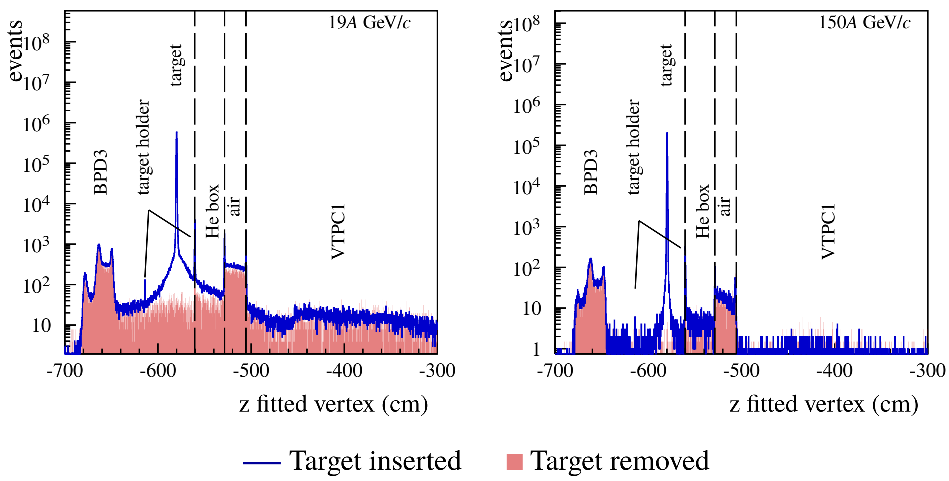

FIGURE 4.3: Distribution of fitted vertex z coordinate for data in ^{40}Ar+^{45}Sc interactions at 19*A* (*left*) and 150*A* GeV/*c* (*right*) with target inserted and target removed for the T2 central interaction trigger. The distribution for the data recorded with the ^{45}Sc target removed was scaled as explained in text. Sources of peaks coming from beam interaction with experimental setup are explained.

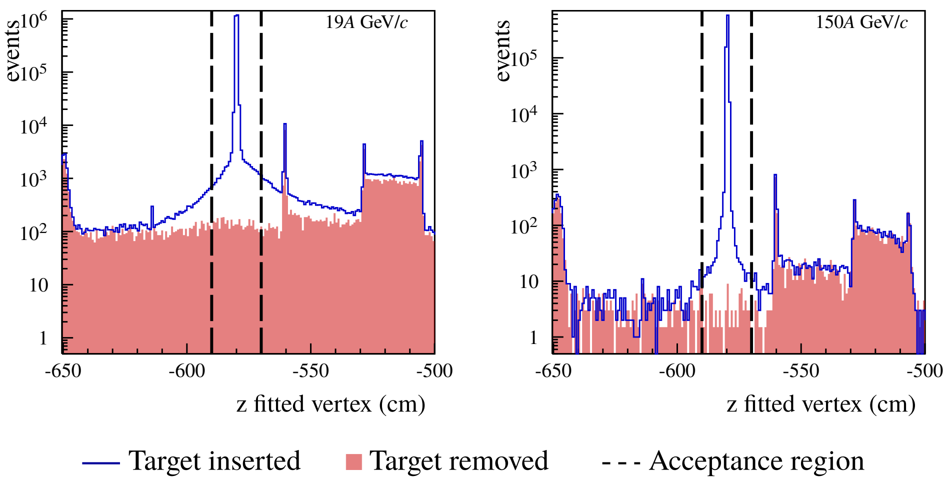

FIGURE 4.4: Distribution of fitted vertex z coordinate for data in ^{40}Ar+^{45}Sc interactions at 19*A* (*left*) and 150*A* GeV/*c* (*right*) with target inserted and target removed for the T2 central interaction trigger. The distribution for the data recorded with the ^{45}Sc target removed was scaled as explained in text. Vertical dashed lines show the acceptance region of beam interactions with target. Note different horizontal axis range in comparison with Fig. 4.3.

4.3 Track cuts in data

Among the selected events there are many tracks, which should be rejected from the analysis. The cuts presented in this section are standard NA61/SHINE cuts common for most analyses in the experiment. The list of cuts is the following:

i) track quality: only tracks fitted to the main interaction vertex are chosen.

ii) track charge: tracks which curvature bent in the magnetic field corresponds to negatively charged particle are selected. Analysis presented in this thesis is only applied to negatively charged pions and therefore we can reject all the positively charged particles.

iii) right side tracks: only the negatively charged tracks with negative momentum component p_x are selected. Negatively charged tracks, which momentum component p_x is positive enter TPCs with an angle that the readout pads are not optimized to. Thanks to the cut one can lower the impact of ionization fluctuations.

iv) minimal number of clusters: this cut ensures good momentum reconstruction and track quality. The threshold for the number of clusters in all TPCs (VTPC1 + VTPC2 + MTPCL + MTPCR) is set to 30. Additional cut for VTPCs only (VTPC1 + VTPC2) is set to have minimum of 15 measured clusters.

v) impact point: the cut enforces that the difference between the track extrapolation to the target z position and the reconstructed interaction vertex is small enough in the x-y plane. In the x axis the threshold is $|b_x| < 4$ cm and in the y axis it is set to $|b_y| < 2$ cm.

vi) electron suppression: in order to remove the contribution of electrons to the negatively charged particles, one can perform a cut based on the dE/dx measurement for tracks. The Bethe-Bloch parametrization allows for selection of a region on the dE/dx- p plot, where electrons are located. Removing the tracks from the region removes the majority of tracks that can be attributed to electrons. This procedure is presented in Fig. 4.5.

The summary of the number of tracks after each cut is presented in Table 4.4

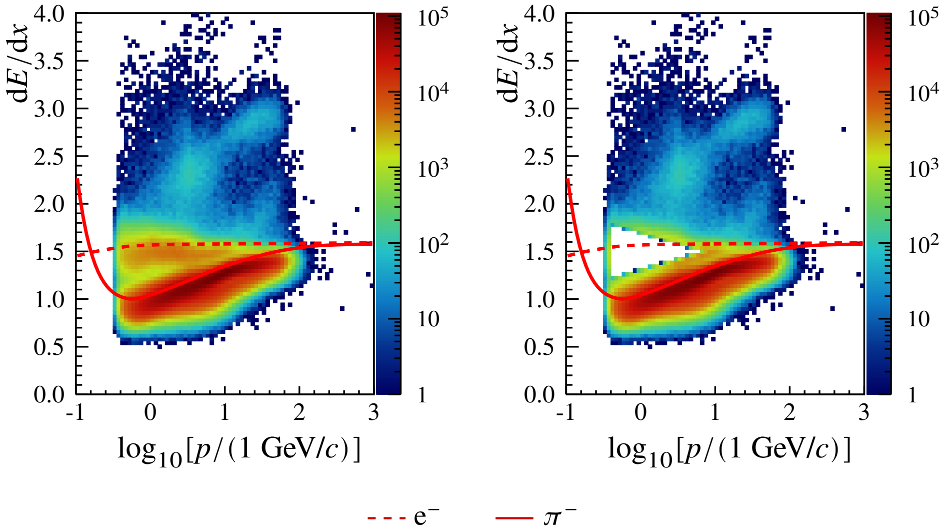

FIGURE 4.5: Histograms of momentum versus specific energy loss dE/dx in ^{40}Ar+^{45}Sc interactions at 150A GeV/c before (*left*) and after (*right*) removing electrons. The Bethe-Bloch functions for electrons e^- and negatively charged pions π^- are plotted with dashed and solid lines, respectively.

4.4 Event and track cuts in MC

A similar set of quality cuts is applied to the Monte-Carlo produced events. The differences are caused mostly because the Monte-Carlo provides us with extra information on particle type and collision geometry. It is also possible to look at generated events (pure events produced by event generator) and reconstructed events (pure events that go through detector simulation and reconstruction) separately. Both version will have different sets of cuts applied.

For the generated tracks the only event selection that will be applied is the centrality class selection. In case of simulation it was not possible to obtain large statistic of events with a reliable PSD or forward energy simulation due to technical reasons. Therefore, selection of events based on E_{PSD} or E_{F} was not possible. However, we are able to choose centrality class in simulation based on the number of wounded nucleons. Since the number is an integer, it is not possible to select exactly 5% centrality class. In order to bypass the problem, one could choose centrality class with the number of wounded nucleons $W|_{5\%}$ closest to, but below 5%. The remaining events are randomly chosen from the events with $W = W|_{5\%} + 1$ to exactly match 5% centrality class. Generated tracks which are not primary generated particles and are not negatively charged pions are rejected. Therefore, the generated MC will consist only of π^- production information.

The MC reconstructed events undergo the following cuts:

III) interaction vertex fit quality,

IV) interaction vertex z position,

V) centrality selection – as described for the generated events.

The MC reconstructed tracks undergo the following cuts:

i) track quality,

ii) track charge,

iii) right side tracks,

iv) minimal number of clusters,

v) impact point,

vi) electron suppression – in case of reconstructed MC, the information about particle type will be used from matched simulated track. The matching chooses for each reconstructed track a simulated track with the highest number of common points.

TABLE 4.4: Number of tracks in events after selection criteria listed in Section 4.3 applied. The numbers are given in millions (M= 10^6), round brackets present the percentage of the initial number of tracks and square brackets express the percentage with respect to the previous cut.

Cut	Data			EPOS MC		
	p_{beam} = 150*A* GeV/*c*					
i)	48.9 M	(100.0)	-	230.1 M	(100.0)	-
ii)	22.2 M	(45.4)	[45.4]	104.3 M	(45.4)	[45.4]
iii)	11.0 M	(22.6)	[49.7]	52.5 M	(22.8)	[50.4]
iv)	7.8 M	(16.0)	[70.9]	39.3 M	(17.1)	[74.9]
v)	7.8 M	(15.9)	[99.4]	39.1 M	(17.0)	[99.3]
vi)	7.4 M	(15.2)	[95.6]	36.7 M	(16.0)	[94.0]
	p_{beam} = 75*A* GeV/*c*					
i)	99.3 M	(100.0)	-	166.3 M	(100.0)	-
ii)	44.0 M	(44.3)	[44.3]	73.3 M	(44.1)	[44.1]
iii)	23.2 M	(23.3)	[52.6]	39.1 M	(23.5)	[53.3]
iv)	16.5 M	(16.6)	[71.1]	29.0 M	(17.4)	[74.3]
v)	16.3 M	(16.4)	[99.1]	28.7 M	(17.3)	[99.0]
vi)	15.6 M	(15.7)	[95.5]	26.9 M	(16.2)	[93.8]
	p_{beam} = 40*A* GeV/*c*					
i)	80.6 M	(100.0)	-	31.0 M	(100.0)	-
ii)	34.4 M	(42.7)	[42.7]	13.2 M	(42.5)	[42.5]
iii)	18.7 M	(23.2)	[54.4]	7.3 M	(23.5)	[55.2]
iv)	12.8 M	(15.9)	[68.6]	5.2 M	(16.8)	[71.4]
v)	12.7 M	(15.7)	[98.5]	5.1 M	(16.5)	[98.4]
vi)	12.1 M	(15.0)	[95.8]	4.8 M	(15.5)	[93.8]
	p_{beam} = 30*A* GeV/*c*					
i)	46.4 M	(100.0)	-	48.2 M	(100.0)	-
ii)	19.2 M	(41.5)	[41.5]	20.0 M	(41.4)	[41.4]
iii)	10.5 M	(22.5)	[54.3]	11.0 M	(22.8)	[55.0]
iv)	7.0 M	(15.2)	[67.4]	7.7 M	(15.9)	[69.7]
v)	6.9 M	(14.9)	[98.3]	7.5 M	(15.6)	[98.2]
vi)	6.6 M	(14.3)	[95.7]	7.1 M	(14.6)	[93.9]
	p_{beam} = 19*A* GeV/*c*					
i)	20.6 M	(100.0)	-	20.5 M	(100.0)	-
ii)	8.0 M	(38.9)	[38.9]	8.0 M	(39.0)	[39.0]
iii)	4.3 M	(20.9)	[53.8]	4.3 M	(21.0)	[53.9]
iv)	2.8 M	(13.5)	[64.5]	2.9 M	(14.0)	[66.4]
v)	2.7 M	(13.2)	[98.0]	2.8 M	(13.7)	[98.0]
vi)	2.6 M	(12.6)	[95.0]	2.6 M	(12.9)	[94.2]
	p_{beam} = 13*A* GeV/*c*					
i)	14.9 M	(100.0)	-	16.2 M	(100.0)	-
ii)	5.4 M	(36.0)	[36.0]	5.8 M	(35.9)	[35.9]
iii)	2.9 M	(19.4)	[54.0]	3.1 M	(19.1)	[53.1]
iv)	1.8 M	(12.2)	[62.9]	1.9 M	(11.9)	[62.5]
v)	1.8 M	(12.0)	[97.8]	1.8 M	(11.1)	[93.2]
vi)	1.7 M	(11.3)	[94.3]	1.7 M	(10.5)	[94.8]

Chapter 5

Analysis

The analysis of the aforementioned data is performed in order to extract spectra and multiplicities of negatively charged pions produced in strong interaction processes and electromagnetic decays of hadrons. To this end the so-called h^- method is utilized. The method is based on the fact that approximately 90% of hadrons produced in a relativistic collision are pions. Thanks to this fact we can construct a multiplicative MC-based correction to the experimental data for negatively charged hadrons which will suppress the contribution of hadrons other than primary π^- mesons. The suppressed particles will in particular include other negatively charged primary hadrons (i.e. $\bar{p}$, K^-) and π^- produced in weak decays of hadrons (i.e. decays of K^0_S or Λ).

Although the NA61/SHINE detector is a spectrometer characterized by wide acceptance, the latter is limited. The limiting effect is the strongest in the backward rapidity region ($y < 0.0$). In order to obtain 4π results (i.e. a measurement in full solid angle or a measurement in full y vs. p_T phase space) an extrapolation procedure has to be applied to the MC-corrected data.

The details of both procedures will be explained in the present chapter.

5.1 Uncorrected spectra

After the event and track cuts mentioned in the previous chapter, the track measurements are transformed into two-dimensional spectra in bins of (y, p_T). The spectra are normalized to the bin size in y (dy) and p_T (dp_T). The spectra are also divided by the number of registered events after event cuts in order to obtain mean multiplicities per event.

The normalized bin content is shown in the Fig. 5.1 and is defined as:

$$n^{i,j}_{\mathrm{data}}[\mathrm{h}^-] = \frac{t^{i,j}_{\mathrm{data}}[\mathrm{h}^-]}{N_{\mathrm{data}}\mathrm{d}y\mathrm{d}p_T} \tag{5.1}$$

where $t^{i,j}_{\mathrm{data}}[\mathrm{h}^-]$ is the number of tracks in a given rapidity i and transverse momentum j bin, N_{data} is the number of events after event cuts and dy dp_T is the bin size – 0.2 × 0.1 GeV/c. The spectra are independently obtained for rapidity y and transverse mass $m_T = \sqrt{m^2 + (p_T c)^2}$ bins as well.

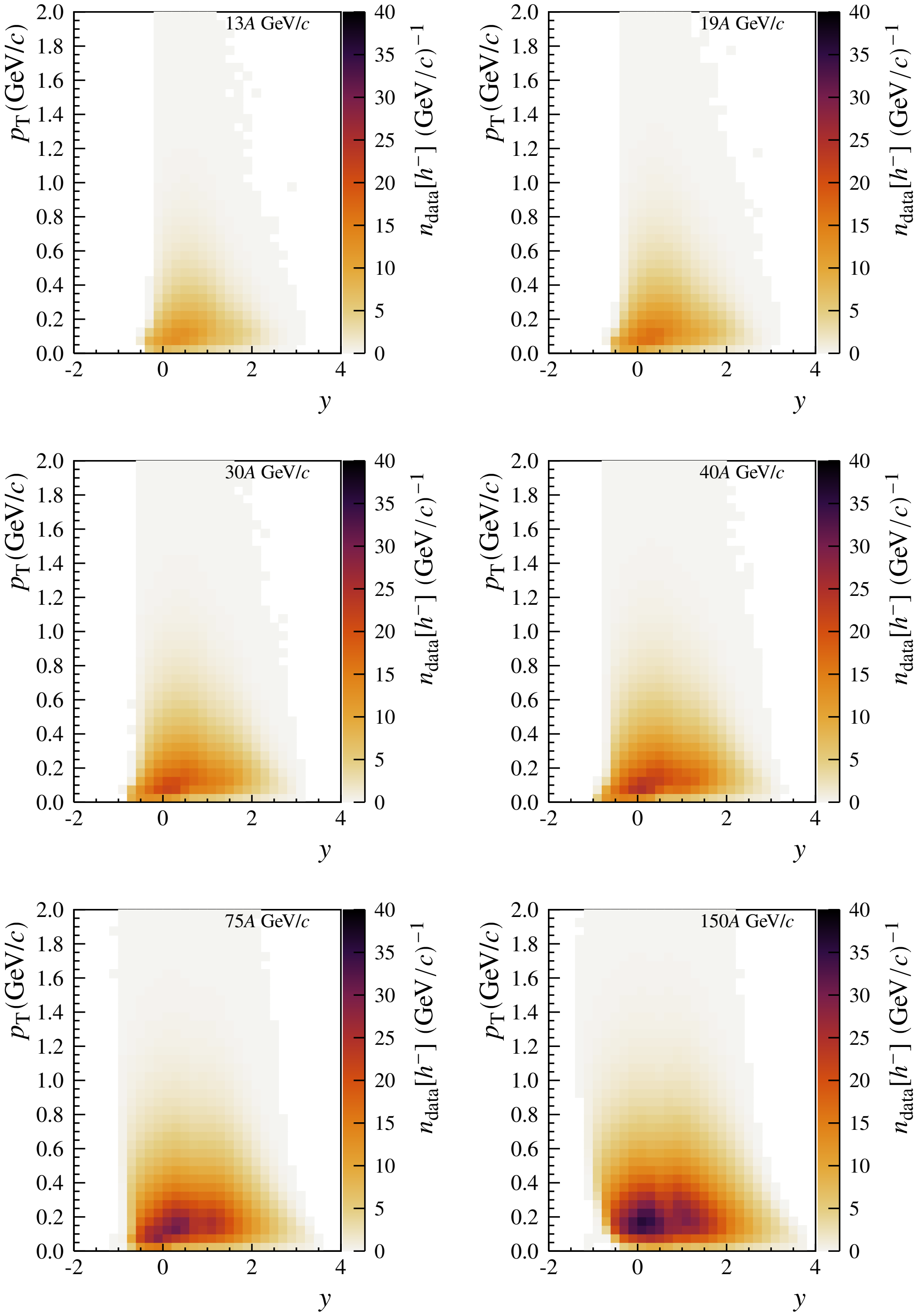

FIGURE 5.1: Negatively charged hadron spectra $n^{i,j}_{data}[h^-]$ after event and track selection for all measured beam momenta.

5.2 The h^- method

The corrections for the h^- method are based on the EPOS1.99 Monte-Carlo event generator. These take into account the small fraction of particles other than pions, secondary pions from decays, as well as the reconstruction efficiency and the detector geometry. A large number of collisions is generated and goes through the event and track selection. After the event and track selection, the generated tracks of negatively charged pions $t^{i,j}_{\mathrm{gen}}[\pi^-]$ are accumulated in y and p_T bins such that:

$$n^{i,j}_{\mathrm{gen}}[\pi^-] = \frac{t^{i,j}_{\mathrm{gen}}[\pi^-]}{N_{\mathrm{gen}}\mathrm{d}y\mathrm{d}p_{\mathrm{T}}} \tag{5.2}$$

where N_{gen} is the number of generated events after cuts. The generated MC events are passed through the detector simulation and regular reconstruction procedure so that tracks of negatively charged hadrons $t^{i,j}_{\mathrm{sel}}[\mathrm{h}^-]$ can be selected:

$$n^{i,j}_{\mathrm{sel}}[\mathrm{h}^-] = \frac{t^{i,j}_{\mathrm{sel}}[\mathrm{h}^-]}{N_{\mathrm{sel}}\mathrm{d}y\mathrm{d}p_{\mathrm{T}}}, \tag{5.3}$$

where N_{sel} is the number of reconstructed events after cuts. The selected negatively charged hadrons $n^{i,j}_{\mathrm{sel}}[\mathrm{h}^-]$ include contributions from the following particles:

1. primary negatively charged pions $n^{i,j}_{\mathrm{sel}}[\pi^-]$,
2. primary negatively charged kaons $n^{i,j}_{\mathrm{sel}}[K^-]$,
3. primary antiprotons $n^{i,j}_{\mathrm{sel}}[\bar{p}]$,
4. secondary negatively charged pions from K^0_S decays $n^{i,j}_{\mathrm{sel}}\left[\pi^-_{K^0_S}\right]$,
5. secondary negatively charged pions from Λ decays $n^{i,j}_{\mathrm{sel}}[\pi^-_{\Lambda}]$,
6. other particles, mostly products of secondary interactions of various particles $n^{i,j}_{\mathrm{sel}}[\mathrm{other}]$,

$$\begin{aligned} n^{i,j}_{\mathrm{sel}}[\mathrm{h}^-] =& n^{i,j}_{\mathrm{sel}}[\pi^-] \\ &+ n^{i,j}_{\mathrm{sel}}[K^-] \\ &+ n^{i,j}_{\mathrm{sel}}[\bar{p}] \\ &+ n^{i,j}_{\mathrm{sel}}\left[\pi^-_{K^0_S}\right] \\ &+ n^{i,j}_{\mathrm{sel}}[\pi^-_{\Lambda}] \\ &+ n^{i,j}_{\mathrm{sel}}[\mathrm{other}] \end{aligned} \tag{5.4}$$

The contributions of different particles to the total EPOS-generated spectrum are presented in Fig. 5.2 for 150A (GeV/c) beam momentum only. Analysis of the plot shows that the vast majority of produced negatively charged hadrons are π^-, their contributions is about 80-90% for the most part of the analysis acceptance. The important contribution of K^- and $\bar{p}$ is found in the high p_T region, but never exceeds 20%. Secondary pions produced in decays of K^0_S ($\pi^-_{K^0_S}$) and Λ (π^-_{Λ}) contribute mostly in the area of small transverse momentum and close to mid-rapidity. The contribution of $\pi^-_{K^0_S}$ is negligible. Other negatively charged hadrons are uniformly distributed around the acceptance region. The number of selected negatively

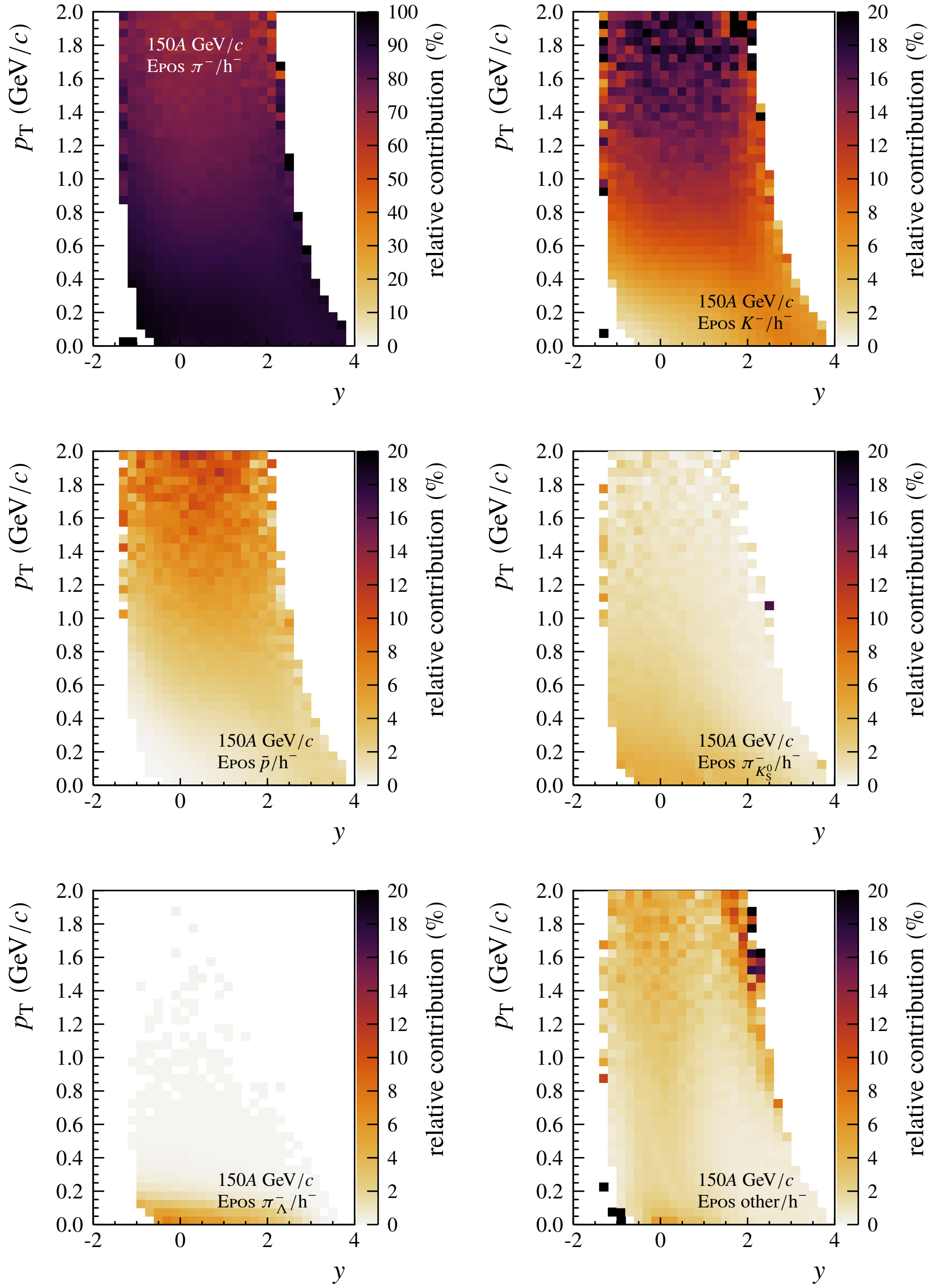

FIGURE 5.2: Separate spectra of primary π^-, K^-, $\bar{p}$, together with secondary π^- coming from K^0_S and Λ decays and all other produced particles. The spectra are divided by the total spectra of negatively charged hadrons h^- and show relative contributions of different hadron species. Rapidity y was calculated for all particles with an assumption of pion mass. Note different scale for the π^- contribution.

charged pion tracks after event and track cuts is obtained using information from track matching and is expressed as:

$$n^{i,j}_{\mathrm{sel}}[\pi^-] = \frac{t^{i,j}_{\mathrm{sel}}[\pi^-]}{N_{\mathrm{sel}}\mathrm{d}y\mathrm{d}p_{\mathrm{T}}}, \tag{5.5}$$

where $t^{i,j}_{\mathrm{sel}}[\pi^-]$ is the number of selected negatively charged pion tracks.

For each bin of transverse momentum p_{T} and rapidity y, two correction factors will be calculated for the π^- spectra. The first h^- correction factor is the ratio of the numbers of selected tracks obtained from the Monte-Carlo simulation:

$$c^{i,j}_{\mathrm{h}^-} = n^{i,j}_{\mathrm{sel}}[\pi^-]/n^{i,j}_{\mathrm{sel}}[\mathrm{h}^-]. \tag{5.6}$$

This factor is used to obtain the spectra of negatively charged pions from the spectra of all negatively charged hadrons. The second correction factor is the ratio of the two Monte-Carlo spectra for negatively charged pions:

$$c^{i,j}_{\mathrm{eff}} = n^{i,j}_{\mathrm{sel}}[\pi^-]/n^{i,j}_{\mathrm{gen}}[\pi^-]. \tag{5.7}$$

This correction is applied in order to correct for the losses of tracks due to inefficiencies in tracking algorithms as well as losses due to events and track quality cuts. The final correction factor will be the ratio of the two:

$$c^{i,j} = c^{i,j}_{\mathrm{h}^-}/c^{i,j}_{\mathrm{eff}} \tag{5.8}$$

and the final spectra $n^{i,j}_{\mathrm{corr}}[\pi^-]$ are constructed in the following way:

$$n^{i,j}_{\mathrm{corr}}[\pi^-] = n^{i,j}_{\mathrm{data}}[\mathrm{h}^-] \times c^{i,j} = n^{i,j}_{\mathrm{data}}[\mathrm{h}^-]\frac{n^{i,j}_{\mathrm{gen}}[\pi-]}{n^{i,j}_{\mathrm{sel}}[\mathrm{h}^-]}. \tag{5.9}$$

The procedure is schematically presented in Fig. 5.3.

5.2.1 Tuning of strange particle spectra in Monte-Carlo

Comparison with preliminary data on *dE/dx* and *tof-dE/dx* particle identification from NA61/SHINE (presented in Ref. [56]) proves that strange particles production in Epos is underestimated. Therefore, the contributions of primary negatively charged kaons K^- and secondary negatively charged pions produced from K^0_{S} and Λ decays $\pi^-_{K^0_{\mathrm{S}}}$ and π^-_{Λ}, respectively, are underestimated as well.

The ratios of the preliminary spectra of K^- and K^+ obtained by the *dE/dx* and *tof-dE/dx* methods to respective Epos MC generated spectra for 19*A* and 150*A* GeV/*c* are presented in Fig. 5.4.

In order to tune the Epos MC produced spectra one has to introduce tuning factors for three particle species that have the biggest bias due to strange particle production underestimation in Epos, namely K^-, $\pi^-_{K^0_{\mathrm{S}}}$ and π^-_{Λ}. Since the spectra or the mean multiplicities of K^0_{S} and Λ from *dE/dx* and *tof-dE/dx* analysis are unknown, empirical formulas presented in Ref. [57] are used to estimate them. For Λ, only the mean multiplicity can be derived from a combination of mean multiplicities for negatively and positively charged kaons, $\langle K^-\rangle$ and $\langle K^+\rangle$, respectively:

$$\langle\Lambda\rangle = \frac{2}{1.6}(\langle K^+\rangle - \langle K^-\rangle), \tag{5.10}$$

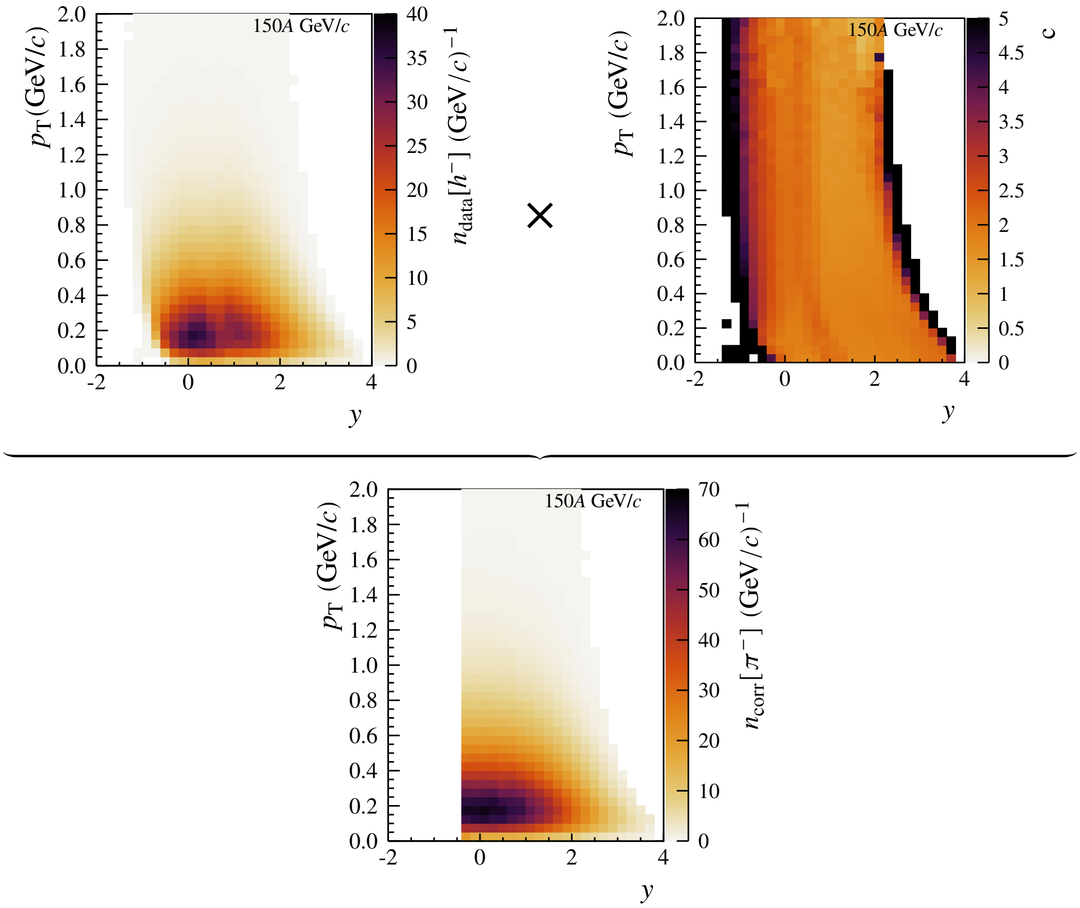

FIGURE 5.3: A schematic overview of the h^- method. Measured data × MC corrections = corrected spectra.

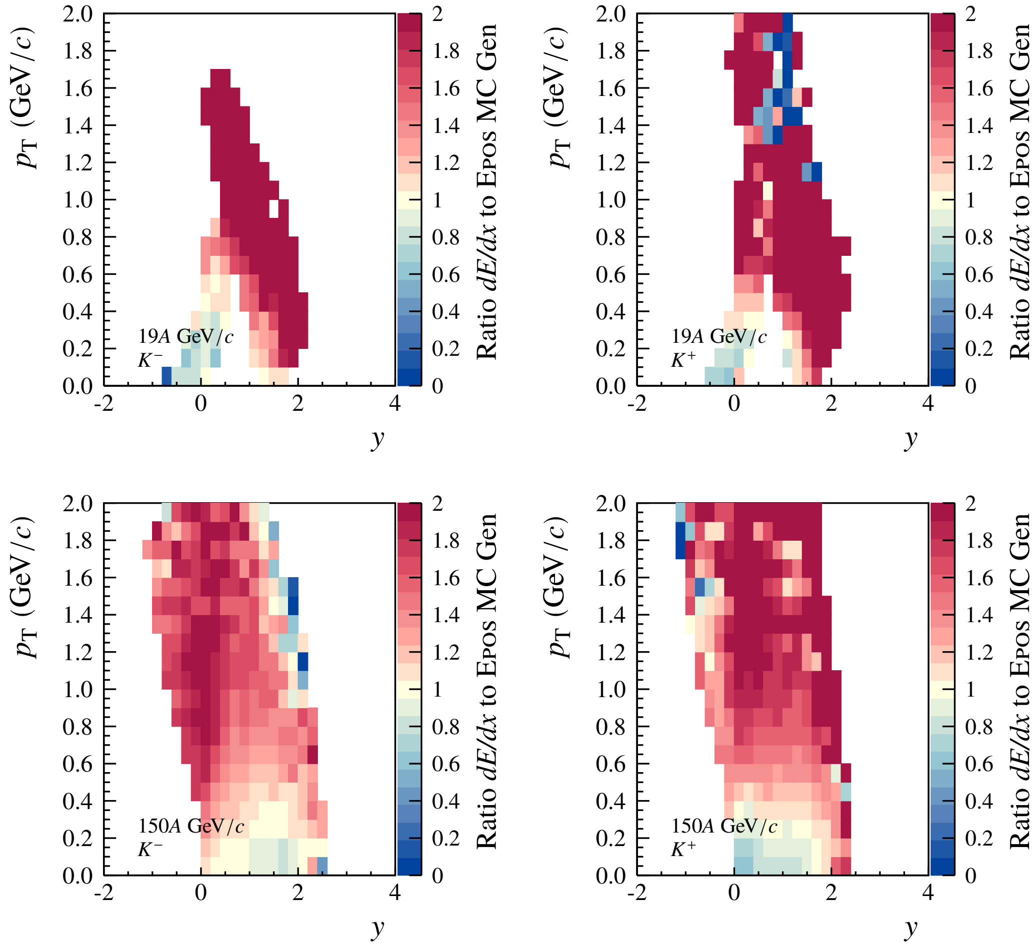

FIGURE 5.4: Ratios of preliminary spectra of K^- (*left*) and K^+ (*right*) obtained by *dE/dx* and *tof-dE/dx* method to EPOS MC generated spectra in common acceptance for ^{40}Ar+^{45}Sc collisions at 19*A* (*top*) and 150*A* (GeV/*c*) (*bottom*) beam momentum.

where the factor 2 is to account for $(K^0 - \bar{K}^0)$ and the factor 1.6 for the part of strange quarks confined within Σ^+ and Σ^-. The formula for K^0_S spectra estimation is the following:

$$n^{i,j}\left[K^0_S\right] = \frac{1}{2}\left(n^{i,j}\left[K^+\right] + n^{i,j}\left[K^-\right]\right). \tag{5.11}$$

The tuning will be applied as a multiplicative factor for the whole spectrum in case of Λ and for separate bins in case of K^0_S and K^-. Since the multiplicities of K^0_S and Λ in Epos are underestimated by factors $T^{i,j}\left[K^0_S\right]$ and $T\left[\langle\Lambda\rangle\right]$, respectively, it is claimed that the pions produced in the decays of theses hadrons ($\pi^-_{K^0_S}$ and π^-_{Λ}) will by underestimated by the same factors.

Since the acceptance of the *dE/dx* and *tof-dE/dx* method is limited (See Fig. 8.1), an extrapolation procedure to obtain full phase space 4π yields was performed. The procedure consists of two steps:

1. fitting and extrapolating identified particle spectra in p_T using an exponential formula:

$$f(p_T) = C p_T \exp\left(\frac{-\sqrt{m^2 + (p_T c)^2}}{T}\right), \tag{5.12}$$

2. extrapolating a Gaussian function fitted to the rapidity spectrum dn/dy.

The procedure is performed in 10 iterations in order to obtain the smoothest result. The original *dE/dx* and *tof-dE/dx* data remains unchanged except for the edge bins which might be affected by the acceptance. The edge bins together with the area outside the acceptance are extrapolated. The resulting extrapolated spectra are presented in Fig. 5.5 for K^- and K^+ for lowest and highest beam momentum, where *dE/dx* and *tof-dE/dx* analyses were performed.

Using the extrapolated spectra and formulas 5.10 and 5.11, one can calculate the final tuning factors for the Epos MC. The tuning factors in case of K^- and $\pi^-_{K^0_S}$ will be calculated for each bin of the spectrum separately in the following way:

$$T^{i,j}\left[K^-\right] = \frac{n^{i,j}_{dE/dx}\left[K^-\right]}{n^{i,j}_{\mathrm{gen}}\left[K^-\right]}\frac{n^{i,j}_{\mathrm{gen}}\left[\pi^-\right]}{n^{i,j}_{dE/dx}\left[\pi^-\right]}, \tag{5.13}$$

$$T^{i,j}\left[K^0_S\right] = \frac{1}{2}\frac{n^{i,j}_{dE/dx}\left[K^-\right] + n^{i,j}_{dE/dx}\left[K^+\right]}{n^{i,j}_{\mathrm{gen}}\left[K^0_S\right]}\frac{n^{i,j}_{\mathrm{gen}}\left[\pi^-\right]}{n^{i,j}_{dE/dx}\left[\pi^-\right]}. \tag{5.14}$$

On the other hand, there will be only one factor for the whole spectrum in case of π^-_{Λ}:

$$T\left[\langle\Lambda\rangle\right] = \frac{2}{1.6}\frac{\langle K^+\rangle_{dE/dx} - \langle K^-\rangle_{dE/dx}}{\langle\Lambda\rangle_{\mathrm{gen}}}\frac{\langle\pi^-\rangle_{\mathrm{gen}}}{\langle\pi^-\rangle_{dE/dx}}. \tag{5.15}$$

The summary of all the tuning factors for π^-_{Λ} is presented in Table 5.1, whereas tuning factors for K^- and $\pi^-_{K^0_S}$ are presented in Fig. 5.6 for 19*A* and 150*A* GeV/*c* beam momentum.

The final MC simulated spectra will be tuned using previously obtained tuning factors. For K^-, the particle will enter the y vs. p_T spectrum with a weight $T^{i,j}\left[K^-\right]$ corresponding

Table 5.1: Λ MC tuning factors $T\left[\langle\Lambda\rangle\right]$ for ^{40}Ar+^{45}Sc collisions from 19*A* to 150*A* GeV/*c* beam momentum.

p_{beam} (GeV/c)	19	30	40	75	150
$T\left[\langle\Lambda\rangle\right]$	1.72	1.56	1.44	1.23	1.02

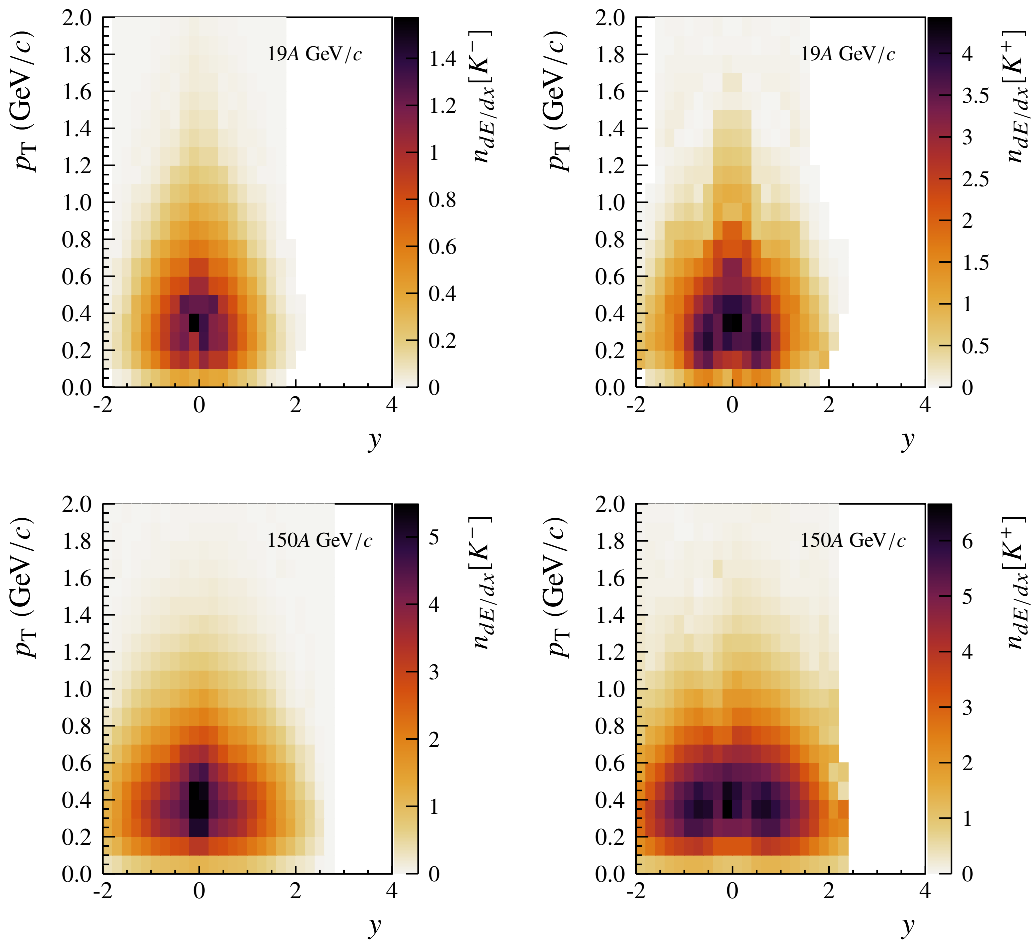

FIGURE 5.5: *dE/dx* and *tof-dE/dx* spectra extrapolated to 4π for K^- (*left*) and K^+ (*right*) for ^{40}Ar+^{45}Sc collisions at 19A (*top*) and 150A GeV/c (*bottom*) beam momentum.

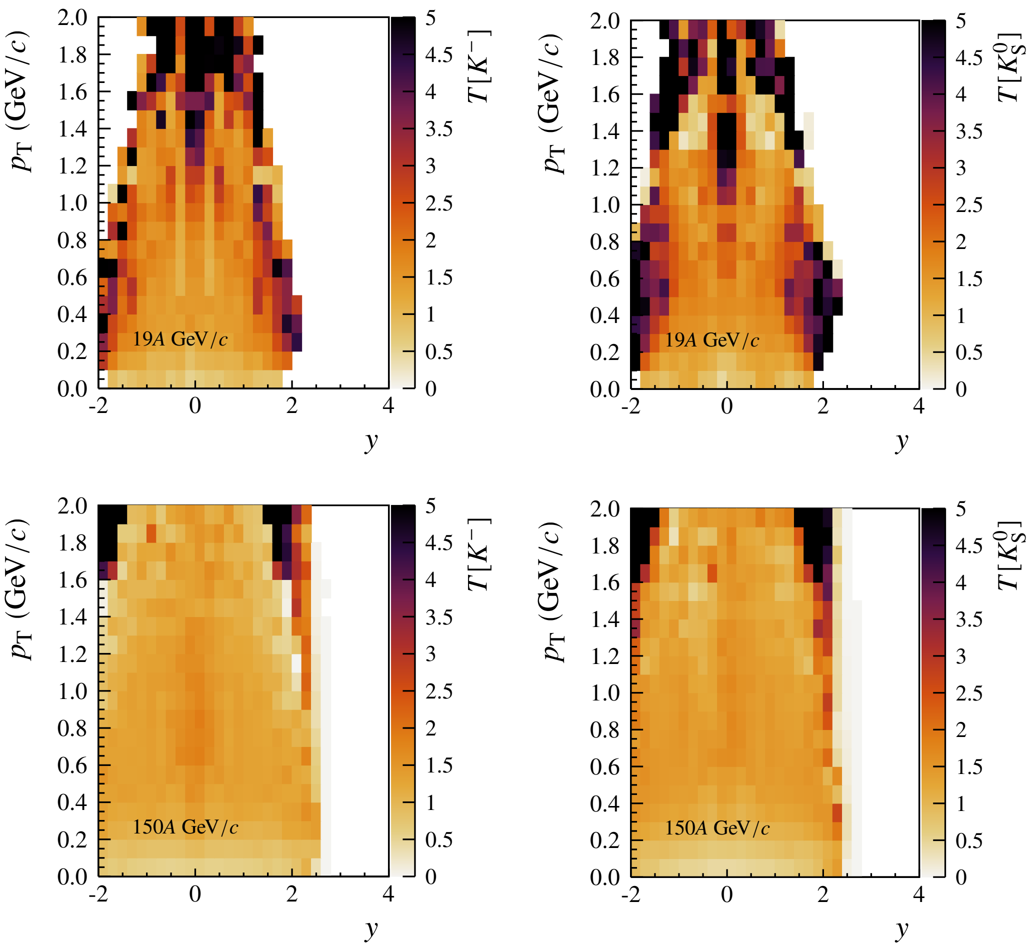

FIGURE 5.6: MC tuning factors for K^- (*left*) and K^0_S (*right*) for ^{40}Ar+^{45}Sc collisions at 19*A* (*top*) and 150*A* GeV/*c* (*bottom*) beam momentum.

to bin calculated for rapidity with assumption of charged kaon mass. For $\pi^-_{K^0_S}$, the procedure will apply the weight factor $T^{i,j}\left[K^0_S\right]$ corresponding to the rapidity and p_T of the parent K^0_S particle. For π^-_Λ, the uniform tuning factor $T\left[\langle\Lambda\rangle\right]$ will be applied to all particles. Therefore, modifying Eq. 5.2, the final selected and tuned spectra $n^{i,j}_{\text{sel, tuned}}\left[\text{h}^-\right]$ will be formed in the following way:

$$\begin{aligned} n^{i,j}_{\text{sel, tuned}}\left[\text{h}^-\right] = & n^{i,j}_{\text{sel}}\left[\pi^-\right] \\ & + T^{i,j}\left[K^-\right] \times n^{i,j}_{\text{sel}}\left[K^-\right] \\ & + n^{i,j}_{\text{sel}}\left[\bar{\text{p}}\right] \\ & + T^{i,j}\left[K^0_S\right] \times n^{i,j}_{\text{sel}}\left[\pi^-_{K^0_S}\right] \\ & + T\left[\langle\Lambda\rangle\right] \times n^{i,j}_{\text{sel}}\left[\pi^-_\Lambda\right] \\ & + n^{i,j}_{\text{sel}}\left[\text{other}\right] \end{aligned} \tag{5.16}$$

In case of 13*A* GeV/*c*, there are no results from *dE/dx* or *tof-dE/dx*. Therefore, in this case the tuning from 19*A* GeV/*c* beam momentum was applied.

5.2.2 Resulting correction factors

The final MC correction factor after tuning is the fraction of the Monte-Carlo spectra from generated and reconstructed tracks for each y vs. p_T bin:

$$c^{i,j}_{\text{tuned}} = n^{i,j}_{\text{gen}}[\pi^-]/n^{i,j}_{\text{sel, tuned}}[\text{h}^-]. \tag{5.17}$$

The correction factors for all beam momenta are presented in Fig. 5.7.

5.2.3 Resulting spectra

The corrected spectra $n^{i,j}_{\text{corr}}[\pi^-]$ from the h^- method are calculated as:

$$n^{i,j}_{\text{corr}}[\pi^-] = n^{i,j}_{\text{data}}[\text{h}^-] \times c^{i,j}_{\text{tuned}} = n^{i,j}_{\text{data}}[\text{h}^-]\frac{n^{i,j}_{\text{gen}}[\pi-]}{n^{i,j}_{\text{sel,tuned}}[\text{h}^-]}. \tag{5.18}$$

The corrected spectra for all beam momenta are presented in Chapter 7.

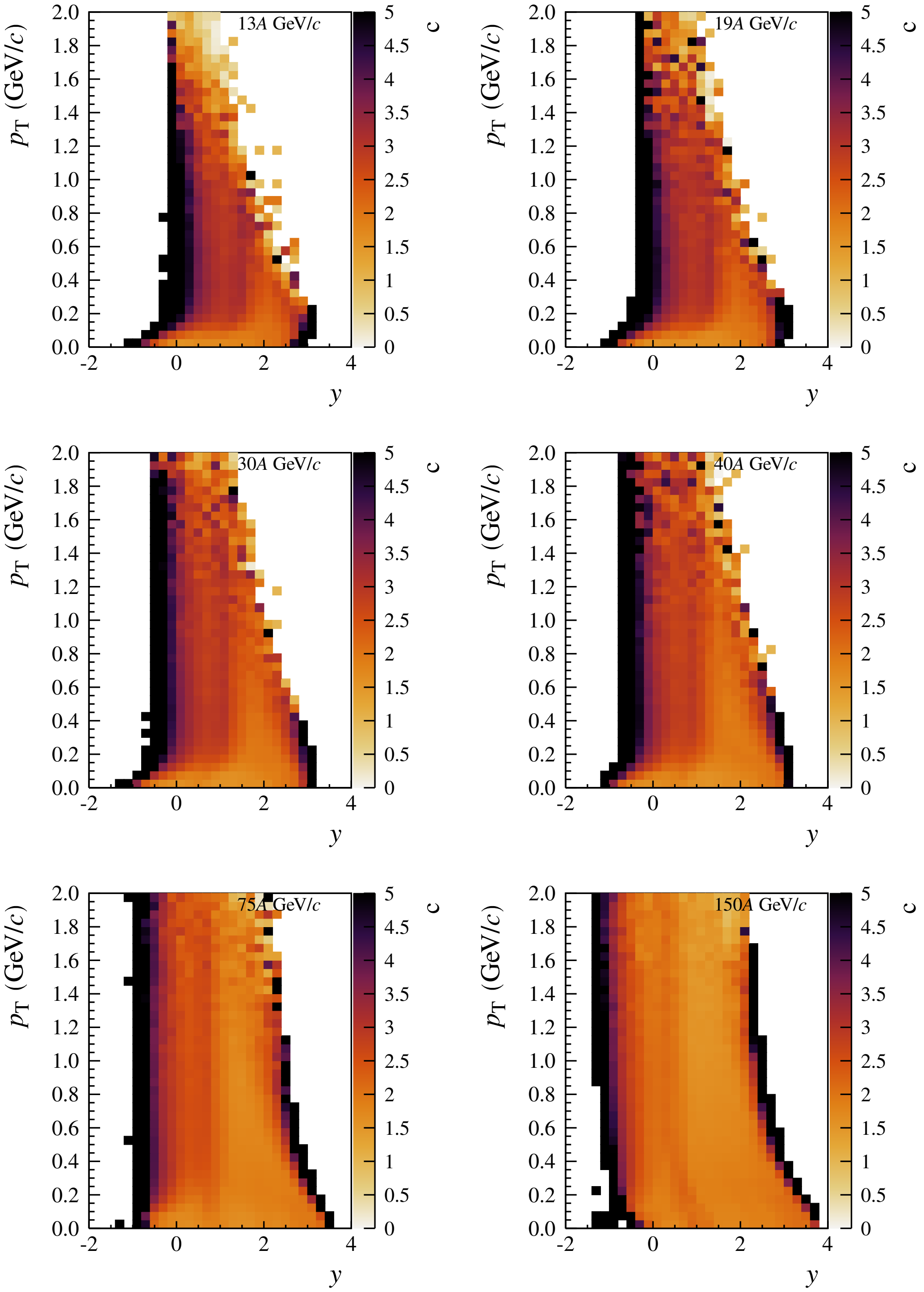

FIGURE 5.7: The final MC correction factors for collisions from 13*A* to 150*A* GeV/*c*. The MC correction factors include tuning necessary to account for strange particle production underestimation in EPOS.

5.3 Statistical and systematic uncertainties

5.3.1 Statistical uncertainties

The impact of the finite statistics on the resulting spectra can be estimated based on the assumption that the number of tracks in each bin is distributed according to the Poisson distribution. The uncertainty has to be calculated for both raw spectra and MC corrections. The impact of the correlations between particles on the uncertainty is expected to be low.

Statistical uncertainties for each bin of data are calculated assuming that the number of entries follows the Poisson probability distribution. In this case the statistical uncertainties $\sigma^{i,j}_{\mathrm{stat,data}}$ can be expressed as a standard deviation of the Poisson distribution with the number of tracks as a mean value:

$$\sigma_{\mathrm{stat}}\left(n^{i,j}_{\mathrm{data}}[\mathrm{h}^-]\right) = \frac{\sqrt{t^{i,j}_{\mathrm{data}}[\mathrm{h}^-]}}{N_{\mathrm{data}}}, \tag{5.19}$$

where N_{data} is the number of events, $t^{i,j}_{\mathrm{data}}[\mathrm{h}^-]$ is the number of negatively charged hadron tracks in bin i, j.

Statistical uncertainties of the MC corrections $c^{i,j}_{\mathrm{tuned}}$ were calculated from two sources:

- MC selected π^- tracks are a subset of selected h^- tracks, i.e. $n_{\mathrm{sel}}[\pi^-] \subset n_{\mathrm{sel}}[\mathrm{h}^-]$. The statistical uncertainty which takes the correlation into account is calculated as:

$$\sigma_{\mathrm{stat}}\left(c^{i,j}_{\mathrm{h}^-}\right) = \frac{n^{i,j}_{\mathrm{sel}}[\pi^-]}{n^{i,j}_{\mathrm{sel}}[\mathrm{h}^-]}\sqrt{\frac{1}{n^{i,j}_{\mathrm{sel}}[\pi^-]} - \frac{1}{n^{i,j}_{\mathrm{sel}}[\mathrm{h}^-]}} \tag{5.20}$$

- MC selected π^- tracks are a subset of generated π^- tracks, i.e. $n_{\mathrm{sel}}[\pi^-] \subset n_{\mathrm{gen}}[\pi^-]$. Thus, the statistical uncertainty which takes the correlation into account is calculated as:

$$\sigma_{\mathrm{stat}}\left(c^{i,j}_{\mathrm{eff}}\right) = \frac{n^{i,j}_{\mathrm{sel}}[\pi^-]}{n^{i,j}_{\mathrm{gen}}[\pi^-]}\sqrt{\frac{1}{n^{i,j}_{\mathrm{sel}}[\pi^-]} - \frac{1}{n^{i,j}_{\mathrm{gen}}[\pi^-]}} \tag{5.21}$$

The statistical uncertainty of the total correction factor is calculated from the law of propagation of uncertainty assuming a high correlation between $c^{i,j}_{\mathrm{eff}}$ and $c^{i,j}_{\mathrm{h}^-}$:

$$\sigma_{\mathrm{stat}}\left(c^{i,j}\right) = c^{i,j}\sqrt{\left(\frac{\sigma_{\mathrm{stat}}\left(c^{i,j}_{\mathrm{h}^-}\right)}{c^{i,j}_{\mathrm{h}^-}}\right)^2 + \left(\frac{\sigma_{\mathrm{stat}}\left(c^{i,j}_{\mathrm{eff}}\right)}{c^{i,j}_{\mathrm{eff}}}\right)^2 - 2\frac{1}{c^{i,j}_{\mathrm{h}^-}c^{i,j}_{\mathrm{eff}}}}. \tag{5.22}$$

Assuming no correlation between the data and MC corrections, the total uncertainty of the corrected data can be expressed as:

$$\sigma_{\mathrm{stat}}\left(n^{i,j}_{\mathrm{corr}}[\pi^-]\right) = n^{i,j}_{\mathrm{corr}}[\pi^-]\sqrt{\left(\frac{\sigma_{\mathrm{stat}}\left(n^{i,j}_{\mathrm{data}}[\mathrm{h}^-]\right)}{n^{i,j}_{\mathrm{data}}[\mathrm{h}^-]}\right)^2 + \left(\frac{\sigma_{\mathrm{stat}}[c^{i,j}]}{c^{i,j}}\right)^2}. \tag{5.23}$$

The resulting relative statistical uncertainties $\sigma_{\mathrm{stat}}\left(n^{i,j}_{\mathrm{corr}}[\pi^-]\right)/n^{i,j}_{\mathrm{corr}}[\pi^-]$ for all beam momenta are presented in Fig. 5.8.

5.3.2 Systematic uncertainties

The systematic uncertainty was estimated varying parameters used during the analysis of the data reconstruction and MC simulation and observing their effects on the final spectra. The

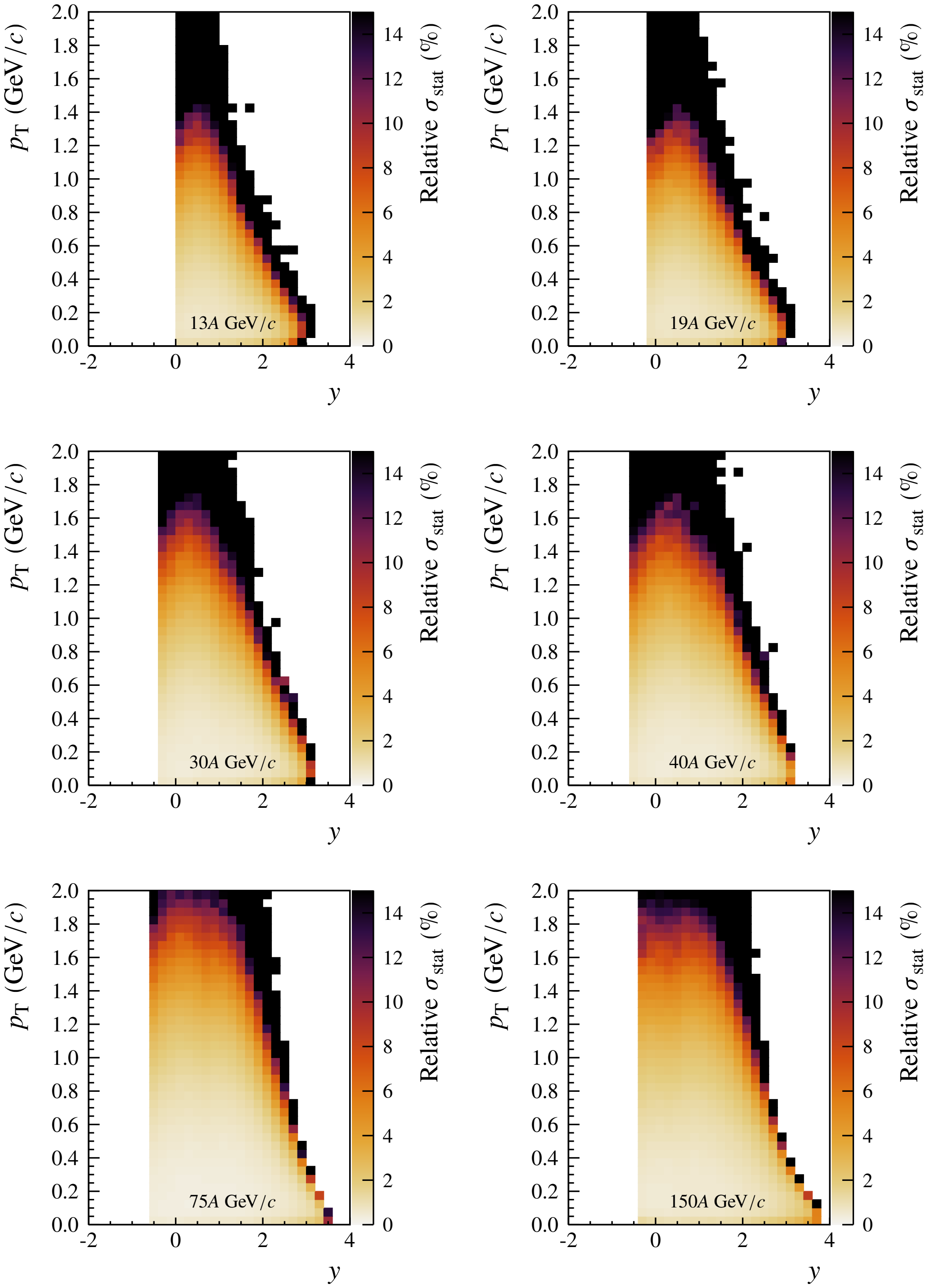

FIGURE 5.8: Relative statistical uncertainties of the corrected data $n^{i,j}_{corr}[\pi^-]$ for all beam momenta.

possible contributions to the systematic uncertainty were calculated taking into account contributions from the following effects:

I Possible biases which were not corrected for. These are:

(a) a possible bias due to the dE/dx cut applied to reject electron tracks,

(b) a possible bias due to the removal of events with off-time beam particles close in time to the trigger particle.

Their magnitude was estimated by varying the values of the corresponding cut. The values of the selected dE/dx band around the Bethe-Bloch function was changed by ± 0.01 dE/dx units (where 1 corresponds to a minimum ionizing particle, and 0.04 is a typical width of the dE/dx distribution for π^-), and the rejection time window was changed to ± 3 μs and ± 5 μs. The systematic uncertainty was estimated as half of the maximum absolute difference between h^- multiplicities when varying the cut values. This contribution is marked with the yellow dashed line (- -) in Fig. 5.9 and is the most pronounced for higher beam momenta.

II Uncertainty of the correction for the track selection cuts used for data and Monte-Carlo data selection were estimated by varying both cut values, the number of points in TPCs by ± 3 and the impact parameter over the range ± 1. The resulting uncertainty was estimated as half of the value of the absolute difference between the most and the least restrictive versions of the cuts. This contribution is marked with green dashed lines (- - -) in Fig. 5.9 and has the biggest impact for most of the beam momenta.

III Uncertainty of the correction for contamination of the primary π^- mesons by daughters of decays and re-interactions. This was estimated using MC simulations as 15% of the fraction of π^- coming from weak decays to the total number of produced π^-. This contribution is shown by the light blue solid line (—) in Fig. 5.9.

IV Uncertainty of the correction for the contamination of particles other than π^- in the negatively charged hadrons spectrum. In order to estimate this, the EPOS MC simulation was used. The relative uncertainty is 15% of the contribution of K^-, Σ^- and $\bar{p}$ to the total number of produced negatively charged hadrons h$^-$. This contribution is shown as a dark blue dotted line (⋯⋯) in Fig. 5.9.

The total systematic uncertainty was obtained adding the separate contributions in quadrature:

$$\sigma_{\text{sys}}\left(n_{\text{corr}}^{i,j}[\pi^-]\right) = \sqrt{\left(\sigma_{\text{I}}^{i,j}\right)^2 + \left(\sigma_{\text{II}}^{i,j}\right)^2 + \left(\sigma_{\text{III}}^{i,j}\right)^2 + \left(\sigma_{\text{IV}}^{i,j}\right)^2}. \tag{5.24}$$

The resulting relative systematic uncertainties $\sigma_{\text{sys}}\left(n_{\text{corr}}^{i,j}[\pi^-]\right)/n_{\text{corr}}^{i,j}[\pi^-]$ for all beam momenta are presented in Fig. 5.10. When integrating the spectra in transverse momentum p_{T}, the uncertainties are added in quadrature:

$$\sigma_i = \sqrt{\sum_j \left(\sigma^{i,j}\right)^2}. \tag{5.25}$$

This allows to plot different contributions to the total systematic uncertainty, which is presented in Fig. 5.9.

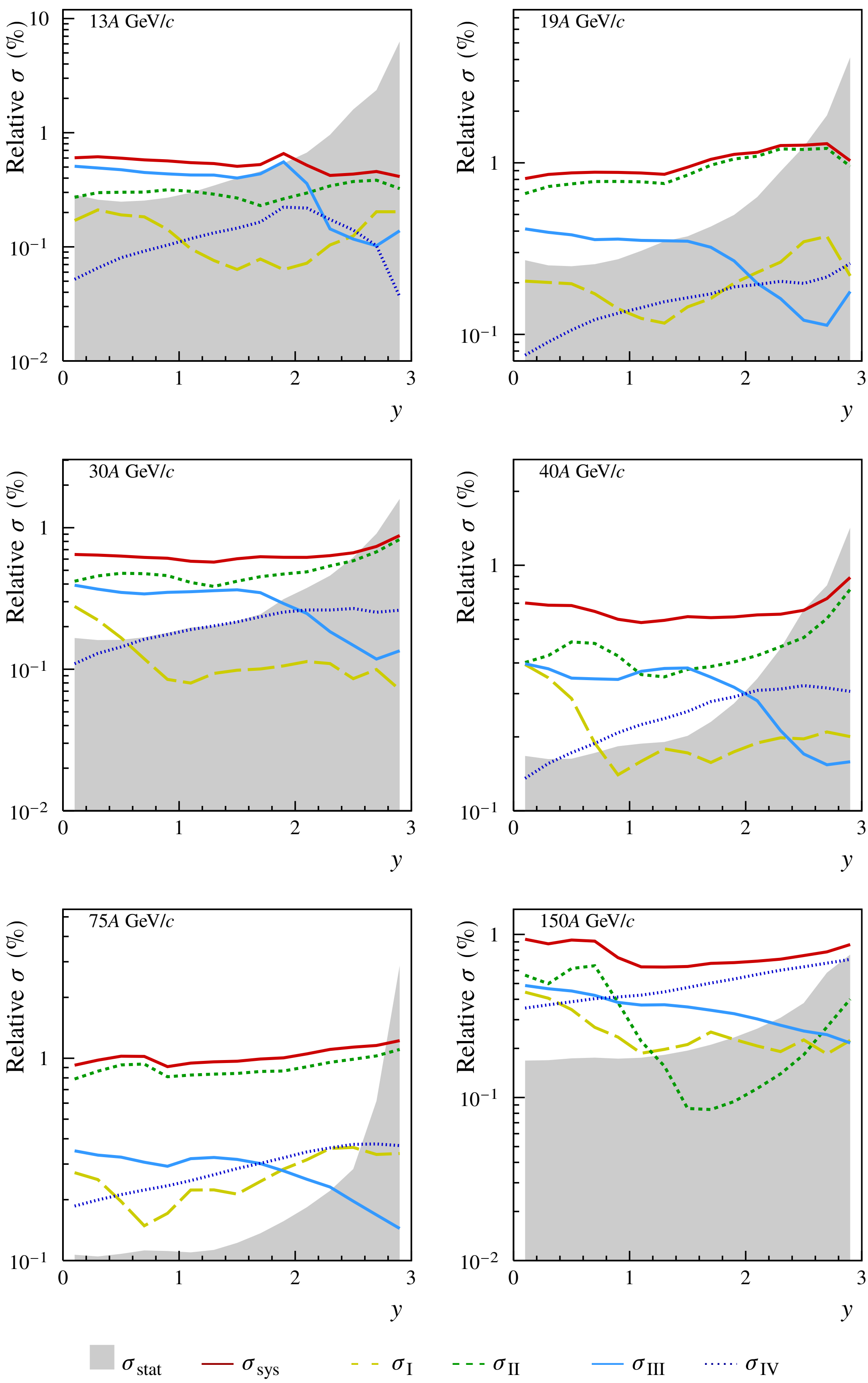

FIGURE 5.9: Different contributions to systematic uncertainties of the rapidity y distribution dn/dy and the statistical uncertainty (gray area in background) for all beam momenta.

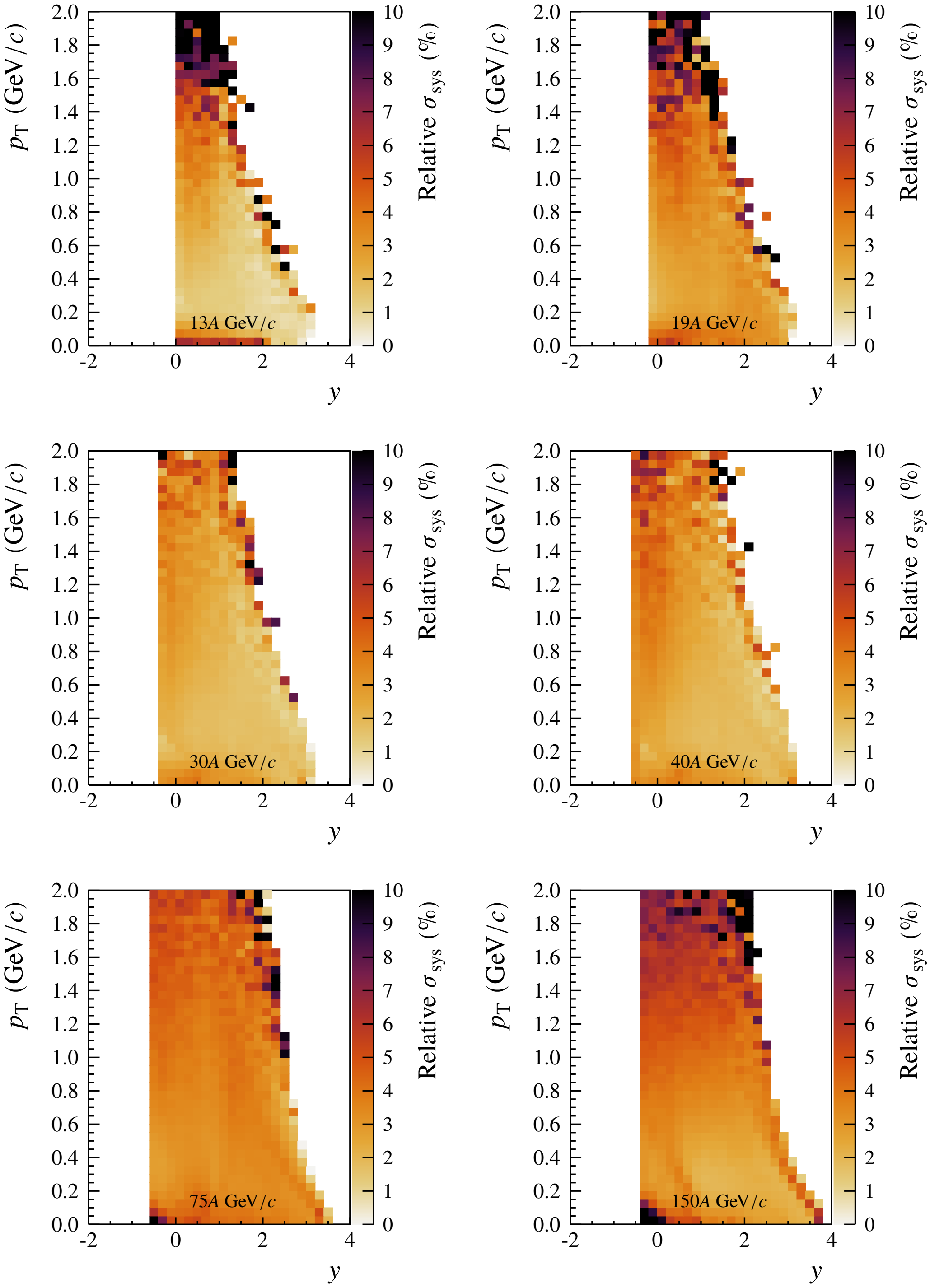

FIGURE 5.10: Relative systematic uncertainties of the corrected data $n^{i,j}_{corr}[\pi^-]$ for all beam momenta.

5.3.3 Rapidity range

Because of the limited backward ($y < 0.0$) acceptance of the NA61/SHINE detector, a cut has been employed to remove backward rapidity bins with high uncertainty values. The cut was set to remove backward rapidity bins with relative statistical uncertainty $\sigma_{\text{stat}}\left(n^{i,j}_{\text{corr}}[\pi^-]\right)/n^{i,j}_{\text{corr}}[\pi^-]$ greater than 30% in case of lower beam momenta (13*A*, 19*A*, 30*A* and 40*A* GeV/*c*) and 20% in case of higher beam momenta (75*A* and 150*A* GeV/*c*). The resulting rapidity range of the spectra that will be used in further steps of the analysis is presented in Table 5.2.

TABLE 5.2: Rapidity y ranges of the corrected spectra $n^{i,j}_{\text{corr}}[\pi^-]$ used in the extrapolation procedure.

p_{beam} (GeV/c)	13	19	30	40	75	150
y_{min}	0.0	-0.2	-0.4	-0.6	-0.6	-0.4
y_{max}	3.2	3.2	3.2	3.2	3.6	3.8

5.4 Extraplation and integration

The procedure of extrapolation to 4π (full solid angle) acceptance is subdivided into two steps:

1. Extrapolation of the corrected spectra $n^{i,j}_{\mathrm{corr}}[\pi^-]$ in p_{T},
2. Integration in p_{T} and extrapolation of $\mathrm{d}n/\mathrm{d}y$ rapidity spectra.

5.4.1 Extrapolation in transverse momentum

Extrapolation of the corrected data $n^{i,j}_{\mathrm{corr}}[\pi^-]$ in p_{T} for each rapidity bin was done using the exponential formula:

$$f(p_{\mathrm{T}}) = Cp_{\mathrm{T}} \exp\left(\frac{-\sqrt{m^2 + (p_{\mathrm{T}}c)^2}}{T}\right), \tag{5.26}$$

where C and T are fitting parameters, m is the charged pion mass. The extrapolation is only performed in y bins with high enough number of entries. Examples of such procedure are presented in Fig. 5.11 for single y bins and in the bottom panel of Fig. 5.12 for the corrected spectra $n^{i,j}_{\mathrm{corr}}[\pi^-]$. The extrapolation was performed up to $p_{\mathrm{T}} = 2.0$ GeV/c and it's effect is small, it does not exceed 1‰ for all beam momenta.

To obtain rapidity spectra $\mathrm{d}n/\mathrm{d}y$, the measured p_{T} data bins are summed and the integral of the extrapolated curve is added:

$$\frac{\mathrm{d}n}{\mathrm{d}y} = \sum_{0}^{p_{\mathrm{T}}^{\mathrm{max}}} \mathrm{d}p_{\mathrm{T}} \left(\frac{\mathrm{d}^2 n}{\mathrm{d}y\mathrm{d}p_{\mathrm{T}}}\right)_{\mathrm{measured}} + \int_{p_{\mathrm{T}}^{\mathrm{max}}}^{2} f(p_{\mathrm{T}})\mathrm{d}p_{\mathrm{T}}. \tag{5.27}$$

5.4.2 Extrapolation in rapidity

In order to extrapolate the rapidity spectra to the missing rapidity acceptance a sum of two symmetrically displaced Gaussian functions is used:

$$g(y) = \frac{A_0 A_{\mathrm{rel}}}{\sigma_0\sqrt{2\pi}} \exp\left(-\frac{(y-y_0)^2}{2\sigma_0^2}\right) + \frac{A_0}{\sigma_0\sqrt{2\pi}} \exp\left(-\frac{(y+y_0)^2}{2\sigma_0^2}\right), \tag{5.28}$$

where A_0 is an amplitude of the first Gaussian function, A_{rel} is the relative amplitude of the second, σ_0 is the standard deviation and y_0 is the peaks displacement from the center-of-mass rapidity $y = 0$. The fitting is only performed for bins defined in Table 5.2.

In the case of the beam momentum of 13A GeV/c, there is no information in the backward rapidity region. This causes the aforementioned fitting procedure to be questionable. Therefore, in this case a different approach was employed, parameters A_{rel} and y_0 were extrapolated from parameters fitted at other beam momenta using linear and quadratic functions, respectively. Next, using the sum of two Gaussians from Eq. 5.28 and previously calculated A_{rel} and y_0, the remaining parameter σ_0 was fitted.

A comparison of the parameters for all beam momenta together with other similar measurements is presented in Fig. 5.13. The resulting parameters of the fit are also presented in Table 5.3. The $\sigma_{\mathrm{d}n/dy}$ parameter is the r.m.s. width $\sqrt{\sigma_0^2 + y_0^2}$ and its uncertainty is calculated from the law of propagation of uncertainty. The r.m.s. widths of the rapidity distributions $\sigma_{\mathrm{d}n/dy}$ differ by less than 5% from the widths approximated by a single Gaussian function.

An overview of the $\mathrm{d}n/\mathrm{d}y$ extrapolation procedure together with resulting y spectra is presented in Fig. 5.14.

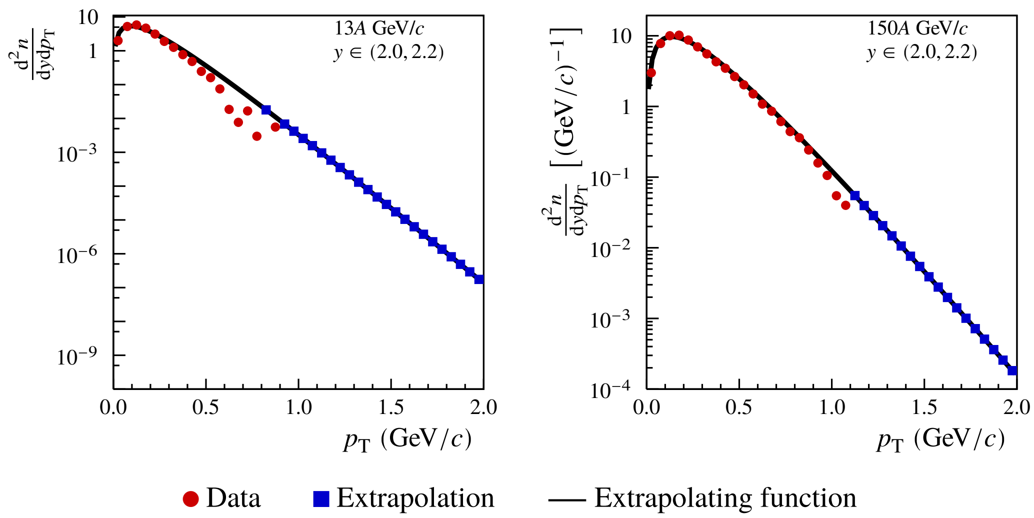

FIGURE 5.11: Examples of the original (red circles) and extrapolated (blue boxes) p_T distribution together with the fitted extrapolation function (black curve) for a given rapidity bin for 13A (left) and 150A GeV/c (right) beam momentum.

TABLE 5.3: Parameters A_{rel}, σ_0 and y_0 of the double Gaussian fit, and r.m.s. width $\sigma_{dn/dy}$ of the rapidity distribution with its uncertainties.

p_{beam} (GeV/c)	13	19	30	40	75	150
A_{rel}	0.833	0.840	0.820	0.920	0.898	0.971
$\sigma_{stat}(A_{rel})$	0.0024	0.0110	0.0046	0.0038	0.0022	0.0052
$\sigma_{sys}(A_{rel})$	0.2062	0.2275	0.1632	0.1284	0.1575	0.1988
σ_0	0.830	0.854	0.905	0.922	0.960	0.996
$\sigma_{stat}(\sigma_0)$	0.0007	0.0038	0.0022	0.0019	0.0011	0.0015
$\sigma_{sys}(\sigma_0)$	0.1125	0.1188	0.1279	0.1508	0.1560	0.2085
y_0	0.441	0.518	0.583	0.627	0.772	0.913
$\sigma_{stat}(y_0)$	0.0293	0.0079	0.0038	0.0030	0.0014	0.0020
$\sigma_{sys}(y_0)$	0.3402	0.2587	0.2415	0.2201	0.2737	0.3356
$\sigma_{dn/dy}$	0.940	0.999	1.077	1.114	1.232	1.351
$\sigma_{stat}(\sigma_{dn/dy})$	0.0156	0.0061	0.0033	0.0028	0.0016	0.0024
$\sigma_{sys}(\sigma_{dn/dy})$	0.0891	0.0824	0.0868	0.0944	0.1026	0.1350

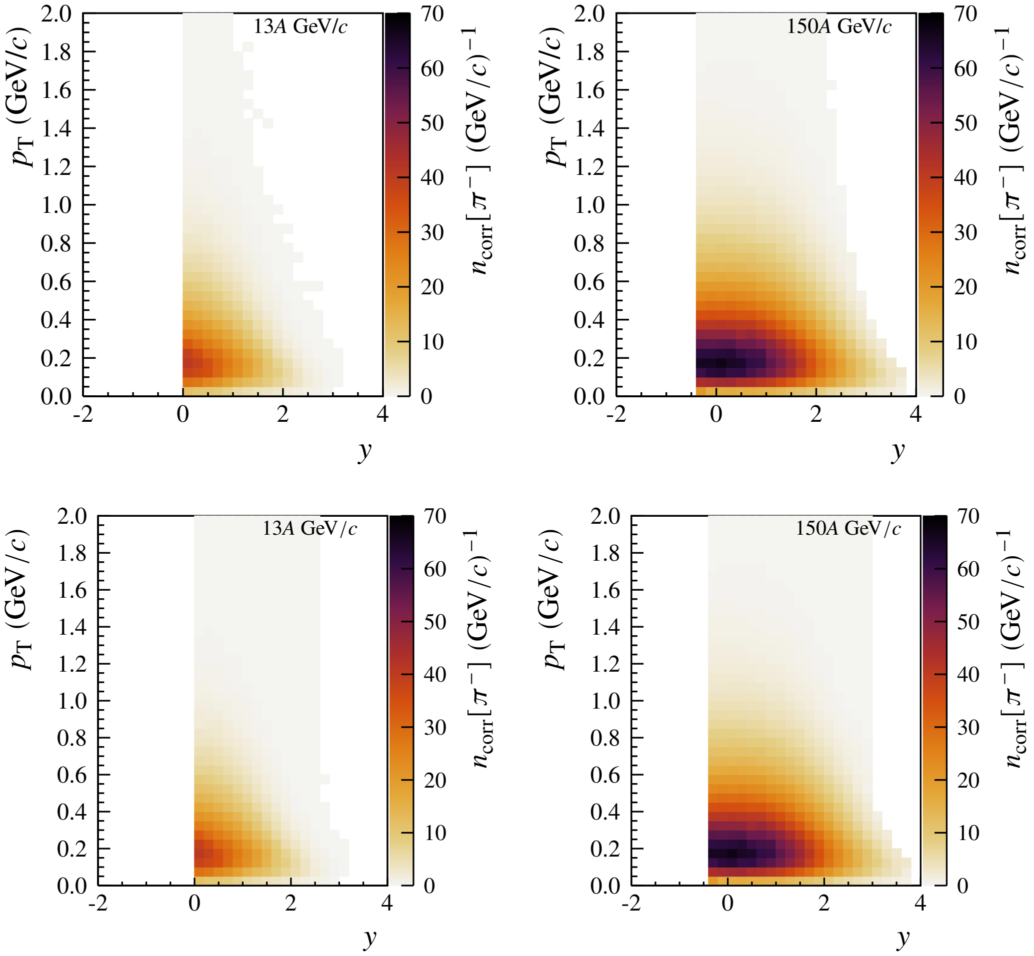

FIGURE 5.12: Examples of the corrected data $n^{i,j}_{corr}[\pi^-]$ (*top*) and examples of the corrected data $n^{i,j}_{corr}[\pi^-]$ extrapolated in transverse momentum p_T (*bottom*) for 13*A* (*left*) and 150*A* GeV/*c* (*right*) beam momentum.

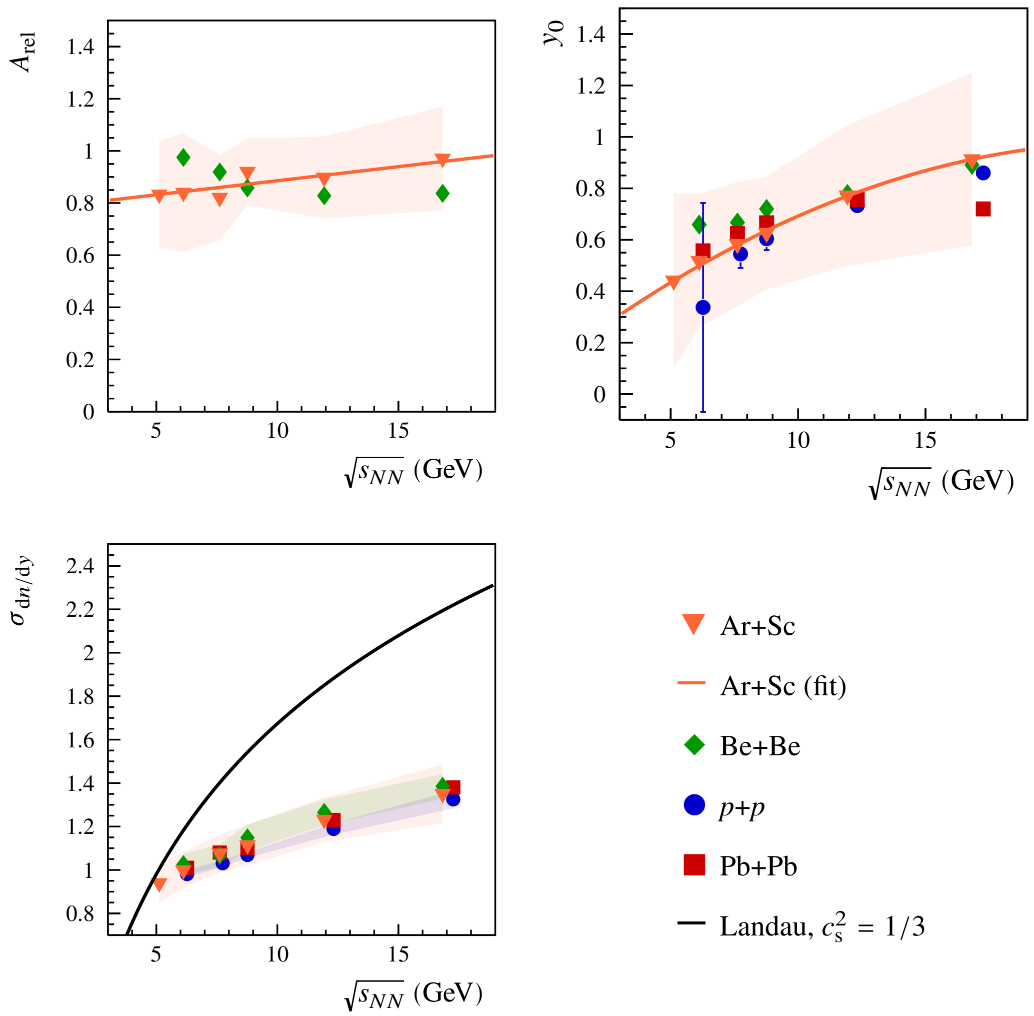

FIGURE 5.13: Comparison of the double Gaussian fit parameters A_{rel}, y_0 and $\sigma_{dn/dy}$ for different beam momenta and different measurements. The orange line corresponds to linear and quadratic fits used for extrapolation of A_{rel} and y_0, respectively, for 13A GeV/c beam momentum.

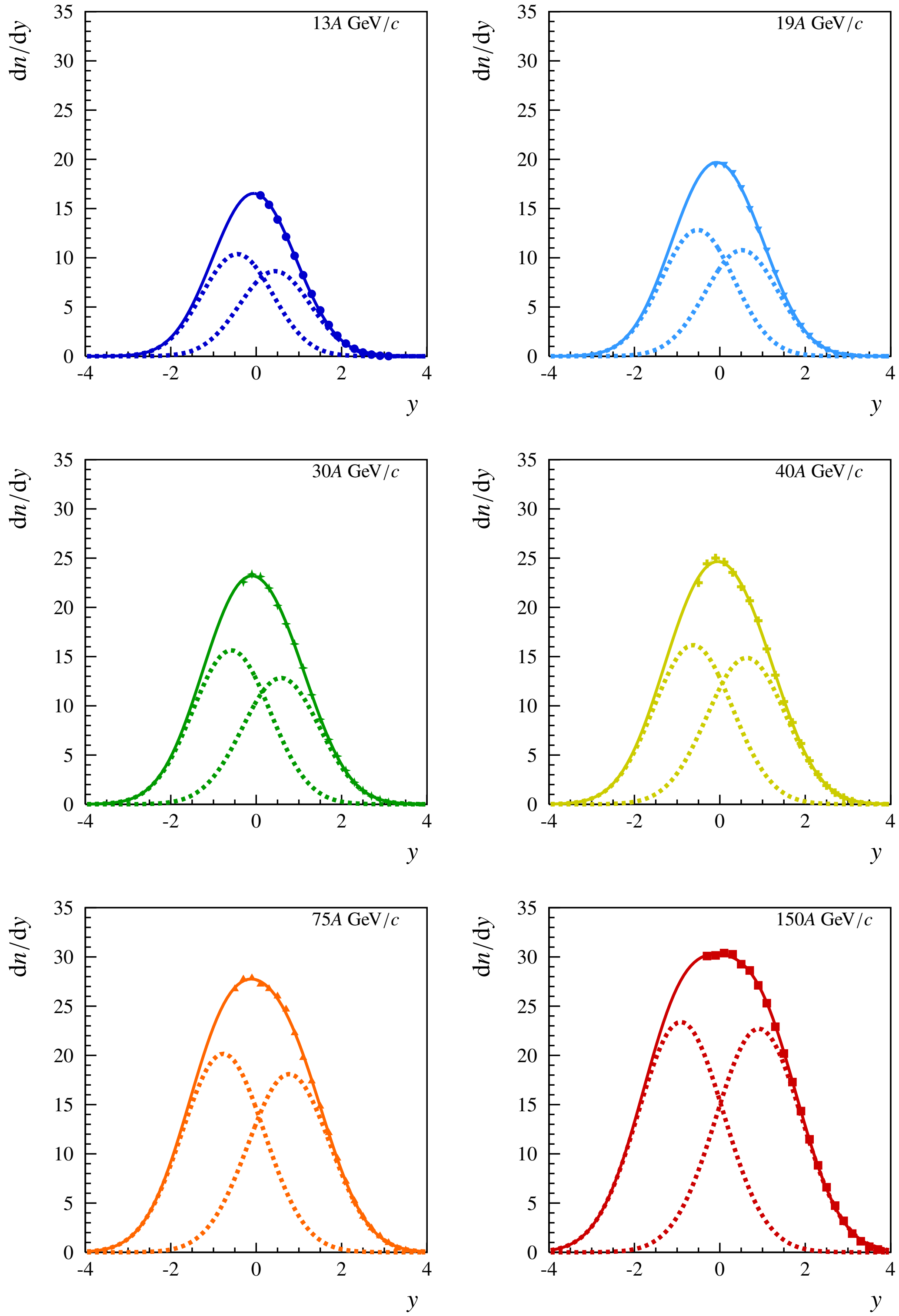

FIGURE 5.14: Illustration of the procedure of extrapolating y spectra using the sum of two Gaussians for all beam momenta. The markers represent the corrected data, the shaded band shows the systematic uncertainty of points and vertical bars statistical uncertainty. For most cases both are smaller than the marker size or line width. The solid line shows the fit of two Gaussians in the region where data has small enough uncertainties. The dotted lines represent separate Gaussians associated with target and projectile contributions.

5.4.3 Integration of the extrapolated spectra

In order to calculate the mean pion multiplicity $\langle\pi^-\rangle$, the following formula is used:

$$\langle\pi^-\rangle = \int_{-4.0}^{y_{\min}} g(y)dy + \sum_{y_{\min}}^{y_{\max}} dy \left(\frac{dn}{dy}\right)_{\text{extrapolated in} p_\text{T}} + \int_{y_{\max}}^{4.0} g(y)dy, \tag{5.29}$$

where $y_{\min}$ and $y_{\max}$ are the limits of measurements in y. Changing the integration boundaries from ∓ 4.0 to $\mp\infty$ results in a change of the π^- multiplicity smaller then 1‰.

The statistical uncertainty of the integral of extrapolated y spectra is calculated using the law of propagation of uncertainty of the fit parameters:

$$h(y) = \int_{\text{a}}^{\text{b}} g(y) \tag{5.30}$$

$$\sigma_{\text{stat}}(h(y)) = \sqrt{\sum_{i=1}^{4}\left(\frac{\partial h(y)}{\partial p_i}\right)^2 \sigma(p_i) + 2\sum_{i=1}^{3}\sum_{j=2}^{4}\frac{\partial h(y)}{\partial p_i}\frac{\partial h(y)}{\partial p^j}\sigma(p_i p_j)}, \tag{5.31}$$

where parameters p_1, p_2, p_3 and p_4 are A_0, A_{rel}, σ_0, y_0, and $\sigma(p_i p_j)$ is the covariance between parameters p_i and p_j.

The uncertainties of the summed bins are added in quadrature:

$$\sigma_{\text{stat,sys}} = \sqrt{\sum_{\text{i}} \sigma^i_{\text{stat,sys}}}. \tag{5.32}$$

The systematic uncertainty connected with the extrapolation procedure was estimated varying assumptions regarding parameters of the double Gaussian function Eq. 5.28. In particular, widths and positions of projectile and target Gaussians were assumed to be independent, i.e. separate parameters $y_{0,\text{proj}}$, $y_{0,\text{targ}}$ and $\sigma_{0,\text{proj}}$, $\sigma_{0,\text{targ}}$ were fitted. The uncertainty of each fitting parameter and the uncertainty of the mean π^- multiplicity were obtained as the standard deviation of the fit results. The resulting value of $\sigma_{\text{d}n/dy}$ takes into account the shift of the width of the projectile and target Gaussians as seen from the formula:

$$\sigma_{\text{d}n/\text{dy}} = \sqrt{\left(\frac{y_{0,\text{proj}} + y_{0,\text{targ}}}{2}\right)^2 + \left(\frac{\sigma_{0,\text{proj}} + \sigma_{0,\text{targ}}}{2}\right)^2}$$

The final results of the integration procedure with statistical, systematic, and total uncertainties are presented in Table 5.4 together with the relative percentage of the total uncertainty to the mean multiplicity.

TABLE 5.4: Mean π^- multiplicities in the 5 % most *central* Ar+Sc collisions with statistical and systematic uncertainties.

p_{beam} (GeV/c)	13	19	30	40	75	150
$\langle\pi^-\rangle$	39.54	50.56	64.56	71.70	92.01	114.93
$\sigma_{\text{stat}}(\langle\pi^-\rangle)$	0.041	0.222	0.121	0.100	0.084	0.216
$\sigma_{\text{sys}}(\langle\pi^-\rangle)$	7.313	4.640	5.255	5.670	6.720	12.780
$\sigma_{\text{total}}(\langle\pi^-\rangle)$	7.314	4.645	5.256	5.671	6.721	12.781
$100 \cdot \sigma_{\text{total}}(\langle\pi^-\rangle)/\langle\pi^-\rangle$ %	18.496	9.188	8.141	7.909	7.305	11.121

Chapter 6

Number of wounded nucleons

The number of wounded nucleons W is the number of nucleons which interacted inelastically in the nucleus-nucleus collision. The quantity cannot be measured experimentally and has to be estimated using theoretical models. W is an important quantity, since it is a proxy of the collision system size. The standard description of the collision geometry was derived by Roy Glauber in Ref. [58]. He used quantum mechanical techniques to describe multi-body scattering of composite systems.

Later, Białas, Bleszyński and Czyż in Ref. [48] developed the Wounded Nucleon Model (WNM). The model predicts that in a collision of two nuclei the average multiplicity produced from each wounded nucleon is the same. The particle production is an incoherent superposition of particle production from wounded nucleons. Properties of wounded nucleons are independent of the size of colliding nuclei.

In this thesis three Monte-Carlo models were used to approximate the number of wounded nucleons, namely Epos1.99 [53], Glissando 2 [59] and Hijing [60]. The latter two are based on the WNM and the former is based on the parton-ladder approach.

Epos provides a separate calculation within the WNM as well. This will be later called "Epos á la WNM" result and used for future calculations of the $\langle\pi\rangle/\langle W\rangle$ ratio. The reason is that the corrections described in the previous chapters were also calculated within Epos and therefore one should use the same model for the calculation of the number of wounded nucleons. On the other hand, the WNM approach to calculate the number of wounded nucleons W is simpler and more intuitive than Epos. Therefore, the combination of both "Epos á la WNM" is utilized.

For consistency between data and simulation, one should use the same centrality class in data and Monte-Carlo. Forward energy simulation E_{F} was used to extract the mean number of wounded nucleons for the 5% centrality selection class.

For comparison, a simplified version of the PSD simulation was used. This included effects of the PSD resolution and the PSD acceptance. The selection of events based on the E_{PSD} was applied to Glissando, Hijing and Epos.

6.1 The Wounded Nucleon Model

The Wounded Nucleon Model was developed in Ref. [48]. The main assumption was that the inelastic collision of two nuclei is an incoherent superposition of collisions of individual nucleons. The average multiplicity in the model is assumed to be proportional to the number of wounded nucleons.

Let us consider a collision of two nuclei – projectile and target with mass numbers A and B, respectively. The impact parameter $\vec{b}$ is the vector joining the centers of the nuclei at the moment of collision (see Fig. 6.1). The probability of finding a nucleon in a volume element $\mathrm{d}\vec{b_A}\mathrm{d}z_A$ in the nucleus A at the position $(\vec{b_A}, z_A)$ is expressed as $\rho_A(\vec{b_A}, z_A)\mathrm{d}\vec{b_A}\mathrm{d}z_A$ which is normalized to one:

$$\int \rho_A(\vec{b_A}, z_A)\mathrm{d}\vec{b_A}\mathrm{d}z_A = 1. \tag{6.1}$$

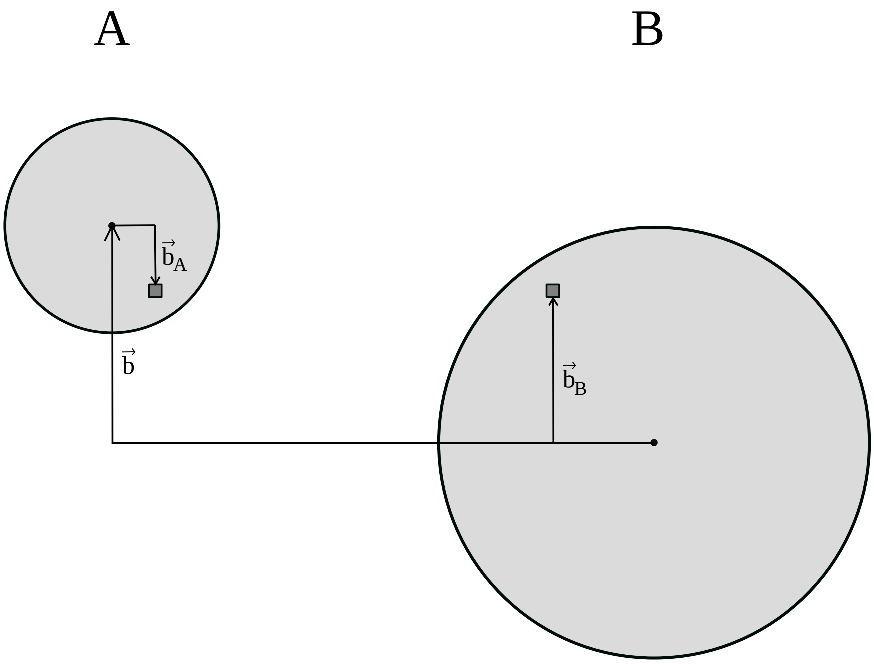

FIGURE 6.1: An overview of a collision of two nuclei at impact parameter $\vec{b}$.

Similarly, for nucleus B:

$$\int \rho_A(\vec{b_A}, z_A)\mathrm{d}\vec{b_A}\mathrm{d}z_A = 1. \tag{6.2}$$

The probability of having a nucleon-nucleon collision within the transverse area element $\mathrm{d}\vec{b}$ is defined as $t(\vec{b})\mathrm{d}\vec{b}$. Therefore, the probability of a nucleon-nucleon collision is given by:

$$T(\vec{b})\delta_{NN} = \int \rho_A(\vec{b_A}, z_A)\mathrm{d}\vec{b_A}\mathrm{d}z_A \rho_B(\vec{b_B}, z_A)\mathrm{d}\vec{b_B}\mathrm{d}z_B t(\vec{b} - \vec{b_A} + \vec{b_A})\delta_{NN}, \tag{6.3}$$

where δ_{NN} is the inelastic nucleon-nucleon cross section. There can be up to $A \times B$ collisions and the probability of occurrence of n collisions is given by the binomial distribution:

$$P(n, \vec{b}) = \binom{AB}{n}(1 - s(\vec{b}))^n (s(\vec{b}))^{AB-n}, \tag{6.4}$$

where $s(\vec{b}) = 1 - T(\vec{b})\delta_{NN}$. The probability of having α wounded nucleons from nucleus A is given by:

$$P(\alpha, \vec{b}) = \binom{A}{\alpha}(1 - s(\vec{b})^B)^\alpha (s(\vec{b}^B))^{A-\alpha}, \tag{6.5}$$

and the probability of having β wounded nucleons from nucleus B is given by:

$$P(\beta, \vec{b}) = \binom{B}{\beta}(1 - s(\vec{b})^A)^\beta (s(\vec{b}^A))^{B-\beta}. \tag{6.6}$$

The average numbers of wounded nucleons coming from projectile A and target B are the following:

$$\langle \alpha \rangle = A[1 - s(\vec{b})^B], \tag{6.7}$$

$$\langle \beta \rangle = B[1 - s(\vec{b})^A], \tag{6.8}$$

Finally, the total average number of wounded nucleons is given by:

$$\langle W \rangle = A[1 - s(\vec{b})^B] + B[1 - s(\vec{b})^A]. \tag{6.9}$$

6.2 Glissando

Glissando 2 [59] is a Monte-Carlo heavy ion collision event generator based on the WNM. The simulation is performed in three steps:

1. Fixing the position of nucleons according to the nuclear density distribution. The Woods-Saxon profile [61] is used to describe the density of heavy nuclei (i.e. A> 16). When deformations are included the density is expressed as:

$$\rho(r, \theta) = \frac{\rho_0}{1 + \exp\left(r - R(1 + \beta_2 Y_{20}(\theta) + \beta_4 Y_{40}(\theta))\right)/a}, \tag{6.10}$$

   where r is the distance from the nucleus center, θ is the polar angle, β_2 and β_4 are the deformation parameters, while $Y_{20}(\theta)$ and $Y_{40}(\theta)$ are the spherical harmonics. R and a are parametrized for an atomic nucleus with mass number A in the following way:

$$R = (1.1A^{1/3} - 0.656A^{-1/3}) \text{ fm}, \tag{6.11}$$

$$a = 0.459 \text{ fm}. \tag{6.12}$$

2. The generated two nuclei are separated by the impact parameter $\vec{b}$, and the wounded nucleons and binary collisions are counted. Here, different collision profiles can be used. In case of ^{40}Ar+^{45}Sc collisions, a Gaussian wounding profile is used instead of the hard-sphere profile. The profile is expressed as:

$$q(r) = G \exp\left(-\frac{Gr^2}{r_0^2}\right), \tag{6.13}$$

   where r is the transverse distance between the centers of nucleons, G controls the central value of the profile and is set to the experimentally obtained value of $G = 0.92$ and $r_0 = \sqrt{\delta_w/\pi}$ with δ_w is the N+N inelastic cross section at the given collision energy.

3. In the last step, event-by-event averaged quantities are calculated.

6.3 Epos

In Epos [62] provided by Crmc1.6, a different approach is utilized. Interactions between nuclei are realized by an exchange of a ”parton ladder”. In this approach a parton emission cascade precedes hard scattering. These partons together with the ones produced in hard scattering process form a ladder-like structure.

Initially, using Monte-Carlo methods, the collision configuration is determined, the number of each kind of pomerons exchanged between projectile and target is fixed and the energy is shared between pomerons and the two remnants. Then, particles are produced from two sources i.e. remnants decay and cut pomerons.

6.4 Hijing

Hijing [60] is a Monte-Carlo event generator based on QCD-inspired models for multiple jet production, soft excitation, nuclear shadowing of partons and final state interactions. It can be used to study jets and particle production in high energy hadronic and nuclear collisions. Multiple scattering in nuclear collisions is based on the binary approximation and the Glauber model. Hijing is written in FORTRAN77, but Crmc1.6 provides a wrapper to easily obtain simulated events.

6.5 Statistical and systematic uncertainties of the mean number of wounded nucleons.

The mean number of wounded nucleons $\langle W \rangle$ is the average over a large number of events. The statistical uncertainty of the calculation will be written in the following way:

$$\sigma_{\text{stat}}(\langle W \rangle) = \sqrt{\frac{1}{N(N-1)} \sum_{i=1}^{N} (W_i - \langle W \rangle)^2}, \tag{6.14}$$

where N is the number of events.

The systematic uncertainty is influenced by the following factors:

I) uncertainty of the nuclear cross-section: the WNM requires the value of the N+N inelastic cross-section $\sigma_{NN,\text{inel.}}$ at a given collision energy. Therefore, the uncertainty in $\sigma_{NN,\text{inel.}}$ will be propagated to all the quantities based on $\sigma_{NN,\text{inel.}}$. In order to estimate the associated uncertainty with this bias, simulations of the mean number of wounded nucleons were performed in Glissando which allows user to modify $\sigma_{NN,\text{inel.}}$ parameter. The uncertainty is taken as half of the difference between $\langle W \rangle$ calculated with $\sigma_{p,\text{inel.}} + \sigma_{\text{tot}}(\sigma_{pp,\text{inel.}})$ and $\sigma_{pp,\text{inel.}} - \sigma_{\text{tot}}(\sigma_{pp,\text{inel.}})$. The values of $\sigma_{pp,\text{inel.}}$ and $\sigma_{\text{tot}}(\sigma_{p,\text{inel.}})$ are taken from Ref. [51] ,

II) uncertainty of the model: this uncertainty is estimated based on calculations for three independent models, i.e. Glissando, Epos and Hijing. The uncertainty is taken as the difference between the lowest and the highest value obtained from the three models.

The total systematic centrality is calculated adding all the above components in quadrature:

$$\sigma_{\text{sys}}(\langle W \rangle) = \sqrt{\sigma_{\text{I}}(\langle W \rangle)^2 + \sigma_{\text{II}}(\langle W \rangle)^2}. \tag{6.15}$$

A summary of the results of the procedure is presented in Table 6.1 and in Fig. 6.2.

TABLE 6.1: Values of $\langle W \rangle$ from "EPOS á la WNM" with event selection based on E_F together with different components of the uncertainty of $\langle W \rangle$ for all beam momenta.

p_{beam} (GeV/c)	$\langle W \rangle$	σ_{stat}	σ_{sys}	$\frac{\sigma_{stat}}{\langle W \rangle} \times 100\%$	$\frac{\sigma_{sys}}{\langle W \rangle} \times 100\%$
13	65.66	0.0047	2.73	0.0072%	4.16%
19	65.40	0.0047	3.45	0.0072%	5.28%
30	65.07	0.0048	3.64	0.0074%	5.59%
40	64.98	0.0047	4.02	0.0072%	6.19%
75	64.87	0.0047	4.39	0.0072%	6.77%
150	65.01	0.0048	4.57	0.0074%	7.03%

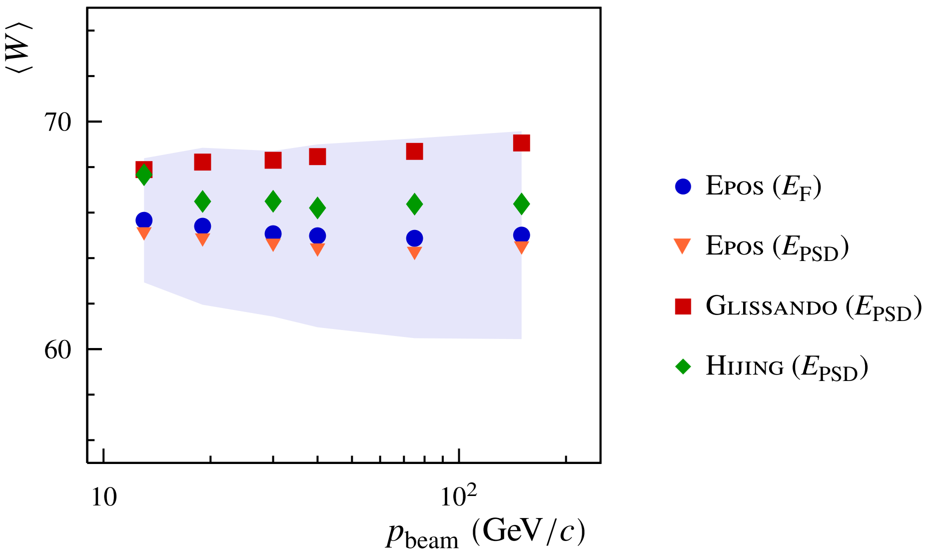

FIGURE 6.2: Comparison of the values of $\langle W \rangle$ calculated from GLISSANDO and HIJING, as well as EPOS "á la WNM" for the 5% of events with the smallest forward energies E_F and smallest PSD energies E_{PSD}. For clarity, only the systematic uncertainty of the value based on EPOS and E_F is presented.

Chapter 7

Results

This chapter is devoted to presentation of the results on π^- meson production spectra in inelastic ^{40}Ar+^{45}Sc interactions at six beam momenta used by NA61/SHINE. The results refer to negatively charged pions produced by strong processes and in electromagnetic decays of produced hadrons.

Numerical results together with systematic and statistical uncertainties are given in Appendix C in plain text format.

7.1 Double differential spectra

The double-differential spectra in bins of rapidity y and transverse momentum p_T – $d^2n/dydp_T$, as well as rapidity y and transverse mass bins – $d^2n/dydm_T$, are equal to the fully corrected bin contents $n^{i,j}_{corr}[\pi^-]$ defined in equation 5.18 and presented in Fig. 7.1. The resulting spectra in rapidity y and transverse mass $m_T - m_\pi$ produced in inelastic ^{40}Ar+^{45}Sc collisions at 13A, 19A, 30A, 40A, 75A and 150A GeV/c are presented in Fig. 7.2. The numerical values are tabulated in Sec. C.1.

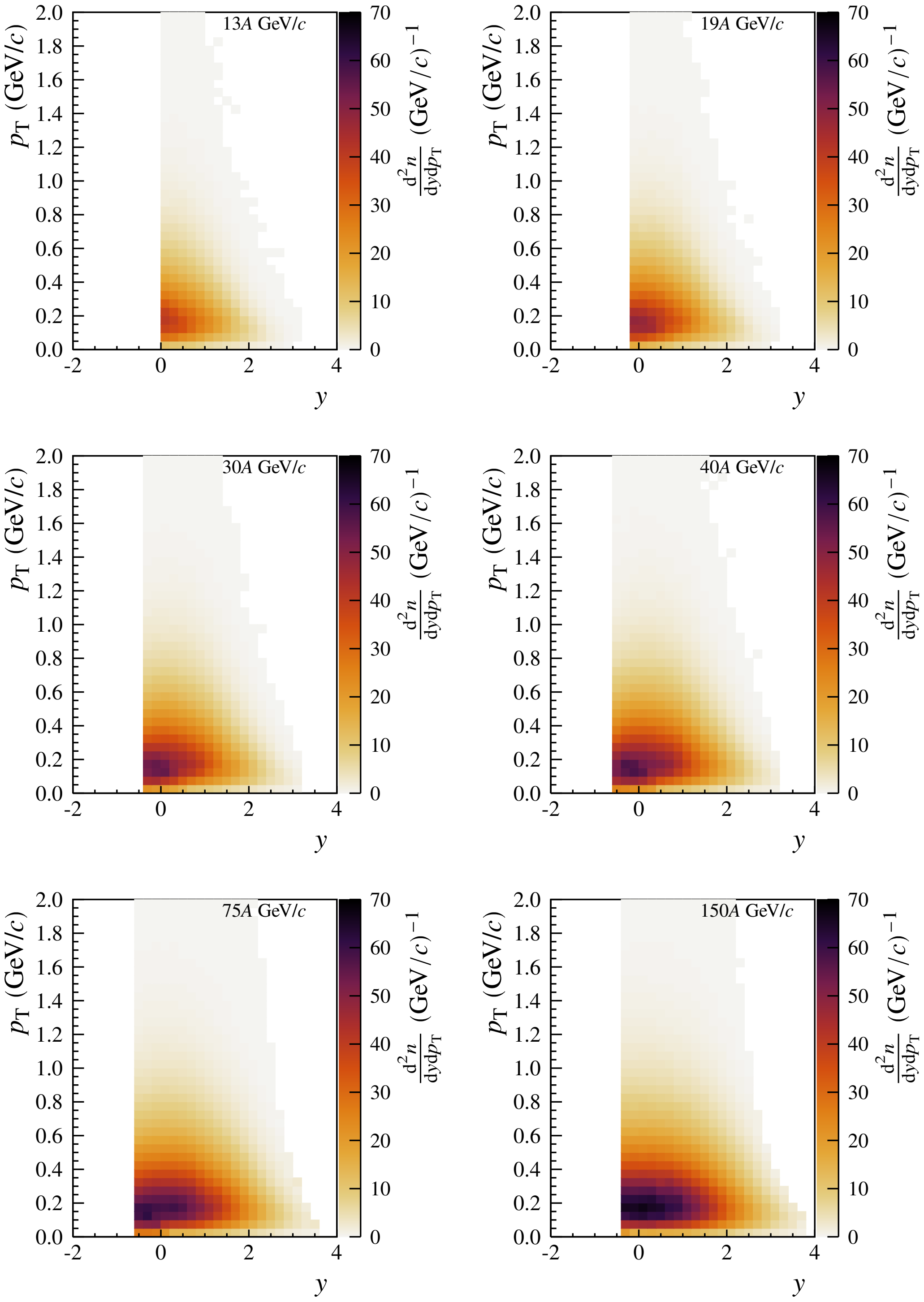

FIGURE 7.1: Final double-differential spectra $d^2n/dydp_T$ $(\mathrm{GeV}/c)^{-1}$ in rapidity y and transverse momentum p_T produced in inelastic ^{40}Ar+^{45}Sc collisions.

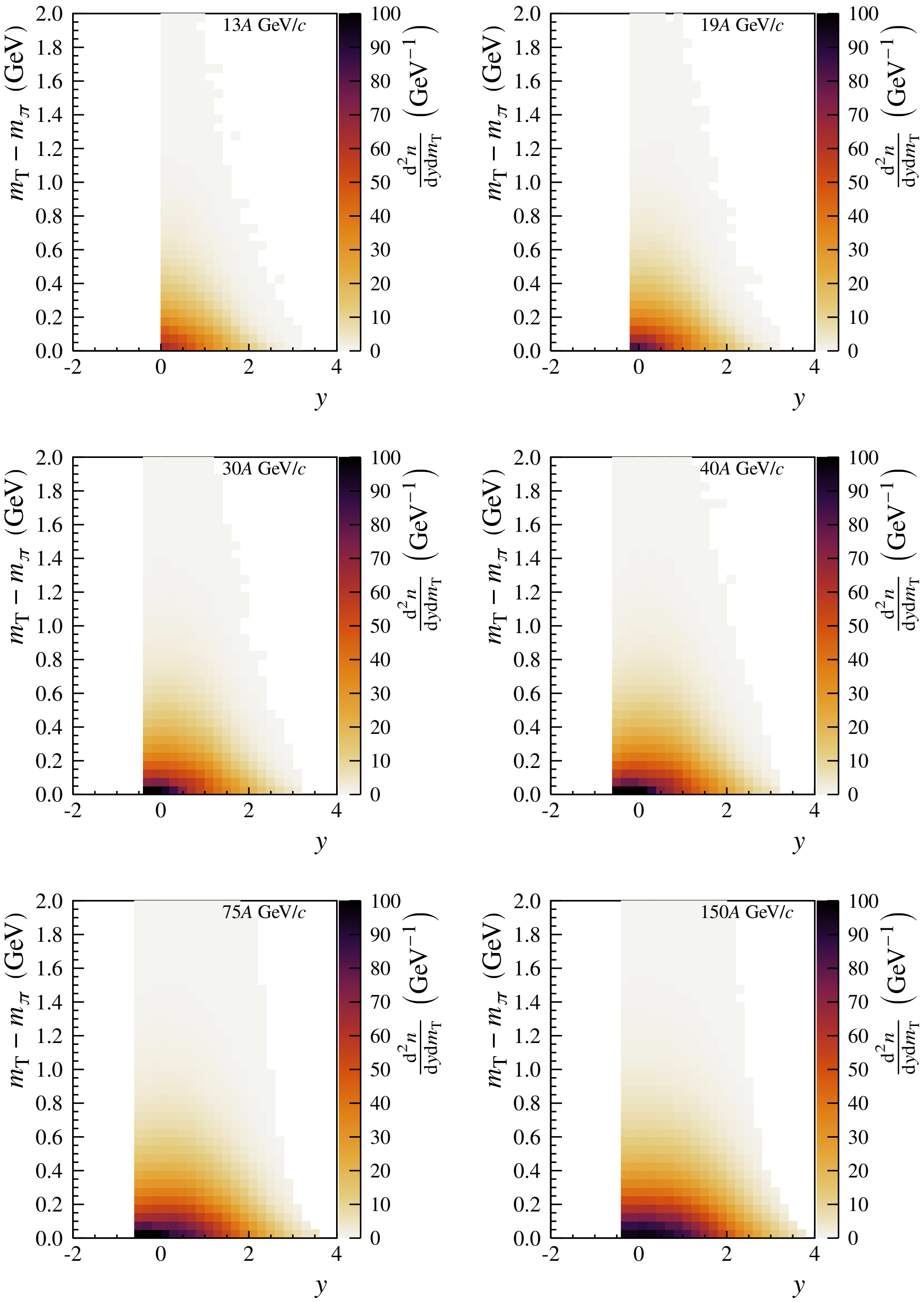

FIGURE 7.2: Final double-differential spectra $d^2n/dydm_T$ (GeV)$^{-1}$ in rapidity y and transverse mass $m_T - m_\pi$ produced in inelastic $^{40}Ar+^{45}Sc$ collisions.

7.2 Transverse momentum and transverse mass spectra

Transverse momentum p_T spectra in mid-rapidity ($0 < y < 0.2$) for all six beam momenta are presented in Fig. 7.3.

In case of transverse mass spectra $m_T = \sqrt{m^2 + (p_T c)^2}$, an exponential function is fitted in the mid-rapidity region ($0.0 < y < 0.2$) in order to extract the inverse slope parameter T:

$$\frac{dn}{dm_T} = A m_T \exp\left(-\frac{m_T}{T}\right). \tag{7.1}$$

The resulting fitted parameters A and T are presented in the Fig. 7.4, where solid lines indicate the fitting range of $0.24 < m_T - m_\pi < 0.72$. The latter was chosen to be consistent with the previous measurements on p+p [21] interactions and Pb+Pb [22, 23] collisions. The fit minimizes the χ^2 function calculated using statistical and systematic uncertainties.

Table 7.1 shows the inverse slope parameter T fitted at mid-rapidity together with the mean transverse mass $\langle m_T \rangle$. In order to calculate the latter, an extrapolation of the fitted function was required, for details see Appendix B.

Figure 7.5 (*top*) shows the fitted inverse slope parameter T and mean transverse mass $\langle m_T \rangle$ (*bottom*) for different rapidity bins, which have sufficient measured pions. Numerical values of the inverse slope parameter T are tabulated in Sec. C.3 and for the mean transverse mass $\langle m_T \rangle$ in Sec. C.4.

TABLE 7.1: The inverse slope parameter T fitted at mid-rapidity ($0 < y < 0.2$) together with the mean transverse mass $\langle m_T \rangle$ at mid-rapidity for all beam momenta used by NA61/SHINE. Shown uncertainties correspond to statistical and systematic errors, respectively.

p_{beam} (GeV/c)	$\langle m_T \rangle - m_\pi$ (MeV)	T (MeV)
13	$214.5 \pm 2.1 \pm 0.3$	$152.9 \pm 0.6 \pm 0.6$
19	$219.4 \pm 2.1 \pm 0.5$	$157.3 \pm 0.6 \pm 1.0$
30	$233.9 \pm 2.1 \pm 0.8$	$165.5 \pm 0.4 \pm 0.9$
40	$237.6 \pm 1.8 \pm 0.7$	$166.7 \pm 0.4 \pm 1.1$
75	$255.7 \pm 1.8 \pm 0.8$	$172.0 \pm 0.2 \pm 1.4$
150	$260.2 \pm 1.9 \pm 0.9$	$171.7 \pm 0.4 \pm 1.4$

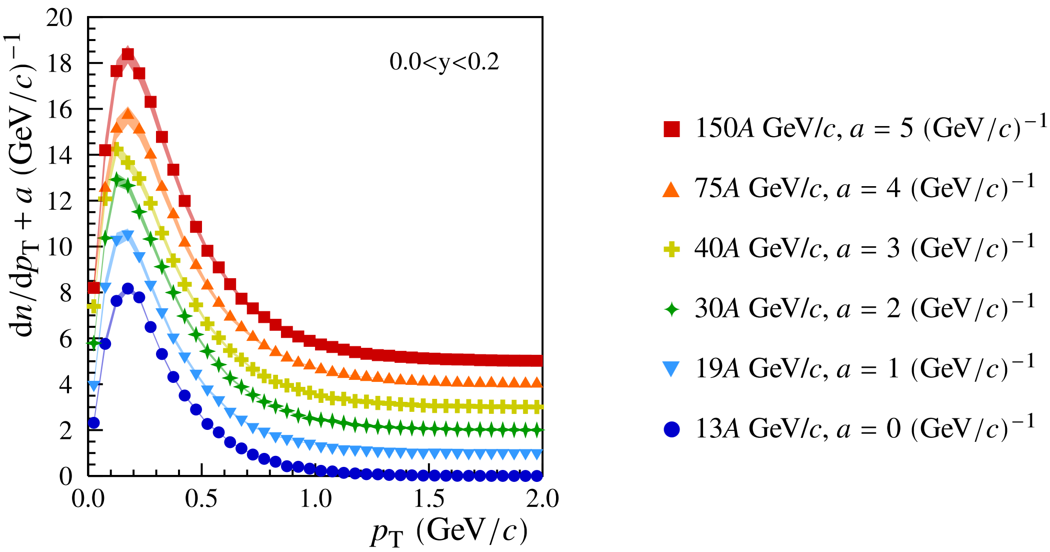

FIGURE 7.3: Transverse momentum spectra at mid-rapidity ($0 < y < 0.2$). The data points for different beam momenta were shifted for better readability. Statistical uncertainties are shown as vertical bars (usually smaller than markers' size) and systematic uncertainties are indicated by shaded bands.

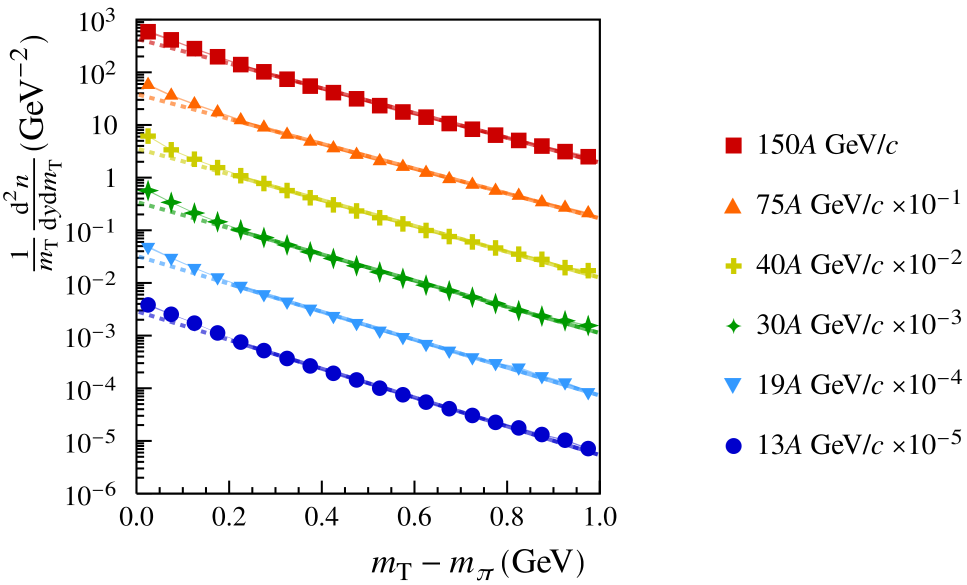

FIGURE 7.4: Transverse mass spectra at mid-rapidity ($0 < y < 0.2$). The fitted exponential function is indicated by solid lines in the fit range $0.24 < m_T - m_\pi < 0.72$ GeV and dashed lines outside the fit range. The data points for different beam momenta were scaled for better readability. Statistical uncertainties are shown as vertical bars (smaller than markers' size) and systematic uncertainties are indicated by shaded bands.

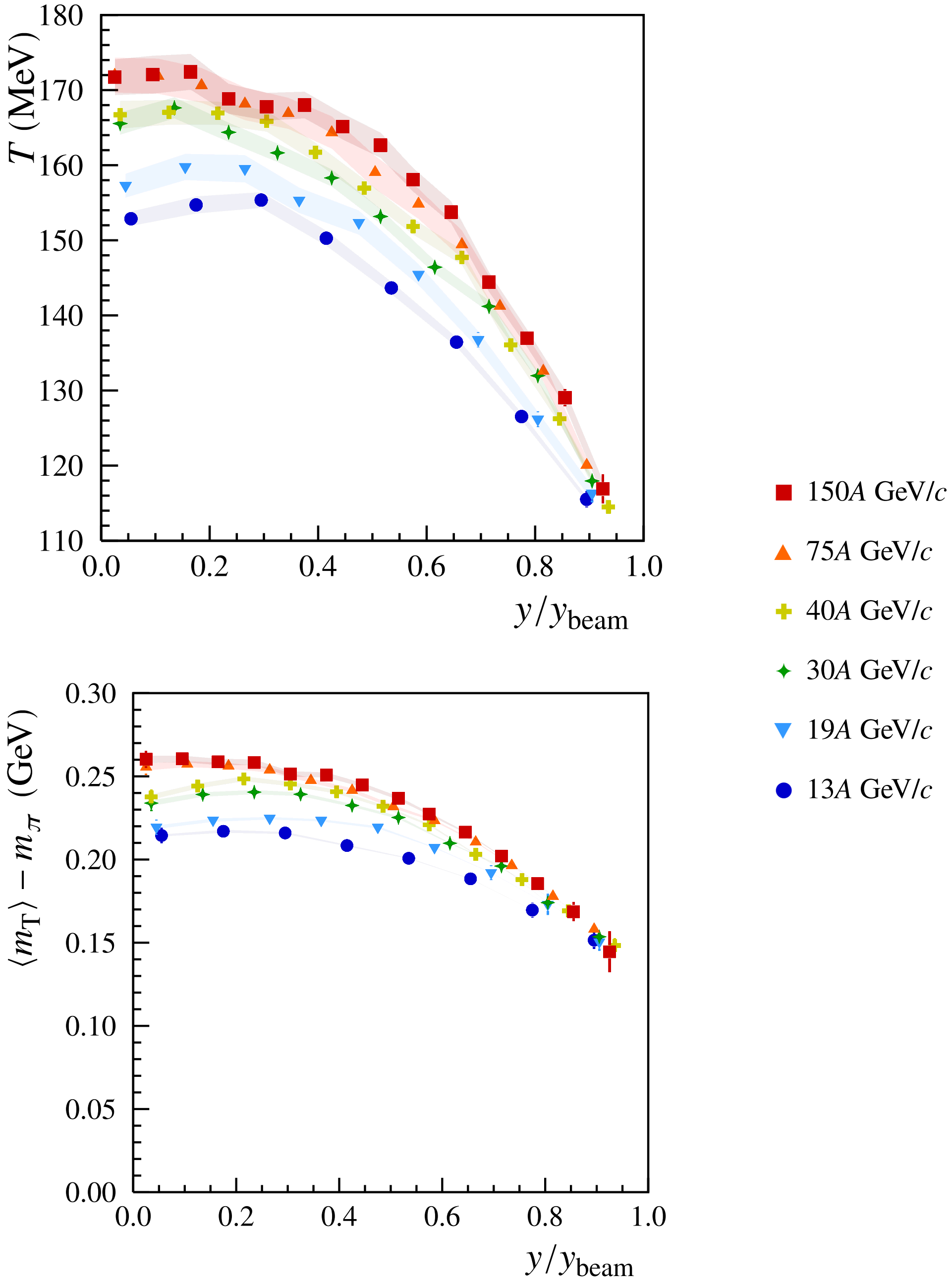

FIGURE 7.5: *Top:* The inverse slope parameter T of the transverse mass spectra as a function of rapidity divided by the beam rapidity. The fit range is $0.24 < m_T - m_\pi < 0.72$ GeV. *Bottom:* The mean transverse mass $\langle m_T \rangle$ as a function of rapidity divided by the beam rapidity. In both panels statistical uncertainties are smaller than markers' size and systematic uncertainties are indicated by shaded bands.

7.3 Rapidity spectra

The rapidity spectra $\mathrm{d}n/\mathrm{d}y$ are obtained by integrating the double-differential spectra $\mathrm{d}^2n/\mathrm{d}y\mathrm{d}p_\mathrm{T}$ extrapolated in p_T. The procedure is described in detail in Sec. 5.4.

The spectra are approximately Gaussian, but a better description is provided by a sum of two Gaussians:

$$g(y) = \frac{A_0 A_\mathrm{rel}}{\sigma_0\sqrt{2\pi}} \exp\left(-\frac{(y-y_0)^2}{2\sigma_0^2}\right) + \frac{A_0}{\sigma_0\sqrt{2\pi}} \exp\left(-\frac{(y+y_0)^2}{2\sigma_0^2}\right), \tag{7.2}$$

with fitted parameters described in Table 5.3.

Figure 7.6 shows the rapidity y spectra $\mathrm{d}n/\mathrm{d}y$ for 13A, 19A, 30A, 40A, 75A and 150A GeV/c together with fitted functions and points evaluated from the latter. The tabulated numerical values are presented in Sec. C.2.

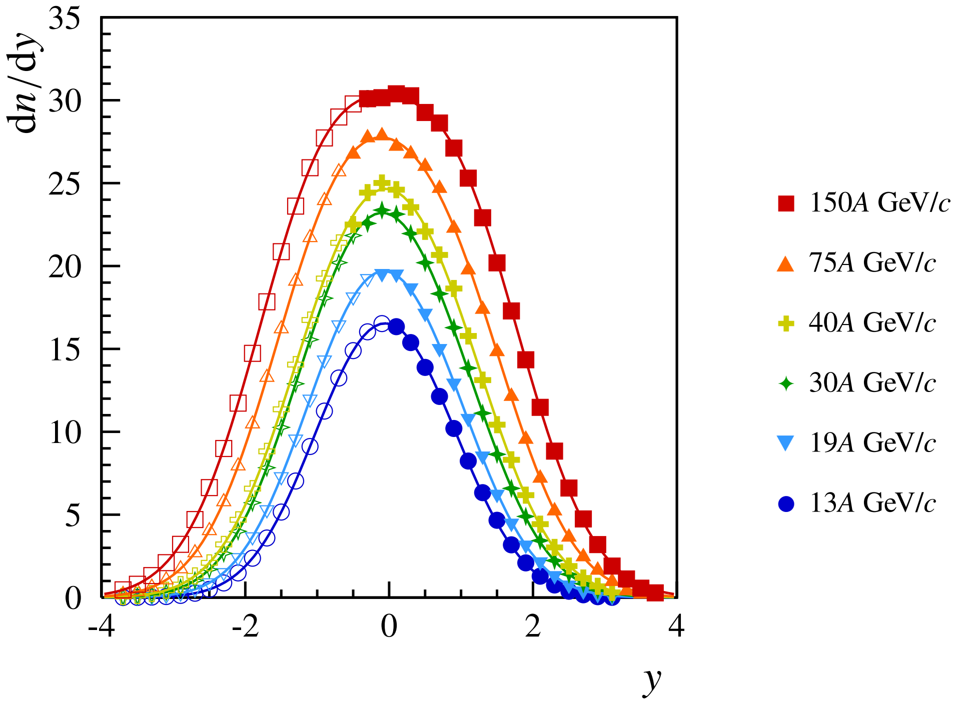

FIGURE 7.6: Rapidity distributions dn/dy for 13A, 19A, 30A, 40A, 75A and 150A GeV/c. Measured points are shown by full markers, values extrapolated by the fit function (see Sec. 5.4) are plotted by open markers. Only total uncertainties are plotted, which are usually smaller than markers' size. Details of calculation of uncertainties are presented in Chapter 5.

7.4 Mean multiplicity

The mean negatively charged pion multiplicity $\langle \pi^- \rangle$ is calculated according to Eq. 5.29. The results of this procedure are summarized in Table 5.4 together with the values of uncertainty.

For ^{40}Ar+^{45}Sc collisions there are presently no results available for $\langle \pi^+ \rangle$. The ^{40}Ar+^{45}Sc initial state is approximately isospin symmetric, so the ratio of $\langle \pi^+ \rangle / \langle \pi^- \rangle$ is only approximately 1, and it was found to change from 0.954 to 0.984 between 13*A* and 150*A* GeV/*c* beam momentum. These values were determined from Epos simulations. The resulting isospin correction factor $c_{\text{isospin}} = \langle \pi^- \rangle / \langle \pi^+ \rangle$ was taken into account when calculating the total pion multiplicity $\langle \pi \rangle = \langle \pi^+ \rangle + \langle \pi^- \rangle + \langle \pi^0 \rangle$:

$$\langle \pi \rangle_{\text{Ar+Sc}} = 1.5 \cdot (\langle \pi^- \rangle + \langle \pi^+ \rangle) = 1.5 \cdot (1 + c_{\text{isospin}}) \cdot \langle \pi^- \rangle. \tag{7.3}$$

The numerical values of the c_{isospin} are presented in the Table 7.2.

Table 7.2: The isospin correction factor c_{isospin} for different beam momenta.

p_{beam} (GeV/c)	13	19	30	40	75	150
c_{isospin}	0.954	0.960	0.968	0.972	0.978	0.984

Chapter 8

Comparison with other data and models

In this chapter the results are compared with different analysis methods applied to the same dataset.

A comparison with the results from other measurements of the NA61/SHINE experiment on *p+p* interactions [21], *central* Be+Be [20] collisions, and central Pb+Pb collisions published by NA49 [22, 23], as well as with Au+Au collisions from the E895 and E802 experiments at AGS [63, 64], and other existing *p+p* data [26–28] is presented below.

Finally, a comparison with MC models' predictions of π^- spectra, their parameters, and mean multiplicities $\langle\pi^-\rangle$ is discussed.

8.1 Comparison with other analysis methods

There are three different analysis methods yielding spectra of identified primary charged hadrons applied to each data-set in NA61/SHINE. All the methods have different characteristics and are complementary to each other. Thanks to the three different analysis methods performed by three independent analyzers, we are able to cross-check their results and minimize the possibility of an error.

The three methods are the following:

- the h^- method: this method (described in detail in Section 5.2) is based on a Monte-Carlo correction applied to experimental data. Using it, one can only obtain information regarding π^-. As presented in Fig. 8.1, it has the biggest momentum acceptance. On the other hand, this method is affected by large (i.e. ≈ 10%) systematic uncertainty.

- the *dE/dx* method: it is based on the information of the particle's specific energy loss dE/dx along its trajectory in the TPCs and their momentum p. This allows for identification of particles other than π^- (PID). The most important in this context are measurements of K^+, that allow to study "the horn", which is an important signal of the onset of deconfinement.

- the *tof-dE/dx* method: it can be used for regions in which additional information on particle's time of flight is used to ensure high PID quality. Note that the quality of results from the *dE/dx* method performance deteriorates for particles in the momentum range $p < 5$ GeV/c.

Ratios of p_T versus y spectra of negatively charged pions π^- obtained with the *dE/dx* method [9] to the h^- method and with the *tof-dE/dx* method [56] to the h^- method are presented in Figs. 8.2 and 8.3, respectively. The differences are small for most regions – below 5% – and up to 10% or 20% in some bins for the *dE/dx* and *tof-dE/dx*, respectively. The spectra for 13A GeV/c for the *tof-dE/dx* and the *dE/dx* methods are not available.

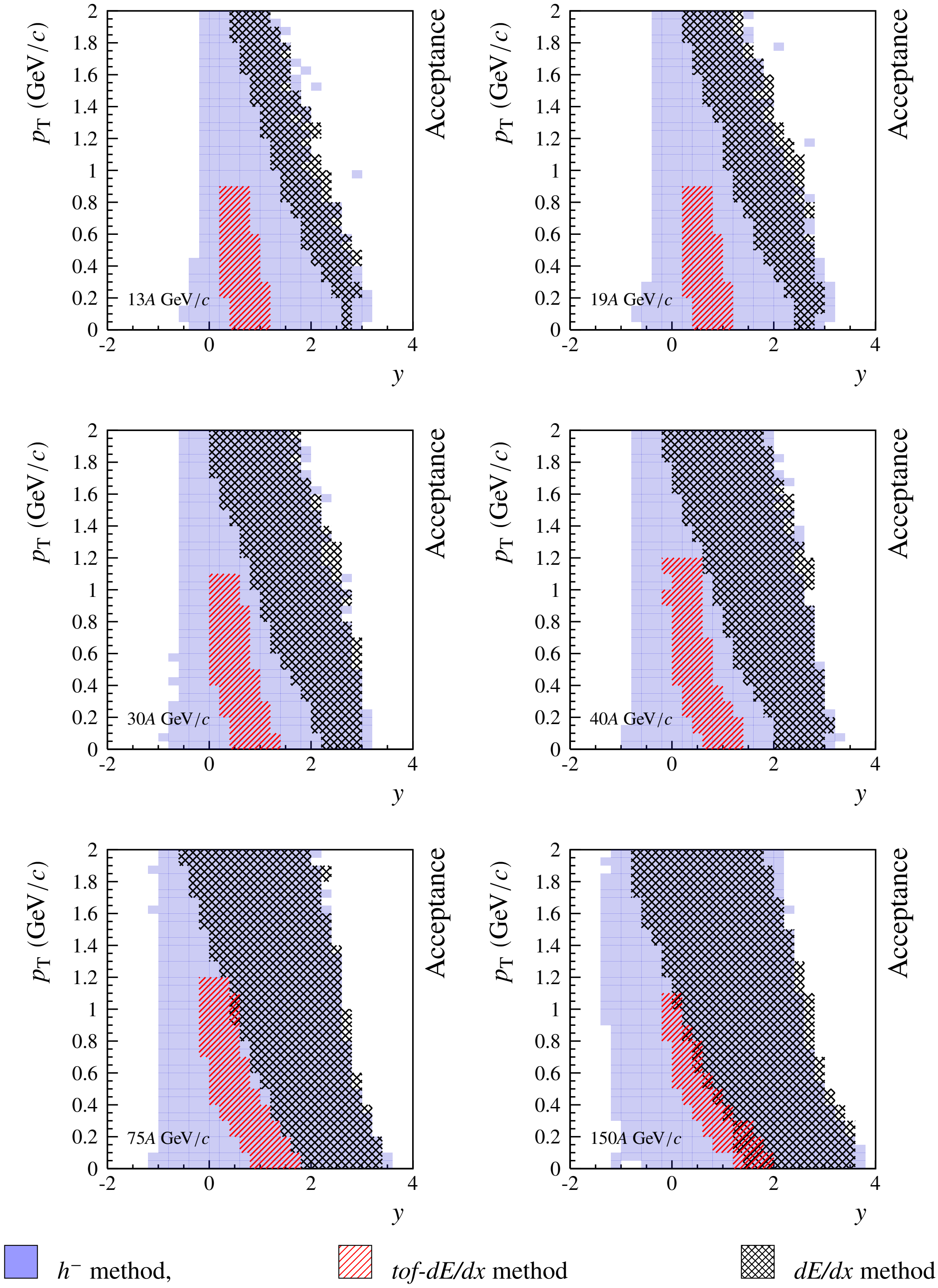

FIGURE 8.1: Comparison of different analysis methods performed by NA61/SHINE. The plots present acceptance of all three methods for all beam momenta used. Here, the advantage of using the h^{-} method is visible as the momentum acceptance region of this method is significantly larger.

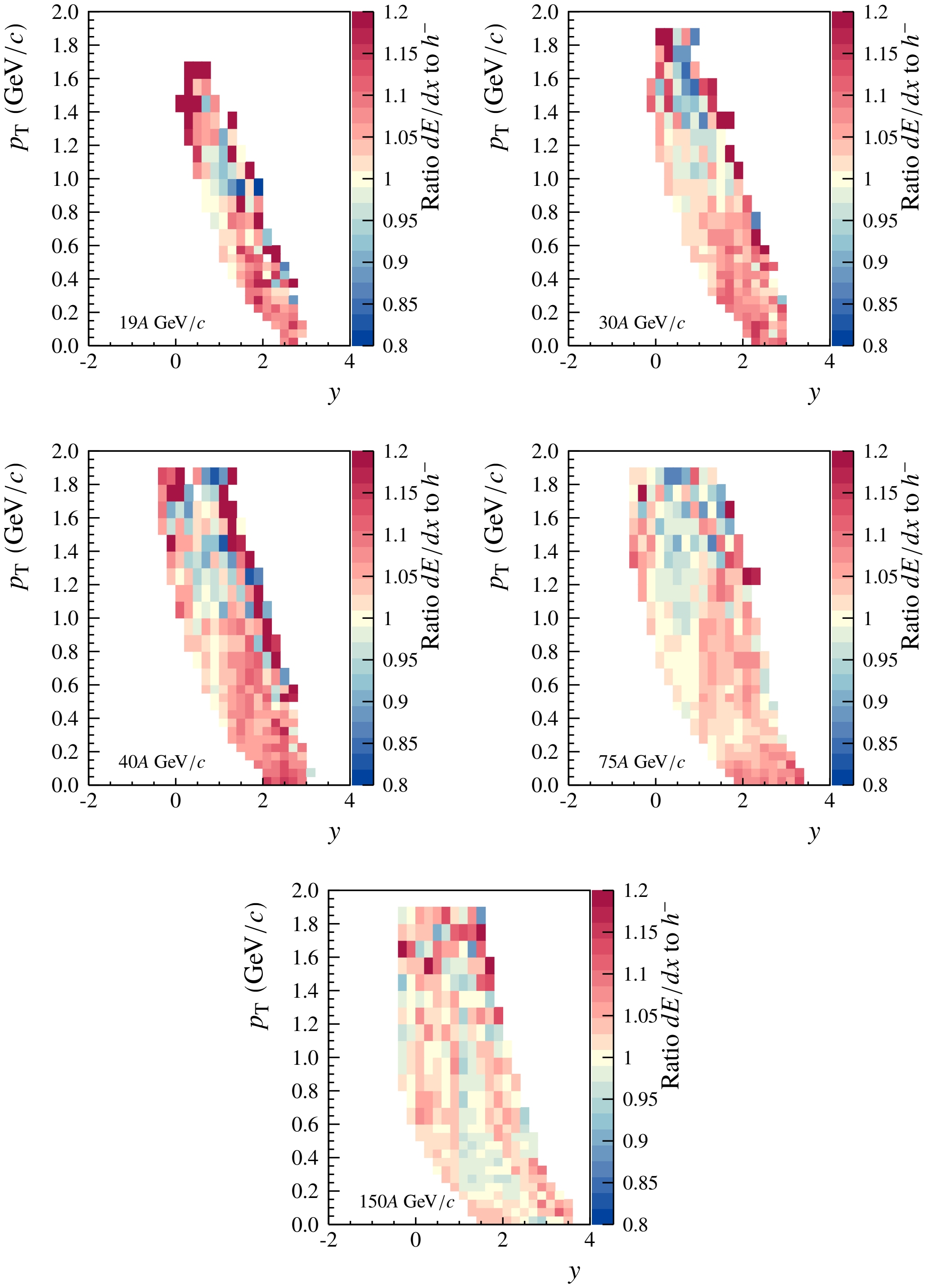

FIGURE 8.2: Ratios of the *dE/dx* to the h^- method double-differential spectra $d^2n/dydp_T$ of negatively charged pions π^- for common acceptance regions of these methods.

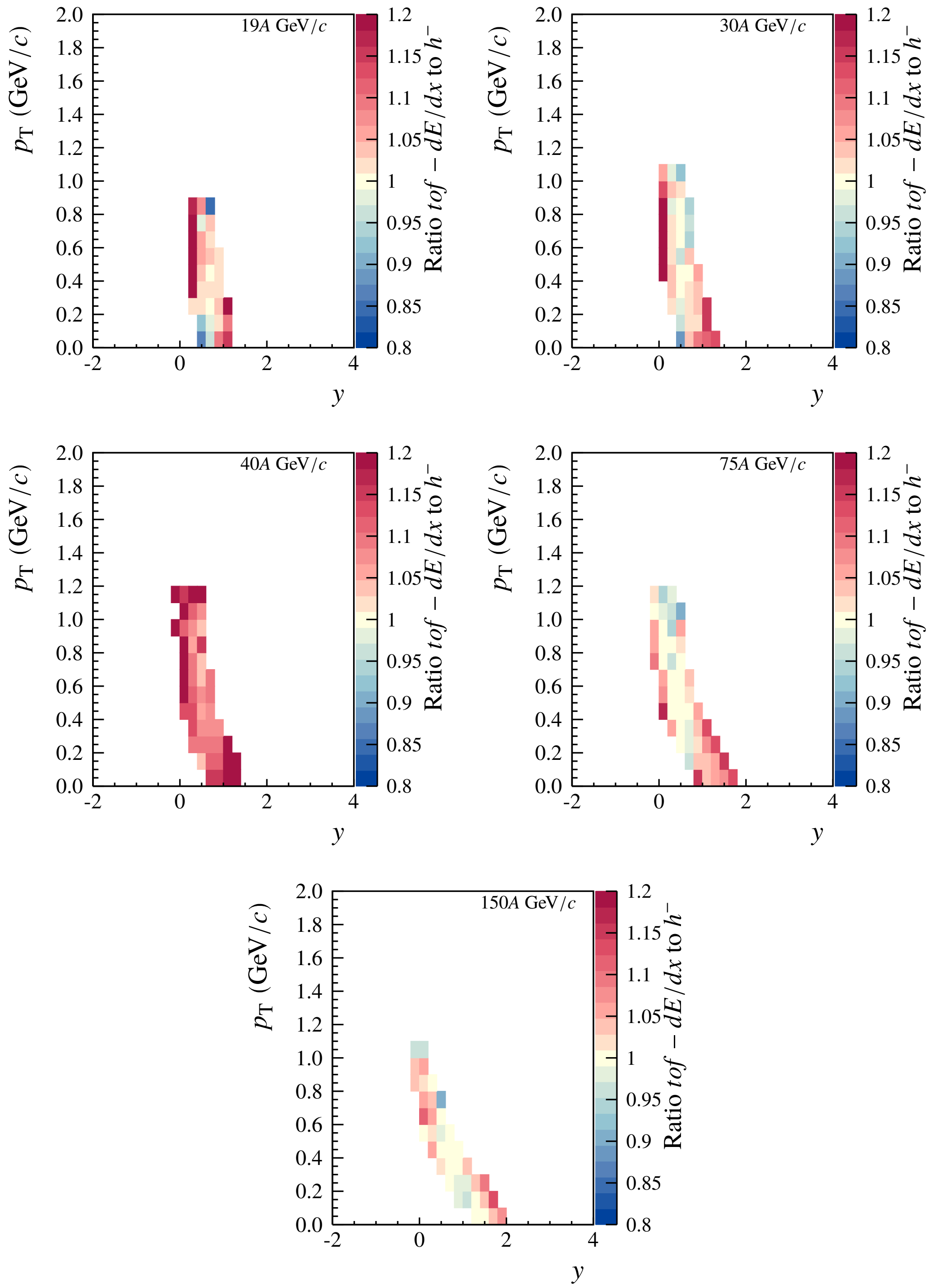

FIGURE 8.3: Ratios of the *tof-dE/dx* to the h^- method double-differential spectra $d^2n/dydp_T$ of negatively charged pions π^- for common acceptance regions of these methods.

8.2 System size dependence

In order to compare the detailed features of the transverse mass m_T spectra, the ratios of the scaled differential yields from *p+p*, Ar+Sc and Pb+Pb reactions to the isospin symmetric Be+Be reference are plotted in Fig. 8.4. The shape of m_T spectra in *central* Ar+Sc collisions is similar to the one observed in *central* Be+Be interactions.

Figure 8.5 (*top*) shows the inverse slope parameter T of the transverse mass spectra at mid-rapidity ($0 < y < 0.2$) as a function of the collision energy for inelastic *p+p*, *central* Ar+Sc, Be+Be and central Pb+Pb collisions. The difference between measurements is found to be quite small, ≈ 0.015 GeV.

Figure 8.5 (*bottom*) shows the comparison of the mean transverse mass $\langle m_T \rangle - m_\pi$ parameter between the Ar+Sc, Be+Be, *p+p*, and Pb+Pb data. The values increase significantly by about 20 to 27 MeV for all four reactions.

Figure 8.6 presents the inverse slope parameter T plotted versus the number of wounded nucleons $\langle W \rangle$ which are a measure of the initial volume of the collision system. Although the uncertainties are large, the measurements show a modest monotonic rise with increasing system size for all beam momenta.

The ratio of the differential yields $\mathrm{d}n/\mathrm{d}y$ from *p+p*, Ar+Sc and Pb+Pb reactions to the Be+Be reference are plotted in Fig. 8.7. All the ratios show a slight monotonic decrease with y up to $y/y_{\mathrm{beam}} \approx 1.0$, where for lower beam momenta the ratio starts to increase. This is particularly apparent in the *p+p*/Be+Be ratio.

The mean multiplicity of π^- mesons is plotted versus the center-of-mass energy in Fig. 8.8 (*top*) for inelastic *p+p* interactions, *central* Be+Be, Ar+Sc and central Pb+Pb collisions. The dependence of the width $\sigma_{\mathrm{d}n/dy}$ of the rapidity distributions of π^- mesons produced in nucleus-nucleus collisions and inelastic nucleon-nucleon interactions against the collision energy is presented in Fig. 8.9. Since the *p+p* collision system is not isospin symmetric the isospin average $(\pi^- + \pi^+)/2$ was used for the comparison. These results are referred to as results for nucleon-nucleon (*N+N*) collisions [65]. One observes that the width normalized to the beam rapidity decreases slowly with increasing collision energy. Clearly, the measured values of $\sigma_{\mathrm{d}n/dy}$ differ very little between the studied reactions in the SPS energy range.

Figure 8.10 shows the ratios of $\langle \pi \rangle$[1] to the mean number of wounded nucleons $\langle W \rangle$ plotted versus the collision system size. In general the measurements are close to the expectations of the Wounded Nucleon Model which are shown as horizontal dashed lines. A trend of increase for $\langle W \rangle$ can be seen at higher beam momenta of 75*A* and 150*A* GeV/*c* in Ar+Sc and Pb+Pb reactions. Such an increase is not evident for lower beam momenta.

Figure 8.11 shows the width $\sigma_{\mathrm{d}n/dy}$ of the rapidity distributions plotted versus the mean number of wounded nucleons $\langle W \rangle$. When correcting the *p+p* data for the isospin asymmetry one finds a monotonic decrease of $\sigma_{\mathrm{d}n/\mathrm{d}y}$ with increasing number of nucleons in the colliding nuclei.

[1] For *p+p* interactions the figure shows isospin symmetrized values [21].

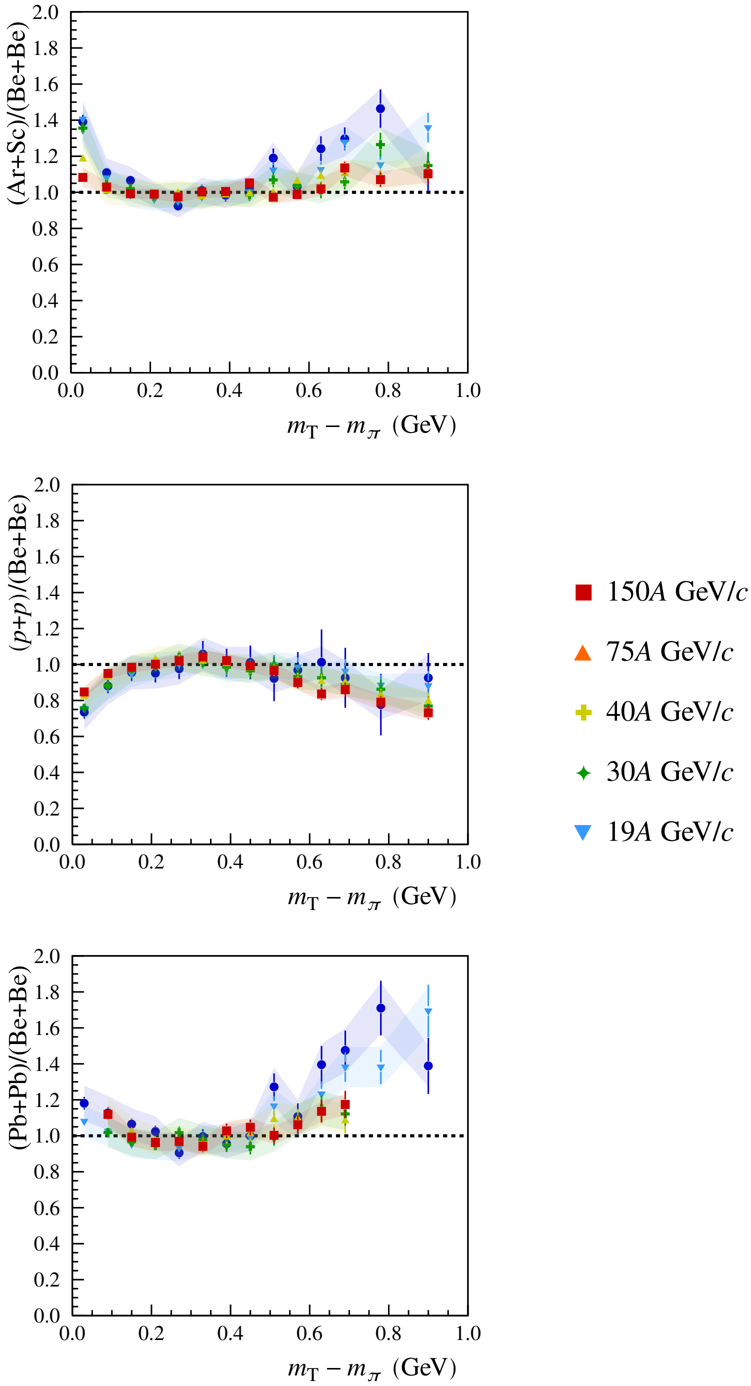

FIGURE 8.4: *Top:* The ratio of transverse mass spectra of π^- mesons at mid-rapidity ($0 < y < 0.2$) produced in *central* ^{40}Ar+^{45}Sc and Be+Be collisions. *Middle:* The ratio of transverse mass spectra of π^- mesons at mid-rapidity ($0 < y < 0.2$) produced in inelastic *p+p* interactions and *central* Be+Be collisions. *Bottom:* The ratio of transverse mass spectra of π^- mesons at mid-rapidity ($0 < y < 0.2$) produced in central Pb+Pb and *central* Be+Be collisions. Statistical uncertainties are shown as vertical bars and systematic uncertainties are indicated by shaded bands.

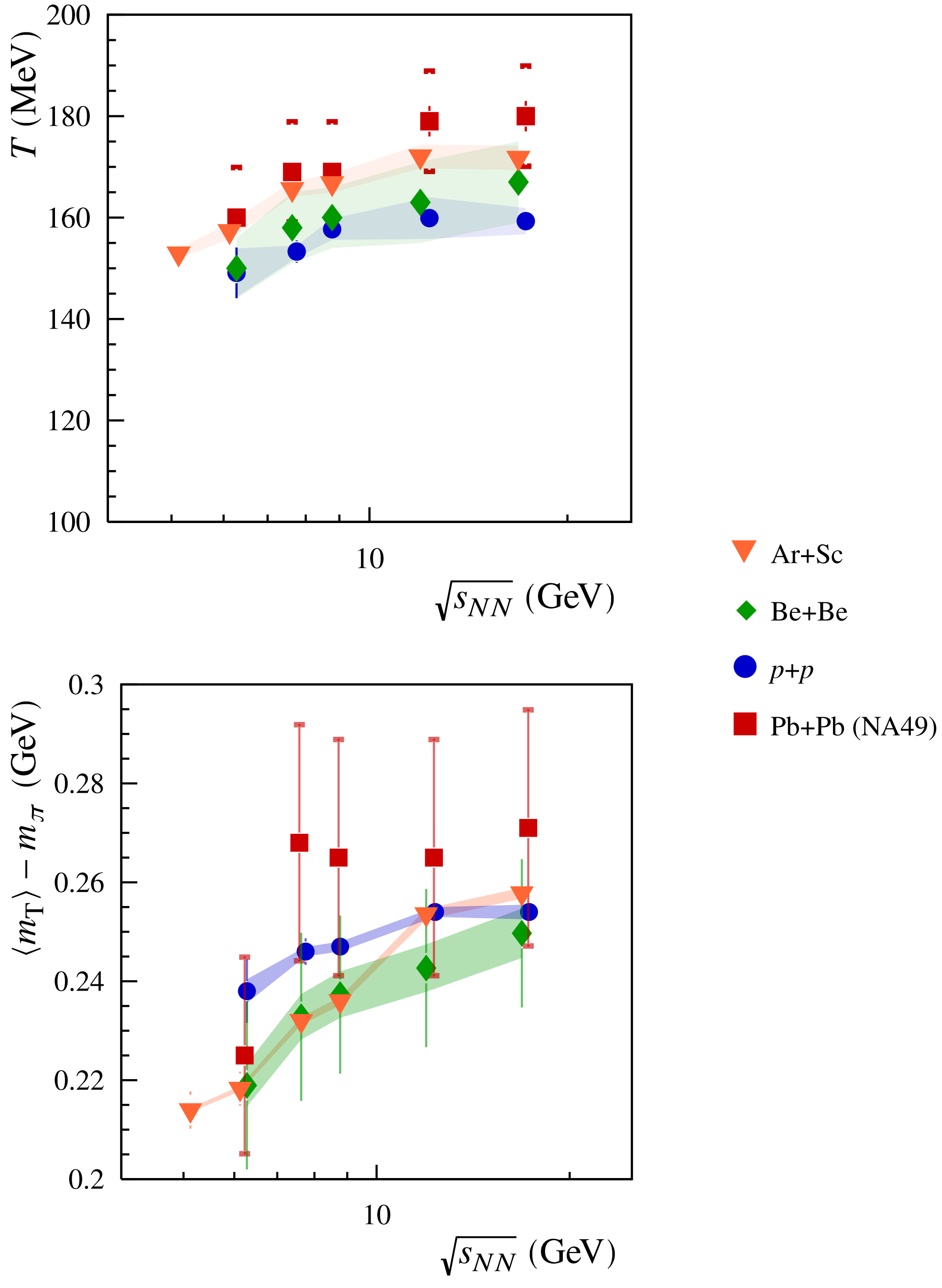

FIGURE 8.5: *Top:* Inverse slope parameter T of the transverse mass spectra at mid-rapidity ($0 < y < 0.2$) plotted against the collision energy per nucleon. The parameter T was fitted in the range $0.24 < m_T - m_\pi < 0.72$ GeV. Statistical uncertainties are shown as vertical bars (often smaller than markers' size) and systematic uncertainties are indicated by shaded bands (or caps for Pb+Pb collisions). *Bottom:* Mean transverse mass $\langle m_T \rangle - m_\pi$ at mid-rapidity ($0 < y < 0.2$) versus the collision energy. The results are compared with the corresponding data on p+p interactions, *central* Be+Be and central Pb+Pb collisions.

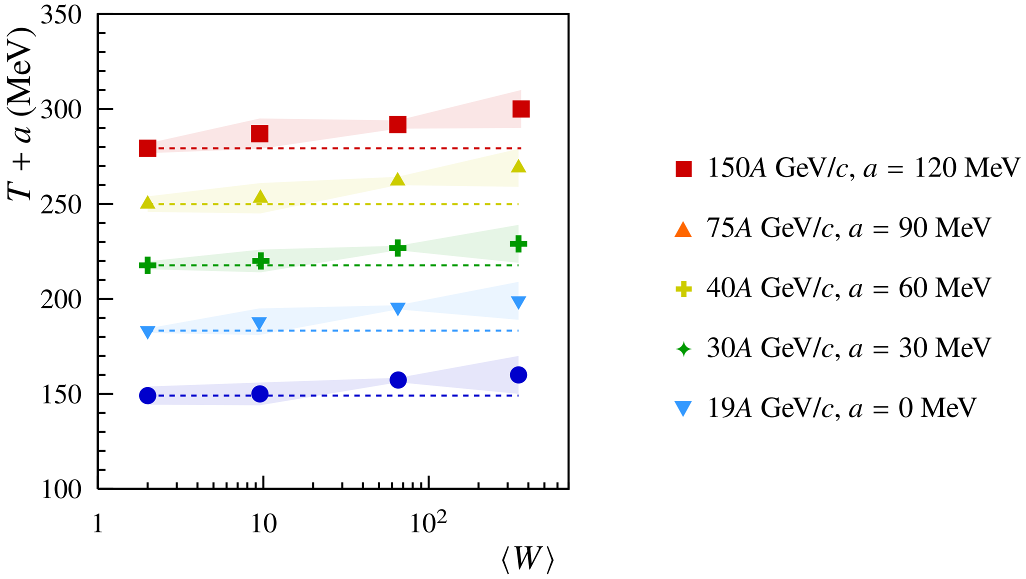

FIGURE 8.6: The inverse slope parameter T versus the mean number of wounded nucleons $\langle W \rangle$ in *central* Ar+Sc, Be+Be and central Pb+Pb collisions and inelastic p+p interactions at beam momenta from 19A to 150A GeV/c. Statistical uncertainties are smaller than the markers' size. Systematic uncertainties are shown by shaded bands. For better visibility different energies are offset vertically.

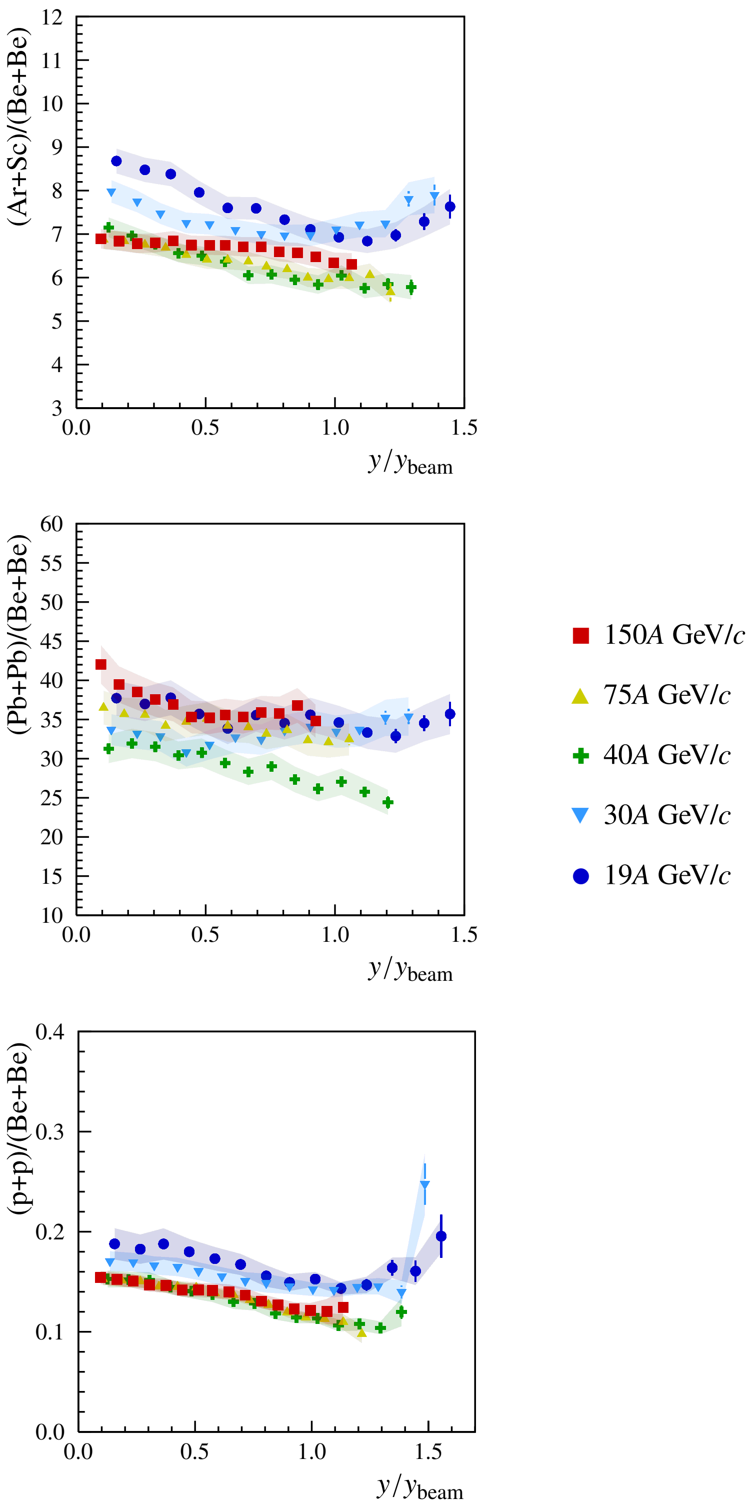

FIGURE 8.7: *Top:* The ratio of the rapidity y spectra of π^- mesons produced in *central* ^{40}Ar+^{45}Sc and Be+Be collisions. *Middle:* The ratio of the rapidity y spectra of π^- mesons produced in central Pb+Pb and *central* Be+Be collisions. *Bottom:* The ratio of the rapidity y spectra of π^- mesons produced in inelastic p+p interactions and *central* Be+Be collisions. Statistical uncertainties are shown as vertical bars (usually smaller than markers' size) and systematic uncertainties are indicated by shaded bands.

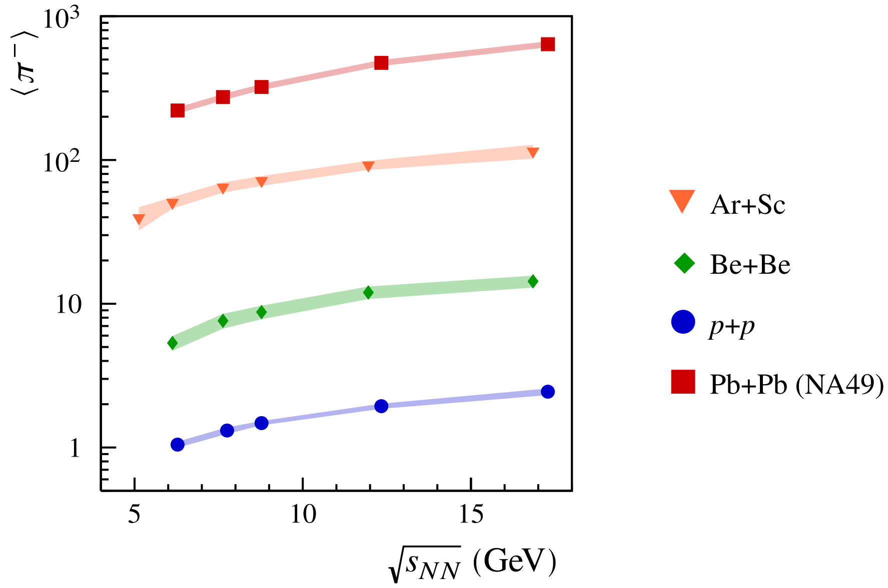

FIGURE 8.8: *Top:* The mean multiplicity of negatively charged pions in inelastic p+p interactions and in *central* Ar+Sc, Be+Be and central Pb+Pb collisions as a function of center of mass collision energy. Statistical uncertainties of the data points are smaller than the marker size. The systematic uncertainties are indicated by shaded bands.

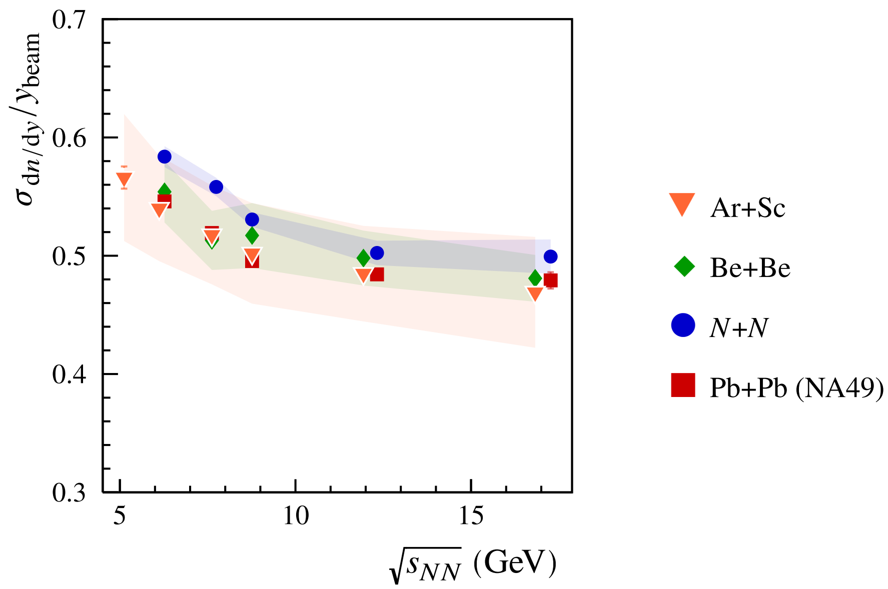

FIGURE 8.9: The width $\sigma_{dn/dy}$ of the rapidity distributions of negatively charged pions to the beam rapidity y_{beam} in inelastic N+N interactions and in *central* Ar+Sc, Be+Be and central Pb+Pb collisions as a function of the center of mass energy $\sqrt{s_{NN}}$. Ar+Sc, N+N and Be+Be measurements are presented with statistical (vertical bars, often smaller than marker size) and systematic (shaded band) uncertainty, whereas Pb+Pb with statistical uncertainty only.

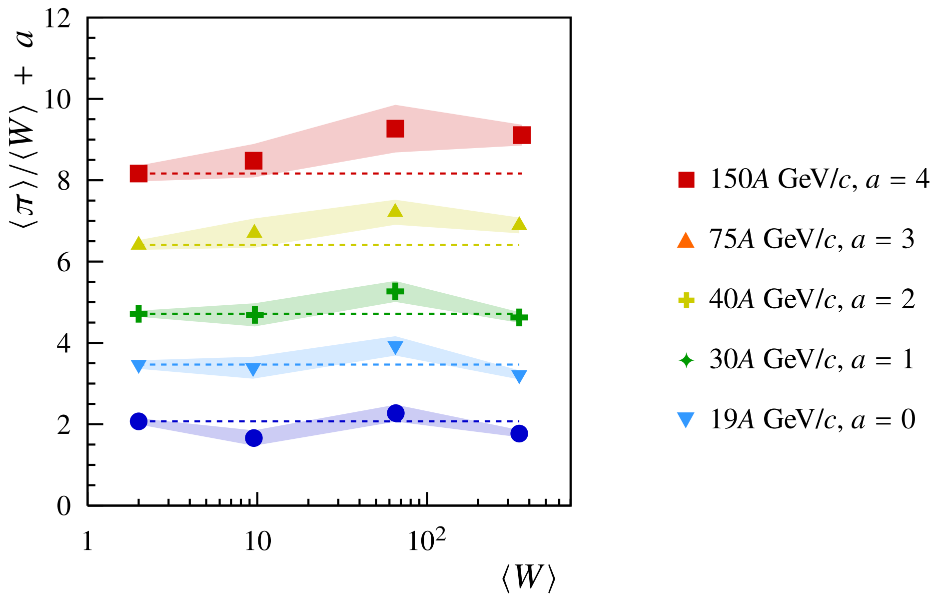

FIGURE 8.10: Ratio of the mean pion multiplicity $\langle \pi \rangle$ to the mean number of wounded nucleons $\langle W \rangle$ plotted versus the collision system size for beam momenta from 19*A* to 150*A* GeV/*c*. The data points for different beam momenta were shifted for better readability. Statistical uncertainties are smaller than marker size. Systematic uncertainties are indicated by shaded bands.

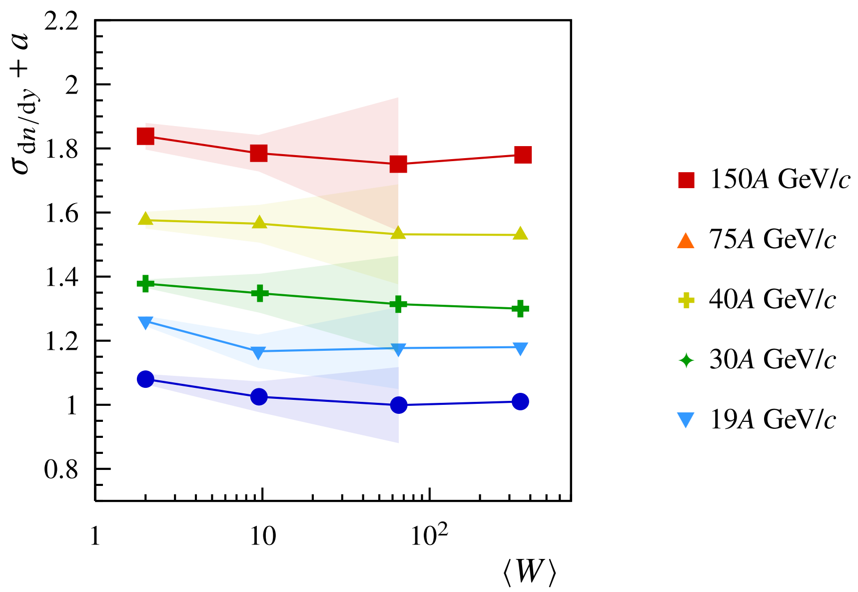

FIGURE 8.11: The width $\sigma_{dn/dy}$ of the rapidity distributions of negatively charged pions versus the mean number of wounded nucleons $\langle W \rangle$ for beam momenta from 19*A* to 150*A* GeV/*c*. Ar+Sc, *N*+*N* and Be+Be measurements are presented with systematic uncertainty as a shaded band. Statistical uncertainty is smaller than marker size. For Pb+Pb statistical uncertainty only was published.

8.3 Comparison with models

A comparison of generated π^- spectra created utilizing the EPOS [62], URQMD [66] and HIJING [60] models with the final spectra for all beam momenta has been performed in Figs. 8.12, 8.13, and 8.14, respectively. There are significant differences present for all beam momenta, although they are getting stronger for the lower momenta. Over-prediction of π^- in EPOS (usually around 50%) occurs mostly in the mid-rapidity region of the spectra, whereas under-prediction in EPOS (as well mostly around 50%) seems to appear closer to the less-populated edges of acceptance in high p_T or y. URQMD has a significant over-estimation only for the edge of acceptance in the forward rapidity region and slight under-estimation at low transverse momentum near mid-rapidity. HIJING is systematically higher than the measured results for almost all beam momenta by 15 to 20% and in case of 13*A* GeV/*c* many bins show more than twice the value of the measurements.

A similar picture is presented in Fig. 8.15 which shows the comparison of the transverse momentum p_T spectra dn/dp_T for all beam momenta with EPOS, URQMD and HIJING model predictions. The EPOS- and URQMD-generated spectra are consistent with the measurements only at the top beam momenta of 75*A* and 150*A* GeV/*c*. Otherwise, EPOS and HIJING are overestimating the measurements, whereas URQMD significantly underestimates the spectra.

Inverse slope parameters T fitted at mid-rapidity ($0 < y < 0.2$) in the range $0.24 < m_T - m_\pi < 0.72$ GeV are plotted versus $\sqrt{s_{NN}}$ together with model predictions in Fig. 8.16 (*top*). The figure shows that EPOS model predictions for Ar+Sc collisions are lower than the NA61/SHINE measurements. Predictions of URQMD exhibit a non-monotonic behavior and lie lower than the measurements at low beam momenta and higher at high beam momenta. HIJING shows a concave behavior and unsatisfactory agreement with measurements. Mean transverse mass $\langle m_T \rangle - m_\pi$ at mid-rapidity versus the collision energy is presented in Fig. 8.16 (*bottom*) and compared to model predictions. The EPOS and URQMD models show a slope that increases less steeply than the measurements. HIJING shows a convex behavior with the extreme points matching the measurements.

Comparison of the rapidity y spectra dn/dy for all beam momenta with the EPOS, URQMD and HIJING model calculations is presented in Fig. 8.17. The EPOS- and URQMD-generated spectra are only consistent with the measurements in case of the top beam momenta of 75*A* and 150*A* GeV/*c*. Otherwise, EPOS is overestimating the mid-rapidity region and URQMD is underestimating it. HIJING is systematically higher than the measurements for all beam momenta.

The value of $\langle \pi^- \rangle$ together with the model calculations is presented in Fig. 8.18 (*top*). As shown by the curves, the predictions of the EPOS and URQMD models reproduce the experimental results reasonably well, staying within the uncertainties of the measurements. The HIJING predictions are systematically higher than the measurements. The width $\sigma_{dn/dy}$ of the rapidity distributions of π^- mesons versus the center-of-mass collision energy is presented in Fig. 8.18 (*bottom*) together with the EPOS, URQMD and HIJING model predictions. These fit well into the measurements' systematic uncertainties band.

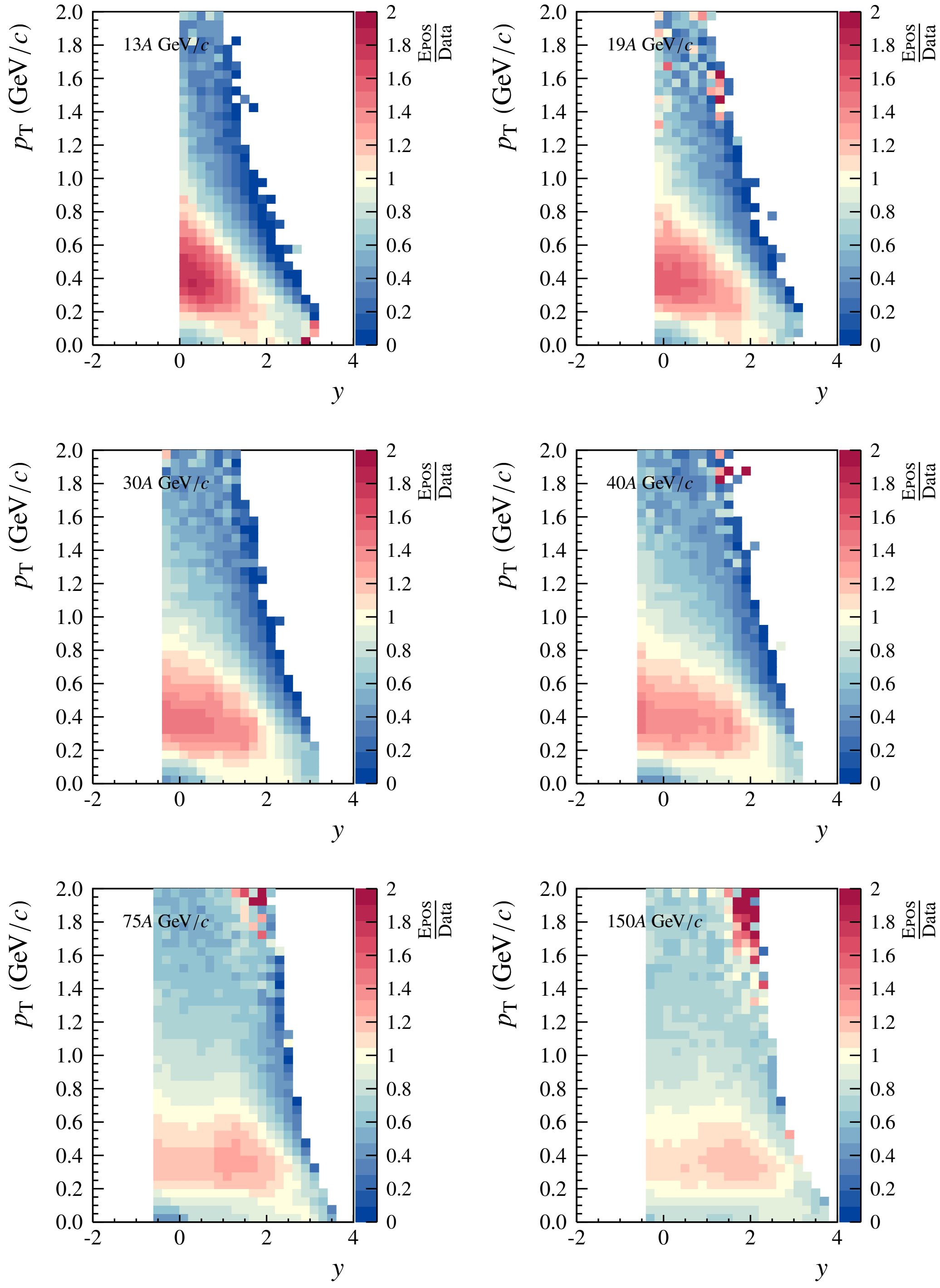

FIGURE 8.12: A comparison of the double-differential spectra $d^2n/dydp_T$ generated with EPOS to the final corrected spectra for all beam momenta.

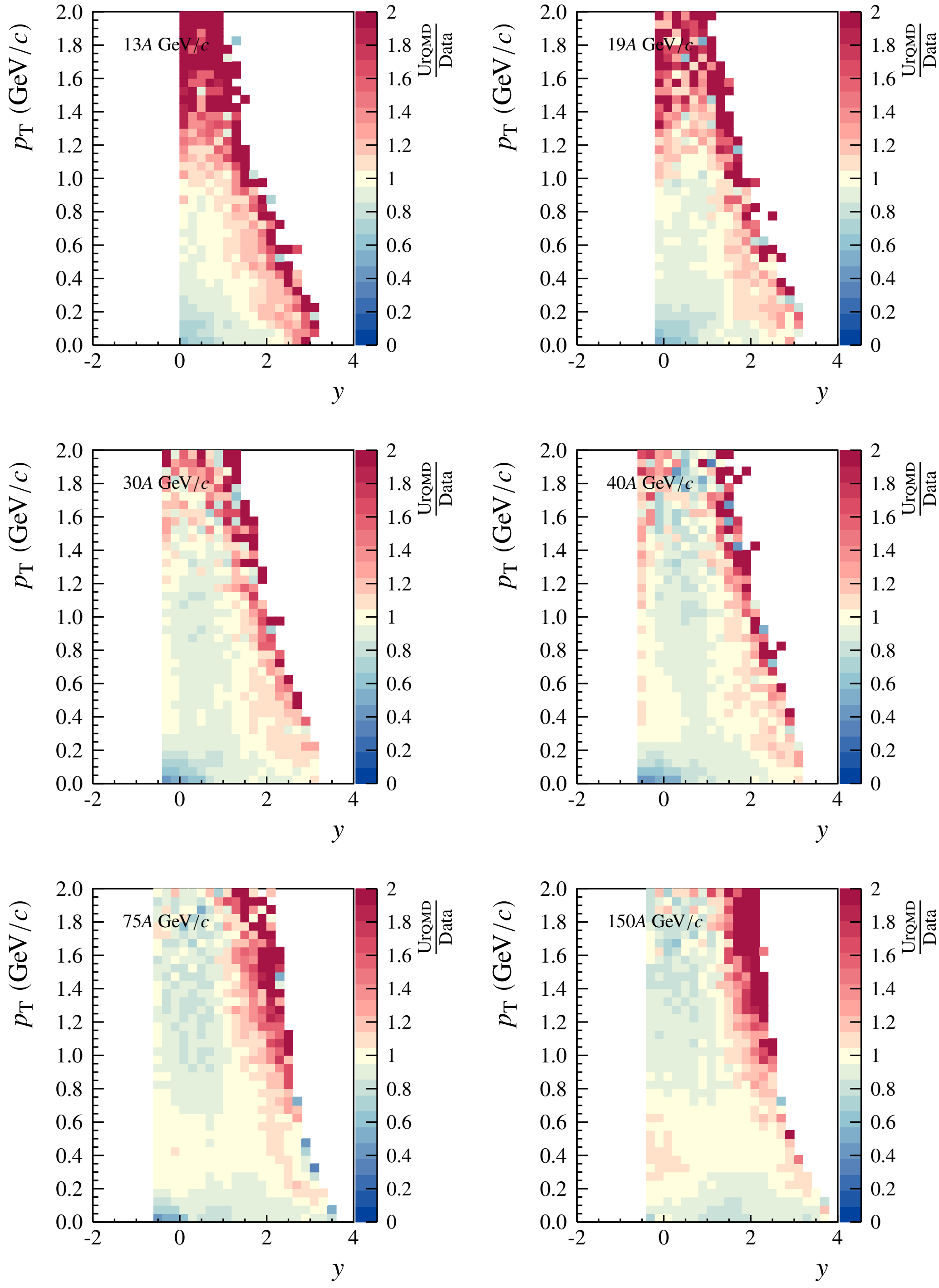

FIGURE 8.13: A comparison of the double-differential spectra $d^2n/dydp_T$ generated with UrQMD to the final corrected spectra for all beam momenta.

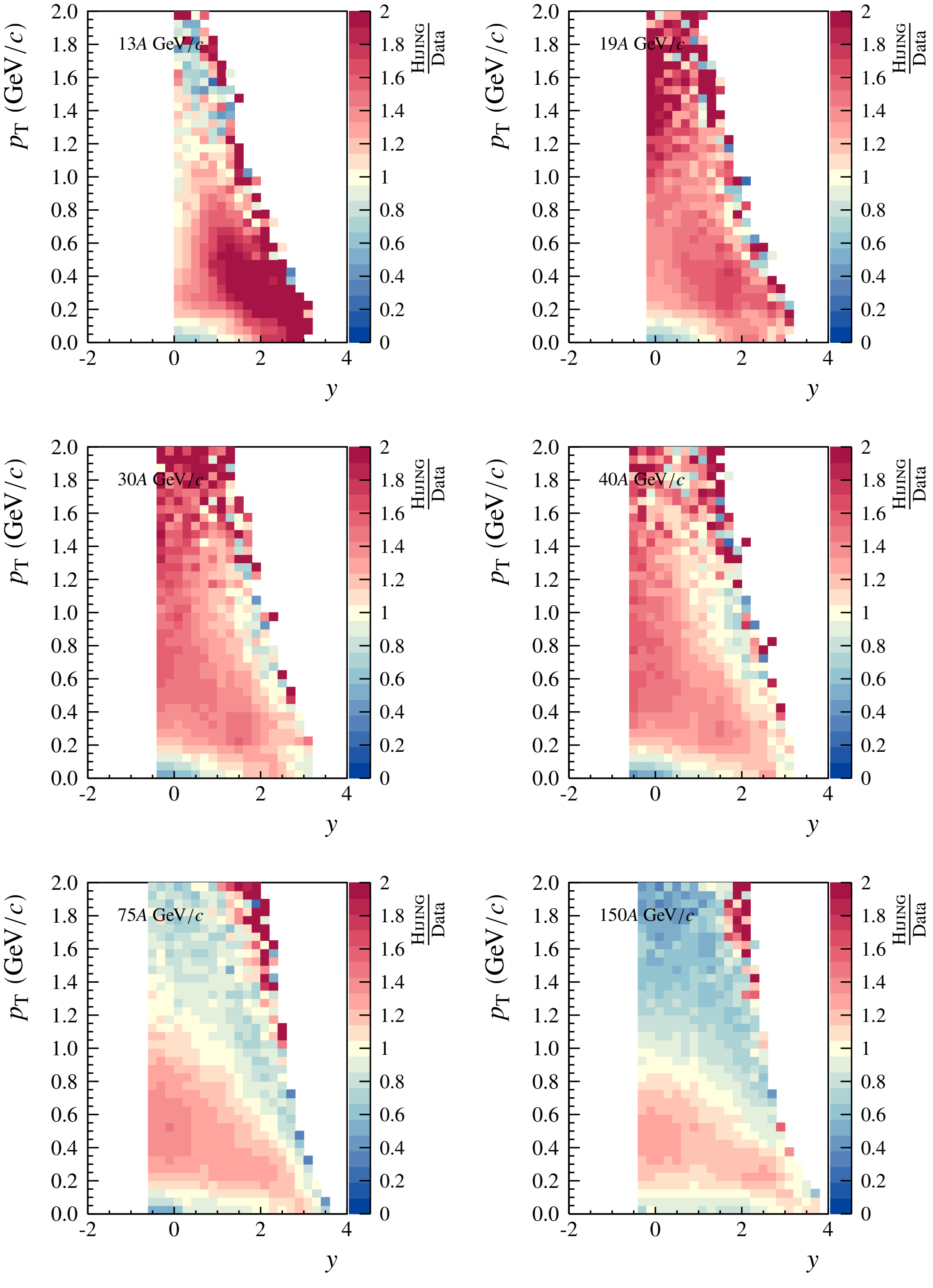

FIGURE 8.14: A comparison of the double-differential spectra $d^2n/dydp_T$ generated with HIJING to the final corrected spectra for all beam momenta.

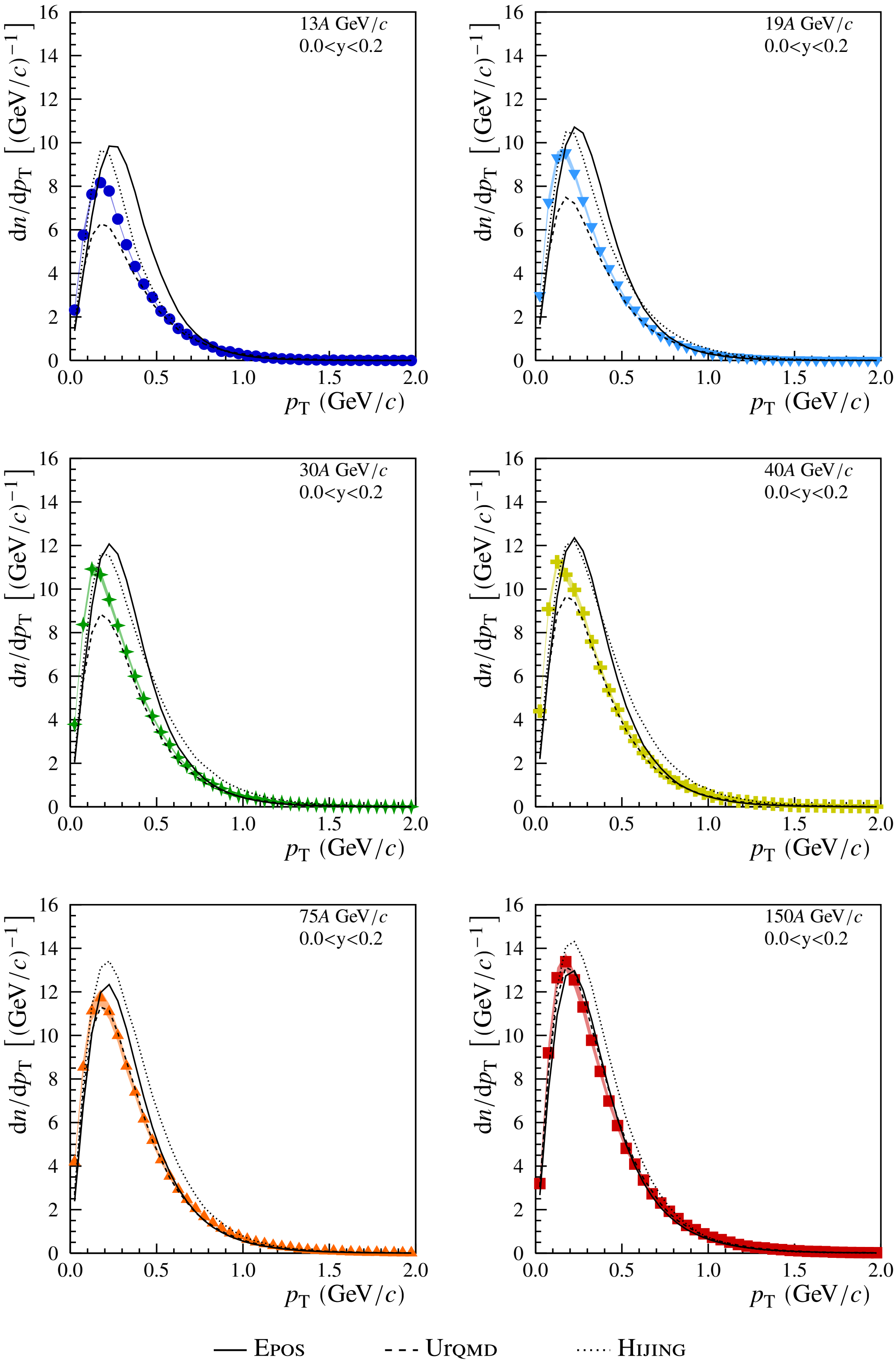

FIGURE 8.15: A comparison of the transverse momentum distributions dn/dp_T at mid-rapidity ($0 < y < 0.2$) for data (full markers) with the EPOS, URQMD and HIJING models. Statistical uncertainties of the data points are smaller than markers' size and systematic uncertainties are indicated by shaded bands

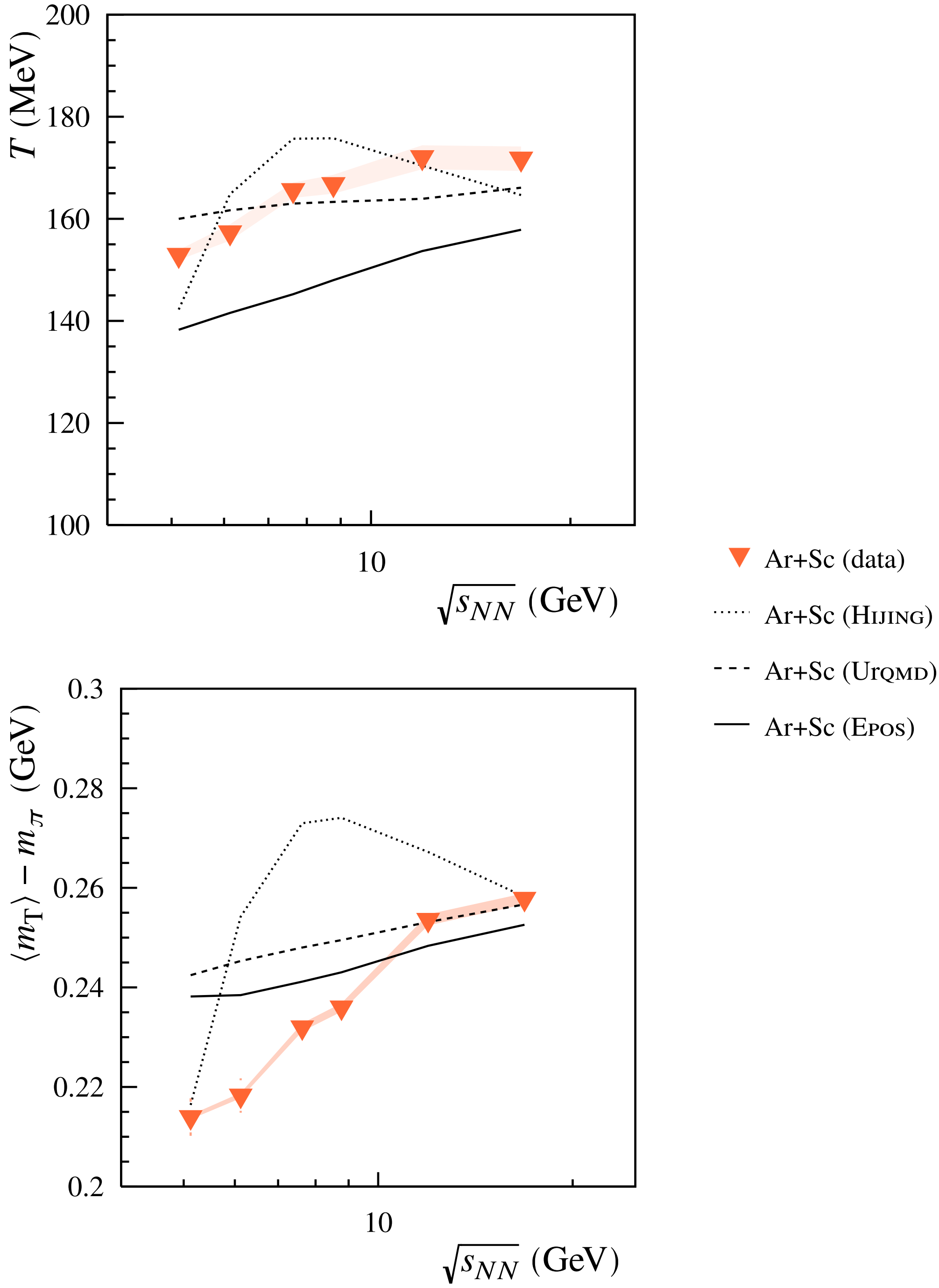

FIGURE 8.16: *Top:* Inverse slope parameter T as a function of collision energy compared to the EPOS, URQMD and HIJING model predictions. Statistical uncertainties are smaller than markers' size and systematic uncertainties are indicated as a shaded band. *Bottom:* Mean transverse mass $\langle m_T \rangle - m_\pi$ as a function of collision energy compared to the EPOS, URQMD and HIJING model predictions. Statistical uncertainties are usually smaller than marker size and systematic uncertainties are marked with shaded band.

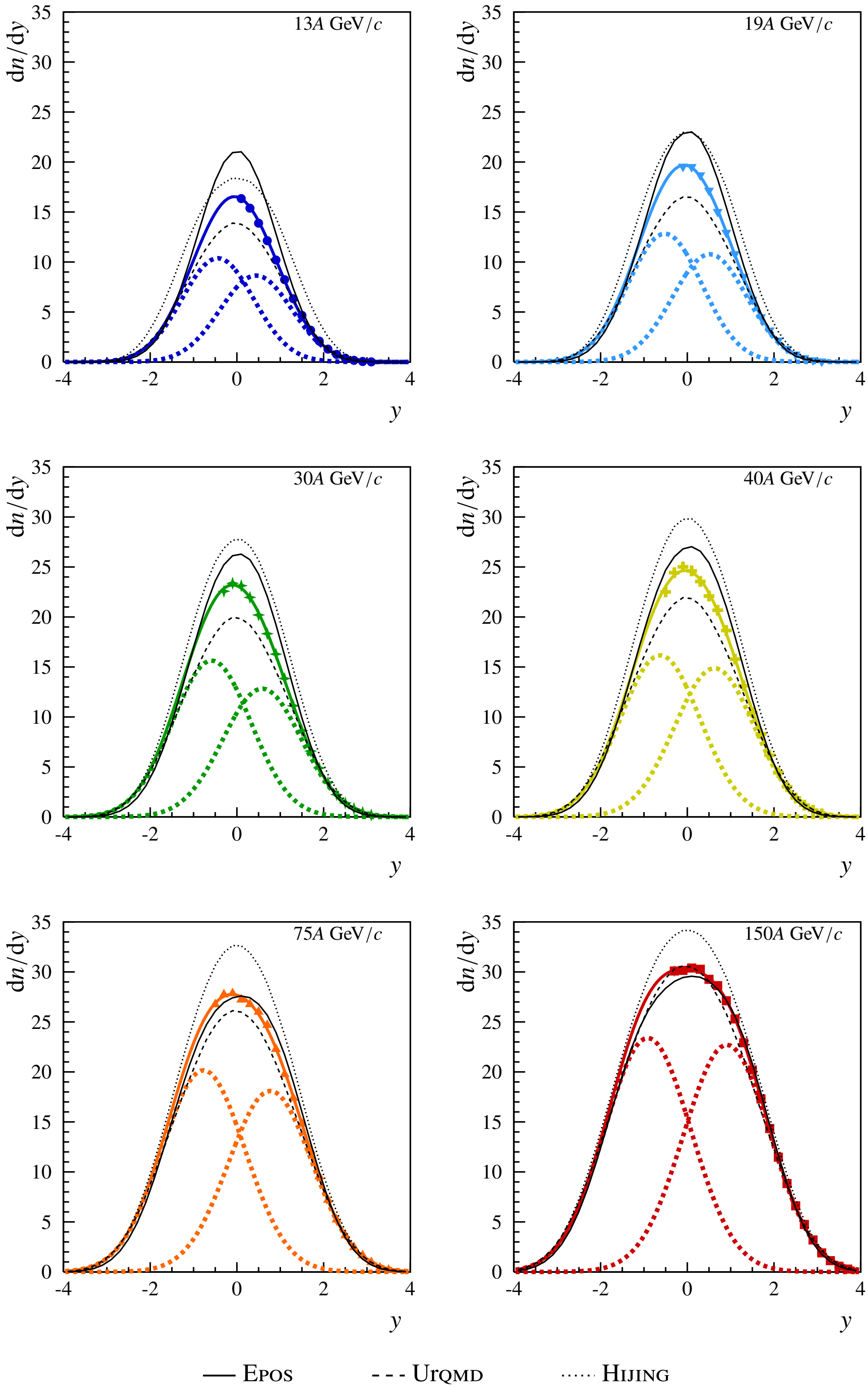

FIGURE 8.17: A comparison of the rapidity distributions dn/dy for data (full markers) with the two fitted symmetrically displaced Gaussians (color dashed curves). Their sum is plotted by the color curves and the EPOS, URQMD and HIJING model predictions are plotted with black curves. Total uncertainties are plotted and they are smaller than the marker size.

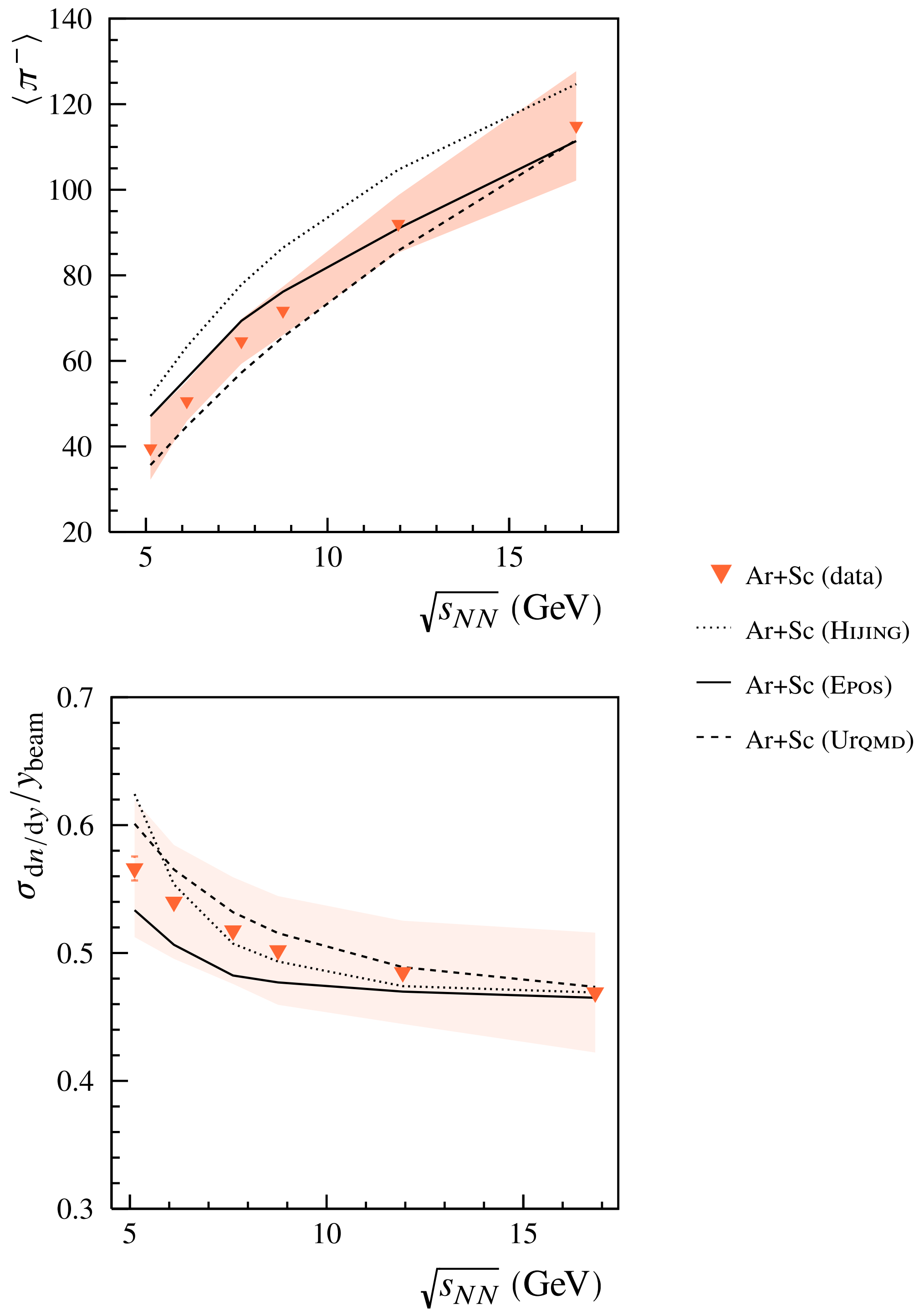

FIGURE 8.18: *Top:* Mean number of negatively charged pions $\langle \pi^- \rangle$ as a function of collision energy compared to the EPOS, URQMD and HIJING model predictions. Statistical uncertainties are smaller than markers' size and systematic uncertainties are indicated as a shaded band. *Bottom:* Width of the rapidity distribution $\sigma_{dn/dy}$ as a function of collision energy compared to the EPOS, URQMD and HIJING model predictions. Statistical uncertainties are usually smaller than marker size and systematic uncertainties are marked with shaded band.

8.4 Results in the context of the onset of deconfinement

The Landau hydrodynamical model of high energy collisions [67, 68] predicts rapidity distributions of Gaussian shape. In fact, this prediction is approximately confirmed by the experimental data, see Ref. [69] and references therein. Moreover, the collision energy dependence of the width was derived by Shuryak [70] from the same model under simplifying assumptions and reads:

$$\sigma^2 = \frac{8}{3} \cdot \frac{c_s^2}{1 - c_s^4} \cdot \ln\left(\frac{\sqrt{s_{NN}}}{2m_p}\right), \tag{8.1}$$

where c_s denotes the speed of sound, and $c_s^2 = 1/3$ for an ideal gas of massless particles.

The above prediction is compared with the experimental data on the width $\sigma_{dn/dy}$ of the rapidity distributions of π^- mesons produced in central nucleus-nucleus collisions and inelastic nucleon-nucleon interactions in Fig. 5.13 (*bottom left*). The model calculations are close to the measured dependence on the beam rapidity y_{beam}. The deviations were attributed to the changes in the equation of state [71, 72], which can be effectively parametrized by allowing the speed of sound to be dependent on collision energy.

By inverting Eq. 8.1 one can express c_s^2 in the medium as a function of the measured width of the rapidity distribution. The energy dependence of the sound velocities extracted from the data are presented in Fig. 8.19. The energy range for results from Ar+Sc, Be+Be *central* collisions and inelastic *p+p* interactions is too limited and the fluctuations in the data too large to allow a significant conclusion about a possible minimum. Data on central Pb+Pb collisions, in combination with results from AGS and RHIC on central Au+Au collisions, cover a much wider energy range. Here the sound velocity exhibits a clear minimum (usually called the softest point) at $\sqrt{s_{NN}} \approx 10$ GeV consistent with the reported onset of deconfinement [22, 23].

Fig. 8.20 shows the "kink" plot, the dependence of the ratio of the mean number of pions produced in a collision to the mean number of wounded nucleons $\langle\pi\rangle/\langle W\rangle$ versus the Fermi energy measure, which is expressed as:

$$F = \left[\frac{(\sqrt{s_{NN}} - 2m_N)^3}{\sqrt{s_{NN}}}\right]^{1/4} \approx \sqrt[4]{s_{NN}}, \tag{8.2}$$

where $\sqrt{s_{NN}}$ is the collision energy per nucleon pair in the center of mass. Systematic uncertainty connected with the calculation of the number of wounded nucleons W was not included in the systematic uncertainties plotted in Fig. 8.20. The uncertainty was of the order of 5%.

Interestingly, $\langle\pi\rangle/\langle W\rangle$ for Ar+Sc reactions equals that for N+N[2] reactions at low SPS energies whereas it is consistent with that for central Pb+Pb reactions at high SPS energies. A suppression of pion yield per wounded nucleon in central Pb+Pb collisions compared to N+N reactions is observed at low energies which is not found for the intermediate size Ar+Sc system. This effect was attributed to pion absorption in the evolving fireball [73, 74]. The behavior of Ar+Sc stands in contradiction to Be+Be measurements, which are close to the Pb+Pb results except for the top SPS beam energy. The steepening of the slope of the $\langle\pi\rangle/\langle W\rangle$, which is considered a signal of the onset of deconfinement within the SMES model is not observed in *central* Ar+Sc measurements.

[2]For *p+p* interactions the figure shows isospin symmetrized values [21] marked as N+N.

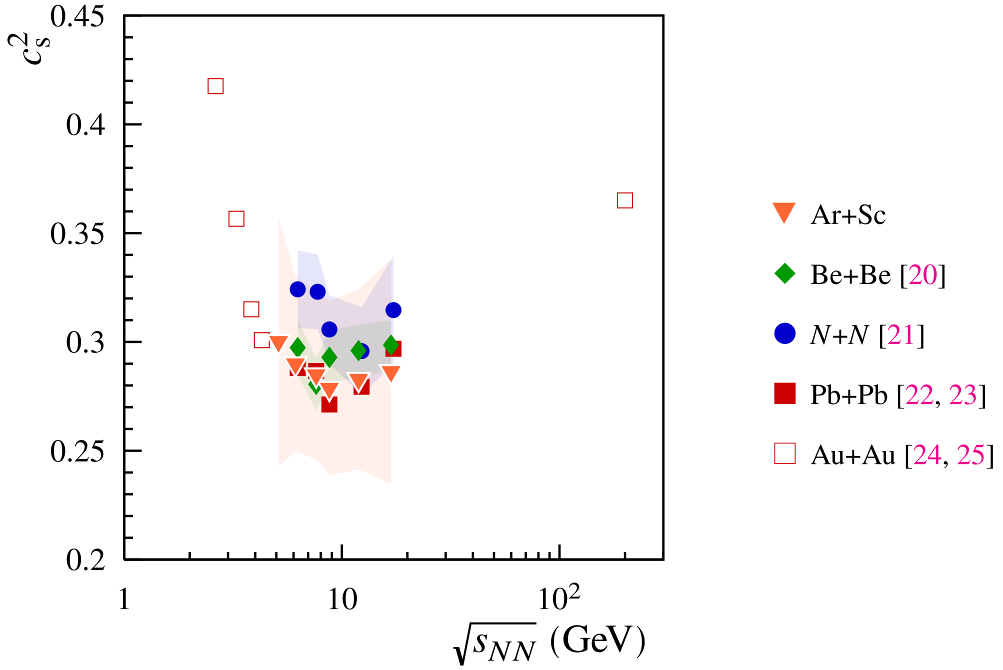

FIGURE 8.19: The speed of sound c_s^2 as a function of center-of-mass collision energy as extracted from the data using Eq. 8.1.

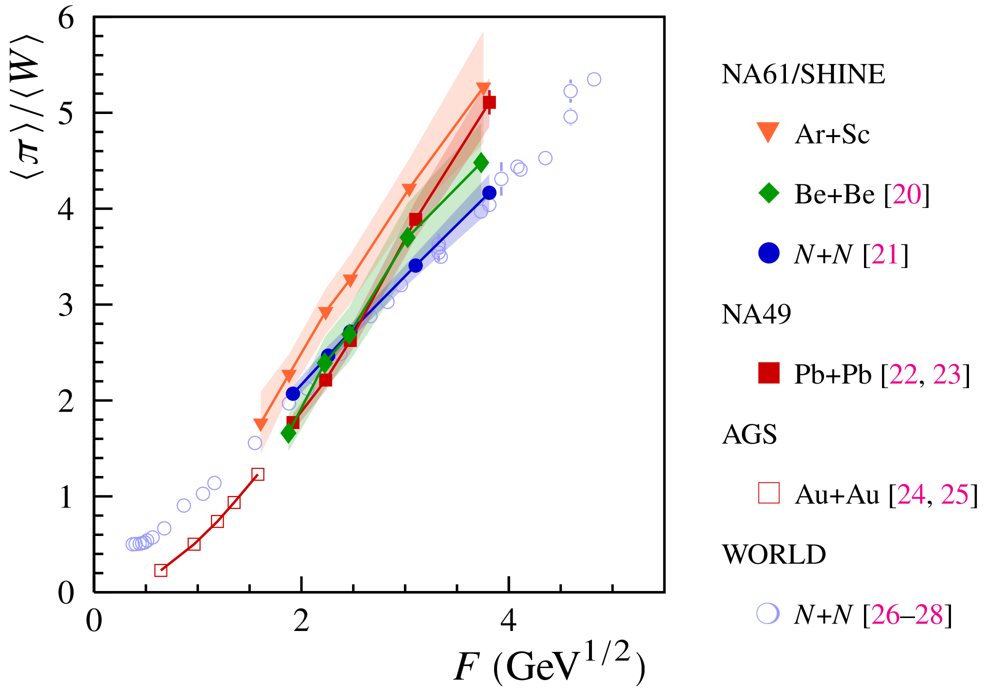

FIGURE 8.20: The "kink" plot showing the ratio of the mean pion multiplicity $\langle\pi\rangle$ to the mean number of wounded nucleons $\langle W\rangle$ versus the Fermi energy variable $F \approx \sqrt[4]{s_{NN}}$. Results for inelastic nucleon-nucleon reactions and central nucleus-nucleus collisions are compared.

Chapter 9

Summary

This thesis presents experimental results on spectra and mean multiplicities of negatively charged pions π^- produced by strong processes and in electromagnetic decays of produced hadrons in the 5% most *central* collisions of ^{40}Ar+^{45}Sc and gives a detailed description of the process of obtaining them. The data was collected by the NA61/SHINE experiment at six beam momenta 13*A*, 19*A*, 30*A*, 40*A*, 75*A* and 150*A* GeV/*c* in year 2015 as part of the strong interactions program. The latter includes a two-dimensional scan of the beam energy and collision system size in order to explore the characteristics of strongly interacting matter.

The results were obtained using the h^- method, which removes the contribution of particles other than primary π^- mesons from the unidentified spectra of negatively charged hadrons. To this end, data from the Epos Monte-Carlo simulation was used.

A detailed analysis of statistical and systematic uncertainties was performed. The magnitude of possible uncertainties of the correction process was calculated. The uncertainties are mostly smaller than 10% (see Figs. 5.8 and 5.10).

Two-dimensional spectra of p_T versus y and $m_T - m_\pi$ versus y were obtained for all beam momenta in Figs. 7.1 and 7.2. Comparisons of the two-dimensional p_T versus y spectra obtained with the *tof-dE/dx* and the *dE/dx* methods were performed in Figs. 8.2 and 8.3. The discrepancies between these methods are mostly below 5%. The p_T versus y spectra were also compared with the Epos, UrQMD, and Hijing models' predictions (see Figs. 8.12, 8.13 and 8.14, respectively). The differences found are significant and can serve to improve the models.

Transverse momentum p_T spectra were presented with corresponding predictions obtained from the Epos, Hijing and UrQMD models in Fig. 8.15.

Transverse mass $m_T - m_\pi$ spectra at different rapidity bins were fitted with an exponential function in order to find the inverse slope parameter T and calculate the mean transverse mass $\langle m_T \rangle - m_\pi$. The transverse mass spectra $m_T - m_\pi$ at mid-rapidity were compared with measurements on *central* Be+Be collisions, an isospin symmetric reference in Fig. 8.4. Comparisons of the mean transverse mass $\langle m_T \rangle - m_\pi$ at mid-rapidity and the inverse slope parameter T with other NA61/SHINE and NA49 measurements in inelastic p+p interactions, *central* Be+Be, and central Pb+Pb collisions were performed (see Fig. 8.5). The two parameters were also compared with corresponding calculations obtained from the Epos, Hijing and UrQMD models in Fig. 8.16.

Two-dimensional spectra of p_T versus y were extrapolated in p_T and integrated in order to obtain rapidity y spectra. These were compared to the Epos, Hijing, and UrQMD models' predictions in Fig. 8.17.

The rapidity spectra were extrapolated utilizing a sum of two Gaussian functions and integrated in order to obtain the 4π multiplicities of π^- mesons. The widths of the distributions together with the mean multiplicities were compared to corresponding values in inelastic p+p interactions, *central* Be+Be, and central Pb+Pb collisions in Figs. 8.8 and 8.9. A similar comparison was performed with the Epos, Hijing, and UrQMD models' predictions (see Fig. 8.18).

A significant effort was put into the calculation of the mean number of wounded nucleons $\langle W \rangle$. Values based on the Wounded Nucleon Model were obtained with the centrality selection performed using the forward energy simulation (see Table 6.1).

The central result of this thesis is the plot showing the ratio of the mean number of pions $\langle \pi \rangle$ to the mean number of wounded nucleons $\langle W \rangle$ in a collision (see Fig. 8.20). The data points for *central* Ar+Sc show monotonous increase with collision energy, which suggest no qualitative change in the behavior of produced entropy with collision energy. The slope of the line of Ar+Sc data is similar to the slope of Pb+Pb points and steeper than the line formed by N+N points, which, according to the SMES model, is a sign of higher entropy production in *central* Ar+Sc collisions than N+N interactions. The line for *central* Ar+Sc lies above the line for central Pb+Pb at the lower SPS energies.

The members of the NA61/SHINE experiment are currently active in multiple analyses of other collision systems, e,g. Xe+La and Pb+Pb, which will complete the present strong interactions program.

An upgrade of the NA61/SHINE detector has started with completion foreseen in summer 2021. This upgraded detector will be used for further studies of nucleus-nucleus collisions in order to complement the already obtained data on hadron production properties by unique data on production of charm mesons.

These measurements of the NA61/SHINE collaboration will help to understand the properties of strongly interacting matter at the CERN SPS energies such as its phases and transitions.

Appendix A

Coordinate system

This appendix is devoted to the coordinate system of NA61/SHINE and calculation of basic kinematic variables used in the experiment as well as throughout this thesis.

A.1 NA61/SHINE coordinate system

An overview of the NA61/SHINE detector together with the indication of the coordinates is presented in Fig. 2.2 in Chapter 2. The origin of the system is placed in the center of the magnet, on the beamline. The system is right-handed and the z axis corresponds to the beamline axis. The y axis is vertical and perpendicular to electron drift velocity, whereas the x axis is horizontal.

The azimuthal angle, ϕ, is defined on the x-y plane so that $\phi = 0$ rad corresponds to the x axis and $\phi = \pi$ rad to the y axis. The definition of ϕ is the following:

$$\phi = \arctan \frac{p_y}{p_x} \tag{A.1}$$

The polar angle *theta* is the angle from the z axis, so that particles produced with $\theta = 0$ move parallel to the beamline. It varies from 0 to 2π rad and is defined as follows:

$$\theta = \arcsin \frac{p_T}{p} \tag{A.2}$$

A.2 Kinematic variables

A.2.1 Total momentum and transverse variables

The total momentum is defined as the square root of momentum components in the coordinate system described in Section A.1 added in quadrature:

$$p = \sqrt{p_x^2 + p_y^2 + p_z^2} \tag{A.3}$$

Since the z axis is defined as parallel to the beamline, the transverse variables are calculated with x and y components. The transverse momentum:

$$p_T = \sqrt{p_x^2 + p_y^2} \tag{A.4}$$

And the transverse mass:

$$m_T = \sqrt{m^2 + (p_T c)^2} \tag{A.5}$$

where m is the invariant mass of a given particle

A.2.2 Rapidity

The rapidity is defined as a combination of particle's energy E and its momentum component parallel to the beamline p_z:

$$y = \frac{1}{2} \ln \frac{E + p_z c}{E - p_z c} \tag{A.6}$$

Rapidity is a dimensionless variable, invariant to Lorentz transformation, which makes it useful for comparisons of data from collider experiments with fixed target experiments. Rapidity can be easily transformed from laboratory to center of mass frame:

$$y_{\text{CMS, frame}} = y_{\text{LAB, frame}} + y_{\text{CMS}} \tag{A.7}$$

where

$$y_{\text{CMS}} = \arctan \frac{p_{\text{beam}} c}{E_{\text{beam}} + m_N} \tag{A.8}$$

p_{beam} is the beam momentum, $E_{\text{beam}} = \sqrt{p_{\text{beam}}^2 c^2 + m_N^2}$ is the beam energy with m_N as the mass of a nucleon. Throughout this work rapidity is given in the center of mass frame.

When mid-rapidity is mentioned in this thesis, it is defined as a region in y close to $y = 0$, usually $y \in (0, 0.2)$. It corresponds to particles produced approximately perpendicular to the beamline in the center of mass system. The regions at $y > 0$ and $y < 0$ are usually referred to as *forward* and *backward* rapidity, respectively.

A.3 Collision energy

The Lorentz-invariant Mandelstam variable describing the energy available in the center of mass is expressed as:

$$\sqrt{s} = \sqrt{(E_{\text{beam}} + E_{\text{target}})^2 - (p_{\text{beam}} + p_{\text{target}})^2 c^2} \tag{A.9}$$

Usually, it is given as center of mass energy per nucleon pair $\sqrt{s_{NN}}$, for which $m_{\text{beam}} = m_{\text{target}} = m_N$. In a fixed target experiment $p_{\text{target}} = 0$ and E_{target} is simply the mass of the ion used as a target.

$$\sqrt{s_{NN}} = \sqrt{(E_{\text{beam}} + m_N)^2 - p_{\text{beam}}^2 c^2} \tag{A.10}$$

The values of the kinematic variables for each analyzed beam momentum are summarized in Table A.1.

TABLE A.1: The values of the kinematic variables for each analyzed beam momentum.

p_{beam} (GeV/c)	E_{beam} (GeV)	$y_{\text{CMS}} = y_{\text{beam}}$	$\sqrt{s_{\text{NN}}}$ (GeV)	F $\left(\sqrt{\text{GeV}}\right)$
13.00	13.03	1.66	5.13	1.61
19.00	19.02	1.85	6.13	1.88
30.00	30.01	2.08	7.63	2.23
40.00	40.01	2.22	8.77	2.47
75.00	75.01	2.54	11.95	3.04
150.00	150.00	2.88	16.85	3.76

Appendix B

Calculation of the mean transverse mass

A function

$$f(m_T) = \frac{d^2n}{dy dm_T} = A m_T \exp - \frac{m_T}{T},$$

where A and T are free parameters is fitted to the transverse mass m_T spectra. To limit the small deviations from exponential dependence at high m_T, the fitting in mid-rapidity is only applied in the following range $0.2 < m_T - m_\pi < 1.5$ (GeV/c).

The mean transverse mass $\langle m_T \rangle - m_\pi$ is calculated as:

$$\langle m_T \rangle = \frac{v_{meas} + v_{ex}}{w_{meas} + w_{ex}}.$$

The measured part is calculated as:

$$v_{meas} = \sum_{m_{T,min}}^{m_{T,max}} \frac{d^2n}{dy dm_T} m_T \Delta m_T,$$

$$w_{meas} = \sum_{m_{T,min}}^{m_{T,max}} \frac{d^2n}{dy dm_T} \Delta m_T,$$

where Δm_T is the bin size. The extrapolated part is calculated as

$$v_{ex} = \int_{m_{T,max}}^{\infty} f(m_T) m_T dm_T = AT \exp\left(-\frac{m_{T,max}}{T}\right)(m_{T,max}^2 + 2T m_{T,max} + 2T^2),$$

$$w_{ex} = \int_{m_{T,max}}^{\infty} f(m_T) dm_T = AT \exp\left(-\frac{m_{T,max}}{T}\right)(m_{T,max} + T).$$

Half of the difference between $\langle m_T \rangle - m_\pi$ calculated with and without extrapolation (i.e. for $w_{ex} - v_{ex} = 0$) is added in quadrature to the systematic uncertainty of $\langle m_T \rangle - m_\pi$.

Appendix C

Tabulated results

This appendix is devoted to presenting numerical values of previously presented quantities related to π^- mesons produced in inelastic ^{40}Ar+^{45}Sc collisions at 13*A*, 19*A*, 30*A*, 40*A*, 75*A* and 150*A* GeV/*c*. For each value, statistical σ_{stat} and systematic σ_{sys} uncertainties are presented as a percentage of the value.

C.1 Double differential spectra

In this section, numerical values of corrected double differential spectra of π^- mesons in bins of rapidity y and transverse momentum p_T– $d^2n/dydp_T$– are presented. They are equal to the fully corrected bin contents $n^{i,j}_{\text{corr}}[\pi^-]$ defined in equation 5.18 and they are graphically presented in Fig. 7.1. Tables C.1, C.2, C.3, C.4, C.5, C.6 refer to 13*A*, 19*A*, 30*A*, 40*A*, 75*A* and 150*A* GeV/*c*, respectively. The results are publicly available in ROOT format under `https://cernbox.cern.ch/index.php/s/kvweqxTVFH2aJg0`.

TABLE C.1: Tabulated final double-differential spectra $d^2n/dydp_T$ $(GeV/c)^{-1}$ in rapidity y and transverse momentum p_T produced in inelastic $^{40}Ar+^{45}Sc$ collisions at $13A$ (GeV/c) together with statistical and systematic uncertainties.

p_T (GeV/c)		$0.0 < y < 0.2$			$0.2 < y < 0.4$			$0.4 < y < 0.6$			$0.6 < y < 0.8$			$0.8 < y < 1.0$			$1.0 < y < 1.2$		
min	max	$\frac{d^2n}{dydp_T}$	σ_{stat}	σ_{sys}	$\frac{d^2n}{dydp_T}$	σ_{stat}	σ_{sys}	$\frac{d^2n}{dydp_T}$	σ_{stat}	σ_{sys}	$\frac{d^2n}{dydp_T}$	σ_{stat}	σ_{sys}	$\frac{d^2n}{dydp_T}$	σ_{stat}	σ_{sys}	$\frac{d^2n}{dydp_T}$	σ_{stat}	σ_{sys}
0.00	0.05	11.564	1.0	6.5	10.435	1.0	6.5	10.032	1.1	5.9	9.064	1.1	5.7	7.705	1.2	6.1	5.988	1.3	5.9
0.05	0.10	28.739	0.8	3.9	27.674	0.7	3.6	24.137	0.7	3.6	21.976	0.8	3.2	18.683	0.8	3.0	15.276	0.9	2.9
0.10	0.15	38.078	0.7	2.5	36.682	0.7	2.5	35.036	0.7	2.3	30.210	0.7	2.2	25.641	0.7	2.1	22.453	0.8	1.9
0.15	0.20	40.761	0.8	1.6	38.916	0.7	1.6	35.161	0.7	1.6	30.936	0.7	1.6	27.001	0.7	1.5	23.209	0.8	1.5
0.20	0.25	38.848	0.8	1.2	35.493	0.8	1.2	30.956	0.7	1.4	28.248	0.8	1.3	24.346	0.8	1.3	20.430	0.8	1.2
0.25	0.30	32.403	0.9	0.9	29.550	0.8	1.4	26.486	0.8	1.4	23.750	0.8	1.3	20.178	0.9	1.3	16.644	0.9	1.3
0.30	0.35	26.528	1.1	1.2	24.717	0.9	1.5	22.086	0.9	1.4	19.629	0.9	1.3	16.772	1.0	1.3	13.431	1.1	1.2
0.35	0.40	21.540	1.2	1.5	20.208	1.1	1.6	18.403	1.0	1.5	15.963	1.0	1.5	13.769	1.1	1.3	10.521	1.2	1.3
0.40	0.45	17.500	1.3	1.5	16.385	1.2	1.8	14.538	1.1	1.6	12.775	1.1	1.6	10.622	1.2	1.5	8.429	1.4	1.4
0.45	0.50	14.456	1.5	1.6	13.406	1.3	1.8	12.021	1.2	1.7	10.230	1.3	1.7	8.282	1.4	1.6	6.609	1.6	1.4
0.50	0.55	11.317	1.7	1.6	10.909	1.5	2.0	9.850	1.4	1.9	8.245	1.4	1.9	6.680	1.6	1.6	4.996	1.8	1.4
0.55	0.60	9.490	1.8	1.7	8.658	1.7	2.1	7.823	1.6	1.9	6.656	1.6	1.8	5.405	1.8	1.7	3.849	2.1	1.7
0.60	0.65	7.346	2.1	1.9	7.090	1.9	2.3	6.402	1.7	2.0	5.416	1.8	2.1	4.306	2.0	1.8	3.019	2.4	1.6
0.65	0.70	5.998	2.4	2.1	5.539	2.1	2.4	5.064	2.0	2.3	4.236	2.0	2.2	3.228	2.3	2.1	2.343	2.8	1.5
0.70	0.75	4.662	2.7	2.2	4.671	2.4	2.4	4.080	2.2	2.3	3.328	2.3	2.7	2.549	2.6	2.0	1.816	3.2	1.7
0.75	0.80	3.729	3.0	2.5	3.747	2.7	2.6	3.282	2.5	2.5	2.591	2.7	2.6	2.064	3.0	2.3	1.407	3.7	1.7
0.80	0.85	3.097	3.4	2.3	2.744	3.1	2.9	2.687	2.8	2.5	2.133	3.0	2.8	1.577	3.5	2.1	1.020	4.3	1.6
0.85	0.90	2.120	4.0	2.7	2.340	3.4	3.2	2.177	3.2	2.6	1.665	3.4	2.9	1.222	4.0	2.2	0.808	4.9	2.1
0.90	0.95	2.000	4.2	2.6	1.867	3.8	3.2	1.645	3.7	3.0	1.291	3.9	2.6	1.000	4.4	2.3	0.604	5.8	1.8
0.95	1.00	1.593	4.9	2.5	1.443	4.3	2.9	1.274	4.2	3.6	1.075	4.6	2.9	0.763	5.2	2.4	0.504	6.6	2.0
1.00	1.05	1.120	5.9	3.3	1.136	5.0	3.7	0.962	4.9	3.5	0.731	5.0	3.5	0.538	5.9	3.1	0.380	7.9	1.9
1.05	1.10	0.995	6.4	2.8	0.877	5.8	3.7	0.769	5.4	3.8	0.636	5.7	3.4	0.409	7.1	2.7	0.284	9.1	2.1
1.10	1.15	0.683	7.6	3.6	0.722	6.5	4.1	0.636	6.2	3.4	0.419	6.5	3.6	0.318	7.9	3.4	0.178	10.3	2.9
1.15	1.20	0.556	8.4	3.7	0.624	7.0	3.9	0.529	6.9	3.6	0.403	7.5	3.5	0.226	9.1	3.2	0.142	12.8	2.4
1.20	1.25	0.387	11.4	3.4	0.401	9.0	4.2	0.373	8.3	4.3	0.265	8.5	5.0	0.216	10.3	3.6	0.083	15.7	1.7
1.25	1.30	0.360	11.2	3.5	0.360	9.4	4.2	0.260	9.7	3.6	0.200	10.1	4.1	0.160	12.1	3.8	0.120	18.7	3.3
1.30	1.35	0.231	13.5	4.4	0.271	11.4	3.8	0.233	9.8	4.4	0.159	11.8	4.3	0.092	14.1	3.4	0.049	19.6	5.3
1.35	1.40	0.175	16.0	5.0	0.214	11.8	4.1	0.147	11.3	6.6	0.135	12.7	4.4	0.089	15.7	6.9	0.061	30.3	2.0
1.40	1.45	0.145	16.3	4.9	0.122	16.1	4.6	0.159	13.3	4.5	0.069	14.0	7.6	0.038	18.7	6.1	0.019	35.9	1.7
1.45	1.50	0.083	21.7	4.9	0.091	16.3	6.1	0.128	15.1	4.3	0.054	15.8	7.2	0.031	19.8	6.5	0.015	32.1	3.4
1.50	1.55	0.090	18.0	6.6	0.083	19.5	5.4	0.123	16.9	5.3	0.057	18.4	5.0	0.027	21.5	2.7	0.011	55.6	3.5
1.55	1.60	0.055	23.0	6.3	0.072	22.8	5.7	0.066	19.5	6.8	0.033	17.9	9.6	0.028	33.9	13.8	0.003	32.7	11.6
1.60	1.65	0.039	34.5	7.3	0.051	22.0	7.4	0.045	21.9	7.1	0.030	22.6	7.2	0.009	57.0	7.7	0.001	39.7	19.4
1.65	1.70	0.032	30.4	5.9	0.034	23.5	14.6	0.022	26.6	8.7	0.017	31.5	8.3	0.010	42.2	7.5	0.002	83.7	7.3
1.70	1.75	0.025	30.4	8.6	0.030	26.7	8.5	0.024	37.2	7.7	0.010	42.1	20.6	0.004	50.0	7.7	0.004	65.1	9.8
1.75	1.80	0.018	34.6	20.1	0.030	35.3	10.2	0.021	39.7	8.0	0.006	32.1	31.8	0.002	47.9	35.1	0.001	59.2	42.9
1.80	1.85	0.017	33.9	11.0	0.006	34.9	13.7	0.017	32.5	8.6	0.005	34.6	26.1	0.001	48.9	35.9			
1.85	1.90	0.011	76.5	9.9	0.007	29.6	17.7	0.009	25.5	4.2	0.005	34.9	26.6	0.001	60.9	58.9			
1.90	1.95	0.006	26.2	19.3	0.009	61.6	7.7	0.005	45.6	11.4	0.002	38.0	30.1	0.001	84.5	41.2			
1.95	2.00	0.003	42.8	27.9	0.004	61.1	15.6	0.005	29.8	20.9	0.002	43.7	16.3	0.001	69.0	16.2			

p_T (GeV/c)		$1.2 < y < 1.4$			$1.4 < y < 1.6$			$1.6 < y < 1.8$			$1.8 < y < 2.0$			$2.0 < y < 2.2$			$2.2 < y < 2.4$		
min	max	$\frac{d^2n}{dydp_T}$	σ_{stat}	σ_{sys}	$\frac{d^2n}{dydp_T}$	σ_{stat}	σ_{sys}	$\frac{d^2n}{dydp_T}$	σ_{stat}	σ_{sys}	$\frac{d^2n}{dydp_T}$	σ_{stat}	σ_{sys}	$\frac{d^2n}{dydp_T}$	σ_{stat}	σ_{sys}	$\frac{d^2n}{dydp_T}$	σ_{stat}	σ_{sys}
0.00	0.05	5.057	1.4	6.2	4.230	1.5	5.4	3.615	1.6	5.5	2.891	1.9	6.4	1.996	2.2	3.6	1.449	2.7	1.0
0.05	0.10	13.062	0.9	2.5	11.093	1.0	2.1	8.871	1.0	1.9	7.032	1.2	2.1	5.224	1.4	1.4	3.579	1.7	1.1
0.10	0.15	18.461	0.9	1.7	14.288	0.9	1.4	10.638	1.0	1.2	8.348	1.1	1.2	5.797	1.3	1.0	3.706	1.7	1.0
0.15	0.20	19.038	0.9	1.3	14.847	1.0	1.2	10.623	1.1	1.0	7.179	1.2	1.0	4.671	1.5	1.0	2.553	2.2	0.9
0.20	0.25	16.127	1.0	1.2	12.422	1.1	1.2	8.618	1.2	1.0	5.089	1.5	1.0	3.117	1.9	0.9	1.688	2.8	1.0
0.25	0.30	12.905	1.1	1.3	9.490	1.3	1.1	6.146	1.5	1.0	3.688	1.9	0.9	1.897	2.6	0.8	0.920	3.8	0.7
0.30	0.35	9.978	1.3	1.3	7.019	1.5	1.2	4.397	1.8	1.1	2.534	2.4	1.0	1.264	3.3	0.9	0.556	5.3	1.1
0.35	0.40	7.982	1.4	1.2	5.443	1.8	1.1	3.314	2.2	1.0	1.728	2.9	0.9	0.769	4.3	0.9	0.352	7.0	0.7
0.40	0.45	6.019	1.7	1.3	4.000	2.1	1.1	2.232	2.8	1.2	1.159	3.7	0.9	0.483	5.8	0.8	0.137	12.2	1.6
0.45	0.50	4.547	1.9	1.2	2.866	2.5	1.2	1.489	3.4	0.9	0.797	4.7	0.7	0.246	7.8	1.2	0.054	26.9	2.4
0.50	0.55	3.434	2.3	1.1	2.119	3.1	1.1	1.190	4.1	1.1	0.579	5.9	0.9	0.160	11.6	1.3	0.085	65.1	0.7
0.55	0.60	2.558	2.6	1.4	1.596	3.6	1.2	0.790	4.9	1.5	0.308	7.8	1.3	0.075	15.8	2.1	0.004	22.9	10.8
0.60	0.65	1.978	3.1	1.3	1.115	4.2	1.3	0.521	6.2	1.1	0.180	10.4	1.3	0.019	148.2	3.9			
0.65	0.70	1.467	3.7	1.3	0.817	5.2	1.2	0.409	7.7	1.0	0.123	29.1	0.6	0.008	18.6	3.9			
0.70	0.75	1.122	4.2	1.7	0.618	6.3	1.3	0.224	11.8	1.2	0.113	31.9	1.4	0.017	85.9	2.3	0.001	57.7	17.1
0.75	0.80	0.821	4.9	1.5	0.389	8.1	1.5	0.201	16.5	0.8	0.012	29.3	6.3	0.003	60.6	12.6			
0.80	0.85	0.606	6.3	1.6	0.305	11.3	1.2	0.094	24.8	2.1	0.024	44.7	0.8						
0.85	0.90	0.463	7.1	1.4	0.219	15.6	1.5	0.056	36.9	1.1	0.004	24.3	10.1	0.006	80.2	4.0			
0.90	0.95	0.267	9.1	1.7	0.131	16.7	1.4	0.055	51.8	0.7									
0.95	1.00	0.227	9.8	1.8	0.060	22.3	4.7	0.006	69.4	4.3	0.002	0.0	4.2						
1.00	1.05	0.158	12.6	2.9	0.042	46.4	1.8	0.038	97.9	0.6									
1.05	1.10	0.093	14.6	2.2	0.023	47.0	5.2												
1.10	1.15	0.049	20.4	3.4	0.013	71.1	4.0												
1.15	1.20	0.043	29.4	3.0	0.003	26.7	6.0												
1.20	1.25	0.019	33.6	6.6															
1.25	1.30	0.017	47.7	6.3															
1.30	1.35	0.006	74.0	10.6															
1.35	1.40	0.013	0.0	4.0															
1.40	1.45	0.011	123.5	4.7				0.002	50.0	9.8									
1.45	1.50				0.000	0.0	3.6												
1.50	1.55	0.002	0.0	15.2															
1.55	1.60																		
1.60	1.65	0.003	0.0	15.0															
1.65	1.70	0.001	0.0	7.2															
1.70	1.75																		
1.75	1.80																		
1.80	1.85	0.002	0.0	3.6															

p_T (GeV/c)		$2.4 < y < 2.6$			$2.6 < y < 2.8$			$2.8 < y < 3.0$			$3.0 < y < 3.2$		
min	max	$\frac{d^2n}{dydp_T}$	σ_{stat}	σ_{sys}	$\frac{d^2n}{dydp_T}$	σ_{stat}	σ_{sys}	$\frac{d^2n}{dydp_T}$	σ_{stat}	σ_{sys}	$\frac{d^2n}{dydp_T}$	σ_{stat}	σ_{sys}
0.00	0.05	0.968	3.5	1.2	0.521	7.0	1.1	0.109	38.3	0.4			
0.05	0.10	2.130	2.4	1.1	1.052	3.8	1.0	0.437	8.8	0.7	0.123	80.1	0.2
0.10	0.15	1.851	2.6	0.8	0.906	4.2	0.9	0.309	8.6	0.8	0.044	38.8	0.6
0.15	0.20	1.266	3.3	0.8	0.521	5.7	0.8	0.135	12.2	1.0	0.081	108.4	0.5
0.20	0.25	0.684	4.6	1.1	0.204	9.2	1.0	0.042	23.2	1.8	0.006	116.5	3.6
0.25	0.30	0.400	6.4	0.8	0.097	12.9	1.0	0.017	41.5	0.9			
0.30	0.35	0.173	9.7	1.1	0.013	54.2	4.9						
0.35	0.40	0.056	20.2	1.4	0.028	63.8	1.2						
0.40	0.45	0.020	339.8	2.3	0.011	94.5	0.9						
0.45	0.50	0.002	105.2	22.1									
0.50	0.55												
0.55	0.60	0.004	100.0	5.8	0.001	108.0	2.4						

TABLE C.2: Tabulated final double-differential spectra $\mathrm{d}^2n/\mathrm{d}y\mathrm{d}p_\mathrm{T}$ (GeV/c)$^{-1}$ in rapidity y and transverse momentum p_T produced in inelastic ^{40}Ar+^{45}Sc collisions at 19A (GeV/c) together with statistical and systematic uncertainties.

p_T (GeV/c)		$-0.2 < y < 0.0$			$0.0 < y < 0.2$			$0.2 < y < 0.4$			$0.4 < y < 0.6$			$0.6 < y < 0.8$			$0.8 < y < 1.0$		
min	max	$\frac{\mathrm{d}^2n}{\mathrm{d}y\mathrm{d}p_\mathrm{T}}$	σ_stat	σ_sys	$\frac{\mathrm{d}^2n}{\mathrm{d}y\mathrm{d}p_\mathrm{T}}$	σ_stat	σ_sys	$\frac{\mathrm{d}^2n}{\mathrm{d}y\mathrm{d}p_\mathrm{T}}$	σ_stat	σ_sys	$\frac{\mathrm{d}^2n}{\mathrm{d}y\mathrm{d}p_\mathrm{T}}$	σ_stat	σ_sys	$\frac{\mathrm{d}^2n}{\mathrm{d}y\mathrm{d}p_\mathrm{T}}$	σ_stat	σ_sys	$\frac{\mathrm{d}^2n}{\mathrm{d}y\mathrm{d}p_\mathrm{T}}$	σ_stat	σ_sys
0.00	0.05	16.544	1.0	4.8	14.913	1.0	5.2	13.462	1.1	5.9	12.204	1.1	5.1	10.474	1.1	4.5	8.097	1.2	3.9
0.05	0.10	37.246	0.8	4.0	36.310	0.8	4.2	33.380	0.7	4.5	29.731	0.8	4.7	25.562	0.8	4.5	20.620	0.8	4.3
0.10	0.15	46.167	0.8	3.1	46.526	0.7	3.2	45.592	0.7	3.3	40.369	0.7	3.5	34.096	0.7	3.6	30.997	0.8	3.5
0.15	0.20	48.238	0.9	2.3	47.682	0.7	2.6	45.264	0.7	2.7	40.171	0.7	2.9	36.591	0.7	3.0	32.993	0.8	3.0
0.20	0.25	43.338	0.9	1.9	42.952	0.8	2.2	40.354	0.7	2.5	38.433	0.7	2.7	33.837	0.7	2.7	29.901	0.8	2.8
0.25	0.30	36.777	1.0	1.7	36.717	0.9	2.2	34.691	0.8	2.4	32.876	0.8	2.5	29.391	0.8	2.6	25.967	0.8	2.6
0.30	0.35	30.129	1.1	1.8	30.727	1.0	2.3	29.733	0.9	2.4	28.031	0.9	2.5	24.538	0.9	2.6	21.566	0.9	2.6
0.35	0.40	25.255	1.2	1.9	25.211	1.1	2.2	24.400	1.0	2.4	22.347	1.0	2.5	20.610	1.0	2.6	17.336	1.0	2.7
0.40	0.45	20.474	1.4	2.1	21.085	1.2	2.3	19.863	1.1	2.6	19.087	1.1	2.6	16.486	1.1	2.6	14.180	1.2	2.7
0.45	0.50	16.911	1.6	2.1	17.339	1.3	2.5	16.541	1.2	2.6	15.162	1.2	2.7	13.252	1.2	2.8	11.277	1.3	2.9
0.50	0.55	13.683	1.7	2.1	13.902	1.5	2.6	13.718	1.4	2.6	12.663	1.3	2.8	10.909	1.4	2.8	9.345	1.5	2.8
0.55	0.60	11.027	1.9	2.3	11.568	1.7	2.7	11.189	1.5	2.8	10.059	1.5	3.1	9.036	1.6	2.9	7.555	1.7	2.8
0.60	0.65	9.055	2.2	2.3	9.046	1.9	2.9	8.804	1.8	3.0	8.251	1.7	3.1	7.137	1.8	3.2	5.770	2.0	3.1
0.65	0.70	7.572	2.5	2.5	7.326	2.2	3.0	7.162	2.0	3.1	6.804	1.9	3.2	5.775	2.0	3.3	4.758	2.3	2.7
0.70	0.75	6.244	2.8	2.5	5.706	2.5	3.3	5.832	2.3	3.2	5.606	2.2	3.3	4.582	2.3	3.3	3.739	2.6	3.2
0.75	0.80	4.652	3.2	2.6	4.714	2.8	3.6	4.961	2.6	3.4	4.331	2.6	3.6	3.589	2.7	3.5	3.064	3.0	3.1
0.80	0.85	3.659	3.7	2.9	3.713	3.4	3.6	3.690	2.9	3.6	3.483	2.8	3.8	3.078	3.0	3.2	2.511	3.4	3.1
0.85	0.90	3.151	4.2	2.9	3.116	3.8	3.6	2.879	3.5	3.9	2.677	3.2	4.2	2.446	3.4	3.7	1.925	4.0	3.5
0.90	0.95	2.398	4.5	2.9	2.523	4.1	3.5	2.560	3.7	3.5	2.095	3.7	4.1	1.996	4.0	3.7	1.510	4.6	3.3
0.95	1.00	1.824	5.3	3.3	2.089	4.7	3.6	2.169	4.2	3.8	1.892	4.5	4.3	1.522	4.5	3.9	1.188	5.3	3.5
1.00	1.05	1.419	6.6	3.5	1.517	6.1	4.1	1.561	5.1	3.9	1.308	5.1	4.5	1.184	5.2	4.0	1.069	6.0	3.6
1.05	1.10	1.150	7.0	3.4	1.206	6.8	4.3	1.303	5.7	4.4	1.146	5.6	4.4	0.978	6.0	4.1	0.809	6.7	3.7
1.10	1.15	0.939	8.4	3.1	0.871	7.5	4.5	0.884	6.5	4.6	0.897	6.4	4.9	0.733	6.9	3.9	0.550	8.0	4.1
1.15	1.20	0.669	9.1	3.9	0.792	9.4	4.6	0.730	7.3	4.8	0.610	6.9	5.1	0.513	7.7	4.3	0.459	9.0	3.5
1.20	1.25	0.646	10.9	3.2	0.631	9.3	5.0	0.625	8.5	5.3	0.633	8.3	4.6	0.503	9.3	3.6	0.321	11.5	4.0
1.25	1.30	0.424	14.7	4.6	0.471	11.5	4.9	0.560	8.8	4.5	0.395	10.0	4.6	0.331	9.7	4.9	0.262	11.2	4.1
1.30	1.35	0.229	17.9	6.5	0.361	15.3	6.0	0.374	11.6	5.4	0.407	10.3	5.0	0.262	10.6	4.8	0.240	12.9	4.0
1.35	1.40	0.245	17.2	5.0	0.321	16.1	4.8	0.266	14.6	6.3	0.365	12.5	4.3	0.263	12.5	4.5	0.162	15.5	3.8
1.40	1.45	0.217	18.1	3.9	0.150	22.2	8.2	0.261	17.0	4.9	0.168	12.6	6.6	0.184	15.1	3.6	0.124	16.4	3.4
1.45	1.50	0.106	29.1	6.3	0.125	25.3	7.7	0.152	16.6	7.9	0.126	15.7	7.4	0.174	18.4	4.2	0.074	19.3	5.9
1.50	1.55	0.128	24.8	4.9	0.155	19.9	4.6	0.167	19.9	5.5	0.150	18.8	4.1	0.097	16.7	7.3	0.091	28.5	6.0
1.55	1.60	0.084	22.5	4.8	0.118	21.7	5.7	0.078	27.9	6.6	0.106	19.8	4.1	0.050	22.3	7.4	0.051	25.6	6.3
1.60	1.65	0.088	23.9	4.9	0.097	26.6	5.6	0.113	23.1	4.6	0.084	22.4	8.0	0.048	27.8	7.7	0.041	27.9	5.1
1.65	1.70	0.040	43.9	7.6	0.021	53.2	16.0	0.062	64.2	7.1	0.033	39.6	9.3	0.062	49.4	4.5	0.024	42.4	11.4
1.70	1.75	0.036	32.1	8.4	0.052	55.9	7.5	0.069	27.2	5.8	0.095	57.7	4.7	0.023	32.8	14.3	0.033	42.1	1.8
1.75	1.80	0.029	47.7	8.5	0.042	54.3	8.7	0.034	25.9	8.4	0.033	41.8	6.2	0.010	68.9	10.9	0.011	34.7	7.5
1.80	1.85	0.020	82.1	31.7	0.048	44.6	5.8	0.044	30.8	6.4	0.019	47.9	7.6	0.018	49.6	10.3	0.030	122.2	2.1
1.85	1.90	0.008	98.4	10.6	0.012	71.7	13.5	0.035	37.2	5.9	0.017	67.2	8.6	0.014	59.2	9.7	0.009	40.5	10.3
1.90	1.95	0.030	50.3	5.0	0.029	48.1	3.7	0.014	36.2	14.2	0.013	43.6	8.0	0.010	53.6	5.9	0.006	82.8	14.4
1.95	2.00	0.004	185.5	20.8	0.022	48.7	7.4	0.012	82.5	22.9	0.014	55.8	11.3	0.002	35.4	27.5	0.001	99.1	30.2

p_T (GeV/c)		$1.0 < y < 1.2$			$1.2 < y < 1.4$			$1.4 < y < 1.6$			$1.6 < y < 1.8$			$1.8 < y < 2.0$			$2.0 < y < 2.2$		
min	max	$\frac{\mathrm{d}^2n}{\mathrm{d}y\mathrm{d}p_\mathrm{T}}$	σ_stat	σ_sys	$\frac{\mathrm{d}^2n}{\mathrm{d}y\mathrm{d}p_\mathrm{T}}$	σ_stat	σ_sys	$\frac{\mathrm{d}^2n}{\mathrm{d}y\mathrm{d}p_\mathrm{T}}$	σ_stat	σ_sys	$\frac{\mathrm{d}^2n}{\mathrm{d}y\mathrm{d}p_\mathrm{T}}$	σ_stat	σ_sys	$\frac{\mathrm{d}^2n}{\mathrm{d}y\mathrm{d}p_\mathrm{T}}$	σ_stat	σ_sys	$\frac{\mathrm{d}^2n}{\mathrm{d}y\mathrm{d}p_\mathrm{T}}$	σ_stat	σ_sys
0.00	0.05	7.027	1.3	3.8	6.053	1.4	3.5	4.867	1.5	4.1	4.151	1.7	4.1	3.495	1.9	3.9	2.707	2.1	3.4
0.05	0.10	18.057	0.8	3.9	15.186	0.9	3.9	13.285	0.9	3.8	11.061	1.0	3.7	9.101	1.2	3.5	6.892	1.4	3.3
0.10	0.15	26.509	0.8	3.4	21.882	0.8	3.3	17.211	0.9	3.3	14.658	0.9	3.3	11.457	1.1	3.1	8.256	1.3	3.3
0.15	0.20	28.877	0.8	2.9	23.292	0.9	2.8	18.194	0.9	2.9	13.579	1.0	3.1	10.569	1.1	3.1	7.786	1.4	3.0
0.20	0.25	25.984	0.9	2.7	21.214	1.0	2.5	15.973	1.0	2.7	11.384	1.1	3.0	8.296	1.3	3.2	5.764	1.7	3.0
0.25	0.30	21.776	1.0	2.6	17.743	1.1	2.4	13.125	1.1	2.6	9.090	1.3	2.9	6.085	1.5	3.2	3.849	2.1	3.1
0.30	0.35	17.838	1.1	2.6	14.382	1.2	2.5	9.899	1.3	2.5	6.841	1.5	2.9	4.266	2.0	3.0	2.669	2.7	3.1
0.35	0.40	14.640	1.2	2.7	11.441	1.4	2.6	7.945	1.6	2.7	5.151	1.9	2.9	3.069	2.4	3.4	1.666	3.5	3.5
0.40	0.45	11.568	1.4	2.7	9.014	1.6	2.7	6.075	1.8	2.7	3.639	2.3	2.9	2.132	3.1	3.0	1.225	4.6	2.9
0.45	0.50	9.379	1.5	2.8	7.029	1.9	2.6	4.723	2.2	2.8	2.755	2.8	3.1	1.508	3.9	3.4	0.721	6.3	2.9
0.50	0.55	7.486	1.7	2.7	5.726	2.2	2.6	3.424	2.7	2.7	2.088	3.5	2.8	1.076	4.7	3.0	0.576	9.1	2.0
0.55	0.60	5.894	2.0	2.9	4.412	2.5	2.7	2.363	3.3	3.1	1.409	4.0	3.4	0.808	6.0	2.7	0.259	16.1	3.8
0.60	0.65	4.756	2.3	2.8	3.195	3.1	2.6	2.041	3.8	3.0	1.207	5.4	2.8	0.483	7.5	3.4	0.288	20.3	3.1
0.65	0.70	3.549	2.7	3.1	2.523	3.5	3.0	1.506	4.5	2.9	0.790	6.8	2.9	0.356	11.0	2.7	0.100	24.0	3.5
0.70	0.75	2.916	3.1	3.1	1.877	4.2	2.7	1.146	5.3	2.7	0.625	7.6	2.9	0.182	20.9	3.9	0.070	47.0	6.7
0.75	0.80	2.022	3.6	3.4	1.490	5.1	2.8	0.839	6.8	2.3	0.406	9.4	2.6	0.069	43.6	7.5			
0.80	0.85	1.848	4.3	3.1	1.150	5.7	2.9	0.560	8.3	3.3	0.291	12.1	3.9	0.092	39.5	3.3	0.010	19.6	7.9
0.85	0.90	1.276	4.9	3.4	0.822	6.7	3.0	0.349	10.0	3.5	0.151	14.8	4.0	0.089	49.8	2.3			
0.90	0.95	1.123	5.8	3.2	0.668	7.9	2.8	0.355	12.5	2.3	0.200	27.0	1.9	0.052	56.4	3.8			
0.95	1.00	0.864	6.6	3.5	0.466	9.9	3.6	0.248	14.8	3.4	0.052	22.7	5.0	0.011	18.9	7.2	0.005	81.6	6.1
1.00	1.05	0.631	8.0	3.1	0.408	11.3	2.8	0.119	17.2	3.7	0.042	30.4	3.3						
1.05	1.10	0.467	8.8	3.6	0.238	12.4	3.0	0.093	24.8	5.1	0.020	232.9	5.8						
1.10	1.15	0.383	11.3	3.1	0.190	16.4	3.5	0.091	26.9	4.2	0.027	72.6	2.2						
1.15	1.20	0.267	12.3	3.2	0.109	18.0	5.6	0.049	29.6	4.1	0.053	0.0	9.6						
1.20	1.25	0.202	12.4	3.3	0.103	32.6	4.4	0.046	40.5	2.8	0.001	266.6	67.9						
1.25	1.30	0.160	15.4	3.5	0.066	24.2	4.4	0.020	45.3	2.0									
1.30	1.35	0.201	23.5	4.0	0.029	29.2	4.9	0.018	40.8	5.7									
1.35	1.40	0.108	20.8	3.6	0.004	579.5	24.6	0.006	0.0	4.3									
1.40	1.45	0.092	21.5	2.8	0.006	1117.7	75.5												
1.45	1.50	0.111	71.5	3.3	0.001	880.9	39.0												
1.50	1.55	0.009	72.1	20.7	0.003	232.0	23.8	0.003	0.0	6.5									
1.55	1.60	0.012	109.9	12.5	0.001	756.4	63.6	0.002	44.7	4.5									
1.60	1.65	0.003	33.5	21.4	0.000	0.0	65.5												
1.65	1.70	0.021	121.3	2.2	0.005	52.7	3.0												
1.70	1.75	0.006	144.4	12.6															
1.75	1.80	0.005	83.3	16.0															
1.80	1.85	0.005	104.1	1.1															
1.85	1.90																		
1.90	1.95																		
1.95	2.00	0.001	0.0	8.8															

p_T (GeV/c)		$2.2 < y < 2.4$			$2.4 < y < 2.6$			$2.6 < y < 2.8$			$2.8 < y < 3.0$			$3.0 < y < 3.2$		
min	max	$\frac{d^2n}{dydp_T}$	σ_{stat}	σ_{sys}	$\frac{d^2n}{dydp_T}$	σ_{stat}	σ_{sys}	$\frac{d^2n}{dydp_T}$	σ_{stat}	σ_{sys}	$\frac{d^2n}{dydp_T}$	σ_{stat}	σ_{sys}	$\frac{d^2n}{dydp_T}$	σ_{stat}	σ_{sys}
0.00	0.05	1.900	2.5	3.1	1.507	3.1	3.1	1.108	4.5	3.3	0.492	12.8	2.5			
0.05	0.10	4.992	1.6	3.3	3.401	2.1	3.2	2.327	3.1	2.8	1.254	5.9	2.4	0.645	34.0	0.2
0.10	0.15	5.876	1.5	3.3	3.778	2.1	3.1	1.875	3.6	2.9	1.015	7.0	1.8	0.310	20.7	1.3
0.15	0.20	4.933	1.8	3.1	2.637	2.7	2.9	1.184	4.8	2.8	0.539	9.6	2.0	0.133	31.1	2.4
0.20	0.25	3.142	2.4	3.2	1.562	3.8	2.7	0.644	6.9	2.4	0.249	16.0	1.3	0.126	101.1	0.6
0.25	0.30	2.053	3.2	3.1	0.909	5.3	3.0	0.431	10.6	2.1	0.182	38.2	2.0			
0.30	0.35	1.305	4.3	3.0	0.525	7.9	2.1	0.143	27.1	2.3	0.019	85.2	4.1			
0.35	0.40	0.910	5.8	2.3	0.297	11.0	3.5	0.023	80.8	5.8						
0.40	0.45	0.458	8.3	3.2	0.175	22.3	3.6									
0.45	0.50	0.355	15.1	2.6	0.105	40.6	1.8									
0.50	0.55	0.107	23.3	3.9	0.064	93.2	2.1	0.001	57.7	35.9						
0.55	0.60	0.034	42.5	8.7	0.002	28.9	12.3									
0.60	0.65	0.101	90.5	1.4												
0.65	0.70															
0.70	0.75															
0.75	0.80				0.001	57.7	4.5									

TABLE C.3: Tabulated final double-differential spectra $d^2n/dydp_T$ $(GeV/c)^{-1}$ in rapidity y and transverse momentum p_T produced in inelastic $^{40}Ar+^{45}Sc$ collisions at 30A (GeV/c) together with statistical and systematic uncertainties.

p_T (GeV/c)		$-0.4<y<-0.2$			$-0.2<y<0.0$			$0.0<y<0.2$			$0.2<y<0.4$			$0.4<y<0.6$			$0.6<y<0.8$		
min	max	$\frac{d^2n}{dydp_T}$	σ_{stat}	σ_{sys}	$\frac{d^2n}{dydp_T}$	σ_{stat}	σ_{sys}	$\frac{d^2n}{dydp_T}$	σ_{stat}	σ_{sys}	$\frac{d^2n}{dydp_T}$	σ_{stat}	σ_{sys}	$\frac{d^2n}{dydp_T}$	σ_{stat}	σ_{sys}	$\frac{d^2n}{dydp_T}$	σ_{stat}	σ_{sys}
0.00	0.05	22.132	0.7	3.2	20.574	0.6	3.4	18.948	0.7	3.6	17.498	0.7	3.8	14.760	0.8	4.0	10.465	0.8	3.3
0.05	0.10	44.013	0.6	3.0	44.763	0.5	3.0	41.855	0.5	3.1	38.694	0.5	3.4	32.648	0.5	3.7	28.093	0.5	3.3
0.10	0.15	52.376	0.6	2.5	54.122	0.5	2.5	54.590	0.5	2.6	48.859	0.4	2.6	43.523	0.5	2.7	40.617	0.5	2.7
0.15	0.20	53.304	0.6	1.9	54.862	0.5	2.0	53.298	0.5	2.0	48.397	0.5	2.2	46.206	0.5	2.2	43.476	0.5	2.2
0.20	0.25	48.810	0.6	1.6	49.256	0.6	1.7	47.580	0.5	2.2	45.499	0.5	2.0	43.432	0.5	1.9	40.840	0.5	1.9
0.25	0.30	41.644	0.7	1.4	41.683	0.6	2.1	41.639	0.5	2.0	40.304	0.5	1.9	38.401	0.5	1.8	35.424	0.5	1.8
0.30	0.35	33.971	0.8	2.0	35.092	0.7	2.2	35.605	0.6	2.0	34.696	0.6	1.8	32.465	0.6	1.7	29.968	0.6	1.8
0.35	0.40	28.090	0.9	2.2	29.756	0.7	2.2	29.980	0.7	2.1	28.776	0.6	1.9	27.260	0.6	1.8	25.002	0.6	1.8
0.40	0.45	23.224	1.0	2.2	24.814	0.8	2.2	24.859	0.7	2.1	24.251	0.7	2.0	22.501	0.7	1.8	20.952	0.7	1.8
0.45	0.50	19.284	1.1	2.3	20.787	0.9	2.4	20.835	0.8	2.1	20.080	0.8	2.0	18.727	0.8	1.9	17.138	0.8	1.8
0.50	0.55	15.618	1.2	2.4	16.777	1.0	2.4	17.179	0.9	2.2	16.846	0.9	2.0	15.590	0.9	1.9	13.813	0.9	1.9
0.55	0.60	12.761	1.4	2.4	13.710	1.1	2.5	14.274	1.0	2.3	13.880	1.0	2.1	12.518	1.0	2.0	11.171	1.0	2.0
0.60	0.65	10.437	1.5	2.5	11.211	1.3	2.6	11.348	1.2	2.4	11.430	1.1	2.3	10.213	1.1	2.1	9.323	1.2	2.0
0.65	0.70	8.394	1.7	2.5	9.366	1.4	2.7	9.432	1.3	2.5	9.255	1.2	2.3	8.474	1.2	2.1	7.587	1.3	2.1
0.70	0.75	6.991	1.9	2.6	7.521	1.6	2.8	7.677	1.5	2.5	7.570	1.4	2.4	6.761	1.4	2.2	6.085	1.5	2.1
0.75	0.80	5.798	2.1	2.6	6.108	1.8	2.9	6.194	1.6	2.6	6.283	1.5	2.5	5.659	1.6	2.4	5.092	1.6	2.2
0.80	0.85	4.672	2.4	2.5	5.133	2.0	3.0	5.226	1.8	2.7	5.136	1.7	2.5	4.628	1.7	2.4	4.156	1.8	2.2
0.85	0.90	3.766	2.7	2.9	4.125	2.3	3.1	4.214	2.1	2.9	4.116	2.0	2.6	3.830	1.9	2.4	3.500	2.1	2.1
0.90	0.95	3.133	3.1	2.8	3.388	2.6	3.2	3.204	2.3	2.8	3.278	2.2	2.7	3.169	2.2	2.3	2.769	2.4	2.2
0.95	1.00	2.511	3.5	2.9	2.706	2.9	3.2	2.594	2.6	3.0	2.744	2.5	2.7	2.507	2.5	2.4	2.131	2.7	2.4
1.00	1.05	2.208	3.9	2.9	2.312	3.3	3.2	2.234	3.0	3.0	2.112	2.7	2.7	2.118	2.9	2.6	1.743	3.0	2.2
1.05	1.10	1.595	4.3	3.0	1.910	3.7	3.2	1.994	3.2	2.9	1.813	3.0	2.9	1.709	3.2	2.6	1.414	3.5	2.4
1.10	1.15	1.427	4.8	2.8	1.505	4.0	3.6	1.556	3.6	3.0	1.551	3.5	3.0	1.410	3.4	2.5	1.158	3.8	2.5
1.15	1.20	1.046	5.3	3.1	1.086	4.5	3.5	1.157	4.0	3.1	1.234	3.8	2.9	1.141	3.9	2.8	0.905	4.4	2.4
1.20	1.25	0.817	6.2	3.5	0.934	5.3	3.4	0.980	4.7	2.8	0.969	4.3	2.7	0.887	4.6	2.9	0.780	5.1	2.7
1.25	1.30	0.680	7.0	2.8	0.747	6.4	3.6	0.758	5.3	3.1	0.795	5.2	3.1	0.598	5.4	2.9	0.584	5.5	2.9
1.30	1.35	0.520	7.8	3.9	0.639	6.6	3.5	0.657	5.6	3.1	0.694	5.6	3.2	0.581	6.2	2.6	0.521	6.7	2.4
1.35	1.40	0.436	8.5	3.1	0.495	7.5	3.3	0.517	6.2	3.2	0.501	6.0	2.8	0.438	6.7	2.8	0.383	7.4	2.8
1.40	1.45	0.351	10.3	3.5	0.437	8.2	4.0	0.444	7.7	3.3	0.377	6.8	3.3	0.376	7.5	2.9	0.348	8.4	2.8
1.45	1.50	0.277	10.8	3.9	0.334	9.1	3.4	0.350	8.3	2.8	0.318	7.5	2.8	0.287	8.0	2.7	0.229	9.4	3.0
1.50	1.55	0.215	12.6	3.4	0.297	11.8	3.4	0.298	9.1	3.3	0.243	8.8	3.3	0.306	10.0	2.4	0.159	10.9	2.7
1.55	1.60	0.175	15.7	3.6	0.195	12.1	4.0	0.269	10.7	3.3	0.186	9.7	3.0	0.167	11.2	3.2	0.169	11.8	2.6
1.60	1.65	0.152	16.8	3.8	0.192	13.1	3.5	0.172	11.2	3.4	0.172	11.3	4.3	0.162	11.3	4.0	0.175	12.7	2.5
1.65	1.70	0.129	20.5	5.2	0.145	15.2	4.4	0.116	13.2	4.5	0.137	12.8	3.5	0.133	13.4	2.7	0.069	15.1	3.4
1.70	1.75	0.105	19.7	3.6	0.103	18.1	4.6	0.115	15.7	3.4	0.106	14.2	3.9	0.100	13.5	3.0	0.064	16.1	3.2
1.75	1.80	0.069	26.6	5.4	0.097	19.5	3.5	0.105	17.8	2.8	0.072	15.2	3.8	0.062	16.5	3.2	0.061	20.7	3.6
1.80	1.85	0.055	27.0	3.8	0.092	19.2	3.1	0.075	19.0	3.2	0.063	18.4	3.0	0.052	24.1	5.7	0.036	25.1	4.0
1.85	1.90	0.088	34.6	1.9	0.041	23.4	4.9	0.064	22.1	4.9	0.049	20.3	4.4	0.040	19.2	3.9	0.028	21.4	4.4
1.90	1.95	0.020	46.4	5.7	0.037	32.4	4.5	0.033	21.3	5.3	0.022	63.5	5.2	0.022	37.3	5.9	0.029	28.7	3.6
1.95	2.00	0.009	37.7	11.2	0.036	50.6	4.8	0.032	30.3	3.7	0.032	31.8	1.1	0.016	45.1	3.5	0.018	62.3	3.6

p_T (GeV/c)		$0.8<y<1.0$			$1.0<y<1.2$			$1.2<y<1.4$			$1.4<y<1.6$			$1.6<y<1.8$			$1.8<y<2.0$		
min	max	$\frac{d^2n}{dydp_T}$	σ_{stat}	σ_{sys}	$\frac{d^2n}{dydp_T}$	σ_{stat}	σ_{sys}	$\frac{d^2n}{dydp_T}$	σ_{stat}	σ_{sys}	$\frac{d^2n}{dydp_T}$	σ_{stat}	σ_{sys}	$\frac{d^2n}{dydp_T}$	σ_{stat}	σ_{sys}	$\frac{d^2n}{dydp_T}$	σ_{stat}	σ_{sys}
0.00	0.05	9.445	0.8	3.1	8.467	0.8	2.9	7.509	0.9	2.9	6.300	1.0	2.9	5.203	1.1	2.9	4.393	1.2	2.8
0.05	0.10	24.992	0.5	3.1	22.171	0.5	3.0	19.525	0.6	2.8	16.893	0.6	2.8	13.948	0.7	2.6	11.448	0.8	2.3
0.10	0.15	36.304	0.5	2.7	30.682	0.5	2.4	26.205	0.5	2.4	22.826	0.5	2.2	19.129	0.6	2.1	15.255	0.7	2.0
0.15	0.20	40.054	0.5	2.2	33.714	0.5	2.0	28.690	0.5	1.9	22.810	0.5	2.0	19.613	0.6	1.9	15.260	0.7	1.8
0.20	0.25	36.765	0.5	1.9	31.864	0.6	1.9	26.350	0.6	1.7	19.898	0.6	1.8	16.504	0.6	1.8	12.714	0.8	1.7
0.25	0.30	31.840	0.6	1.8	27.935	0.6	1.7	22.465	0.6	1.6	17.298	0.7	1.7	12.957	0.7	1.7	9.895	0.9	1.7
0.30	0.35	26.950	0.6	1.8	23.316	0.7	1.7	18.534	0.7	1.6	14.149	0.8	1.7	10.192	0.8	1.7	7.517	1.0	1.8
0.35	0.40	22.599	0.7	1.8	19.364	0.8	1.7	15.164	0.8	1.6	11.370	0.9	1.6	7.933	1.0	1.7	5.642	1.2	1.7
0.40	0.45	18.423	0.8	1.8	15.692	0.9	1.7	12.112	0.9	1.7	9.002	1.0	1.7	6.247	1.2	1.7	4.109	1.5	1.7
0.45	0.50	14.874	0.9	1.8	13.068	1.0	1.8	9.669	1.0	1.7	7.261	1.2	1.7	4.820	1.4	1.7	3.222	1.8	1.7
0.50	0.55	12.109	1.0	1.8	10.014	1.1	1.8	7.696	1.2	1.7	5.578	1.3	1.6	3.868	1.6	1.6	2.375	2.2	1.6
0.55	0.60	9.661	1.1	1.9	8.298	1.3	1.9	6.190	1.4	1.7	4.470	1.6	1.6	2.804	2.0	1.6	1.715	2.7	1.7
0.60	0.65	8.132	1.3	2.0	6.708	1.5	1.9	4.715	1.6	1.7	3.468	1.9	1.6	2.115	2.4	1.6	1.227	3.4	1.6
0.65	0.70	6.514	1.5	2.1	5.285	1.7	1.9	3.807	1.9	1.8	2.667	2.3	1.7	1.564	2.8	1.6	0.934	4.1	1.3
0.70	0.75	5.401	1.7	2.0	4.280	2.0	1.9	3.033	2.2	1.8	2.109	2.6	1.8	1.337	3.4	1.5	0.642	5.3	1.8
0.75	0.80	4.289	1.9	2.1	3.317	2.3	2.0	2.445	2.6	1.7	1.554	3.2	1.7	0.949	4.1	1.6	0.486	6.4	1.3
0.80	0.85	3.511	2.1	2.0	2.686	2.7	2.0	1.825	3.0	1.7	1.205	3.6	1.7	0.723	4.7	1.4	0.275	8.0	2.0
0.85	0.90	2.701	2.5	2.2	2.212	3.1	2.1	1.400	3.5	2.1	0.992	4.1	1.3	0.480	6.0	1.8	0.228	11.9	1.3
0.90	0.95	2.303	2.8	2.2	1.662	3.4	2.1	1.190	4.0	1.8	0.749	4.9	1.3	0.397	7.7	1.5	0.152	12.3	1.4
0.95	1.00	1.699	3.2	2.1	1.307	4.1	2.2	0.928	4.6	1.8	0.582	6.1	1.5	0.276	8.7	2.2	0.095	18.0	1.8
1.00	1.05	1.436	3.7	2.0	1.088	4.6	2.3	0.660	5.5	1.7	0.410	7.2	2.0	0.187	10.3	2.1	0.071	28.4	2.4
1.05	1.10	1.118	4.1	2.1	0.834	5.1	2.1	0.514	6.1	2.0	0.356	8.3	1.3	0.141	14.4	1.8	0.063	191.7	5.5
1.10	1.15	0.998	4.6	2.3	0.655	5.7	2.1	0.483	7.3	1.6	0.234	10.0	1.5	0.089	15.1	2.0			
1.15	1.20	0.646	5.3	2.3	0.477	6.8	2.2	0.302	8.0	1.8	0.141	11.5	1.7	0.075	30.6	2.1			
1.20	1.25	0.601	6.3	2.5	0.426	7.6	2.5	0.262	9.4	2.1	0.126	13.6	2.1	0.074	38.0	5.1	0.010	0.0	9.2
1.25	1.30	0.473	6.8	2.2	0.320	9.0	2.0	0.209	11.7	2.4	0.124	18.0	1.8	0.050	51.0	6.3	0.002	39.3	7.4
1.30	1.35	0.332	7.9	2.7	0.259	11.6	2.0	0.114	12.4	2.4	0.033	55.1	4.3	0.002	131.6	16.4			
1.35	1.40	0.321	9.1	2.7	0.210	11.4	1.9	0.099	14.1	2.7	0.065	23.1	1.7	0.015	36.4	4.6			
1.40	1.45	0.251	10.4	2.4	0.148	13.9	2.3	0.068	17.1	2.0	0.057	35.3	3.1	0.007	50.8	7.5			
1.45	1.50	0.191	11.1	2.6	0.117	16.9	2.3	0.044	18.2	3.3	0.018	39.9	3.7	0.005	20.4	6.3			
1.50	1.55	0.155	12.7	2.3	0.081	22.5	3.9	0.039	25.7	3.6	0.022	40.1	3.5	0.006	75.6	3.3			
1.55	1.60	0.145	15.7	1.9	0.046	22.2	3.1	0.053	30.5	4.1	0.011	86.8	7.5	0.002	33.3	2.8			
1.60	1.65	0.066	15.4	2.7	0.035	28.0	4.2	0.023	32.9	3.1	0.006	45.5	5.0						
1.65	1.70	0.089	21.0	2.7	0.028	40.1	5.6	0.035	43.7	1.7	0.005	47.9	3.6						
1.70	1.75	0.050	20.0	2.6	0.036	37.8	3.4	0.024	47.4	1.5									
1.75	1.80	0.032	27.3	3.0	0.015	36.1	4.8	0.021	69.2	1.4									
1.80	1.85	0.039	34.7	2.9	0.012	46.4	4.3	0.004	118.2	14.1									
1.85	1.90	0.021	30.5	3.2	0.014	59.9	5.1	0.006	48.8	3.9									
1.90	1.95	0.036	52.2	3.9	0.005	115.0	7.1	0.003	0.0	19.3									
1.95	2.00	0.016	34.8	3.3	0.005	46.8	5.0	0.001	81.6	15.3									

p_T (GeV/c)		$2.0 < y < 2.2$			$2.2 < y < 2.4$			$2.4 < y < 2.6$			$2.6 < y < 2.8$			$2.8 < y < 3.0$			$3.0 < y < 3.2$		
min	max	$\frac{d^2n}{dydp_T}$	σ_{stat}	σ_{sys}	$\frac{d^2n}{dydp_T}$	σ_{stat}	σ_{sys}	$\frac{d^2n}{dydp_T}$	σ_{stat}	σ_{sys}	$\frac{d^2n}{dydp_T}$	σ_{stat}	σ_{sys}	$\frac{d^2n}{dydp_T}$	σ_{stat}	σ_{sys}	$\frac{d^2n}{dydp_T}$	σ_{stat}	σ_{sys}
0.00	0.05	3.635	1.3	2.4	2.781	1.6	2.0	2.040	1.9	1.7	1.599	2.3	1.7	1.098	3.6	3.0	0.589	26.0	0.7
0.05	0.10	9.413	0.9	2.1	6.968	1.0	1.8	5.165	1.2	1.7	3.850	1.5	1.9	2.616	2.4	2.2	1.393	8.1	1.6
0.10	0.15	11.682	0.8	1.8	8.379	0.9	1.8	5.990	1.2	1.7	3.904	1.7	1.9	2.324	2.8	1.6	1.177	9.0	1.2
0.15	0.20	11.411	0.8	1.7	7.840	1.0	1.7	5.160	1.4	1.8	2.969	2.1	1.6	1.518	3.8	1.6	0.616	16.1	0.8
0.20	0.25	9.016	0.9	1.7	5.950	1.2	1.8	3.545	1.8	1.8	1.845	3.1	1.6	0.712	6.3	1.8	0.253	62.6	0.1
0.25	0.30	6.753	1.1	1.7	4.220	1.5	1.7	2.238	2.4	1.5	1.027	4.3	1.4	0.463	9.0	1.4			
0.30	0.35	4.740	1.4	1.7	2.768	2.0	1.7	1.531	3.2	1.6	0.702	6.2	1.2	0.269	17.7	1.2			
0.35	0.40	3.554	1.7	1.6	1.944	2.6	1.6	0.943	4.4	1.2	0.323	9.4	1.3	0.103	41.3	0.8			
0.40	0.45	2.571	2.1	1.6	1.301	3.4	1.5	0.552	6.0	1.0	0.201	14.7	1.3						
0.45	0.50	1.815	2.7	1.6	0.937	4.3	1.3	0.321	8.2	1.3	0.051	44.6	2.0						
0.50	0.55	1.311	3.4	1.4	0.550	5.9	1.2	0.202	12.4	1.5	0.012	13.5	7.9						
0.55	0.60	0.928	4.5	1.7	0.324	8.2	1.0	0.101	22.6	1.8									
0.60	0.65	0.643	5.9	1.4	0.206	11.0	1.4	0.020	10.5	6.6									
0.65	0.70	0.391	7.3	1.5	0.150	19.3	1.1												
0.70	0.75	0.245	9.4	1.4	0.055	20.9	1.8												
0.75	0.80	0.206	14.4	1.4	0.051	58.8	1.2												
0.80	0.85	0.097	20.3	2.3															
0.85	0.90	0.063	32.9	3.1															
0.90	0.95	0.091	90.1	1.1															
0.95	1.00	0.015	0.0	7.0	0.002	35.4	8.3												

TABLE C.4: Tabulated final double-differential spectra $d^2n/dydp_T$ $(\mathrm{GeV}/c)^{-1}$ in rapidity y and transverse momentum p_T produced in inelastic ^{40}Ar+^{45}Sc collisions at 40A (GeV/c) together with statistical and systematic uncertainties.

p_T (GeV/c)		$-0.6<y<-0.4$			$-0.4<y<-0.2$			$-0.2<y<0.0$			$0.0<y<0.2$			$0.2<y<0.4$			$0.4<y<0.6$		
min	max	$\frac{d^2n}{dydp_T}$	σ_{stat}	σ_{sys}	$\frac{d^2n}{dydp_T}$	σ_{stat}	σ_{sys}	$\frac{d^2n}{dydp_T}$	σ_{stat}	σ_{sys}	$\frac{d^2n}{dydp_T}$	σ_{stat}	σ_{sys}	$\frac{d^2n}{dydp_T}$	σ_{stat}	σ_{sys}	$\frac{d^2n}{dydp_T}$	σ_{stat}	σ_{sys}
0.00	0.05	25.435	0.8	3.5	24.488	0.7	3.2	23.141	0.7	3.4	21.962	0.7	3.4	20.028	0.7	3.7	13.297	0.8	3.8
0.05	0.10	45.229	0.6	3.2	47.212	0.6	2.8	47.615	0.5	3.0	45.387	0.5	3.0	40.420	0.5	3.3	34.238	0.5	3.9
0.10	0.15	52.547	0.7	3.1	56.010	0.6	2.6	58.018	0.5	2.5	56.247	0.5	2.5	49.274	0.4	3.0	46.961	0.4	3.0
0.15	0.20	52.342	0.7	3.2	57.713	0.6	2.0	56.804	0.5	2.0	53.299	0.5	2.5	51.598	0.4	2.5	50.656	0.4	2.4
0.20	0.25	47.397	0.8	3.1	51.199	0.6	1.8	50.375	0.5	2.4	49.814	0.5	2.4	48.863	0.5	2.2	46.866	0.5	2.1
0.25	0.30	40.922	0.8	2.8	43.414	0.7	2.4	44.308	0.6	2.4	44.418	0.5	2.4	42.647	0.5	2.1	41.684	0.5	2.0
0.30	0.35	33.103	0.9	2.8	36.557	0.7	2.6	38.080	0.6	2.4	37.925	0.6	2.4	37.118	0.6	2.1	35.635	0.6	2.0
0.35	0.40	27.344	1.0	3.1	30.938	0.8	2.7	31.759	0.7	2.5	31.963	0.7	2.5	31.781	0.6	2.1	30.054	0.6	2.1
0.40	0.45	22.627	1.1	2.9	25.505	0.9	2.7	26.629	0.8	2.7	26.769	0.7	2.6	26.041	0.7	2.2	25.302	0.7	2.1
0.45	0.50	18.644	1.3	3.0	20.999	1.0	2.8	22.136	0.9	2.8	22.293	0.8	2.6	21.931	0.8	2.3	21.001	0.8	2.2
0.50	0.55	15.765	1.4	2.9	17.290	1.2	3.0	18.186	1.0	3.0	18.168	0.9	2.8	18.057	0.9	2.4	17.032	0.9	2.3
0.55	0.60	12.894	1.6	3.0	14.139	1.3	3.1	15.155	1.1	3.1	15.126	1.0	2.8	14.803	1.0	2.5	14.014	1.0	2.4
0.60	0.65	10.209	1.7	3.1	11.680	1.5	3.2	12.396	1.3	3.3	12.344	1.2	3.0	12.349	1.1	2.7	11.615	1.1	2.5
0.65	0.70	8.864	2.0	3.0	9.714	1.7	3.2	9.929	1.4	3.4	10.358	1.3	3.0	10.125	1.3	2.8	9.778	1.3	2.5
0.70	0.75	7.331	2.3	3.0	7.779	1.9	3.4	8.233	1.6	3.5	8.292	1.5	3.1	8.159	1.4	2.9	8.113	1.4	2.6
0.75	0.80	5.426	2.5	3.3	6.398	2.1	3.6	6.703	1.8	3.7	6.765	1.7	3.2	6.768	1.6	3.0	6.427	1.6	2.7
0.80	0.85	4.502	2.9	3.2	5.112	2.3	3.6	5.374	2.1	3.7	5.513	1.9	3.4	5.553	1.8	3.0	5.124	1.8	2.8
0.85	0.90	3.784	3.3	3.3	4.256	2.7	3.7	4.506	2.3	3.9	4.736	2.1	3.5	4.703	2.1	3.1	4.383	2.1	2.8
0.90	0.95	2.917	3.8	3.5	3.266	3.0	4.0	3.876	2.7	3.9	3.888	2.3	3.5	3.799	2.3	3.1	3.546	2.3	2.7
0.95	1.00	2.465	4.0	3.4	2.816	3.3	4.0	3.109	2.9	3.7	3.149	2.7	3.7	3.070	2.6	3.2	2.894	2.6	3.0
1.00	1.05	2.032	4.5	3.3	2.338	3.7	3.8	2.449	3.4	4.0	2.474	3.1	3.7	2.569	2.9	3.1	2.447	3.0	2.9
1.05	1.10	1.510	5.1	3.6	1.823	4.3	4.0	2.027	3.8	4.0	1.944	3.5	3.9	2.007	3.1	3.4	2.025	3.5	3.0
1.10	1.15	1.267	5.8	3.4	1.498	4.8	4.2	1.869	4.1	3.7	1.809	3.8	3.9	1.690	3.5	3.3	1.548	3.8	3.4
1.15	1.20	1.001	6.8	3.7	1.244	5.6	4.4	1.392	4.4	3.9	1.318	4.1	4.4	1.327	3.9	3.6	1.375	4.3	3.1
1.20	1.25	0.909	7.8	3.8	0.995	6.0	4.4	1.084	5.1	4.2	1.200	4.7	4.1	1.129	4.7	3.8	1.120	4.8	2.9
1.25	1.30	0.692	8.4	3.8	0.768	7.0	4.3	0.900	5.8	4.3	0.914	5.3	4.7	0.950	5.5	3.9	0.892	5.4	3.3
1.30	1.35	0.524	9.6	4.2	0.637	7.9	5.0	0.740	6.3	4.4	0.816	5.9	4.0	0.844	5.8	3.4	0.698	6.4	3.0
1.35	1.40	0.415	9.9	3.5	0.496	8.4	4.9	0.621	7.8	4.2	0.627	6.7	4.0	0.608	6.4	3.3	0.599	7.0	3.3
1.40	1.45	0.349	12.1	4.3	0.475	10.0	4.2	0.447	7.8	4.4	0.522	7.6	4.2	0.494	7.8	3.9	0.447	7.4	2.9
1.45	1.50	0.280	13.7	4.3	0.364	11.0	4.6	0.361	9.1	4.7	0.366	7.5	4.8	0.353	8.3	4.0	0.397	8.9	2.9
1.50	1.55	0.232	14.6	3.8	0.316	12.9	4.0	0.427	11.4	3.9	0.262	9.6	4.6	0.341	9.4	3.4	0.306	9.2	3.4
1.55	1.60	0.208	16.8	3.7	0.173	14.5	6.5	0.306	12.1	4.1	0.262	10.3	3.8	0.331	10.7	2.9	0.252	10.3	3.5
1.60	1.65	0.212	26.0	4.7	0.145	18.4	6.2	0.267	14.2	3.5	0.234	11.1	4.1	0.249	12.4	3.9	0.207	12.8	3.5
1.65	1.70	0.131	18.4	4.2	0.188	18.9	4.4	0.231	17.4	4.1	0.208	13.5	4.5	0.179	10.8	3.5	0.143	12.5	4.1
1.70	1.75	0.099	28.9	5.4	0.092	18.6	5.0	0.203	21.0	5.9	0.142	15.3	4.4	0.127	14.4	4.5	0.101	12.4	3.7
1.75	1.80	0.089	34.6	6.6	0.111	22.2	4.0	0.110	15.9	5.1	0.088	17.5	6.0	0.132	17.3	3.9	0.140	20.4	3.8
1.80	1.85	0.065	30.5	4.6	0.057	22.0	5.8	0.094	21.8	5.3	0.113	20.0	3.7	0.145	19.9	2.0	0.106	19.7	2.6
1.85	1.90	0.035	34.5	6.7	0.051	24.9	7.2	0.060	22.6	6.9	0.063	24.4	7.2	0.126	27.4	3.7	0.073	24.0	3.6
1.90	1.95	0.038	48.1	6.6	0.076	38.0	5.5	0.058	22.5	4.0	0.068	27.7	5.0	0.050	20.7	4.9	0.056	24.1	3.7
1.95	2.00	0.031	48.7	4.7	0.035	45.2	8.9	0.040	29.0	5.6	0.037	22.7	6.4	0.060	35.0	5.1	0.066	35.4	4.6

p_T (GeV/c)		$0.6<y<0.8$			$0.8<y<1.0$			$1.0<y<1.2$			$1.2<y<1.4$			$1.4<y<1.6$			$1.6<y<1.8$		
min	max	$\frac{d^2n}{dydp_T}$	σ_{stat}	σ_{sys}	$\frac{d^2n}{dydp_T}$	σ_{stat}	σ_{sys}	$\frac{d^2n}{dydp_T}$	σ_{stat}	σ_{sys}	$\frac{d^2n}{dydp_T}$	σ_{stat}	σ_{sys}	$\frac{d^2n}{dydp_T}$	σ_{stat}	σ_{sys}	$\frac{d^2n}{dydp_T}$	σ_{stat}	σ_{sys}
0.00	0.05	11.725	0.8	3.4	10.491	0.8	3.1	9.825	0.8	3.0	8.458	0.9	3.1	7.275	1.0	3.0	6.178	1.1	2.9
0.05	0.10	31.519	0.5	3.4	28.584	0.5	3.0	25.446	0.5	3.0	22.055	0.5	2.9	19.427	0.6	2.8	16.195	0.7	2.7
0.10	0.15	44.462	0.5	2.9	39.390	0.5	2.5	34.577	0.5	2.5	30.698	0.5	2.4	26.390	0.5	2.3	22.030	0.6	2.2
0.15	0.20	48.233	0.5	2.3	43.572	0.5	2.3	37.582	0.5	1.9	31.782	0.5	2.1	27.747	0.5	2.0	23.080	0.6	1.9
0.20	0.25	44.734	0.5	2.1	41.313	0.5	2.0	34.943	0.5	1.8	29.868	0.5	1.9	24.572	0.5	1.9	20.698	0.6	1.8
0.25	0.30	39.690	0.5	1.9	36.371	0.6	1.8	31.224	0.6	1.8	26.036	0.6	1.8	20.688	0.6	1.9	17.062	0.7	1.8
0.30	0.35	33.505	0.6	1.9	31.240	0.6	1.8	26.027	0.6	1.8	21.985	0.6	1.7	16.689	0.7	1.9	13.463	0.8	1.8
0.35	0.40	28.084	0.6	2.0	25.933	0.7	1.9	22.092	0.7	1.8	18.053	0.7	1.8	13.549	0.8	1.9	10.799	0.9	1.8
0.40	0.45	23.424	0.7	2.0	21.339	0.8	1.9	18.159	0.8	1.9	14.413	0.8	1.8	10.898	0.9	1.9	8.245	1.0	1.9
0.45	0.50	19.877	0.8	2.1	17.547	0.9	1.9	14.639	0.9	1.9	11.884	0.9	1.9	8.697	1.0	2.0	6.520	1.2	1.9
0.50	0.55	15.859	0.9	2.2	14.451	1.0	2.0	11.801	1.1	1.9	9.670	1.1	1.9	6.956	1.2	2.0	5.008	1.4	1.9
0.55	0.60	13.239	1.0	2.2	12.018	1.2	2.0	9.734	1.2	2.0	7.661	1.3	2.0	5.568	1.4	2.0	3.935	1.7	1.9
0.60	0.65	10.813	1.2	2.2	9.545	1.3	2.1	7.763	1.4	2.1	6.147	1.5	2.0	4.413	1.6	2.1	3.167	2.0	1.8
0.65	0.70	8.944	1.3	2.2	7.849	1.5	2.2	6.193	1.6	2.1	4.940	1.7	2.0	3.518	1.9	1.9	2.288	2.4	1.8
0.70	0.75	7.418	1.5	2.3	6.364	1.7	2.2	5.102	1.9	2.1	3.846	2.1	2.1	2.819	2.4	1.9	1.801	2.9	2.0
0.75	0.80	5.869	1.8	2.5	5.220	2.0	2.3	4.017	2.2	2.2	3.065	2.4	2.2	2.147	2.8	1.9	1.436	3.7	1.8
0.80	0.85	4.727	2.0	2.5	4.254	2.3	2.3	3.445	2.5	2.2	2.502	2.7	2.1	1.697	3.0	2.0	1.101	4.2	1.6
0.85	0.90	3.963	2.3	2.6	3.407	2.6	2.5	2.505	3.0	2.3	2.029	3.2	2.2	1.271	3.7	1.9	0.786	5.2	1.8
0.90	0.95	3.166	2.5	2.5	2.788	3.1	2.5	2.107	3.2	2.2	1.551	3.7	2.1	1.002	4.3	1.9	0.633	6.4	1.9
0.95	1.00	2.656	2.9	2.6	2.107	3.3	2.4	1.659	3.7	2.4	1.244	4.4	2.3	0.763	4.7	1.7	0.473	7.8	2.1
1.00	1.05	2.183	3.3	2.7	1.829	3.8	2.5	1.425	4.1	2.1	1.054	4.9	1.8	0.613	5.7	1.7	0.352	8.9	1.5
1.05	1.10	1.777	3.9	2.8	1.478	4.4	2.6	1.086	4.6	2.2	0.804	5.8	2.5	0.435	7.4	2.2	0.254	10.5	1.4
1.10	1.15	1.421	4.0	2.8	1.197	4.8	2.6	0.850	5.7	3.2	0.594	6.5	2.0	0.376	7.9	2.1	0.199	12.1	1.5
1.15	1.20	1.175	4.8	2.8	0.858	5.3	2.8	0.722	6.1	2.5	0.452	6.9	2.3	0.263	9.0	2.1	0.134	16.9	2.9
1.20	1.25	0.911	5.3	3.0	0.793	6.5	2.9	0.549	6.7	2.0	0.386	8.5	2.2	0.167	9.6	2.6	0.103	23.1	2.2
1.25	1.30	0.746	6.1	2.9	0.593	6.8	2.8	0.495	8.4	2.3	0.280	9.1	2.2	0.157	12.4	1.9	0.057	18.9	2.5
1.30	1.35	0.632	7.2	3.2	0.470	7.8	2.4	0.317	9.1	2.2	0.229	10.7	1.8	0.126	21.3	2.5	0.016	66.0	5.1
1.35	1.40	0.531	8.0	2.8	0.359	8.7	2.7	0.284	10.8	2.7	0.166	12.2	2.8	0.064	22.7	2.3	0.018	89.9	3.5
1.40	1.45	0.426	8.7	2.4	0.329	10.6	3.7	0.253	12.2	2.8	0.136	14.9	2.4	0.047	24.1	2.6	0.082	66.5	0.6
1.45	1.50	0.370	10.1	3.0	0.218	12.1	3.2	0.189	12.8	2.2	0.094	19.4	3.6	0.075	23.6	0.8	0.027	63.0	4.8
1.50	1.55	0.248	11.6	3.6	0.233	15.1	2.8	0.148	16.8	3.2	0.049	24.7	2.9	0.022	62.4	3.2	0.016	69.5	5.0
1.55	1.60	0.198	12.4	3.8	0.155	17.1	5.0	0.104	16.0	3.8	0.062	28.2	2.3	0.071	46.5	0.9	0.011	52.6	3.5
1.60	1.65	0.150	12.5	3.2	0.092	22.3	3.5	0.085	28.5	2.4	0.029	30.5	2.9	0.008	56.9	3.1			
1.65	1.70	0.126	15.9	3.7	0.090	13.5	1.8	0.045	30.9	2.9	0.026	45.0	1.6	0.036	63.9	0.8			
1.70	1.75	0.130	20.1	4.0	0.079	23.2	4.3	0.027	39.2	2.8	0.024	38.6	4.4	0.004	75.5	7.7			
1.75	1.80	0.108	23.0	4.3	0.062	29.5	4.5	0.036	56.6	4.0	0.032	92.6	2.7	0.007	53.1	5.0			
1.80	1.85	0.086	26.1	4.2	0.081	35.0	5.7	0.031	22.5	3.1	0.002	104.9	11.5				0.001	0.0	15.5
1.85	1.90	0.060	19.2	3.0	0.035	28.8	3.5	0.017	26.9	3.7	0.006	224.6	3.9	0.000	831.1	120.3			
1.90	1.95	0.043	25.1	2.7	0.015	88.8	5.5	0.038	62.8	5.4	0.006	101.3	11.9						
1.95	2.00	0.031	26.5	4.4	0.035	50.9	2.5	0.018	37.1	1.6	0.002	271.1	5.4	0.002	28.9	5.1			

p_T (GeV/c)		$1.8 < y < 2.0$			$2.0 < y < 2.2$			$2.2 < y < 2.4$			$2.4 < y < 2.6$			$2.6 < y < 2.8$			$2.8 < y < 3.0$		
min	max	$\frac{d^2n}{dydp_T}$	σ_{stat}	σ_{sys}	$\frac{d^2n}{dydp_T}$	σ_{stat}	σ_{sys}	$\frac{d^2n}{dydp_T}$	σ_{stat}	σ_{sys}	$\frac{d^2n}{dydp_T}$	σ_{stat}	σ_{sys}	$\frac{d^2n}{dydp_T}$	σ_{stat}	σ_{sys}	$\frac{d^2n}{dydp_T}$	σ_{stat}	σ_{sys}
0.00	0.05	5.107	1.2	2.8	4.110	1.3	2.7	3.348	1.5	2.3	2.430	1.8	1.9	1.841	2.1	1.9	1.394	2.7	2.0
0.05	0.10	13.337	0.7	2.5	10.927	0.8	2.2	8.490	1.0	2.0	6.243	1.2	1.8	4.531	1.4	1.8	3.235	1.9	2.3
0.10	0.15	17.759	0.7	2.1	14.171	0.8	2.0	10.716	0.9	1.8	7.616	1.1	1.8	5.120	1.4	1.9	3.366	2.2	2.2
0.15	0.20	18.448	0.7	1.8	13.938	0.8	1.7	10.176	0.9	1.7	6.858	1.2	1.7	4.221	1.8	2.0	2.480	3.0	1.9
0.20	0.25	15.845	0.7	1.8	11.423	0.9	1.8	7.980	1.1	1.8	4.978	1.5	2.0	2.937	2.4	1.8	1.467	5.0	1.8
0.25	0.30	12.355	0.8	1.8	8.794	1.0	1.8	5.867	1.3	1.9	3.294	2.0	1.8	1.850	3.5	1.5	0.780	7.6	1.9
0.30	0.35	9.675	0.9	1.7	6.688	1.2	1.8	4.092	1.7	1.8	2.111	2.7	1.7	1.277	4.9	1.7	0.600	15.6	1.3
0.35	0.40	7.691	1.1	1.8	5.030	1.5	1.9	2.965	2.2	1.7	1.558	3.5	1.3	0.718	6.4	1.5	0.178	24.3	1.6
0.40	0.45	5.757	1.3	1.9	3.807	1.8	1.8	2.187	2.8	1.5	1.063	4.9	1.3	0.393	10.4	1.4	0.061	60.0	1.7
0.45	0.50	4.483	1.6	1.8	2.706	2.2	1.8	1.503	3.6	1.3	0.649	6.8	1.5	0.243	19.0	1.9			
0.50	0.55	3.301	1.9	1.9	2.028	2.9	1.6	1.090	4.8	1.3	0.379	9.7	1.7	0.118	34.3	0.9			
0.55	0.60	2.602	2.4	1.7	1.381	3.6	1.7	0.668	6.5	1.4	0.276	14.3	0.9	0.030	0.0	3.8			
0.60	0.65	1.878	2.8	1.8	1.206	4.9	1.4	0.543	10.2	1.5	0.182	21.1	1.3						
0.65	0.70	1.449	3.7	1.7	0.696	5.7	1.6	0.303	11.5	1.0	0.081	49.4	4.8						
0.70	0.75	1.027	4.6	1.9	0.577	7.2	1.3	0.151	17.3	1.6	0.129	94.1	0.5						
0.75	0.80	0.755	5.2	1.7	0.340	10.0	2.1	0.075	31.2	3.2	0.009	13.0	4.5						
0.80	0.85	0.606	7.1	1.7	0.229	14.4	2.0	0.050	161.0	5.5				0.000	57.7	2.9			
0.85	0.90	0.406	7.9	1.5	0.148	23.4	3.6	0.047	55.5	1.4									
0.90	0.95	0.350	11.2	1.7	0.057	31.3	2.4	0.068	90.1	0.8									
0.95	1.00	0.250	13.9	1.4	0.043	50.3	3.4												
1.00	1.05	0.134	13.4	2.1	0.053	84.6	2.6												
1.05	1.10	0.114	25.5	3.4	0.065	87.2	0.4												
1.10	1.15	0.066	25.0	4.2															
1.15	1.20	0.025	27.0	5.5															
1.20	1.25	0.039	46.8	1.0															
1.25	1.30	0.019	64.1	5.1															
1.30	1.35	0.011	36.4	0.9															
1.35	1.40	0.010	53.1	3.1															
1.40	1.45				0.001	40.8	13.8												
1.45	1.50																		
1.50	1.55																		
1.55	1.60																		
1.60	1.65																		
1.65	1.70																		
1.70	1.75																		
1.75	1.80																		
1.80	1.85																		
1.85	1.90	0.000	100.0	2.9															

p_T (GeV/c)		$3.0 < y < 3.2$		
min	max	$\frac{d^2n}{dydp_T}$	σ_{stat}	σ_{sys}
0.00	0.05	0.879	6.1	3.5
0.05	0.10	2.082	4.2	2.5
0.10	0.15	1.666	5.4	2.0
0.15	0.20	0.938	10.4	1.4
0.20	0.25	0.653	34.8	0.4

TABLE C.5: Tabulated final double-differential spectra $d^2n/dydp_T$ $(GeV/c)^{-1}$ in rapidity y and transverse momentum p_T produced in inelastic $^{40}Ar+^{45}Sc$ collisions at 75A (GeV/c) together with statistical and systematic uncertainties.

p_T (GeV/c)		$-0.6 < y < -0.4$			$-0.4 < y < -0.2$			$-0.2 < y < 0.0$			$0.0 < y < 0.2$			$0.2 < y < 0.4$			$0.4 < y < 0.6$		
min	max	$\frac{d^2n}{dydp_T}$	σ_{stat}	σ_{sys}	$\frac{d^2n}{dydp_T}$	σ_{stat}	σ_{sys}	$\frac{d^2n}{dydp_T}$	σ_{stat}	σ_{sys}	$\frac{d^2n}{dydp_T}$	σ_{stat}	σ_{sys}	$\frac{d^2n}{dydp_T}$	σ_{stat}	σ_{sys}	$\frac{d^2n}{dydp_T}$	σ_{stat}	σ_{sys}
0.00	0.05	27.578	0.5	11.4	27.421	0.5	7.5	26.801	0.4	5.2	20.955	0.5	4.6	14.750	0.5	5.0	14.615	0.6	5.2
0.05	0.10	48.962	0.4	6.2	50.137	0.3	4.8	50.598	0.3	4.1	42.736	0.3	4.2	40.321	0.3	4.3	39.529	0.3	4.5
0.10	0.15	59.247	0.4	4.4	61.633	0.3	3.5	56.568	0.3	3.6	55.635	0.3	4.0	55.361	0.3	4.0	53.745	0.3	4.2
0.15	0.20	59.700	0.4	3.4	60.592	0.3	3.2	59.076	0.3	3.4	58.631	0.3	3.3	59.331	0.3	3.8	57.413	0.3	4.2
0.20	0.25	53.714	0.4	3.0	55.128	0.4	2.9	55.603	0.3	3.2	55.454	0.3	3.3	55.877	0.3	3.6	54.456	0.3	3.8
0.25	0.30	47.131	0.5	2.9	48.863	0.4	2.8	49.887	0.4	3.0	49.988	0.3	3.3	49.694	0.3	3.5	48.593	0.3	3.5
0.30	0.35	40.410	0.5	2.7	42.310	0.4	2.8	43.249	0.4	2.9	42.961	0.4	3.2	43.003	0.4	3.3	41.927	0.4	3.4
0.35	0.40	34.225	0.6	2.8	35.854	0.5	2.7	36.761	0.5	3.0	36.974	0.4	3.1	36.716	0.4	3.2	35.883	0.4	3.2
0.40	0.45	28.836	0.6	2.8	29.928	0.5	2.8	30.290	0.5	3.1	30.808	0.5	3.1	30.959	0.5	3.2	30.060	0.5	3.2
0.45	0.50	23.770	0.7	2.9	25.062	0.6	2.9	25.434	0.6	3.1	25.909	0.5	3.2	25.805	0.5	3.2	25.182	0.5	3.2
0.50	0.55	20.107	0.8	3.0	20.883	0.7	3.1	21.291	0.6	3.2	21.457	0.6	3.2	21.415	0.6	3.3	20.912	0.6	3.2
0.55	0.60	16.174	0.8	3.1	17.115	0.8	3.2	17.578	0.7	3.3	17.690	0.7	3.2	17.949	0.6	3.2	17.206	0.7	3.2
0.60	0.65	13.322	0.9	3.2	14.115	0.8	3.3	14.550	0.8	3.4	14.676	0.7	3.3	14.700	0.7	3.3	14.254	0.7	3.3
0.65	0.70	11.070	1.1	3.4	11.707	0.9	3.5	12.062	0.9	3.4	12.361	0.8	3.4	12.309	0.8	3.4	11.749	0.8	3.3
0.70	0.75	9.100	1.2	3.5	9.533	1.0	3.6	10.037	1.0	3.5	10.259	0.9	3.4	10.290	0.9	3.4	9.668	0.9	3.4
0.75	0.80	7.478	1.3	3.5	7.869	1.2	3.6	8.340	1.1	3.5	8.413	1.0	3.5	8.371	1.0	3.5	8.094	1.0	3.5
0.80	0.85	6.243	1.5	3.7	6.635	1.3	3.9	6.813	1.2	3.7	6.947	1.1	3.5	6.797	1.1	3.6	6.636	1.2	3.6
0.85	0.90	4.977	1.6	3.8	5.171	1.4	4.0	5.607	1.3	3.8	5.755	1.2	3.6	5.663	1.2	3.8	5.396	1.3	3.5
0.90	0.95	4.296	1.8	3.8	4.322	1.6	4.1	4.637	1.5	3.8	4.657	1.4	3.7	4.724	1.4	3.7	4.502	1.4	3.7
0.95	1.00	3.355	2.0	3.9	3.611	1.8	4.1	3.874	1.6	3.9	4.043	1.5	3.7	3.871	1.5	3.7	3.664	1.6	3.8
1.00	1.05	2.788	2.2	3.9	2.997	2.0	4.3	3.213	1.8	4.0	3.192	1.7	3.8	3.131	1.7	3.8	3.071	1.8	3.7
1.05	1.10	2.267	2.5	4.1	2.299	2.2	4.4	2.583	2.0	4.2	2.586	1.9	3.9	2.500	1.9	4.0	2.490	2.0	3.8
1.10	1.15	1.820	2.8	4.3	2.133	2.4	4.2	2.193	2.1	4.1	2.178	2.0	4.1	2.121	2.1	4.0	2.017	2.2	3.8
1.15	1.20	1.514	3.0	4.2	1.672	2.7	4.3	1.880	2.4	4.1	1.763	2.3	4.2	1.691	2.3	3.9	1.606	2.5	3.7
1.20	1.25	1.285	3.4	4.4	1.400	2.9	4.4	1.476	2.7	4.3	1.516	2.5	4.0	1.402	2.6	4.1	1.367	2.7	3.8
1.25	1.30	1.017	3.9	4.3	1.131	3.2	4.4	1.197	3.0	4.5	1.323	2.8	4.1	1.170	2.9	3.9	1.108	3.1	4.0
1.30	1.35	0.791	4.2	4.6	0.929	3.5	4.6	0.977	3.2	4.6	1.023	3.1	4.2	0.966	3.2	4.1	0.929	3.4	4.0
1.35	1.40	0.645	4.7	4.8	0.801	4.0	4.4	0.771	3.6	4.5	0.781	3.5	4.4	0.812	3.5	4.6	0.743	3.7	4.2
1.40	1.45	0.570	5.2	4.7	0.597	4.4	4.7	0.692	4.1	4.5	0.671	4.0	4.5	0.654	3.9	4.6	0.650	4.1	4.2
1.45	1.50	0.489	6.1	5.1	0.526	4.9	4.7	0.534	4.6	4.4	0.532	4.3	4.6	0.523	4.3	4.6	0.513	4.5	4.0
1.50	1.55	0.386	6.3	5.0	0.434	5.4	4.6	0.464	5.0	4.7	0.487	4.7	4.3	0.407	4.7	4.8	0.415	5.1	4.3
1.55	1.60	0.349	7.0	5.0	0.328	6.1	4.9	0.373	5.6	4.9	0.377	5.2	4.3	0.356	5.2	4.3	0.343	5.6	4.1
1.60	1.65	0.243	7.9	4.6	0.291	6.6	5.0	0.294	6.4	5.1	0.291	5.9	5.1	0.288	5.8	4.5	0.283	6.2	4.6
1.65	1.70	0.212	9.1	4.9	0.253	7.3	5.2	0.262	6.9	4.8	0.243	6.4	4.6	0.261	6.4	4.1	0.200	7.3	4.8
1.70	1.75	0.162	9.8	5.0	0.160	9.5	4.8	0.216	7.5	4.8	0.200	6.6	5.2	0.218	7.2	4.7	0.198	8.1	4.2
1.75	1.80	0.133	11.2	5.5	0.139	9.8	5.7	0.165	8.5	4.9	0.209	8.0	5.0	0.171	8.2	4.4	0.159	8.7	5.0
1.80	1.85	0.103	14.1	4.9	0.134	10.5	4.6	0.128	9.0	4.9	0.129	8.8	4.5	0.131	8.7	4.1	0.112	9.0	4.3
1.85	1.90	0.085	15.8	5.3	0.103	12.1	5.1	0.119	10.0	5.1	0.105	9.7	5.4	0.109	9.8	5.5	0.124	10.4	4.9
1.90	1.95	0.086	15.0	5.3	0.092	12.9	5.8	0.092	11.8	4.9	0.085	11.1	6.0	0.089	11.1	5.3	0.072	12.1	5.1
1.95	2.00	0.056	18.1	5.9	0.080	13.5	5.0	0.066	12.0	5.4	0.083	13.1	4.7	0.079	12.4	5.6	0.062	13.6	5.3

p_T (GeV/c)		$0.6 < y < 0.8$			$0.8 < y < 1.0$			$1.0 < y < 1.2$			$1.2 < y < 1.4$			$1.4 < y < 1.6$			$1.6 < y < 1.8$		
min	max	$\frac{d^2n}{dydp_T}$	σ_{stat}	σ_{sys}	$\frac{d^2n}{dydp_T}$	σ_{stat}	σ_{sys}	$\frac{d^2n}{dydp_T}$	σ_{stat}	σ_{sys}	$\frac{d^2n}{dydp_T}$	σ_{stat}	σ_{sys}	$\frac{d^2n}{dydp_T}$	σ_{stat}	σ_{sys}	$\frac{d^2n}{dydp_T}$	σ_{stat}	σ_{sys}
0.00	0.05	14.249	0.6	4.6	13.075	0.6	4.3	11.580	0.6	4.2	10.491	0.6	4.1	9.332	0.7	4.2	8.152	0.7	4.1
0.05	0.10	37.796	0.4	4.6	35.289	0.4	4.1	31.482	0.4	4.0	28.220	0.4	3.9	25.133	0.4	4.0	21.925	0.4	3.9
0.10	0.15	51.150	0.3	4.7	47.149	0.3	3.9	43.587	0.3	3.6	38.761	0.3	3.6	33.847	0.3	3.6	29.359	0.4	3.5
0.15	0.20	53.429	0.3	4.0	50.600	0.3	3.4	46.022	0.3	3.4	41.697	0.3	3.3	36.253	0.3	3.3	30.586	0.4	3.3
0.20	0.25	51.643	0.3	3.6	47.290	0.3	3.2	42.296	0.3	3.5	39.328	0.3	3.2	33.455	0.4	3.2	28.112	0.4	3.2
0.25	0.30	46.904	0.3	3.4	41.928	0.4	3.0	37.340	0.3	3.3	34.292	0.4	3.2	29.320	0.4	3.2	24.425	0.4	3.3
0.30	0.35	40.328	0.4	3.3	36.051	0.4	3.0	32.100	0.4	3.2	28.525	0.4	3.4	24.580	0.4	3.3	20.102	0.5	3.3
0.35	0.40	34.295	0.4	3.2	30.770	0.4	2.9	27.189	0.4	3.2	23.777	0.4	3.4	20.239	0.5	3.3	16.258	0.5	3.5
0.40	0.45	28.809	0.5	3.1	25.529	0.5	3.0	22.450	0.5	3.3	19.406	0.5	3.5	16.702	0.5	3.4	13.144	0.6	3.5
0.45	0.50	24.199	0.5	3.1	21.014	0.5	3.0	18.741	0.5	3.3	15.817	0.5	3.5	13.696	0.6	3.5	10.499	0.7	3.5
0.50	0.55	19.713	0.6	3.1	17.650	0.6	3.1	15.313	0.6	3.4	12.981	0.6	3.6	10.862	0.7	3.6	8.536	0.8	3.5
0.55	0.60	16.254	0.7	3.1	14.333	0.7	3.2	12.702	0.6	3.4	10.580	0.7	3.7	8.790	0.7	3.6	6.730	0.9	3.6
0.60	0.65	13.335	0.8	3.2	11.987	0.7	3.2	10.312	0.7	3.5	8.554	0.8	3.8	7.023	0.8	3.8	5.359	1.0	3.7
0.65	0.70	11.060	0.9	3.3	9.747	0.8	3.3	8.359	0.8	3.5	6.993	0.8	3.9	5.625	0.9	3.7	4.280	1.1	3.7
0.70	0.75	9.032	1.0	3.3	7.876	0.9	3.4	6.873	0.9	3.6	5.622	0.9	3.9	4.571	1.1	3.9	3.364	1.2	3.7
0.75	0.80	7.484	1.1	3.4	6.515	1.0	3.4	5.525	1.0	3.6	4.493	1.1	4.1	3.625	1.2	4.0	2.690	1.4	3.8
0.80	0.85	6.197	1.2	3.3	5.392	1.1	3.5	4.413	1.2	3.8	3.594	1.2	4.2	2.864	1.4	3.9	2.098	1.6	3.9
0.85	0.90	5.086	1.3	3.4	4.396	1.3	3.4	3.641	1.3	3.8	2.865	1.4	4.0	2.259	1.5	4.1	1.610	1.9	3.9
0.90	0.95	4.227	1.5	3.4	3.642	1.4	3.6	2.941	1.4	3.8	2.299	1.5	4.1	1.848	1.7	4.0	1.266	2.2	3.9
0.95	1.00	3.408	1.7	3.5	2.852	1.6	3.7	2.427	1.6	3.7	1.870	1.7	4.2	1.392	2.0	4.2	0.982	2.5	3.6
1.00	1.05	2.763	1.9	3.4	2.382	1.8	3.6	1.957	1.8	3.9	1.523	1.9	4.1	1.164	2.3	4.1	0.788	2.9	3.8
1.05	1.10	2.281	2.1	3.7	1.923	2.0	3.8	1.574	2.0	3.9	1.236	2.1	4.2	0.930	2.6	4.1	0.624	3.3	3.6
1.10	1.15	1.807	2.3	3.7	1.509	2.3	3.9	1.312	2.3	4.1	0.933	2.5	4.3	0.692	2.9	3.9	0.445	3.8	4.1
1.15	1.20	1.535	2.5	3.6	1.273	2.5	3.9	1.020	2.5	4.1	0.801	2.8	4.2	0.537	3.4	4.2	0.354	4.4	3.7
1.20	1.25	1.265	2.9	3.7	1.013	2.8	3.9	0.836	2.9	3.9	0.647	3.1	4.0	0.429	3.9	4.0	0.250	5.1	4.1
1.25	1.30	1.018	3.2	3.8	0.790	3.2	4.0	0.650	3.2	4.4	0.478	3.5	4.4	0.357	4.2	3.9	0.193	5.8	4.0
1.30	1.35	0.830	3.6	3.8	0.740	3.5	4.0	0.554	3.5	4.0	0.433	3.8	4.1	0.293	4.7	3.7	0.149	6.8	4.2
1.35	1.40	0.657	3.9	4.1	0.536	3.8	4.1	0.421	4.0	4.5	0.307	4.5	4.2	0.220	5.4	3.8	0.116	7.5	4.4
1.40	1.45	0.544	4.5	4.0	0.440	4.4	4.2	0.352	4.3	4.0	0.262	4.8	4.2	0.158	6.2	3.9	0.081	9.2	5.4
1.45	1.50	0.422	5.1	4.0	0.363	4.9	4.4	0.289	4.8	4.2	0.261	5.5	3.9	0.129	6.9	4.4	0.069	9.7	4.1
1.50	1.55	0.385	5.6	4.4	0.318	5.5	4.5	0.222	5.5	4.5	0.163	6.2	4.0	0.091	8.4	5.2	0.054	12.8	4.4
1.55	1.60	0.327	6.2	3.9	0.240	5.7	4.0	0.164	6.4	4.8	0.115	7.0	4.4	0.080	9.3	4.6	0.045	13.6	4.2
1.60	1.65	0.236	6.8	4.1	0.201	6.5	4.5	0.146	7.0	4.4	0.094	7.9	4.4	0.059	10.5	3.2	0.026	16.2	4.8
1.65	1.70	0.193	7.7	4.5	0.167	7.6	4.8	0.137	7.6	4.2	0.076	9.4	4.5	0.044	10.7	4.4	0.026	18.0	2.6
1.70	1.75	0.169	8.4	4.3	0.124	8.2	5.0	0.087	9.1	3.7	0.078	10.5	4.6	0.038	13.4	4.5	0.020	25.7	4.4
1.75	1.80	0.124	9.3	4.8	0.116	9.0	4.2	0.069	10.4	4.8	0.041	10.9	4.2	0.028	13.4	4.4	0.008	33.5	4.0
1.80	1.85	0.113	9.8	4.1	0.074	9.9	3.7	0.061	10.6	4.9	0.043	12.3	5.5	0.016	18.9	5.1	0.011	27.8	5.7
1.85	1.90	0.081	10.9	4.2	0.058	10.6	4.7	0.047	13.1	5.2	0.025	16.4	6.7	0.014	19.9	5.3	0.007	35.7	7.7
1.90	1.95	0.068	11.6	4.1	0.049	13.5	4.2	0.032	12.3	5.0	0.021	19.2	6.6	0.013	27.7	4.4	0.002	56.3	6.3
1.95	2.00	0.045	13.3	5.9	0.045	13.8	4.9	0.030	14.9	4.8	0.011	28.4	6.9	0.004	37.6	10.4	0.005	40.7	3.8

p_T (GeV/c)		$1.8 < y < 2.0$			$2.0 < y < 2.2$			$2.2 < y < 2.4$		
min	max	$\frac{d^2n}{dydp_T}$	σ_{stat}	σ_{sys}	$\frac{d^2n}{dydp_T}$	σ_{stat}	σ_{sys}	$\frac{d^2n}{dydp_T}$	σ_{stat}	σ_{sys}
0.00	0.05	6.889	0.8	3.9	5.801	0.9	3.9	4.660	0.9	3.8
0.05	0.10	18.290	0.5	3.7	15.127	0.5	3.6	12.210	0.6	3.6
0.10	0.15	24.655	0.4	3.4	20.106	0.5	3.4	16.043	0.5	3.4
0.15	0.20	25.161	0.4	3.3	20.344	0.5	3.4	15.970	0.5	3.4
0.20	0.25	22.730	0.4	3.2	17.803	0.5	3.4	13.358	0.6	3.4
0.25	0.30	19.271	0.5	3.3	14.462	0.6	3.5	10.506	0.7	3.4
0.30	0.35	15.645	0.5	3.4	11.622	0.6	3.4	8.164	0.8	3.4
0.35	0.40	12.713	0.6	3.5	9.097	0.7	3.4	6.144	0.9	3.5
0.40	0.45	9.955	0.7	3.4	6.978	0.8	3.4	4.623	1.1	3.6
0.45	0.50	7.978	0.8	3.6	5.530	1.0	3.7	3.507	1.3	3.7
0.50	0.55	6.242	0.9	3.6	4.254	1.1	3.6	2.595	1.6	3.4
0.55	0.60	4.870	1.0	3.6	3.257	1.4	3.6	1.889	2.1	3.3
0.60	0.65	3.905	1.2	3.7	2.559	1.6	3.5	1.432	2.5	3.0
0.65	0.70	2.991	1.4	3.7	1.875	1.9	3.3	1.062	3.2	2.9
0.70	0.75	2.326	1.6	3.7	1.396	2.4	3.3	0.703	4.0	2.9
0.75	0.80	1.730	1.9	3.6	1.048	2.8	3.6	0.531	5.0	2.7
0.80	0.85	1.384	2.2	3.5	0.787	3.4	3.3	0.379	5.8	2.5
0.85	0.90	1.061	2.6	3.4	0.574	4.0	3.3	0.270	7.0	2.8
0.90	0.95	0.829	3.0	3.7	0.444	5.0	3.0	0.185	9.6	3.0
0.95	1.00	0.599	3.6	3.5	0.272	6.2	3.7	0.107	10.9	2.7
1.00	1.05	0.456	4.0	4.0	0.217	6.8	3.5	0.076	14.9	3.3
1.05	1.10	0.363	4.7	3.5	0.137	8.8	3.2	0.050	19.5	3.9
1.10	1.15	0.272	5.8	3.3	0.109	9.9	4.3	0.036	22.0	5.3
1.15	1.20	0.180	6.9	3.8	0.085	13.1	4.7	0.025	36.4	7.2
1.20	1.25	0.132	7.4	3.5	0.053	15.3	3.3	0.017	38.6	5.2
1.25	1.30	0.096	8.7	3.8	0.035	18.7	4.7	0.010	37.8	3.4
1.30	1.35	0.098	9.7	3.9	0.031	23.3	3.7	0.017	61.7	6.0
1.35	1.40	0.063	12.5	3.9	0.014	30.2	4.3	0.003	90.4	8.2
1.40	1.45	0.029	17.9	5.4	0.007	28.8	8.2	0.009	0.0	23.1
1.45	1.50	0.030	21.4	4.6	0.007	44.9	5.8	0.006	0.0	24.3
1.50	1.55	0.018	19.1	4.4	0.004	67.6	6.5	0.002	124.5	9.1
1.55	1.60	0.013	26.1	7.6	0.005	63.3	4.2	0.002	95.7	4.4
1.60	1.65	0.009	26.8	5.3	0.002	58.7	4.9	0.000	0.0	5.8
1.65	1.70	0.010	43.1	5.0	0.002	142.5	4.1			
1.70	1.75	0.002	73.9	12.6	0.001	115.8	9.8			
1.75	1.80	0.005	44.4	4.6	0.002	116.5	0.6			
1.80	1.85	0.002	136.8	8.9	0.001	40.8	17.1			
1.85	1.90	0.004	47.7	3.3	0.001	129.1	1.3			
1.90	1.95	0.000	906.7	13.0						
1.95	2.00	0.000	388.1	15.6	0.001	134.2	0.8			

p_T (GeV/c)		$2.4 < y < 2.6$			$2.6 < y < 2.8$			$2.8 < y < 3.0$		
min	max	$\frac{d^2n}{dydp_T}$	σ_{stat}	σ_{sys}	$\frac{d^2n}{dydp_T}$	σ_{stat}	σ_{sys}	$\frac{d^2n}{dydp_T}$	σ_{stat}	σ_{sys}
0.00	0.05	3.872	1.1	3.8	2.964	1.3	3.4	2.083	1.5	3.4
0.05	0.10	9.661	0.7	3.6	7.365	0.8	3.3	5.202	1.0	3.3
0.10	0.15	12.245	0.6	3.4	9.017	0.7	3.2	6.319	0.9	3.2
0.15	0.20	11.825	0.6	3.2	8.234	0.8	3.2	5.534	1.0	3.6
0.20	0.25	9.413	0.7	3.2	6.231	0.9	3.5	4.005	1.4	3.7
0.25	0.30	7.160	0.8	3.3	4.625	1.1	3.7	2.759	1.9	3.1
0.30	0.35	5.159	1.0	3.7	3.227	1.5	3.2	1.924	3.1	2.5
0.35	0.40	3.855	1.3	3.7	2.263	2.0	3.0	1.306	5.7	1.8
0.40	0.45	2.911	1.7	3.3	1.648	2.8	2.6	1.059	13.8	0.8
0.45	0.50	2.061	2.0	3.1	1.103	4.0	2.5	1.089	80.1	0.0
0.50	0.55	1.528	2.7	2.7	0.767	6.1	2.1			
0.55	0.60	1.071	3.5	2.7	0.540	10.3	2.0			
0.60	0.65	0.793	4.4	2.4	0.302	15.8	1.2			
0.65	0.70	0.472	5.8	2.5	0.205	33.6	3.9			
0.70	0.75	0.317	7.5	2.1	0.296	75.3	0.4			
0.75	0.80	0.224	10.4	2.0						
0.80	0.85	0.115	13.1	3.8						
0.85	0.90	0.078	18.9	3.5						
0.90	0.95	0.050	31.2	3.3						
0.95	1.00	0.054	58.2	3.0						
1.00	1.05	0.017	72.7	9.6						
1.05	1.10	0.002	69.7	7.7						
1.10	1.15	0.003	0.0	9.6						
1.15	1.20									
1.20	1.25									
1.25	1.30									
1.30	1.35									
1.35	1.40									
1.40	1.45									
1.45	1.50									
1.50	1.55									
1.55	1.60									
1.60	1.65									
1.65	1.70									
1.70	1.75									
1.75	1.80									
1.80	1.85									
1.85	1.90									
1.90	1.95									
1.95	2.00									

p_T (GeV/c)		$3.0 < y < 3.2$			$3.2 < y < 3.4$			$3.4 < y < 3.6$		
min	max	$\frac{d^2n}{dydp_T}$	σ_{stat}	σ_{sys}	$\frac{d^2n}{dydp_T}$	σ_{stat}	σ_{sys}	$\frac{d^2n}{dydp_T}$	σ_{stat}	σ_{sys}
0.00	0.05	1.593	1.8	3.2	1.155	2.3	4.4	0.871	10.0	2.1
0.05	0.10	3.799	1.2	3.3	2.588	1.7	5.2	3.244	13.5	1.4
0.10	0.15	4.315	1.2	3.8	2.766	2.7	3.4			
0.15	0.20	3.429	1.7	3.8	1.711	8.2	1.5			
0.20	0.25	2.235	3.1	2.6						
0.25	0.30	1.488	8.6	1.2						
0.30	0.35	2.549	115.5	0.0						

TABLE C.6: Tabulated final double-differential spectra $\mathrm{d}^2n/\mathrm{d}y\mathrm{d}p_\mathrm{T}$ $(\mathrm{GeV}/c)^{-1}$ in rapidity y and transverse momentum p_T produced in inelastic ^{40}Ar+^{45}Sc collisions at 150A (GeV/c) together with statistical and systematic uncertainties.

p_T (GeV/c)		$-0.4<y<-0.2$			$-0.2<y<0.0$			$0.0<y<0.2$			$0.2<y<0.4$			$0.4<y<0.6$			$0.6<y<0.8$		
min	max	$\frac{\mathrm{d}^2n}{\mathrm{d}y\mathrm{d}p_\mathrm{T}}$	σ_stat	σ_sys	$\frac{\mathrm{d}^2n}{\mathrm{d}y\mathrm{d}p_\mathrm{T}}$	σ_stat	σ_sys	$\frac{\mathrm{d}^2n}{\mathrm{d}y\mathrm{d}p_\mathrm{T}}$	σ_stat	σ_sys	$\frac{\mathrm{d}^2n}{\mathrm{d}y\mathrm{d}p_\mathrm{T}}$	σ_stat	σ_sys	$\frac{\mathrm{d}^2n}{\mathrm{d}y\mathrm{d}p_\mathrm{T}}$	σ_stat	σ_sys	$\frac{\mathrm{d}^2n}{\mathrm{d}y\mathrm{d}p_\mathrm{T}}$	σ_stat	σ_sys
0.00	0.05	20.652	1.3	15.9	15.825	1.1	14.4	15.987	1.0	9.4	16.589	0.9	5.6	15.867	1.0	5.1	15.811	1.0	5.0
0.05	0.10	44.299	0.7	16.3	44.996	0.6	8.9	45.994	0.6	5.4	46.165	0.6	4.2	43.706	0.6	4.1	43.125	0.6	4.4
0.10	0.15	60.052	0.5	7.4	62.341	0.5	4.9	63.247	0.5	3.6	60.930	0.5	3.4	61.447	0.5	3.5	58.177	0.5	3.8
0.15	0.20	65.894	0.5	4.1	65.607	0.5	3.8	66.922	0.5	3.0	65.522	0.5	2.9	64.520	0.5	3.2	61.224	0.5	3.6
0.20	0.25	61.917	0.6	3.2	62.220	0.5	3.0	62.758	0.5	3.0	63.137	0.5	2.8	60.178	0.5	3.3	58.869	0.6	3.8
0.25	0.30	56.010	0.6	3.0	55.878	0.6	2.7	56.529	0.5	3.0	56.601	0.5	3.0	54.017	0.6	3.6	53.751	0.6	3.1
0.30	0.35	49.225	0.7	3.1	48.917	0.6	2.8	48.890	0.6	2.9	48.783	0.6	3.3	46.372	0.6	3.7	47.545	0.6	2.5
0.35	0.40	41.166	0.7	3.0	41.322	0.7	2.8	41.742	0.6	3.0	41.255	0.6	3.5	40.677	0.7	3.3	40.375	0.7	2.5
0.40	0.45	34.547	0.8	3.0	35.122	0.7	3.0	34.937	0.7	3.1	35.075	0.7	3.5	33.958	0.7	3.0	33.642	0.7	2.5
0.45	0.50	28.910	0.9	3.1	29.714	0.8	3.3	29.294	0.8	3.3	29.703	0.8	3.5	28.524	0.8	3.0	27.874	0.8	2.5
0.50	0.55	23.953	1.0	3.3	24.632	0.9	3.5	24.074	0.9	3.3	24.429	0.9	3.5	23.735	0.9	3.2	23.285	0.9	2.7
0.55	0.60	20.055	1.1	3.4	20.412	1.0	3.7	20.463	1.0	3.5	20.351	1.0	3.5	19.885	1.0	3.2	19.447	1.0	2.9
0.60	0.65	16.474	1.2	3.6	16.376	1.1	3.7	16.805	1.1	3.6	16.583	1.1	3.6	16.063	1.1	3.3	15.770	1.1	3.0
0.65	0.70	13.501	1.3	3.7	13.689	1.2	3.6	13.636	1.2	3.6	13.868	1.2	3.7	13.525	1.2	3.4	12.655	1.2	3.3
0.70	0.75	11.246	1.5	3.8	11.335	1.4	3.8	11.526	1.3	3.8	11.452	1.4	3.8	11.067	1.3	3.6	10.972	1.3	3.5
0.75	0.80	9.320	1.6	4.1	9.311	1.5	3.8	9.629	1.5	3.9	9.349	1.5	3.9	9.025	1.5	3.6	8.833	1.4	3.5
0.80	0.85	7.943	1.7	4.3	7.923	1.6	4.0	7.949	1.6	4.1	7.906	1.7	4.0	7.567	1.7	3.8	7.248	1.6	3.8
0.85	0.90	6.442	1.9	4.2	6.592	1.8	4.2	6.381	1.8	4.3	6.528	1.9	4.1	6.205	1.8	3.8	6.091	1.7	3.9
0.90	0.95	5.317	2.1	4.6	5.483	2.0	4.3	5.405	2.0	4.1	5.429	2.1	4.4	5.143	2.0	4.0	4.926	1.9	4.0
0.95	1.00	4.421	2.3	4.6	4.399	2.2	4.5	4.449	2.2	4.5	4.587	2.2	4.4	4.233	2.2	4.2	4.188	2.1	4.2
1.00	1.05	3.550	2.6	4.7	3.747	2.4	4.7	3.659	2.5	4.5	3.753	2.5	4.5	3.514	2.5	4.4	3.357	2.3	4.2
1.05	1.10	2.986	2.8	4.7	2.998	2.7	4.8	3.112	2.7	4.5	3.035	2.8	4.6	2.754	2.8	4.5	2.843	2.5	4.4
1.10	1.15	2.529	3.1	5.1	2.571	2.9	4.8	2.532	3.0	4.9	2.495	3.1	4.8	2.416	3.0	4.6	2.163	2.9	4.5
1.15	1.20	2.028	3.3	5.1	2.067	3.2	4.9	2.000	3.3	4.8	2.026	3.4	5.1	1.901	3.3	5.1	1.767	3.1	4.8
1.20	1.25	1.675	3.7	5.1	1.713	3.6	4.9	1.632	3.7	5.1	1.753	3.7	5.2	1.595	3.7	5.0	1.551	3.3	4.7
1.25	1.30	1.388	4.0	5.6	1.376	4.0	5.2	1.337	4.1	5.3	1.444	4.0	5.3	1.269	4.1	5.3	1.259	3.8	5.1
1.30	1.35	1.150	4.4	5.6	1.132	4.4	5.3	1.213	4.4	5.3	1.148	4.6	5.1	1.094	4.4	5.1	1.005	4.2	5.5
1.35	1.40	0.937	4.9	6.2	0.913	4.9	5.6	0.962	4.9	5.3	0.958	4.9	5.2	0.854	4.9	5.6	0.856	4.5	5.2
1.40	1.45	0.821	5.2	5.8	0.783	5.2	5.9	0.819	5.2	5.9	0.779	5.4	5.7	0.750	5.3	5.5	0.694	5.0	5.3
1.45	1.50	0.709	5.6	6.1	0.649	5.7	6.2	0.648	5.7	5.7	0.641	6.1	6.2	0.626	5.7	5.7	0.595	5.4	5.5
1.50	1.55	0.529	6.5	6.5	0.571	6.2	6.2	0.560	6.4	6.0	0.476	6.9	6.0	0.481	6.5	6.0	0.476	5.9	5.5
1.55	1.60	0.372	7.4	6.6	0.436	6.8	6.1	0.439	7.3	6.0	0.405	7.6	6.4	0.415	7.1	5.9	0.371	6.9	5.9
1.60	1.65	0.300	9.4	6.0	0.306	8.1	5.7	0.394	7.5	6.0	0.400	7.7	6.0	0.287	8.3	6.2	0.307	7.5	5.9
1.65	1.70	0.237	10.2	5.8	0.308	8.5	5.8	0.352	8.1	6.4	0.340	8.5	6.7	0.247	9.1	5.9	0.253	8.0	6.4
1.70	1.75	0.207	10.5	7.0	0.236	9.4	6.4	0.245	9.7	7.6	0.247	9.7	6.7	0.216	9.5	6.5	0.216	8.7	6.0
1.75	1.80	0.182	11.2	6.5	0.203	10.5	7.6	0.205	10.6	6.3	0.198	10.9	6.7	0.201	10.2	6.0	0.179	10.0	6.7
1.80	1.85	0.181	10.4	7.3	0.154	11.1	6.5	0.154	12.2	6.6	0.152	11.7	7.6	0.146	11.8	7.2	0.146	10.4	6.8
1.85	1.90	0.149	11.8	7.3	0.136	12.7	6.5	0.134	13.2	6.2	0.131	13.1	8.3	0.126	12.6	9.4	0.105	12.0	8.2
1.90	1.95	0.098	14.3	6.8	0.107	13.3	7.0	0.124	14.2	7.6	0.131	13.7	6.6	0.102	14.3	5.6	0.099	14.2	6.2
1.95	2.00	0.093	14.9	7.6	0.076	15.3	7.0	0.110	14.7	7.2	0.076	17.0	8.3	0.087	15.6	6.2	0.056	16.8	10.8

p_T (GeV/c)		$0.8<y<1.0$			$1.0<y<1.2$			$1.2<y<1.4$			$1.4<y<1.6$			$1.6<y<1.8$			$1.8<y<2.0$		
min	max	$\frac{\mathrm{d}^2n}{\mathrm{d}y\mathrm{d}p_\mathrm{T}}$	σ_stat	σ_sys	$\frac{\mathrm{d}^2n}{\mathrm{d}y\mathrm{d}p_\mathrm{T}}$	σ_stat	σ_sys	$\frac{\mathrm{d}^2n}{\mathrm{d}y\mathrm{d}p_\mathrm{T}}$	σ_stat	σ_sys	$\frac{\mathrm{d}^2n}{\mathrm{d}y\mathrm{d}p_\mathrm{T}}$	σ_stat	σ_sys	$\frac{\mathrm{d}^2n}{\mathrm{d}y\mathrm{d}p_\mathrm{T}}$	σ_stat	σ_sys	$\frac{\mathrm{d}^2n}{\mathrm{d}y\mathrm{d}p_\mathrm{T}}$	σ_stat	σ_sys
0.00	0.05	15.243	1.1	5.3	14.812	1.1	3.6	13.404	1.1	3.8	12.300	1.1	3.4	10.964	1.2	4.0	9.789	1.2	3.4
0.05	0.10	41.241	0.7	3.6	39.434	0.7	3.1	35.974	0.7	3.0	32.424	0.7	3.0	29.433	0.7	3.0	25.219	0.8	2.9
0.10	0.15	56.092	0.6	2.9	53.184	0.6	2.5	48.800	0.6	2.4	44.551	0.6	2.4	38.943	0.6	2.5	33.935	0.7	2.4
0.15	0.20	60.386	0.5	2.8	55.526	0.5	2.2	51.909	0.5	2.2	46.804	0.6	2.1	41.588	0.6	2.2	35.061	0.7	2.2
0.20	0.25	58.178	0.5	2.3	52.959	0.5	2.0	49.224	0.6	2.0	43.905	0.6	2.0	38.386	0.6	2.1	32.628	0.7	2.1
0.25	0.30	52.152	0.5	2.1	48.356	0.6	1.9	44.191	0.6	2.0	39.246	0.6	2.0	33.857	0.7	2.1	28.567	0.7	2.1
0.30	0.35	44.448	0.6	2.1	41.301	0.6	2.0	37.174	0.6	2.0	33.222	0.7	2.1	28.144	0.7	2.1	23.219	0.8	2.2
0.35	0.40	37.746	0.6	2.2	35.034	0.7	2.1	31.686	0.7	2.2	27.780	0.7	2.2	23.670	0.8	2.3	19.554	0.9	2.3
0.40	0.45	31.592	0.7	2.4	29.273	0.7	2.3	26.487	0.8	2.3	22.866	0.8	2.3	19.620	0.9	2.5	15.936	1.0	2.5
0.45	0.50	25.827	0.8	2.6	24.377	0.8	2.5	22.031	0.8	2.4	18.947	0.9	2.5	15.748	1.0	2.6	12.966	1.1	2.6
0.50	0.55	21.121	0.9	2.7	20.148	0.9	2.6	17.991	0.9	2.6	15.555	1.0	2.6	12.997	1.1	2.7	10.357	1.2	2.7
0.55	0.60	17.534	0.9	2.9	16.596	1.0	2.9	14.730	1.0	2.8	12.616	1.1	2.7	10.439	1.2	2.8	8.227	1.4	2.7
0.60	0.65	14.781	1.0	3.0	13.318	1.1	3.0	11.929	1.1	3.0	10.306	1.2	3.0	8.335	1.4	3.0	6.753	1.5	2.8
0.65	0.70	12.125	1.1	3.3	11.067	1.2	3.1	9.948	1.2	3.1	8.389	1.4	3.1	6.742	1.5	3.1	5.378	1.7	3.1
0.70	0.75	9.829	1.3	3.4	9.316	1.3	3.3	7.853	1.4	3.4	6.840	1.5	3.3	5.554	1.7	3.2	4.221	2.0	3.1
0.75	0.80	8.208	1.4	3.5	7.701	1.4	3.4	6.537	1.5	3.5	5.488	1.7	3.5	4.452	1.9	3.3	3.340	2.2	3.1
0.80	0.85	6.575	1.5	3.8	6.196	1.6	3.6	5.515	1.7	3.6	4.642	1.8	3.6	3.411	2.1	3.5	2.708	2.5	3.5
0.85	0.90	5.299	1.7	3.8	4.982	1.8	3.8	4.250	1.9	3.8	3.600	2.1	3.7	2.794	2.4	3.6	1.965	2.9	3.8
0.90	0.95	4.195	1.9	4.0	4.166	1.9	3.9	3.608	2.1	3.8	2.969	2.3	3.9	2.324	2.6	3.7	1.561	3.3	4.1
0.95	1.00	3.532	2.1	4.2	3.415	2.1	4.0	2.790	2.3	4.0	2.291	2.5	3.9	1.793	2.9	3.6	1.271	3.7	3.7
1.00	1.05	2.903	2.3	4.2	2.764	2.3	4.2	2.427	2.5	4.2	1.780	2.9	4.1	1.406	3.3	3.9	0.996	4.3	4.2
1.05	1.10	2.374	2.5	4.4	2.290	2.6	4.6	1.845	2.8	4.2	1.526	3.1	4.2	1.118	3.7	4.1	0.794	4.8	4.3
1.10	1.15	1.968	2.8	4.8	1.795	2.9	4.5	1.449	3.2	4.4	1.199	3.5	4.4	0.920	4.1	4.3	0.591	5.8	3.7
1.15	1.20	1.679	3.0	4.7	1.473	3.2	4.7	1.243	3.4	4.5	0.963	3.9	4.7	0.711	4.6	4.4	0.450	6.6	4.3
1.20	1.25	1.320	3.3	4.8	1.209	3.5	4.8	0.971	3.9	4.6	0.707	4.5	5.0	0.552	5.3	5.0	0.360	7.5	4.2
1.25	1.30	1.089	3.7	5.1	1.041	3.8	4.9	0.854	4.2	4.8	0.604	4.8	5.0	0.420	6.2	5.2	0.230	9.2	4.3
1.30	1.35	0.893	4.1	4.9	0.808	4.3	5.2	0.668	4.6	5.2	0.539	5.3	5.4	0.347	7.1	4.8	0.179	11.0	4.5
1.35	1.40	0.719	4.6	5.5	0.633	4.9	5.4	0.545	5.2	5.5	0.386	6.2	4.7	0.295	7.8	4.7	0.136	13.2	5.4
1.40	1.45	0.610	4.9	5.6	0.509	5.3	6.1	0.380	6.0	6.0	0.285	7.3	5.4	0.224	9.2	5.0	0.122	13.7	4.9
1.45	1.50	0.464	5.5	5.8	0.450	5.6	5.0	0.385	6.3	5.5	0.221	8.1	4.7	0.139	11.1	6.6	0.121	15.4	6.7
1.50	1.55	0.399	6.0	5.7	0.350	6.4	5.3	0.263	7.2	5.5	0.200	8.7	5.7	0.114	12.5	5.9	0.067	20.1	5.4
1.55	1.60	0.347	6.6	6.0	0.300	7.1	6.0	0.233	7.6	5.2	0.127	11.1	7.1	0.103	14.2	5.5	0.053	23.2	6.3
1.60	1.65	0.249	7.6	5.6	0.236	7.8	5.7	0.198	8.8	5.4	0.110	12.0	4.9	0.059	18.9	4.3	0.033	30.4	6.0
1.65	1.70	0.207	8.3	6.1	0.204	8.4	5.5	0.156	9.4	6.7	0.112	12.3	5.6	0.040	23.0	5.2	0.024	38.5	5.9
1.70	1.75	0.160	9.4	6.2	0.169	9.0	5.8	0.110	11.0	6.3	0.064	16.0	10.6	0.030	31.8	5.2	0.015	52.0	7.5
1.75	1.80	0.139	10.2	6.7	0.100	11.0	7.8	0.086	12.5	8.6	0.064	16.8	6.4	0.027	36.0	7.1	0.004	98.5	19.0
1.80	1.85	0.138	10.8	6.0	0.093	12.4	5.6	0.081	13.7	5.5	0.044	19.7	6.4	0.017	47.2	8.4	0.008	66.0	11.7
1.85	1.90	0.088	12.9	9.8	0.081	13.5	6.6	0.059	16.0	6.0	0.031	23.2	8.5	0.008	69.6	11.6	0.005	101.1	4.7
1.90	1.95	0.081	14.6	7.4	0.064	15.3	6.4	0.047	18.4	6.1	0.028	28.9	7.7	0.009	62.5	3.7	0.003	131.6	12.9
1.95	2.00	0.076	15.4	6.0	0.039	19.3	10.6	0.033	21.5	6.7	0.017	36.1	5.9	0.015	58.0	12.9	0.002	123.0	83.0

p_T (GeV/c)		$2.0 < y < 2.2$			$2.2 < y < 2.4$			$2.4 < y < 2.6$			$2.6 < y < 2.8$			$2.8 < y < 3.0$			$3.0 < y < 3.2$		
min	max	$\frac{d^2n}{dydp_T}$	σ_{stat}	σ_{sys}	$\frac{d^2n}{dydp_T}$	σ_{stat}	σ_{sys}	$\frac{d^2n}{dydp_T}$	σ_{stat}	σ_{sys}	$\frac{d^2n}{dydp_T}$	σ_{stat}	σ_{sys}	$\frac{d^2n}{dydp_T}$	σ_{stat}	σ_{sys}	$\frac{d^2n}{dydp_T}$	σ_{stat}	σ_{sys}
0.00	0.05	8.305	1.3	3.0	6.779	1.5	2.7	5.630	1.6	2.7	4.574	1.8	2.7	3.725	2.1	2.7	2.685	2.5	2.3
0.05	0.10	21.830	0.8	2.7	17.800	0.9	2.5	14.612	1.0	2.6	11.790	1.1	2.6	9.115	1.3	2.4	6.524	1.6	2.2
0.10	0.15	28.057	0.7	2.4	23.464	0.8	2.4	18.842	0.9	2.5	15.044	1.0	2.3	10.801	1.2	2.2	8.234	1.5	2.1
0.15	0.20	29.234	0.7	2.2	23.888	0.8	2.3	19.174	0.9	2.3	14.332	1.1	2.2	10.837	1.3	2.2	7.610	1.6	2.1
0.20	0.25	26.811	0.8	2.2	21.522	0.9	2.2	16.373	1.0	2.2	11.986	1.2	2.1	8.201	1.5	2.1	5.555	1.9	3.2
0.25	0.30	23.201	0.8	2.2	18.304	0.9	2.3	13.104	1.1	2.2	9.350	1.4	2.1	6.181	1.8	2.4	3.709	2.9	4.8
0.30	0.35	18.888	0.9	2.2	14.159	1.1	2.2	10.421	1.3	2.1	6.886	1.6	2.1	4.369	2.4	3.6	2.442	5.8	3.6
0.35	0.40	15.410	1.0	2.3	11.484	1.2	2.2	8.058	1.5	2.2	5.252	2.0	2.7	3.158	3.3	4.3	1.254	21.8	1.2
0.40	0.45	12.425	1.1	2.5	9.072	1.4	2.3	6.531	1.6	2.4	4.257	2.3	3.4	2.298	5.2	3.5			
0.45	0.50	10.006	1.3	2.6	7.196	1.5	2.4	4.982	1.9	2.8	3.137	3.0	3.7	1.474	10.4	3.0			
0.50	0.55	7.915	1.4	2.7	5.784	1.7	2.6	3.805	2.3	3.3	2.155	4.3	4.2	0.585	43.6	2.3			
0.55	0.60	6.410	1.6	2.7	4.350	2.0	3.0	2.826	2.9	3.3	1.508	6.3	3.9						
0.60	0.65	4.772	1.9	2.8	3.112	2.5	3.2	2.030	3.6	3.6	0.938	9.9	4.1						
0.65	0.70	3.819	2.1	3.0	2.580	2.9	3.5	1.610	4.6	3.5	0.915	16.1	2.7						
0.70	0.75	3.028	2.4	3.2	1.899	3.5	3.4	1.149	5.8	3.7	1.025	30.1	2.3						
0.75	0.80	2.269	2.8	3.5	1.484	4.0	3.5	0.829	7.8	3.8									
0.80	0.85	1.622	3.5	3.4	1.004	5.4	3.4	0.678	10.3	4.0									
0.85	0.90	1.354	3.9	3.5	0.730	6.7	3.8	0.455	15.6	4.1									
0.90	0.95	1.044	4.6	3.9	0.632	7.6	3.7	0.298	19.6	3.5									
0.95	1.00	0.745	5.7	3.6	0.354	9.8	4.2	0.198	28.7	6.4									
1.00	1.05	0.561	6.5	3.8	0.286	11.5	3.6	0.102	49.8	4.5									
1.05	1.10	0.481	7.3	3.9	0.206	15.2	5.2	0.075	92.6	7.8									
1.10	1.15	0.364	8.7	4.0	0.205	16.0	3.9												
1.15	1.20	0.247	10.8	4.0	0.122	22.5	4.1												
1.20	1.25	0.212	12.1	3.8	0.065	31.7	8.0												
1.25	1.30	0.147	15.0	4.4	0.061	36.2	4.2												
1.30	1.35	0.072	21.5	6.6	0.030	44.4	6.5												
1.35	1.40	0.075	21.7	7.3	0.026	62.6	4.9												
1.40	1.45	0.049	29.3	5.5	0.009	81.1	5.1												
1.45	1.50	0.036	31.7	4.8	0.022	80.8	2.1												
1.50	1.55	0.033	35.2	6.3															
1.55	1.60	0.012	51.5	13.6															
1.60	1.65	0.011	61.2	9.7	0.011	157.1	13.8												
1.65	1.70	0.007	103.0	10.8															
1.70	1.75	0.003	136.0	3.3															
1.75	1.80	0.010	67.6	11.1															
1.80	1.85	0.002	154.7	28.6															
1.85	1.90	0.001	206.5	15.5															
1.90	1.95	0.005	82.1	17.9															
1.95	2.00	0.001	478.7	9.8															

p_T (GeV/c)		$3.2 < y < 3.4$			$3.4 < y < 3.6$			$3.6 < y < 3.8$		
min	max	$\frac{d^2n}{dydp_T}$	σ_{stat}	σ_{sys}	$\frac{d^2n}{dydp_T}$	σ_{stat}	σ_{sys}	$\frac{d^2n}{dydp_T}$	σ_{stat}	σ_{sys}
0.00	0.05	2.104	2.9	2.2	1.410	3.6	2.1	0.889	5.5	6.8
0.05	0.10	4.828	1.9	2.1	3.530	2.4	2.9	1.850	5.5	5.9
0.10	0.15	5.794	1.8	2.3	3.604	2.9	5.5	2.926	25.9	1.4
0.15	0.20	4.583	2.2	4.4	2.788	8.6	2.6			
0.20	0.25	3.223	4.4	4.4						
0.25	0.30	1.909	22.1	1.2						

C.2 Rapidity spectra

The final results concerning rapidity y distributions $\mathrm{d}n/\mathrm{d}y$ are presented in Table C.7.

C.3 Inverse slope parameter

The y distributions of the inverse slope parameter T (MeV) are presented in Table C.8.

C.4 Mean transverse mass

The y distributions of the mean transverse mass $v = (\langle m_\mathrm{T} \rangle - m_\pi)$ (GeV) are presented in Table C.9.

TABLE C.7: Tabulated final rapidity y spectra $\mathrm{d}n/\mathrm{d}y$ produced in inelastic ^{40}Ar+^{45}Sc collisions at 13*A*, 19*A*, 30*A*, 40*A*, 75*A* and 150*A* GeV/*c* together with statistical and systematic uncertainties.

y		p_{beam} = 13 (GeV/c)			p_{beam} = 19 (GeV/c)			p_{beam} = 30 (GeV/c)			p_{beam} = 40 (GeV/c)			p_{beam} = 75 (GeV/c)			p_{beam} = 150 (GeV/c)		
min	max	$\mathrm{d}n/\mathrm{d}y$	σ_{stat}	σ_{sys}	$\mathrm{d}n/\mathrm{d}y$	σ_{stat}	σ_{sys}	$\mathrm{d}n/\mathrm{d}y$	σ_{stat}	σ_{sys}	$\mathrm{d}n/\mathrm{d}y$	σ_{stat}	σ_{sys}	$\mathrm{d}n/\mathrm{d}y$	σ_{stat}	σ_{sys}	$\mathrm{d}n/\mathrm{d}y$	σ_{stat}	σ_{sys}
-0.6	-0.4										22.502	0.2	0.9	26.750	0.1	1.2			
-0.4	-0.2							22.569	0.2	0.6	24.427	0.2	0.7	27.736	0.1	1.0	30.092	0.2	1.7
-0.2	0.0				19.546	0.3	0.7	23.374	0.2	0.6	25.010	0.2	0.7	27.855	0.1	0.9	30.154	0.2	1.2
0.0	0.2	16.341	0.3	0.6	19.513	0.3	0.8	23.129	0.2	0.6	24.604	0.2	0.7	27.224	0.1	0.9	30.389	0.2	0.9
0.2	0.4	15.381	0.3	0.6	18.681	0.3	0.9	21.958	0.2	0.6	23.550	0.2	0.7	26.767	0.1	1.0	30.269	0.2	0.9
0.4	0.6	13.884	0.2	0.6	17.147	0.2	0.9	20.199	0.2	0.6	22.091	0.2	0.7	26.013	0.1	1.0	29.261	0.2	0.9
0.6	0.8	12.133	0.3	0.6	15.020	0.3	0.9	18.328	0.2	0.6	20.670	0.2	0.6	24.685	0.1	1.0	28.626	0.2	0.9
0.8	1.0	10.200	0.3	0.6	12.934	0.3	0.9	16.282	0.2	0.6	18.643	0.2	0.6	22.281	0.1	0.9	27.114	0.2	0.7
1.0	1.2	8.235	0.3	0.5	10.804	0.3	0.9	13.843	0.2	0.6	15.780	0.2	0.6	19.769	0.1	0.9	25.301	0.2	0.6
1.2	1.4	6.327	0.3	0.5	8.536	0.3	0.9	11.121	0.2	0.6	13.117	0.2	0.6	17.390	0.1	1.0	22.912	0.2	0.6
1.4	1.6	4.657	0.4	0.5	6.229	0.4	0.9	8.639	0.2	0.6	10.428	0.2	0.6	14.837	0.1	1.0	20.191	0.2	0.6
1.6	1.8	3.176	0.5	0.5	4.484	0.4	1.0	6.586	0.2	0.6	8.309	0.2	0.6	12.138	0.1	1.0	17.290	0.2	0.7
1.8	2.0	2.089	0.5	0.7	3.160	0.5	1.1	4.886	0.3	0.6	6.175	0.3	0.6	9.551	0.2	1.0	14.344	0.2	0.7
2.0	2.2	1.287	0.7	0.5	2.142	0.6	1.2	3.429	0.4	0.6	4.421	0.3	0.6	7.203	0.2	1.1	11.474	0.3	0.7
2.2	2.4	0.754	1.0	0.4	1.308	0.9	1.3	2.221	0.5	0.6	3.016	0.5	0.6	5.230	0.2	1.1	8.832	0.3	0.7
2.4	2.6	0.378	1.6	0.4	0.748	1.2	1.3	1.390	0.6	0.7	1.893	0.7	0.7	3.644	0.3	1.1	6.589	0.4	0.7
2.6	2.8	0.168	2.4	0.5	0.387	1.9	1.3	0.824	0.9	0.7	1.164	0.8	0.7	2.439	0.6	1.2	4.657	0.6	0.8
2.8	3.0	0.052	6.3	0.4	0.188	4.1	1.0	0.455	1.6	0.9	0.678	1.4	0.9	1.564	2.9	1.2	3.037	0.8	0.9
3.0	3.2	0.013	52.6	0.2	0.061	21.8	0.4	0.201	7.1	0.7	0.311	4.5	1.1	0.970	15.2	1.3	1.901	1.1	1.0
3.2	3.4													0.411	2.0	2.1	1.122	2.1	1.3
3.4	3.6													0.206	10.8	1.2	0.567	2.5	2.1
3.6	3.8																0.283	13.5	2.3

TABLE C.8: Tabulated final rapidity y dependence of the inverse slope parameter T (MeV) calculated at 13*A*, 19*A*, 30*A*, 40*A*, 75*A* and 150*A* GeV/*c* together with statistical and systematic uncertainties.

y		p_{beam} = 13 (GeV/c)			p_{beam} = 19 (GeV/c)			p_{beam} = 30 (GeV/c)			p_{beam} = 40 (GeV/c)			p_{beam} = 75 (GeV/c)			p_{beam} = 150 (GeV/c)		
min	max	T	σ_{stat}	σ_{sys}	T	σ_{stat}	σ_{sys}	T	σ_{stat}	σ_{sys}	T	σ_{stat}	σ_{sys}	T	σ_{stat}	σ_{sys}	T	σ_{stat}	σ_{sys}
0.0	0.2	152.868	0.6	0.6	157.276	0.6	1.0	165.547	0.4	0.9	166.719	0.4	1.1	171.999	0.2	1.4	171.715	0.4	1.4
0.2	0.4	154.710	0.6	0.7	159.764	0.5	1.1	167.636	0.3	0.8	167.045	0.3	1.0	171.851	0.2	1.4	172.050	0.4	1.5
0.4	0.6	155.356	0.5	0.7	159.527	0.5	1.1	164.380	0.3	0.8	166.933	0.3	0.9	170.636	0.2	1.4	172.427	0.4	1.4
0.6	0.8	150.276	0.5	0.7	155.332	0.5	1.1	161.644	0.3	0.8	165.855	0.3	0.8	168.179	0.2	1.3	168.846	0.4	1.2
0.8	1.0	143.656	0.6	0.6	152.358	0.6	1.1	158.306	0.4	0.7	161.715	0.4	0.8	166.904	0.2	1.2	167.787	0.3	1.1
1.0	1.2	136.441	0.6	0.5	145.439	0.6	1.0	153.172	0.4	0.7	156.952	0.4	0.7	164.356	0.2	1.3	168.012	0.3	1.1
1.2	1.4	126.531	0.7	0.4	136.750	0.7	0.9	146.417	0.4	0.6	151.841	0.4	0.7	159.048	0.2	1.4	165.157	0.4	1.1
1.4	1.6	115.508	0.9	0.3	126.171	0.8	0.8	141.203	0.5	0.6	147.721	0.4	0.7	154.859	0.2	1.3	162.664	0.4	1.0
1.6	1.8				116.297	1.0	0.8	131.970	0.5	0.5	136.062	0.5	0.6	149.447	0.3	1.3	158.061	0.4	1.0
1.8	2.0							117.955	0.6	0.5	126.227	0.6	0.5	141.241	0.3	1.2	153.752	0.5	1.0
2.0	2.2										114.493	0.8	0.5	132.593	0.4	1.1	144.443	0.5	0.9
2.2	2.4													120.052	0.5	0.8	136.964	0.6	0.9
2.4	2.6																129.043	0.9	0.9
2.6	2.8																116.898	1.6	0.9

TABLE C.9: Tabulated final rapidity y dependence of the mean transverse mass $v = (\langle m_{\mathrm{T}} \rangle - m_{\pi})$ (GeV) calculated at 13*A*, 19*A*, 30*A*, 40*A*, 75*A* and 150*A* GeV/*c* together with statistical and systematic uncertainties.

y		p_{beam} = 13 (GeV/c)			p_{beam} = 19 (GeV/c)			p_{beam} = 30 (GeV/c)			p_{beam} = 40 (GeV/c)			p_{beam} = 75 (GeV/c)			p_{beam} = 150 (GeV/c)		
min	max	v	σ_{stat}	σ_{sys}	v	σ_{stat}	σ_{sys}	v	σ_{stat}	σ_{sys}	v	σ_{stat}	σ_{sys}	v	σ_{stat}	σ_{sys}	v	σ_{stat}	σ_{sys}
0.0	0.2	0.214	2.1	0.3	0.219	2.1	0.5	0.234	2.1	0.8	0.238	1.8	0.7	0.256	1.8	0.8	0.260	1.9	0.9
0.2	0.4	0.217	1.6	0.4	0.224	1.4	0.5	0.239	0.9	0.6	0.244	0.9	0.6	0.257	0.5	0.7	0.261	0.8	0.8
0.4	0.6	0.216	1.5	0.3	0.225	1.4	0.4	0.241	0.9	0.5	0.249	0.8	0.6	0.256	0.5	0.7	0.259	0.9	0.8
0.6	0.8	0.208	1.6	0.3	0.224	1.5	0.3	0.239	0.9	0.5	0.245	0.9	0.5	0.254	0.6	0.7	0.258	0.9	0.7
0.8	1.0	0.201	1.7	0.2	0.219	1.6	0.3	0.232	1.0	0.4	0.241	1.0	0.5	0.248	0.6	0.6	0.251	0.9	0.7
1.0	1.2	0.188	2.0	0.1	0.207	1.9	0.2	0.225	1.1	0.4	0.232	1.0	0.4	0.242	0.6	0.5	0.251	0.9	0.6
1.2	1.4	0.170	2.6	0.0	0.192	2.3	0.1	0.210	1.3	0.2	0.221	1.1	0.3	0.232	0.6	0.5	0.245	0.9	0.5
1.4	1.6	0.152	3.4	0.0	0.173	3.6	0.0	0.196	1.5	0.1	0.203	1.2	0.2	0.223	0.7	0.3	0.237	1.0	0.5
1.6	1.8				0.150	3.6	0.0	0.174	1.9	0.1	0.188	1.8	0.1	0.211	0.8	0.2	0.227	1.2	0.4
1.8	2.0							0.154	2.3	0.0	0.169	2.1	0.0	0.196	1.0	0.1	0.216	1.4	0.3
2.0	2.2										0.148	3.0	0.0	0.178	1.3	0.1	0.202	1.6	0.2
2.2	2.4													0.158	1.8	0.0	0.185	2.2	0.1
2.4	2.6																0.169	3.4	0.0
2.6	2.8																0.145	8.5	0.0

Bibliography

[1] Ulrich W. Heinz and Maurice Jacob. “Evidence for a new state of matter: An Assessment of the results from the CERN lead beam program”. In: (Jan. 2000). arXiv: nucl-th/0002042.

[2] Miklos Gyulassy and Larry McLerran. “New forms of QCD matter discovered at RHIC”. In: *Nucl. Phys. A* 750 (2005). Ed. by D. Rischke and G. Levin, pp. 30–63. DOI: 10.1016/j.nuclphysa.2004.10.034. arXiv: nucl-th/0405013.

[3] Claudia Ratti. “Lattice QCD and heavy ion collisions: a review of recent progress”. In: *Rept. Prog. Phys.* 81.8 (2018), p. 084301. DOI: 10.1088/1361-6633/aabb97. arXiv: 1804.07810 [hep-lat].

[4] Grazyna Odyniec. “Beam Energy Scan Program at RHIC (BES I and BES II) – Probing QCD Phase Diagram with Heavy-Ion Collisions”. In: *PoS* CORFU2018 (2019). Ed. by Konstantinos Anagnostopoulos et al., p. 151. DOI: 10.22323/1.347.0151.

[5] Blaschke, David et al. “Topical issue on Exploring Strongly Interacting Matter at High Densities - NICA White Paper”. In: *Eur. Phys. J. A* 52.8 (2016), p. 267. DOI: 10.1140/epja/i2016-16267-x. URL: https://doi.org/10.1140/epja/i2016-16267-x.

[6] Ingo Augustin et al. “New Physics at the International Facility for Antiproton and Ion Research (FAIR) Next to GSI”. In: *4th International Conference on Fission and Properties of Neutron Rich nuclei*. Apr. 2008. DOI: 10.1142/9789812833433_0016. arXiv: 0804.0177 [hep-ph].

[7] M. Cheng et al. “The QCD equation of state with almost physical quark masses”. In: *Phys. Rev. D* 77 (2008), p. 014511. DOI: 10.1103/PhysRevD.77.014511. arXiv: 0710.0354 [hep-lat].

[8] F. Becattini, J. Manninen, and M. Gazdzicki. “Energy and system size dependence of chemical freeze-out in relativistic nuclear collisions”. In: *Phys. Rev.* C73 (2006), p. 044905. DOI: 10.1103/PhysRevC.73.044905. arXiv: hep-ph/0511092 [hep-ph].

[9] Maciej Lewicki. “Charged hadron production in central Ar+Sc collisions at the CERN SPS”. PhD thesis. University of Wroclaw, 2020.

[10] Katarzyna Grebieszkow. “NA49 and NA61/SHINE experiments: Results and perspectives”. In: *Acta Phys. Polon. B* 41 (2010). Ed. by Marek Pfutzner and Tomasz Matulewicz, pp. 427–440. arXiv: 0911.1902 [nucl-ex].

[11] Y. Aoki et al. “The Order of the quantum chromodynamics transition predicted by the standard model of particle physics”. In: *Nature* 443 (2006), pp. 675–678. DOI: 10.1038/nature05120. arXiv: hep-lat/0611014.

[12] Anton Andronic et al. “Decoding the phase structure of QCD via particle production at high energy”. In: *Nature* 561.7723 (2018), pp. 321–330. DOI: 10.1038/s41586-018-0491-6. arXiv: 1710.09425 [nucl-th].

[13] Reinhard Stock. “Relativistic Nucleus-Nucleus Collisions and the QCD Matter Phase Diagram”. In: *Particle Physics Reference Library: Volume 1: Theory and Experiments*. Ed. by Herwig Schopper. 2020, pp. 311–453. DOI: 10.1007/978-3-030-38207-0_7.

[14] A. Bazavov et al. “Equation of state in (2+1)-flavor QCD”. In: *Phys. Rev. D* 90 (2014), p. 094503. DOI: 10.1103/PhysRevD.90.094503. arXiv: 1407.6387 [hep-lat].

[15] Asakawa Masayuki and Yazaki Koichi. “Chiral restoration at finite density and temperature”. In: *Nuclear Physics A* 504.4 (1989), pp. 668–684. ISSN: 0375-9474. DOI: https://doi.org/10.1016/0375-9474(89)90002-X. URL: http://www.sciencedirect.com/science/article/pii/037594748990002X.

[16] A. Barducci et al. “Chiral-symmetry breaking in QCD at finite temperature and density”. In: *Physics Letters B* 231.4 (1989), pp. 463–470. ISSN: 0370-2693. DOI: https://doi.org/10.1016/0370-2693(89)90695-3. URL: http://www.sciencedirect.com/science/article/pii/0370269389906953.

[17] Marek Gazdzicki and Mark I. Gorenstein. “On the early stage of nucleus-nucleus collisions”. In: *Acta Phys. Polon.* B30 (1999), p. 2705. arXiv: hep-ph/9803462 [hep-ph].

[18] L.D. Landau. “On the multiparticle production in high-energy collisions”. In: *Izv. Akad. Nauk Ser. Fiz.* 17 (1953), pp. 51–64.

[19] N. Abgrall et al. “Measurement of negatively charged pion spectra in inelastic p+p interactions at p_{lab} = 20, 31, 40, 80 and 158 GeV/c”. In: *Eur.Phys.J.* C74 (2014), p. 2794. DOI: 10.1140/epjc/s10052-014-2794-6. arXiv: 1310.2417 [hep-ex].

[20] A. Acharya et al. “Measurements of π^- production in ^{7}Be+^{9}Be collisions at beam momenta from 19A to 150AGeV/c in the NA61/SHINE experiment at the CERN SPS”. In: *Eur. Phys. J. C* 80.10 (2020), p. 961. DOI: 10.1140/epjc/s10052-020-08514-6. arXiv: 2008.06277 [nucl-ex].

[21] N. Abgrall et al. “Measurement of negatively charged pion spectra in inelastic p+p interactions at p_{lab} = 20, 31, 40, 80 and 158 GeV/c”. In: *Eur. Phys. J.* C74.3 (2014), p. 2794. DOI: 10.1140/epjc/s10052-014-2794-6. arXiv: 1310.2417 [hep-ex].

[22] S. V. Afanasiev et al. “Energy dependence of pion and kaon production in central Pb + Pb collisions”. In: *Phys. Rev.* C66 (2002), p. 054902. DOI: 10.1103/PhysRevC.66.054902. arXiv: nucl-ex/0205002 [nucl-ex].

[23] C. Alt et al. “Pion and kaon production in central Pb + Pb collisions at 20-A and 30-A-GeV: Evidence for the onset of deconfinement”. In: *Phys. Rev.* C77 (2008), p. 024903. DOI: 10.1103/PhysRevC.77.024903. arXiv: 0710.0118 [nucl-ex].

[24] Marek Gaździcki. “Pion and strangeness puzzles”. In: *Acta Physica Hungarica New Series Heavy Ion Physics* 4.1 (Dec. 1996), pp. 33–44. ISSN: 1588-2675. DOI: 10.1007/BF03155597. URL: https://doi.org/10.1007/BF03155597.

[25] M.I Gorenstein, M Gaździcki, and K.A Bugaev. “Transverse activity of kaons and deconfinement phase transition in nucleus–nucleus collisions”. In: *Physics Letters B* 567.3 (2003), pp. 175–178. ISSN: 0370-2693. DOI: https://doi.org/10.1016/j.physletb.2003.06.043. URL: http://www.sciencedirect.com/science/article/pii/S0370269303009432.

[26] The NA49 Collaboration. “Inclusive production of charged pions in p+p collisions at 158 GeV/c beam momentum”. In: *The European Physical Journal C - Particles and Fields* 45.2 (Feb. 2006), pp. 343–381. ISSN: 1434-6052. DOI: 10.1140/epjc/s2005-02391-9. URL: https://doi.org/10.1140/epjc/s2005-02391-9.

[27] E. E. Zabrodin et al. “Inclusive spectra of charged particles in pp and $\bar{p}$p interactions at 32 GeV/c”. In: *Phys. Rev. D* 52 (3 Aug. 1995), pp. 1316–1342. DOI: 10.1103/PhysRevD.52.1316. URL: https://link.aps.org/doi/10.1103/PhysRevD.52.1316.

[28] V. V. Ammosov et al. "A study of $\pi+$, $\pi-$ and proton production in pp interactions at 69 GeV/c". In: *Il Nuovo Cimento A (1965-1970)* 40.3 (Aug. 1977), pp. 237–268. ISSN: 1826-9869. DOI: 10.1007/BF02776862. URL: https://doi.org/10.1007/BF02776862.

[29] A. Aduszkiewicz et al. "Proton-Proton Interactions and Onset of Deconfinement". In: (Dec. 2019). arXiv: 1912.10871 [hep-ex].

[30] Michael Kliemant, Benjamin Lungwitz, and Marek Gazdzicki. "Energy dependence of transverse mass spectra of kaons produced in p + p and p + anti-p interactions: A Compilation". In: *Phys. Rev. C* 69 (2004), p. 044903. DOI: 10.1103/PhysRevC.69.044903. arXiv: hep-ex/0308002.

[31] K. Aamodt et al. "Production of pions, kaons and protons in *pp* collisions at $\sqrt{s} = 900$ GeV with ALICE at the LHC". In: *Eur. Phys. J. C* 71 (2011), p. 1655. DOI: 10.1140/epjc/s10052-011-1655-9. arXiv: 1101.4110 [hep-ex].

[32] B. Alper et al. "Production Spectra of pi+-, K+-, rho+- at Large Angles in Proton Proton Collisions in the CERN Intersecting Storage Rings". In: *Nucl. Phys. B* 100 (1975), pp. 237–290. DOI: 10.1016/0550-3213(75)90618-5.

[33] B.I. Abelev et al. "Systematic Measurements of Identified Particle Spectra in pp, d^+ Au and Au+Au Collisions from STAR". In: *Phys.Rev.* C79 (2009), p. 034909. DOI: 10.1103/PhysRevC.79.034909. arXiv: 0808.2041 [nucl-ex].

[34] Betty Bezverkhny Abelev et al. "Production of charged pions, kaons and protons at large transverse momenta in pp and Pb–Pb collisions at $\sqrt{s_{\rm NN}}$ =2.76 TeV". In: *Phys.Lett.* B736 (2014), pp. 196–207. DOI: 10.1016/j.physletb.2014.07.011. arXiv: 1401.1250 [nucl-ex].

[35] L. Ahle et al. "Particle production at high baryon density in central Au + Au reactions at 11.6-A-GeV/c". In: *Phys. Rev.* C57 (1998), p. 466. DOI: 10.1103/PhysRevC.57.466.

[36] I.G. Bearden et al. "Charged meson rapidity distributions in central Au+Au collisions at s(NN)**(1/2) = 200-GeV". In: *Phys. Rev. Lett.* 94 (2005), p. 162301.

[37] L. Ahle et al. "Kaon production in Au + Au collisions at 11.6-A-GeV/c". In: *Phys. Rev. C* 58 (1998), pp. 3523–3538. DOI: 10.1103/PhysRevC.58.3523.

[38] L. Ahle et al. "Centrality dependence of kaon yields in Si + A and Au + Au collisions at the AGS". In: *Phys. Rev. C* 60 (1999), p. 044904. DOI: 10.1103/PhysRevC.60.044904. arXiv: nucl-ex/9903009.

[39] L. Ahle et al. "Excitation function of K+ and pi+ production in Au + Au reactions at 2/A-GeV to 10/A-GeV". In: *Phys. Lett. B* 476 (2000), pp. 1–8. DOI: 10.1016/S0370-2693(00)00037-X. arXiv: nucl-ex/9910008.

[40] L Ahle et al. "An Excitation function of K- and K+ production in Au + Au reactions at the AGS". In: *Phys. Lett. B* 490 (2000), pp. 53–60. DOI: 10.1016/S0370-2693(00)00916-3. arXiv: nucl-ex/0008010.

[41] J. Barrette et al. "Proton and pion production in Au + Au collisions at 10.8A-GeV/c". In: *Phys. Rev. C* 62 (2000), p. 024901. DOI: 10.1103/PhysRevC.62.024901. arXiv: nucl-ex/9910004.

[42] D. Pelte et al. "Charged pion production in Au on Au collisions at 1-A/GeV". In: *Z. Phys. A* 357 (1997), pp. 215–234. DOI: 10.1007/s002180050236.

[43] L. Adamczyk et al. "Bulk Properties of the Medium Produced in Relativistic Heavy-Ion Collisions from the Beam Energy Scan Program". In: *Phys. Rev. C* 96.4 (2017), p. 044904. DOI: 10.1103/PhysRevC.96.044904. arXiv: 1701.07065 [nucl-ex].

[44] Betty Abelev et al. “Centrality determination of Pb-Pb collisions at $\sqrt{s_{NN}} = 2.76$ TeV with ALICE”. In: *Phys. Rev. C* 88.4 (2013), p. 044909. DOI: 10.1103/PhysRevC.88.044909. arXiv: 1301.4361 [nucl-ex].

[45] Jaroslav Adam et al. “Measurement of pion, kaon and proton production in proton–proton collisions at $\sqrt{s} = 7$ TeV”. In: *Eur. Phys. J. C* 75.5 (2015), p. 226. DOI: 10.1140/epjc/s10052-015-3422-9. arXiv: 1504.00024 [nucl-ex].

[46] C. Alt et al. “System-size dependence of strangeness production in nucleus-nucleus collisions at s(NN)**(1/2) = 17.3-GeV”. In: *Phys. Rev. Lett.* 94 (2005), p. 052301. DOI: 10.1103/PhysRevLett.94.052301. arXiv: nucl-ex/0406031.

[47] V.V. Begun et al. “Particle number fluctuations in canonical ensemble”. In: *Phys. Rev. C* 70 (2004), p. 034901. DOI: 10.1103/PhysRevC.70.034901. arXiv: nucl-th/0404056.

[48] A. Bialas, M. Bleszynski, and W. Czyz. “Multiplicity Distributions in Nucleus-Nucleus Collisions at High-Energies”. In: *Nucl. Phys. B* 111 (1976), pp. 461–476. DOI: 10.1016/0550-3213(76)90329-1.

[49] A. Acharya et al. “Spectra and mean multiplicities of π^- in *central* ^{40}Ar+^{45}Sc collisions at 13*A*, 19*A*, 30*A*, 40*A*, 75*A* and 150*A* GeV/*c* beam momenta measured by the NA61/SHINE spectrometer at the CERN SPS”. In: (Jan. 2021). arXiv: 2101.08494 [hep-ex].

[50] A Aduszkiewicz. *Study of Hadron-Nucleus and Nucleus-Nucleus Collisions at the CERN SPS: Early Post-LS2 Measurements and Future Plans*. Tech. rep. CERN-SPSC-2018-008. SPSC-P-330-ADD-10. Geneva: CERN, Mar. 2018. URL: https://cds.cern.ch/record/2309890.

[51] M. Tanabashi et al. “Review of Particle Physics”. In: *Phys. Rev. D* 98 (3 Aug. 2018), p. 030001. DOI: 10.1103/PhysRevD.98.030001. URL: https://link.aps.org/doi/10.1103/PhysRevD.98.030001.

[52] N. Abgrall et al. “NA61/SHINE facility at the CERN SPS: beams and detector system”. In: *JINST* 9.CERN-PH-EP-2014-003. CERN-PH-EP-2014-003 (Jan. 2014), P06005. 55 p. DOI: 10.1088/1748-0221/9/06/P06005. URL: https://cds.cern.ch/record/1642156.

[53] Klaus Werner. “The hadronic interaction model EPOS”. In: *Nucl. Phys. Proc. Suppl.* 175-176 (2008), pp. 81–87. DOI: 10.1016/j.nuclphysbps.2007.10.012.

[54] S. Agostinelli et al. “Geant4—a simulation toolkit”. In: *Nuclear Instruments and Methods in Physics Research Section A: Accelerators, Spectrometers, Detectors and Associated Equipment* 506.3 (2003), pp. 250–303. ISSN: 0168-9002. DOI: https://doi.org/10.1016/S0168-9002(03)01368-8. URL: http://www.sciencedirect.com/science/article/pii/S0168900203013688.

[55] A. Seryakov. *PSD acceptance maps for event selection*. https://edms.cern.ch/document/1867336/1. note. CERN EDMS. 2017.

[56] Piotr Podlaski. *Strangeness production at the CERN SPS energies*. Presentation at Strangness in Quark Matter 2019. June 11, 2019. URL: https://indico.cern.ch/event/755366/contributions/3357938/.

[57] M. Gazdzicki and Ole Hansen. “Hadron production in nucleon-nucleon collisions at 200 GeV/c — A compilation”. In: *Nuclear Physics A* 528.3 (1991), pp. 754–770. ISSN: 0375-9474. DOI: https://doi.org/10.1016/0375-9474(91)90261-4. URL: http://www.sciencedirect.com/science/article/pii/0375947491902614.

[58] R. J. Glauber. “Theory of High Energy Hadron-Nucleus Collisions”. In: *High-Energy Physics and Nuclear Structure*. Ed. by Samuel Devons. Boston, MA: Springer US, 1970, pp. 207–264. ISBN: 978-1-4684-1827-9.

[59] Maciej Rybczyński et al. “GLISSANDO 2: GLauber Initial-State Simulation AND mOre…, ver. 2”. In: *Computer Physics Communications* 185.6 (2014), pp. 1759–1772. ISSN: 0010-4655. DOI: https://doi.org/10.1016/j.cpc.2014.02.016. URL: http://www.sciencedirect.com/science/article/pii/S0010465514000502.

[60] Xin-Nian Wang and Miklos Gyulassy. “HIJING: A Monte Carlo model for multiple jet production in pp, pA, and AA collisions”. In: *Phys. Rev. D* 44 (11 Dec. 1991), pp. 3501–3516. DOI: 10.1103/PhysRevD.44.3501. URL: https://link.aps.org/doi/10.1103/PhysRevD.44.3501.

[61] Roger D. Woods and David S. Saxon. “Diffuse Surface Optical Model for Nucleon-Nuclei Scattering”. In: *Phys. Rev.* 95 (2 July 1954), pp. 577–578. DOI: 10.1103/PhysRev.95.577. URL: https://link.aps.org/doi/10.1103/PhysRev.95.577.

[62] K. Werner et al. “The Physics of EPOS”. In: *EPJ Web Conf.* 52 (2013), p. 05001. DOI: 10.1051/epjconf/20125205001.

[63] J. L. Klay et al. “Charged pion production in 2A to 8A GeV central Au + Au Collisions”. In: *Phys. Rev. C* 68 (5 Nov. 2003), p. 054905. DOI: 10.1103/PhysRevC.68.054905. URL: https://link.aps.org/doi/10.1103/PhysRevC.68.054905.

[64] L. Ahle et al. “Particle production at high baryon density in central Au+Au reactions at 11.6A GeV/c”. In: *Phys. Rev. C* 57 (2 Feb. 1998), R466–R470. DOI: 10.1103/PhysRevC.57.R466. URL: https://link.aps.org/doi/10.1103/PhysRevC.57.R466.

[65] M. Gazdzicki and D. Roehrich. “Pion multiplicity in nuclear collisions”. In: *Z.Phys.* C65 (1995), p. 215. DOI: 10.1007/BF01571878.

[66] M. Bleicher et al. “Relativistic hadron hadron collisions in the ultrarelativistic quantum molecular dynamics model”. In: *J.Phys.* G25 (1999), pp. 1859–1896. DOI: 10.1088/0954-3899/25/9/308. arXiv: hep-ph/9909407 [hep-ph].

[67] L. Landau. In: *Izv.Akad.Nauk SSSR* Ser.Fiz. 17 (1953), p. 51.

[68] S.Z. Belenkij and L.D. Landau. “Hydrodynamic theory of multiple production of particles”. In: *Nuovo Cim. Suppl.* 3S10 (1956), p. 15. DOI: 10.1007/BF02745507.

[69] C. Blume. “Energy dependence of hadronic observables”. In: *J. Phys. G* 31 (2005). Ed. by F. Antinori et al., S57–S68. DOI: 10.1088/0954-3899/31/4/008.

[70] Edward V. Shuryak. “Multiparticle production in high energy particle collisions.” In: *Yad.Fiz.* 16 (1972), pp. 395–405.

[71] Marcus Bleicher. “Evidence for the onset of deconfinement from longitudinal momentum distributions? Observation of the softest point of the equation of state”. In: (Sept. 2005). arXiv: hep-ph/0509314.

[72] Hannah Petersen and Marcus Bleicher. “Longitudinal flow and onset of deconfinement”. In: *PoS* CPOD2006 (2006). Ed. by Francesco Becattini, p. 025. DOI: 10.22323/1.029.0025. arXiv: nucl-th/0611001.

[73] R. Stock. In: *Phys.Rep* 135 (1986), p. 259.

[74] M. Gazdzicki and D. Rhoerich. In: *Z.Phys* C65 (1994), p. 215.